Jigsaws Falling into Place: Advances in Event Reconstruction and Electroweak Supersymmetry at ATLAS

Abhishek S. Sharma

Supervisors:
A/Prof Paul Jackson
A/Prof Martin White

A thesis submitted toward the degree of
Doctor of Philosophy
at
School of Physical Sciences
The University of Adelaide
October 2020

Contents

Abstract

Searches for beyond the Standard Model (BSM) physics are difficult to undertake, especially so at hadron colliders where the true energy of the collisions cannot be determined. An industry of analysis techniques and variables has been developed to more clearly separate BSM processes of interest, the archetype being supersymmetric (SUSY) particle decays, from Standard Model backgrounds.

Recursive Jigsaw Reconstruction (RJR) is a technique which attempts to find the centre-of-mass reference frame of particle decays, solving for combinatoric and kinematic ambiguities by defining decay trees. This work describes the application of this technique to the electroweak production and decay of SUSY particles, using data collected by the ATLAS experiment at the Large Hadron Collider. A global likelihood analysis using the GAMBIT framework is also presented, placing the analysis in context with other results in high energy physics. Additionally, studies in analysis development using RJR are outlined, with the focus being on addressing combinatoric ambiguities in top quark processes.

The development of electron identification efficiency at low energies at ATLAS is also presented in this work. While collision energies and intensities increase the requirement for low energy object reconstruction and identification remains a key factor in both Standard Model and BSM analyses. The results presented in this work allowed for the lower bound on electron energy to be reduced from 7 GeV to 4.5 GeV.

Declaration

I certify that this work contains no material which has been accepted for the award of any other degree or diploma in my name, in any university or other tertiary institution and, to the best of my knowledge and belief, contains no material previously published or written by another person, except where due reference has been made in the text. Plots which are labelled ATLAS have been published by the ATLAS Collaboration, otherwise they are my own. In addition, I certify that no part of this work will, in the future, be used in a submission in my name, for any other degree or diploma in any university or other tertiary institution without the prior approval of the University of Adelaide and where applicable, any partner institution responsible for the joint-award of this degree.

I acknowledge that copyright of published works contained within this thesis resides with the copyright holder(s) of those works.

I also give permission for the digital version of my thesis to be made available on the web, via the University's digital research repository, the Library Search and also through web search engines, unless permission has been granted by the University to restrict access for a period of time.

I acknowledge the support I have received for my research through the provision of an Australian Government Research Training Program Scholarship.

IN MEMORY OF MY GRANDFATHER

PERMAL SWAMY

WHO TAUGHT ME MUCH ABOUT
CURIOUSITY, PATIENCE, AND HUMILITY

Acknowledgements

उत्तिष्ठत जाग्रत
प्राप्य वरान्निबोधत ।
क्षुरस्य धारा निशिता दुरत्यया
दुर्गं पथस्तत्कवयोवदन्ति ॥

Arise, awake, and learn by approaching those most excellent teachers.
The wise ones describe that path to be as impassable as a razor's edge, which, when sharpened, is difficult to tread upon.

- Katha Upanishad I.iii.14

Thanks to my supervisor Paul Jackson for so generously sharing his support, knowledge, and encouragement throughout my PhD. It has been an absolute pleasure to have worked under your guidance. I am grateful to my co-supervisor Martin White for his insights and wisdom, particularly in the interplay between experiment and phenomenology, often delivered in the most humorous way possible. Special thanks must go to Andreas Petridis who taught me so much about how physics research is done, and whose confidence in my abilities often outstripped my own. I'm much obliged to RJR wizards Chris Rogan and Marco Santoni for sharing their secrets with me. I'm very thankful that Frédéric Déliot landed on our shores and took the time to teach me a lot about top quark physics.

It takes a lot of work to run the LHC and the ATLAS detector: thanks to all those who make it happen. Within the ATLAS Collaboration I extend my gratitude to the Electroweak SUSY group, the Electron ID group, and those working in ITK, for lending their considerable expertise to my work and making me feel at home in the

collaboration. Thanks to those from Freiburg, LBL, and SLAC who kindly hosted me for ITK related activities.

I've been lucky to have done most of my work with a local group of friends and colleagues, all very appreciated: Jason, Damir, Tristan, Anum, Emily, Albert, and Charles. The strength and range of experience of the Adelaide group is something to be proud of. Many thanks to Sharon and Silvana, the CSSM/CoEPP administrators, for their help with travel, funds, and other essentials.

Thanks to the denizens of Room 119, Room 123, and the faraway Siberians, for creating a stimulating and lively work environment. Varied (often ridiculous) discussions over tea, coffee, beers and gin were always a highlight. To my officemates in 123a, thanks for putting up with me all these years.

Thanks to Tomasz, Joel, Paul, Tom, Millie, Cameron, Steve, and Gen, who I don't get to see much these days but are always supportive!

Finally thanks to my family: my parents for providing me with the opportunities to improve myself and encouraging me in all my endeavours; my sister Jaya for being simultaneously brilliant and hilarious; my cousin Shiven for sharing his considerable energy and enthusiasm and; my aunts Pam, Jyoti, and Uma, and uncle Asvin for their support; and especially my grandmother for always checking to make sure I'm doing OK.

1 Introduction

परोक्षप्रिया इव हि देवाः प्रत्यक्षद्विषः ॥

"The gods love what is mysterious and dislike what is evident."

- Brihadaranyaka Upanishad I.ii.2

While the Standard Model of particle physics, describing all known particles and their interactions (bar gravity) has performed admirably in the 50 years of its existence, it cannot be the final theory of matter. The existence of dark matter, lack of gauge coupling unification in the Standard Model, and the scarcity of antimatter in the universe point to a further theory which encompasses the Standard Model and its shortcomings. One such theory is supersymmetry, where at some energy scale partners of the existing particles will be produced. Supersymmetry can stabilise the mass of the Higgs boson and achieve gauge coupling unification, while providing a dark matter candidate. To test the Standard Model and to search for its successor, particle colliders and detectors form the experimental apparatus: in this case the Large Hadron Collider and the ATLAS detector accelerating, colliding, and analysing (mostly) protons on the Franco-Swiss border.

While the Large Hadron Collider era has not thus far lead to the discovery of strongly coupled supersymmetry, an increasing dataset and the development of analysis techniques presents the opportunity to study electroweak supersymmetry. The supersymmetric partners of the electroweak bosons offset their lower production rates with distinctive signals and more amenable final states, but advances in reconstruction and identification of particles in the detector, along with robust analysis techniques are required nonetheless.

This thesis will centre around a search for an archetypal electroweak supersymmetry process, the production of a chargino and neutralino decaying to lighter neutralinos via a W and a Z boson. The decay mode of the W separates the two lepton + jets channel from the three lepton channel. These two channels are reconstructed using Recursive Jigsaw Reconstruction and signal regions are defined for a broad range of masses and mass splittings. The results with 2015-16 data and then an update with the full 2015-18 dataset will be shown, along with a global fit of electroweak supersymmetry parameters.

The thesis begins in Chapter 2 with a brief description of the Standard Model particles and their interactions. Chapter 3 describes supersymmetric theories, with particular focus on the particle content of the Minimal Supersymmetric Standard Model, and the electroweak sector thereof. The Large Hadron Collider and the ATLAS Experiment are summarised in Chapter 4, describing the various detector systems and the reconstruction of objects used in physics analysis. Monte Carlo simulation of physics processes is also outlined.

A brief detour to performance work in electron efficiency measurements is taken in Chapter 5, where tag-and-probe methods with J/ψ mesons are used to determine the identification efficiency of the lowest energy electrons that ATLAS can reconstruct. Improvements to the method and studies of trigger behaviour lead to lower thresholds of viable electrons at ATLAS, with an application being electroweak supersymmetry searches where the mass splittings are small.

Chapter 6 discusses Recursive Jigsaw Reconstruction, a method for resolving kinematic and combinatoric ambiguities at proton-proton colliders. Through a set of examples, different jigsaw rules are defined and applied to decay trees which attempt to reconstruct the centre-of-mass frames of various particles in an event. The treatment of ISR boosted processes is also discussed, and finally the classes of variables that can be derived from the method are listed.

The initial electroweak supersymmetry search is described in Chapter 7, with the definition of regions with respect to benchmark models and background estimation techniques. The results are examined in some detail, and a global likelihood analysis

using GAMBIT is presented. A follow-up analysis of the regions targeting mass splittings around the Z boson mass is documented in Chapter 8.

Finally other studies, mostly top quark processes and all relying upon Recursive Jigsaw Reconstruction, form Chapter 9. Here ideas on how to reconstruct processes with many objects both visible and invisible, and hence with larger kinematic and combinatoric ambiguities, are discussed. The majority of these processes are currently studied using low level inputs combined with careful machine learning treatments, so a purely kinematic treatment is novel.

2 The Standard Model

The Standard Model of particle physics (SM) is a quantum field theory describing the constituents of matter and the three forces that govern their interactions: strong, weak, and electromagnetic [1–3]. The SM is the culmination of subatomic physics in the 20th century and is the result of progressive unification theories of matter and interactions. A wide variety of experimental measures agree very precisely with theoretical calculations, but there are some limitations to the model and some phenomena that it cannot predict.

2.1 Particle content and interactions

There are a number of ways to categorise the fundamental particles of the SM. One basic descriptor is the type of spin statistics they obey: fermions have half integer spin values and obey Fermi-Dirac statistics, while bosons have integer spin and are governed by Bose-Einstein statistics.

The SM fermions consist of the quarks and the leptons, the fundamental building blocks of matter, and both the quarks and leptons fall into three generations. Each particle has an anti-matter counterpart with the same mass but opposite quantum numbers. Quarks interact with all three SM forces, while the charged leptons interact via electromagnetic and weak forces. The neutrinos, which as their name suggests are electrically uncharged, only interact via the weak force and are assumed to be massless in the SM. These particles are treated as point-like, and have no detectable substructure.

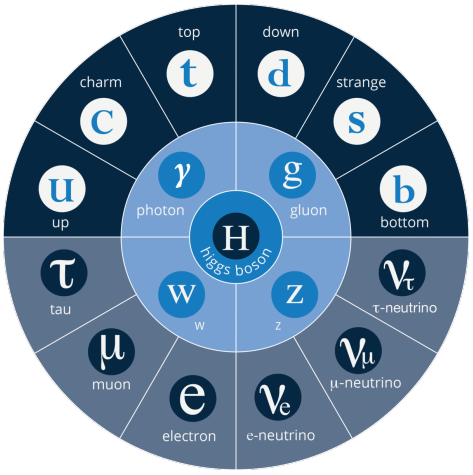

Figure 2.1: An artistic representation of the SM particle content. From the outside in, the fermions with the quarks in the top half and the leptons in the bottom half, the gauge bosons inside that, and the Higgs boson in the centre [6].

Spin 1 bosons are the force carriers of the SM, and mediate interactions between the fermions. The electromagnetic, weak, and strong forces are mediated by the photon, W & Z bosons, and the gluon respectively.

In 2012 the final piece of the SM, the Higgs boson, was discovered by the two general-purpose LHC experiments [4, 5]. The Higgs boson is a spin 0 (scalar) particle responsible for giving masses to the fundamental fermions and the weak bosons via spontaneous symmetry breaking.

Electrons, muons and tau leptons have electric charge -1 (+1 for their corresponding anti-particles), while quarks have fractional electric charge, $^{+2}/_{3}$ for the up type quarks and $^{-1}/_{3}$ for the down type quarks (anti-particles have opposite sign charge again). Quarks also have three colour species, red, blue, and green; gluons carry eight combinations of two separate colours, thereby allowing quarks of different colour to interact. Gluons can also interact among themselves.

The weak interaction couples to leptons in each generation while abiding by the overall charge of the leptons, $W^+ \rightarrow \ell^+ \nu_\ell$. The weak bosons couple to the weak eigenstates of the quarks which are linear combinations of the mass eigenstates, mixed by the Cabibbo-Kobayashi-Maskawa (CKM) matrix. This mixing leads to the

weak interaction violating quark flavour, and furthermore due to the complex phase term in the CKM matrix the weak interaction is also CP-violating.

2.2 Construction of the Standard Model

2.2.1 Quantum field theories and symmetries of nature

Symmetry is a vital part of the development of the Standard Model, with symmetries corresponding to conservation laws from Noether's famous theorem [7]. In the macroscopic world some intuitive laws have their mathematical basis given by this principle, for example saying that the laws of physics are the same at all spatial locations leads to the conservation of linear momentum. When moving to the microscopic, quantum field theories (QFTs) are the mathematical framework on which theories are constructed, but the symmetry remains vital. Point particles are generalised to quantised fields.

The starting point for the SM, as with any QFT, is the action. This is defined as the space-time integral of the Lagrangian density. [1]

$$S = \int d^4x \mathcal{L}(\Phi(x), \partial_\mu \Phi(x)), \tag{2.1}$$

where $\Phi(x)$ is a generic field.
Dynamics and interactions are expressed by the Euler-Lagrange equation:

$$\partial_\mu \frac{\delta \mathcal{L}}{\delta(\partial_\mu \Phi)} - \frac{\delta \mathcal{L}}{\delta \Phi} = 0. \tag{2.2}$$

When the action has a continuous symmetry a conserved current J^μ can be constructed by Noether's theorem which satisfies

$$\partial_\mu J^\mu = 0 \tag{2.3}$$

[1] The Lagrangian density is often simply known as the Lagrangian, a convention that will be applied herein.

and the charge associated with the current

$$Q \equiv \int d^3x J^0 \tag{2.4}$$

is a constant of motion,

$$\frac{dQ}{dt} = 0 \tag{2.5}$$

The Standard Model is a relativistic QFT which is based on the internal symmetry transformations known as gauge transformations. When the symmetry principle is applied to the Lagrangian new vector fields are introduced to maintain gauge invariance. To explain the experimental measurements of massive W and Z bosons spontaneous symmetry breaking and the Higgs mechanism are introduced. The SM is based on internal symmetries of $SU(3)_C \times SU(2)_L \times U(1)_Y$ where C, L and Y are the colour, left-handed weak isospin and hypercharge quantum numbers respectively.

2.2.2 Quantum Electrodynamics

Quantum electrodynamics (QED) is the prototypical gauge field theory, covering interactions of electrically charged particles and light, invariant under complex phase rotations of the particle fields. QED is based on the Abelian $U(1)_Q$, where Q (electric charge) is the generator.

The Dirac formulation describes the Lagrangian of a free fermionic field:

$$\mathcal{L}_D = i\bar{\Psi}_D \gamma^\mu \partial_\mu \Psi_D - m\bar{\Psi}_D \Psi_D \tag{2.6}$$

where Ψ_D is a four component Dirac field. This Lagrangian is invariant under global transformations but on promoting a global transformation to a local gauge one

$$\Psi_D \to e^{i\theta(x)} \Psi_D \tag{2.7}$$

there is an extra term in the Lagrangian. Gauge invariance is maintained by the additional term

$$\mathcal{L} \to \mathcal{L}_D - g_e \bar{\Psi}_D \gamma^\mu A_\mu \Psi_D \tag{2.8}$$

with the gauge field A_μ transforming like

$$A_\mu \rightarrow A_\mu + \partial_\mu \lambda, \text{ where } \lambda(x) = -\frac{\theta(x)}{g_e}. \tag{2.9}$$

A free term must be added to the Lagrangian. Defining the electromagnetic field tensor $F \equiv \partial_\mu A_\nu - \partial_\nu A_\mu$, a non interacting Lagrangian for the field A_μ can be written as

$$\mathcal{L} = -\frac{1}{4} F^{\mu\nu} F_{\mu\nu} + \frac{1}{2} m_A^2 A^\mu A_\mu \tag{2.10}$$

where the mass term is not invariant under gauge transforms of the type specified in Equation 2.9. To maintain local gauge invariance the vector is made massless ($m_A = 0$). Thus the QED Lagrangian is

$$\mathcal{L}_{QED} = \bar{\Psi}_D (i\gamma^\mu \mathcal{D}_\mu - m)\Psi_D + \mathcal{L}_\gamma \tag{2.11}$$

where $\mathcal{D}_\mu \equiv \partial_\mu + i g_e A_\mu$ is the covariant derivative, and $\mathcal{L}_\gamma = -\frac{1}{4} F^{\mu\nu} F_{\mu\nu}$ is the free massless photon term.

QED is a renormalisable theory, like the other gauge theories making up the SM, meaning the infinities from loop Feynman diagrams contributing to the self energies of the fields can be eliminated from the theory. Physically, this translates to the QED coupling $g_e(E)$, more commonly written as the fine structure constant $\alpha_e(E) = \frac{g_e^2(E)}{4\pi}$, being dependent on energy, running with the scale of the interaction.

2.2.3 Quantum Chromodynamics

To explain the myriad baryons constructed from quarks and their associated force carriers a gauge group of dimension $N = 3$, following the Yang-Mills theory describing non-Abelian local gauge transformations is required. Quantum Chromodynamics (QCD) follows the $SU(3)_C$ group, with C being the colour charge. Making $SU(3)_C$ gauge invariant to the quark fields introduces $N^2 - 1 = 8$ gauge coloured fields called gluons.

The six flavours of quarks (q) are fermionic fields (Ψ_D) arranged in a triplet

$$\psi \equiv \begin{pmatrix} q_r \\ q_g \\ q_b \end{pmatrix}, \bar{\psi} \equiv (\bar{q}_r, \bar{q}_g, \bar{q}_b) \tag{2.12}$$

with the Lagrangian written very similarly to that of QED

$$\mathcal{L}_{QCD} = \bar{\psi}(i\gamma^\mu \mathcal{D}_\mu - m)\psi - \frac{1}{4}\mathbf{G}^{\mu\nu} \cdot \mathbf{G}^{\mu\nu}, \tag{2.13}$$

where the covariant derivative $\mathcal{D}$ and the field strength tensor $\mathbf{G}$ are defined

$$\mathcal{D}_\mu \equiv \partial_\mu - ig_s \mathbf{T} \cdot \mathbf{A}_\mu, \tag{2.14}$$

$$\mathbf{G}_{\mu\nu} \equiv \partial_\mu \mathbf{A}_\nu - \partial_\nu \mathbf{A}_\mu - ig_s[\mathbf{A}_\mu, \mathbf{A}_\nu]. \tag{2.15}$$

The generators of this group are the 8 Gell-Mann matrices (up to a factor), with non-commuting algebra

$$[\lambda^a, \lambda^b] = 2if^{abc}\lambda^c \tag{2.16}$$

The commutator in Equation 2.15 $[\mathbf{A}_\mu, \mathbf{A}_\nu]^a = if^{abc}A^b_\mu A^c_\nu$ leads to triple and quartic gluon couplings, a marked difference from the interactions in QED. Gluons carry colour charge unlike the photon which has no electrical charge.

QCD has two features which distinguish it from the other components of the SM: asymptotic freedom and confinement. The strength of the interaction ($\alpha_s(E)$) decreases logarithmically with increasing energy, and at energies probed by the LHC quarks and gluons in the protons interact directly: they are effectively free at short ranges. On the other end of the energy range, at lower energies perturbative methods cannot be applied due to the strength of the interaction. In addition baryons and mesons are only observed as colour singlets, a consequence of confinement, where individual coloured particles cannot be isolated and detected. Due to the strong gluon fields near coloured particles, at some point it is energetically favourable for a quark anti-quark pair to manifest from the vacuum. For very high energy coloured particles the hadronisation process can repeat many times, leading to collimated jets of hadrons.

2.2.4 Electroweak unification

The unification of the weak and electromagnetic forces $SU(2)_L \times U(1)_Y$ stems from Glashow in 1961 [1], where the $SU(2)_L$ acts on left-handed fermions (or right-handed anti-fermions) and $U(1)_Y$ is the weak hypercharge group, where hypercharge is given by the Gell-Mann-Nishijima formula

$$Y = Q - I_3/2 \tag{2.17}$$

is the average electric charge of the multiplet, with Q being the electric charge and I_3 the third component of weak isospin. Hypercharge is conserved under strong interactions. Due to the nature of the weak force, the chiral-left component of the electrically charged leptons and associated neutrinos are in the $SU(2)_L$ doublet while the chiral-right electron, muon and tau are in a separate singlet. Up-type quarks behave like neutrinos (weak isospin $+^1/_2$ and down-type quarks behave like the charged leptons (weak isospin $-^1/_2$),

$$\psi_L^{doublet} \equiv \begin{pmatrix} \nu_L^e \\ e_L \end{pmatrix} = \begin{pmatrix} \nu_e \\ e \end{pmatrix}_L, \begin{pmatrix} \nu_\mu \\ \mu \end{pmatrix}_L, \begin{pmatrix} \nu_\tau \\ \tau \end{pmatrix}_L, \begin{pmatrix} u \\ d \end{pmatrix}_L, \begin{pmatrix} c \\ s \end{pmatrix}_L, \begin{pmatrix} t \\ b \end{pmatrix}_L \tag{2.18}$$

$$\psi_R^{singlet} \equiv e_R, \mu_R, \tau_R, u_R, d_R, c_R, s_R, t_R, b_R. \tag{2.19}$$

Imposing local gauge invariance leads to four new massless vector (spin 1) bosons. The covariant derivative is defined as

$$\mathcal{D}_\mu \equiv \partial_\mu - i g_w \boldsymbol{\sigma} \cdot \mathbf{W}_\mu - i g_Y Y B_\mu, \tag{2.20}$$

where $\tau^i = \sigma^i/2$ are (up to a factor) the Pauli matrices, and g_w and g_Y are the weak and electromagnetic running coupling constants.
The total Dirac Lagrangian for the electroweak theory is

$$\mathcal{L}_{EW} = \bar{\psi}(i\gamma^\mu \mathcal{D}_\mu - m)\psi - \frac{1}{4}\mathbf{W}^{\mu\nu} \cdot \mathbf{W}_{\mu\nu} - \frac{1}{4} B^{\mu\nu} B_{\mu\nu}, \tag{2.21}$$

where ψ are the chiral-left or chiral-right fields. As per the restrictions of weak interactions W_μ in the covariant derivative is zero for right-handed states.

2.2.5 Spontaneous symmetry breaking and the Higgs mechanism

The weak nature of nuclear decays was well known prior to the inception of QFT, with Fermi describing beta decay $n \to pe\bar{\nu}_e$, and introducing the neutrino in the process. The half-life of the neutron is about 15 minutes and the contact interaction

$$H = \frac{G_F}{\sqrt{2}}(\bar{p}\gamma^\mu n)(\bar{e}\gamma_\mu \nu_e) + h.c., \tag{2.22}$$

where the Fermi constant is a parameter relating to the proton mass

$$G_F \simeq \frac{10^{-5}}{m_p^2}. \tag{2.23}$$

The discovery of parity violation suggested some sort of vector-axial theory and when weak interactions were included in a gauge theory, it was clear that massive vector bosons were required. The weakness of the weak force is not related to the coupling but is instead solved with the introduction of a mass term in the Feynman propagator. Weinberg and Salam obtained the complete solution using the *Higgs mechanism* which uses spontaneous electroweak symmetry breaking (EWSB) [2, 3, 8–10]. The Higgs acquires a non-zero expectation value (VEV), which breaks the groups $SU(2)_L \times U(1)_Y$. Introducing four real scalar fields, or a complex $SU(2)_L$ doublet of scalars, an $SU(2)_L \times U(1)_Y$ gauge invariant Lagrangian for the scalar field ϕ can be added to Equation 2.21:

$$\mathcal{L}_\phi = |(\partial_\mu - ig_w \boldsymbol{\sigma} \cdot \mathbf{W}_\mu - ig_Y Y B_\mu)\phi|^2 - V(\phi), \tag{2.24}$$

where $|\cdot|^2 = (\cdot)^\dagger(\cdot)$ and the four fields ϕ_i are in an isospin doublet with hypercharge $Y = \frac{1}{2}$,

$$\phi = \begin{pmatrix} \phi^+ \\ \phi^0 \end{pmatrix} \equiv \begin{pmatrix} 1/\sqrt{2}(\phi_1 + i\phi_2) \\ 1/\sqrt{2}(\phi_3 + i\phi_4) \end{pmatrix}. \tag{2.25}$$

The potential $V(\phi)$ in Equation 2.24 can be expressed as

$$V = \mu^2 \phi^\dagger \phi + \lambda(\phi^\dagger \phi)^2, \tag{2.26}$$

and when $\mu^2 < 0$ and $\lambda > 0$ it takes the well known sombrero-like shape. When the potential is minimised for the ground state $\phi^\dagger \phi = -\frac{\mu^2}{2\lambda}$ is found. By choosing the ground state, spontaneous symmetry breaking occurs due to the underlying

symmetry of the Lagrangian being hidden by the asymmetric vacuum. The usual choice for the vacuum expectation value is

$$\phi^0 = \frac{1}{\sqrt{2}}\begin{pmatrix}0\\v\end{pmatrix}, \tag{2.27}$$

which permits only neutral scalars to acquire a VEV, conserving electric charge. Thus the Weinberg-Salam model preserves a massless photon, while in general any choice of ϕ^0 which breaks symmetry will generate mass for the corresponding gauge boson. The choice made in Equation 2.27 is good for the case of $SU(2)_L \times U(1)_Y$ as the vacuum is invariant under the subgroup $U(1)_Q$ ($Q\phi^0 = 0$), with the gauge boson being massless. This is valid for hypercharge as constructed in Equation 2.17. Expanding around this chosen vacuum value, due to the $SU(2)_L$ gauge invariance, the expression

$$\phi = \frac{1}{\sqrt{2}}\begin{pmatrix}0\\v + H(x)\end{pmatrix} \tag{2.28}$$

can be substituted into the Lagrangian, where $H(x)$ is the Higgs boson of the Standard Model. The generic expansion of the scalar field $\varphi = \frac{1}{\sqrt{2}}(v + \eta + i\xi)$ can be chosen fixing $\eta \to H$ and $\xi \to \theta$ are real, $\varphi \to \frac{1}{\sqrt{2}}(v + H(x))e^{i\theta(x)/v}$. The unwanted massless Goldstone boson ($\xi \to \theta$) doesn't appear in the theory, and the kinetic term is absorbed into the gauge field definition, with the upshot being a mass for the gauge field from the VEV. For the $SU(2)_L$ theory, there are 4 real fields, but only the Higgs survives in the Lagrangian while the other three fields $\theta_1, \theta_2, \theta_3$ are taken by the gauge bosons providing masses (and longitudinal polarisation states) for the $W^{\pm}$ and Z bosons.

Gauge invariance and spontaneous symmetry breaking applied to electroweak theory is known as the Higgs mechanism, providing the mass of the Higgs and masses of fermions and vector bosons in the SM.

2.2.6 Masses of SM particles

The Higgs mechanism provides a massive Higgs boson. The quartic term in the Higgs potential results in the mass term for the Higgs

$$m_H = \sqrt{2\lambda}v, \tag{2.29}$$

where the three massless Goldstone bosons are "eaten" by the gauge fields. The W and Z boson and the photon are now linear combinations of the electroweak fields

$$W_\mu^\pm = \frac{1}{\sqrt{2}}(W_\mu^1 \mp iW_\mu^2), \tag{2.30}$$

$$Z_\mu = cos\theta_W W_\mu^3 - sin\theta_W B_\mu, \tag{2.31}$$

$$A_\mu = cos\theta_W B_\mu + sin\theta_W W_\mu^3, \tag{2.32}$$

where θ_W is the Weinberg angle, parameterising the relative strengths of the hypercharge and weak interactions ($tan\theta_W = \frac{g_Y}{g_w}$). Looking at the expected mass terms in Equation 2.24 and comparing with terms proportional to the Higgs VEV, the following are obtained

$$M_{W^\pm} = \frac{1}{2}vg_w \tag{2.33}$$

$$M_Z = \frac{1}{2}v\sqrt{g_w^2 + g_Y^2} \tag{2.34}$$

where $\frac{M_{W^\pm}}{M_Z} = cos\theta_W$. ϕ couples with both left- and right-handed fermion fields, generating their masses. As an example, the electron is represented as

$$\mathcal{L}_{e\phi}^{int} = -\frac{y_e}{\sqrt{2}}v(\bar{e}_L e_R + \bar{e}_R e_L) - \frac{y_e}{\sqrt{2}}(\bar{e}_L e_R + \bar{e}_R e_L)H. \tag{2.35}$$

Importantly the mass of the electron, $m_e = \frac{y_e v}{\sqrt{2}}$ along with the other fermions, depends on an arbitrary y_e known as the Yukawa coupling. The masses of the quarks are generated in a similar fashion with a change for the up-type quarks, where the Higgs doublet is written with opposite hypercharge $\phi_c = -i\sigma_2\phi^*$, which transforms identically to ϕ for $SU(2)_L$. $v \sim 246\,\text{GeV}$ is the governing scale of the masses in the SM. The general fermion mass equation

$$m_f = \frac{y_f v}{\sqrt{2}} \tag{2.36}$$

means that by measuring both the mass of the fermion in question and determining the value of v, done by precision electroweak measurements, the Yukawa coupling can be understood.

While the Higgs is responsible for the masses of the fundamental fermions and electroweak bosons, the masses of colourless mesons and baryons are not solely due to the constituent quarks but through QCD binding.

2.3 Limitations and tensions

Despite being a wildly successful theory there are a number of shortcomings of the SM: some stemming from its inability to describe certain phenomena, others relating to its theoretical structure and stability at high energies. This section will present some of the most prominent issues with the SM.

2.3.1 Dark matter

Based on astrophysical and cosmological observations it has been deduced that the greater part of the mass-energy of the universe is not described by SM particles. Indeed 85% of the mass of the universe is unaccounted for, forming a mysterious bloc that is known as dark matter (DM)[2].

The first indications that there is more matter than is observed came from velocity dispersions of stars within the Milky Way and clusters of galaxies in the 1930's [11]. Later on by measuring the rotation curves of spiral galaxies as functions of radius, objects which are constrained by conservation of angular momentum and should follow Keplerian behaviour, but instead showed roughly constant stellar velocities independent of radial position [12, 13]. This implied uniform mass density far beyond the visible matter in the galaxies.

With advanced gravitational lensing techniques being able to measure lens masses and distributions more accurately, it has been shown that the mass required to produce the observed amount of lensing from galaxy clusters is much more than the luminous matter [14]. On the cosmological scale, precision measurements of

[2] There are explanations for the missing mass that do not involve dark matter, such as modified gravity theories, but they are disfavoured by the body of astrophysical evidence.

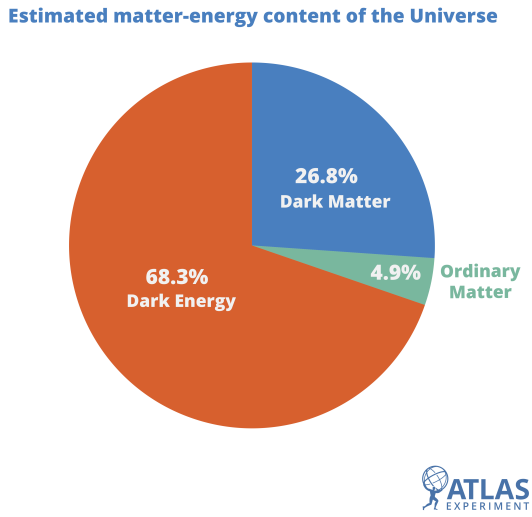

Figure 2.2: A schematic representation of the matter-energy density of the universe [16].

the cosmic microwave background (CMB) cannot be reproduced without a sizeable dark matter component to the total energy density of the universe [15].

The candidates for dark matter span a huge mass range, from sub-eV axions to massive astrophysical objects such as primordial black holes, though the astrophysical objects cannot be abundant enough to account for all the dark matter that is inferred.

2.3.2 Neutrino masses

The discovery of neutrino mixing implies that neutrinos have some (very small) intrinsic mass, which is at odds with the long held view that they are massless [17]. There is no way for the neutrino to gain mass within the SM Higgs mechanism so other extensions to the SM need to be implemented, and there are a different set of ambiguities to be resolved with each proposed extension, chief among them being whether neutrinos behave like ordinary Dirac fermions or whether they are their own anti-particles following Majorana statistics. Many extensions of the neutrino sector also involve the introduction of new particles such as sterile neutrinos.

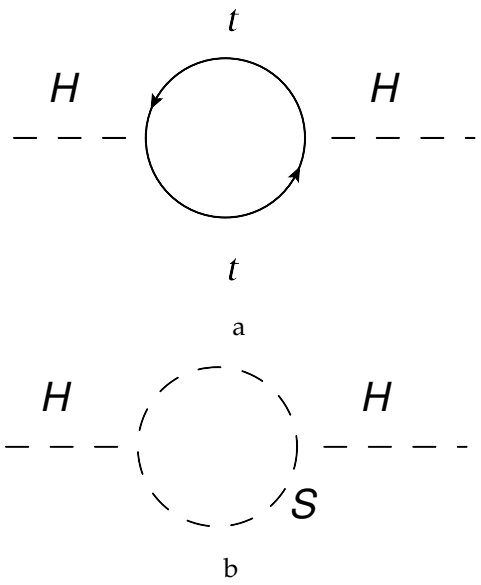

Figure 2.3: One loop corrections to the Higgs mass due to (a) fermions, and (b) due to a scalar.

2.3.3 Hierarchy problem

A more structural issue with the SM is that of the hierarchy problem. The Higgs self-energy (m_h^2) has quantum corrections from all the particles it interacts with, either directly or indirectly.

Regularising the SM introduces an ultraviolet cutoff scale Λ_{UV}, interpreted as the scale at which new physics will enter to affect the high energy behaviour of the theory. The SM particles contribute one-loop corrections to the Higgs mass

$$\Delta m_H^2|_{fermion} = -\frac{y_f^2 \Delta_{UV}^2}{8\pi^2}, \Delta m_H^2|_{gauge} = -\frac{9g^2 \Delta_{UV}^2}{64\pi^2}, \Delta m_H^2|_{Higgs} = -\frac{\lambda \Delta_{UV}^2}{16\pi^2} \qquad 2.37$$

with the top quark having the largest effect due to its large Yukawa coupling. The amount of cancellation required to achieve a Higgs mass at the electroweak scale is then proportional to the cutoff scale. So if $M_{\Delta_{UV}} / M_{Higgs} \sim 10^{12}$ GeV, the cancellations must be $O(10^{12})$ GeV, known as as the hierarchy problem. This arbitrary and convenient cancellation can be the result of additional particles appearing at higher energies than currently accessible.

3 Supersymmetry

Supersymmetry (SUSY) [18–23] is a well motivated and popular beyond the Standard Model (BSM) theoretical construct which can resolve many of the shortcomings of the SM, some of which were presented in Section 2.3. The hierarchy problem is a particularly troublesome issue in the SM, with the corrections to the Higgs boson mass being many orders of magnitude greater than the measured mass, and is resolved when supersymmetric extensions are considered. Supersymmetry is also capable of unifying gauge couplings in some high energy regime (as shown in Figure 3.1), and can also provide a suitable dark matter candidate (provided some reasonable model constraints). This chapter will discuss the basic idea of supersymmetry, the Minimal Supersymmetric Standard Model, supersymmetric electroweak interactions, and simplified models that are used in LHC searches[1].

[1] This chapter will largely draw from [24], an excellent introduction to supersymmetry and its implications in collider experiments.

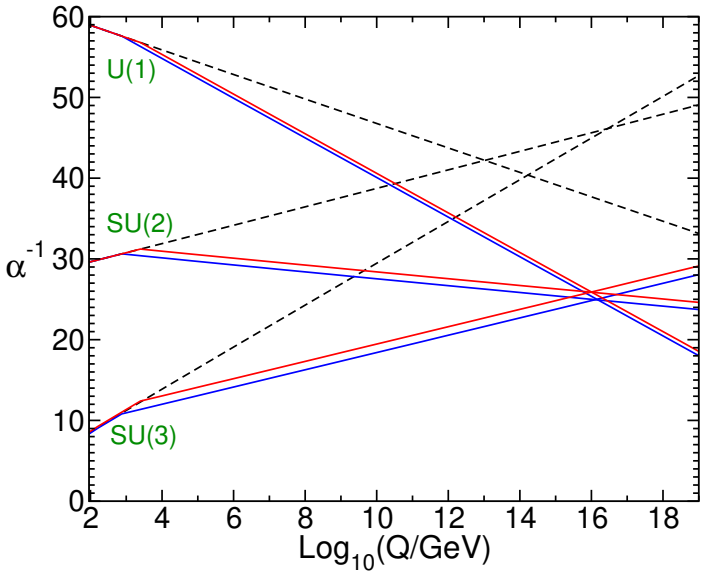

Figure 3.1: The running of the strong, weak and EM coupling constants with energy scale for the SM (dashed lines) and MSSM (solid lines) [24].

3.1 Why SUSY?

As written in Section 2.3.3 the fermionic loop corrections to the Higgs mass in the SM take the form

$$\Delta m_H^2|_{\text{fermion}} = -\frac{y_f^2 \Delta_{UV}^2}{8\pi^2}, \tag{3.1}$$

with the top quark having the greatest contribution due to its Yukawa coupling. Since the Higgs boson that is observed has a mass close to the electroweak scale, not the nearly arbitrarily large UV cutoff scale, there must be a cancellation at work to stabilise the Higgs mass. Now considering a complex scalar S with mass m_S that couples to the Higgs, the loop correction takes the form

$$\Delta m_H^2|_S = \frac{\lambda}{16\pi^2}(\Delta_{UV}^2 - 2m_s^2 log(\Delta_{UV}/m_S + ...) \tag{3.2}$$

then there is no way to remove the dependence on the new particle even using dimensional regularisation. Noticing the relationship between the fermion and boson terms for these Higgs loop corrections it seems reasonable to look for some symmetry property which will explain the eerie cancellation that stabilises the Higgs mass. If each SM fermion is partnered by two complex scalars satisfying

$\lambda_S = |\lambda_f|^2$, then the contributions will cancel nicely. This symmetry is known as *supersymmetry*.

A supersymmetric transformation turns bosons into fermions or vice versa, via an anticommutating spinor Q and its hermitian conjugate $Q^\dagger$. These operators are fermionic and so supersymmetry must be a spacetime symmetry. Indeed the forms that these operators can take are highly restricted by the Haag-Łopuszański-Sohnius extension [25] of the Coleman-Mandula theorem [26], which states that the only non-trivial extension of the Poincaré algebra is found by allowing commuting and anticommuting symmetry generators. Q and $Q^\dagger$ transforms a bosonic state $|B\rangle$ to a fermionic state $|F\rangle$

$$Q|B\rangle = |F\rangle, Q|F\rangle = |B\rangle. \tag{3.3}$$

The general procedure for supersymmetrising a QFT is to extend the four usual spacetime coordinates with additional Grassmann algebra obeying coordinates to form a *superspace*

$$x^\mu, \theta^\alpha, \theta^\dagger_{\dot{\alpha}}, \tag{3.4}$$

and then defining some *superfields* in this new coordinate system. A new *superlagrangian* λ is constructed from these superfields, with action given by

$$A = \int d^4x \int d\theta^2 d\theta^{\dagger 2} \Lambda(S_i(x, \theta, \theta^\dagger)) = \int d^4x \mathcal{L}_{SUSY}, \tag{3.5}$$

which reduces to a more familiar Lagrangian after integrating over the Grassmann coordinates. Thus SUSY transformations are translations in superspace. For theories with chiral fermions, such as the SM with its weak interaction, Q and $Q^\dagger$ must abide by some commutation and anticommutation relationships of the type

$$\{Q, Q^\dagger\} = P^\mu, \tag{3.6}$$

$$\{Q, Q\} = \{Q^\dagger, Q^\dagger\} = 0 \tag{3.7}$$

$$[P^\mu, Q] = [P^\mu, Q^\dagger], \tag{3.8}$$

where P^μ is the generator of the spacetime transformations [2].

[2] The spinor indices of the generators Q and $Q^\dagger$ are suppressed.

SUSY transformations of superspace require covariant derivatives

$$\begin{cases} D_\alpha & = \partial_\alpha + i(\sigma^\mu)_{\alpha\dot{\beta}}\theta^{\dagger\dot{\beta}}\partial_\mu \\ D^{\dagger\dot{\alpha}} & = \partial^{\dagger\dot{\alpha}} - i\theta^\beta(\sigma^\mu)^{\dot{\alpha}}_{\beta}\partial_\mu \end{cases} \tag{3.9}$$

The irreducible representations of the new *superalgebra* are chiral superfields Φ obtained by imposing the covariant constraint

$$D^\dagger_{\dot{\alpha}} S(x, \theta, \theta^\dagger) = 0. \tag{3.10}$$

Usually, new bosonic coordinates are introduced

$$y^\mu \equiv x^\mu + i\theta\sigma^\mu\theta^\dagger \; D^\dagger_{\dot{\alpha}} y^\mu \tag{3.11}$$

such that the left-handed chiral superfield is not dependent on the conjugate coordinate $\theta^\dagger$ and can be written as a Taylor expansion

$$\Phi(y, \theta) = \phi(y) + \sqrt{2}\theta\psi(y) + \theta^2 F(y). \tag{3.12}$$

With these new coordinates and descendent superfields a Lagrangian can be constructed by combining the *superpotential* $W(\Phi)$, and the Kähler potential $K(\Phi^\dagger\Phi)$ and integrating on the fermionic coordinates as in Equation 3.5.

3.2 The Minimal Supersymmetric Standard Model

After deriving the principle of supersymmetry it can be applied to extensions of the SM. The smallest extension is known as the Minimal Supersymmetric Standard Model, where the bosons and fermions are *superpartners* of each other and organised in representations known as *supermultiplets*. This is a form of $N = 1$ supersymmetry as there is a single instance of $Q, Q^\dagger$. Each of these supermultiplets has the same number of bosonic and fermionic degrees of freedom, and each of the single particle states in a supermultiplet has the same mass, colour, weak isospin, and hypercharge.

There are two varieties of supermultiplet: *chiral supermultiplets* (Φ) containing the fermions and their spin 0 counterparts, and *gauge supermultiplets* (V) with spin 1 bosons and spin 1/2 fermionic counterparts. The SM fermions must be in chiral

supermultiplets due to their left-handed components transforming differently to the right-handed components. The partners of the SM fermions are named by adding a prefix "s" for scalar to the existing fermion names, so the partners of the quarks are *squarks* (sup, stop, sbottom as examples) and the lepton partners are *sleptons* (selectron, stau, and a number of sneutrinos). Left and right-handed fermions have unique sfermion partners, which are denoted with tildes: $e_{\mathrm{L}} \rightarrow \tilde{e}_{\mathrm{L}}$ [3] for example. Given that the SM neutrinos are only left-handed, the sneutrinos are simply noted as $\tilde{\nu}$ with the appropriate flavour label attached. Finally there are $\tilde{q}_{\mathrm{L}}$, $\tilde{q}_{\mathrm{R}}$ for the six quark flavours. The gauge interactions of the sfermions are the same as the SM fermions they partner, most notably that the chirality is preserved so $\tilde{t}_{\mathrm{L}}$ and $\tilde{b}_{\mathrm{L}}$ will interact with the W but $\tilde{t}_{\mathrm{R}}$ and $\tilde{b}_{\mathrm{R}}$ won't.

The Higgs, being of spin 0, must be in a chiral supermultiplet. But to make the expanded theory consistent and free of gauge anomalies a single supermultiplet will not suffice. The fermionic partners of the Higgs will need to be of hypercharge $Y = +1$ or $Y = -1$, based on the normalisation in Equation 2.17, and then will not satisfy the anomaly cancellation based on the traces of the hypercharge and weak isospin parameters. In the SM the left-handed fermionic interactions satisfy these anomaly constraints "out of the box," so the minimal addition must be two Higgs chiral supermultiplets. This has an added benefit: a $Y = +1$ Higgs supermultiplet is needed to generate up-type quark masses, and a $Y = -1$ Higgs is needed to generate the down-type quark and charged lepton masses. These supermultiplets are named H_u and H_d respectively, with H_u containing neutral and positively charged components and H_d having neutral and negatively charged components.

The set of chiral supermultiplets for the MSSM is now complete, and is listed in Table 3.1, split into how they transform under the SM $SU(3)_C \times SU(2)_L \times U(1)_Y$ gauge group and defined in terms of the left-handed spinors (hence the conjugates of the right-handed particles in the supermultuplets).

The next aspect of the MSSM is the treatment of the gauge fields of the SM. The superpartners of the gauge bosons are spin $\frac{1}{2}$ fermions known as *gauginos*. The

[3] The $_{\mathrm{L}}$ and $_{\mathrm{R}}$ subscripts in the sfermion naming scheme are purely to reference which fermion they are partnered with, not the chirality of sfermions themselves.

Table 3.1: The chiral supermultiplets of the MSSM with complex scalar spin 0 fields and left-handed spin $\frac{1}{2}$ fermions.

Φ	spin 0	spin $\frac{1}{2}$	$SU(3)_C, SU)(2)_L, U(1)_Y$
	squarks	quarks	
Q	$(\tilde{u}_L\ \tilde{d}_L)$, $(\tilde{c}_L\ \tilde{s}_L)$, $(\tilde{t}_L\ \tilde{b}_L)$	$(u_L d_L)$, $(c_L s_L)$, $(t_L b_L)$	$(\mathbf{3}, \mathbf{2}, \frac{1}{6})$
U	$\tilde{u}^*_R$, $\tilde{c}^*_R$, $\tilde{t}^*_R$	$u^\dagger_R$, $c^\dagger_R$, $t^\dagger_R$	$(\bar{\mathbf{3}}, \mathbf{1}, \text{-}\frac{2}{3})$
D	$\tilde{d}^*_R$, $\tilde{s}^*_R$, $\tilde{b}^*_R$	$d^\dagger_R$, $s^\dagger_R$, $b^\dagger_R$	$(\bar{\mathbf{3}}, \mathbf{1}, \text{-}\frac{1}{3})$
	sleptons	leptons	
L	$(\tilde{\nu}_e\ \tilde{e}_L)$, $(\tilde{n}u_\mu\ \tilde{\mu}_L)$, $(\tilde{\nu}_\tau\ \tilde{\tau}_L)$	$(\nu_e\ e_L)$, $(\nu_\mu\ \mu_L)$, $(\nu_\tau\ \tau_L)$	$(\mathbf{1}, \mathbf{2}, -1)$
E	$\tilde{e}^*_R$, $\tilde{\mu}^*_R$, $\tilde{\tau}^*_R$	$e^\dagger_R$, $\mu^\dagger_R$, $\tau^\dagger_R$	$(\bar{\mathbf{1}}, \mathbf{1}, 1)$
	Higgs	Higgsinos	
H_u	$(H^+_u\ H^0_u)$	$(\tilde{H}^+_u\ \tilde{H}^0_u)$	$(\mathbf{1}, \mathbf{2}, \frac{1}{2})$
H_d	$(H^0_d\ H^-_d)$	$(\tilde{H}^0_d\ \tilde{H}^0_d)$	$(\mathbf{1}, \mathbf{2}, -\frac{1}{2})$

Table 3.2: The gauge supermultiplets of the MSSM.

V	spin $\frac{1}{2}$	spin 0	$SU(3)_C, SU)(2)_L, U(1)_Y$
g	$\tilde{g}$ gluino	g gluon	$(\mathbf{8}, \mathbf{1}, 0)$
W	$\tilde{W}^\pm$, $\tilde{W}^0$ winos	$W^\pm$, W^0 W bosons	$(\mathbf{1}, \mathbf{3}, 0)$
B	$\tilde{B}^0$ bino	B^0 B-boson	$(\mathbf{1}, \mathbf{1}, 0)$

$SU(3)_C$ of QCD has the gluon as force carrier and a spin $\frac{1}{2}$ colour octet supersymmetric partner called the *gluino*, know as g and $\tilde{g}$ respectively. The electroweak symmetry $SU(2)_L \times U(1)_Y$ has gauge bosons $W^\pm$, W^0, and B^0 with spin 1 and spin $\frac{1}{2}$ superpartners $\tilde{W}^\pm$, $\tilde{W}^0$, and $\tilde{B}^0$, the *winos* and *bino*. Once electroweak symmetry is broken then the neutral bosons give rise to the Z and γ mass eigenstates. The corresponding gauginos are zinos ($\tilde{Z}$) and photino ($\tilde{\gamma}$), and would have masses of m_Z and 0 respectively if supersymmetry was unbroken. The full set of gauge supermultiplets are summarised in Table 3.2.

In a SUSY theory all particle masses and interactions are determined by gauge transformation properties and W. The superpotential is constructed of superfields, themselves containing bosonic, fermionic, and auxiliary fields of a supermultiplet.

In this concise format the superpotential for the MSSM can be written as

$$W = U\mathbf{y_u}QH_u - D\mathbf{y_d}QH_d - E\mathbf{y_e}LH_d - \mu H_u H_d, \tag{3.13}$$

where each of the supermultiplets from Table 3.1 is included. The SUSY Lagrangian for the MSSM can be written as

$$\begin{aligned}\mathcal{L}_{SUS}^{\text{MSSM}} = &\int d\theta^2 d\theta^{\dagger 2} \sum_{\text{chiral}} \Phi^\dagger e^{\Sigma_a g_b V_a}\Phi + \int d\theta^2 \vec{Tr}\left(\frac{1}{4g_a^2} W_a^\alpha W_{a\alpha}\right) + h.c. \\ &+ \int d\theta^2 \mu H_u H_d + \mathbf{y}_u QUH_u - \mathbf{y}_d QDH_d - \mathbf{y}_l LEH_d + \text{h.c.}\end{aligned} \tag{3.14}$$

where the first term is the gauge and SUSY invariant kinetic terms and the W_α generalised field strength tensors. The second line represents the superpotential of the MSSM, and has the sign convention to produce positive fermion masses.

3.2.1 R-parity

The superpotential Equation 3.14 provides a minimal phenomenological model, however there are other terms that can be added neatly into the gauge and chiral structures, but are omitted due to violating baryon number (B) or lepton number (L). These terms take the form

$$W_{L-\text{violating}} = \frac{1}{2}\lambda_1 LLE + \lambda_2 LQD + \lambda_3 LH \tag{3.15}$$

and

$$W_{B-\text{violating}} = \frac{1}{2}\lambda_4 UDD, \tag{3.16}$$

with λ_4^{ijk} being antisymmetric in the last two flavour indices relating to the down-type superfields ($j \neq k = 1, 2, 3$).

There are very strong constraints on lepton and baryon number violating processes, especially on the stability of the proton[4], which means that at least one of the possible B and L-violating terms must be suppressed. The conservation of a discrete $\mathbb{Z}_2$ symmetry called R-parity is assumed in the MSSM, with R-parity defined as

$$R_p = (-1)^{3(B-L)+2s}, \tag{3.17}$$

[4] The Particle Data Group combined mean lifetime of the proton is at least 2.1×10^{29} years [27]

and s is the spin of the particle. The particles of the SM and the other Higgs bosons have $R_p = 1$, while the superpartners are R-parity odd. For a theory abiding by R-parity conservation there is no particle-sparticle mixing and every interaction vertex has either an even number of sparticles or none. In terms of phenomenology R-parity conservation means an even number of sparticles will be produced from a hard scattering event, since the inputs are SM particles, and that these particles will each decay to an odd number of sparticles until a lightest supersymmetric particle (LSP) is produced. Final states likely contain two of these LSPs which will escape the detector without interacting electromagnetically and/or strongly. Neutral LSPs provide a suitable dark matter candidate.

3.2.2 SUSY breaking and soft Lagrangians

Unbroken SUSY leads to sparticles with the same masses as their SM counterparts, something which clearly cannot exist. A bosonic electron for instance would lead to completely different chemistry, and the non-discovery of any sparticles means that any realistic SUSY model must have some sort of spontaneous symmetry breaking leading to sparticle masses of around the TeV scale.

Any breaking must still stabilise the Higgs mass, otherwise the structural issues of the SM will still persist. Symmetry breaking that still provides a solution for the hierarchy problem and cancellation of quadratic divergences is known as *soft* supersymmetry breaking. The total Lagrangian can be broken up

$$\mathcal{L} = \mathcal{L}_{\text{SUSY}} + \mathcal{L}_{\text{soft}}, \tag{3.18}$$

where $\mathcal{L}_{\text{SUSY}}$ contains only supersymmetry conserving terms and $\mathcal{L}_{\text{soft}}$ contains supersymmetry violating terms. This necessitates the introduction of a soft SUSY breaking scale m_{soft}, which modifies the Higgs correction terms to be of the following form

$$\Delta m_H^2 = m_{\text{soft}}^2 [\frac{\lambda}{16\pi^2} (\frac{\Delta_{UV}}{m_{\text{soft}}}) + ...] \tag{3.19}$$

with λ the general dimensionless coupling. m_{soft} is responsible for the splitting between the SM and SUSY particle mass spectra. This implies that the MSSM scale

is not much higher than the TeV scale, otherwise the m_{soft} contributions become unnaturally large, known as the *little hierarchy problem*.

Most SUSY breaking mechanisms rely on a *hidden* sector interacting with the SUSY theory via some mediator. Depending on what kind of mediator is used, there are three major categories of SUSY breaking:

- gravity mediated or Planck-scale mediated
- gauge mediated
- extra dimension and anomaly mediated

Each of these categories leads to different phenomenology in the SUSY sector. Like EWSB, the vacuum is not invariant under SUSY transformations and has positive energy when broken, and since the SUSY generators are fermionic, the Nambu-Goldstone particle is a massless neutral *goldstino*. The goldstino lends mass to the *gravitino*, the spin $\frac{3}{2}$ partner of the graviton. In some scenarios the gravitino can be the LSP, such as in gauge or anomaly mediated MSSM.

Supersymmetry can only be spontaneously broken under some specific conditions: when terms in the covariant derivatives on the superspace (D-term or Fayet-Iliopoulos [28]) or the chiral superfield (F-term or O'Raifeartaigh [29]) have non-zero expectation values, leading to different behaviour from the theory. Only using the D-term cannot provide MSSM sfermion masses.

Regardless of the method of SUSY breaking procedure there are 105 new independent parameters introduced into the MSSM, consisting of masses, phases and mixing angles.

3.3 SUSY electroweak interactions

3.3.1 EWSB in the MSSM

The requirement for two complex Higgs doublets somewhat complicates EWSB in the MSSM compared to the SM. The pertinent terms in the classical potential relate to the neutral Higgs components and are F and D terms along with $\mathcal{L}_{soft}$ contributions. The charged Higgs terms can be set to zero by a gauge transformation

$$\begin{aligned} V_{H^0}^{\text{MSSM}} = &\left(|\mu|^2 + m_{H_u}^2\right)\left|H_u^0\right|^2 + \left(|\mu|^2 + m_{H_d}^2\right)\left|H_d^0\right|^2 - \left(bH_u^0 H_d^0 + c.c.\right) \\ &+ \frac{1}{8}\left(g^2 + g'^2\right)\left(\left|H_u^0\right|^2 - \left|H_d^0\right|^2\right)^2 \end{aligned} \tag{3.20}$$

The D-terms in the second line are always positive and serve to stabilise the potential, while in the case where the quartic contributions to the Higgs fields is zero ($|H_u^0| = |H_d^0|$), V has a minimum

$$2b < 2|\mu^2| + m_{H_u}^2 + m_{H_d}^2. \tag{3.21}$$

To have electroweak symmetry the mass term for a linear combination of H_u^0 and H_d^0 must be negative and

$$b^2 > (|\mu|^2 + m_{H_u}^2)(|\mu|^2 + m_{H_d}^2) \tag{3.22}$$

must be satisfied. The ratio between the two Higgs VEVs is the famous parameter

$$\tan\beta \equiv \frac{v_u}{v_d} = \frac{\langle H_u^0 \rangle}{\langle H_d^0 \rangle}, \tag{3.23}$$

which is related to the mass of the Z boson and electroweak couplings by Equation 2.34 with $v^2 = v_u^2 + v_d^2$. The potential has a minimum when

$$\begin{aligned} |\mu|^2 + m_{H_u}^2 - b\cot\beta - \frac{1}{2}M_Z^2\cos 2\beta = 0 \\ |\mu|^2 + m_{H_u}^2 - b\tan\beta + \frac{1}{2}M_Z^2\cos 2\beta = 0 \end{aligned} \tag{3.24}$$

and the parameters b and $|\mu|$ can be substituted with $\tan\beta$ and the sign of the Higgsino mass. The renormalisation group equations from the visible scale (nominally the electroweak scale) up to the scale of SUSY breaking unify the masses of the

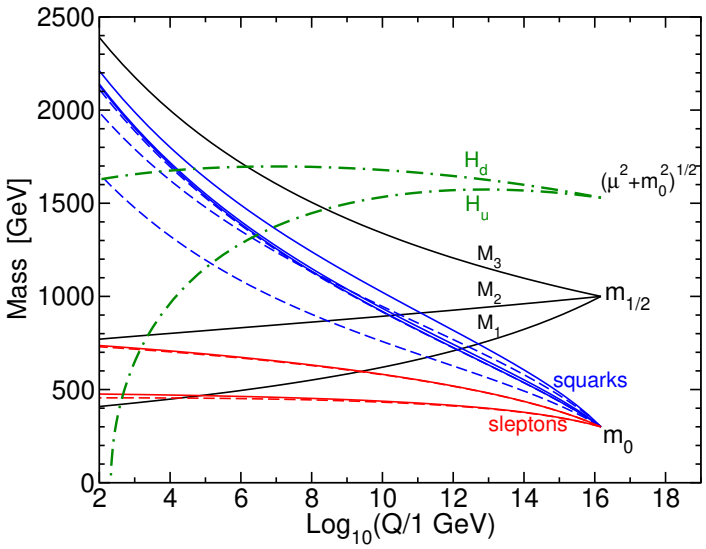

Figure 3.2: The renormalisation group evolution of the gauginos and scalars of the MSSM with mSUGRA boundary conditions at $Q_0 = 1.5 \times 10^{16}$ GeV [24].

scalars and gauginos, shown in Figure 3.2.

A combination of supersymmetry and general relativity known as *minimal supergravity* (mSUGRA) is defined by four parameters and sign: scalar superpartners at the SUSY breaking scale have common mass m_0, gauginos have mass $m_{1/2}$, the universal trilinear coupling is A_0, $tan\beta$ is as defined previously, and the sign of the Higgsino mass parameter μ is unknown. Along with a range of experimental constraints, from direct searches for SUSY and precision measurements of SM particles and processes, these parameters form the Constrained Minimal Supersymmetric Standard Model (CMSSM).

3.3.2 MSSM particles

For some sign(μ) value, all points in this four dimensional parameter constitutes a possible SUSY scenario, with the evolution of nearby points providing different mass spectra and phenomenology at the electroweak scale. Once electroweak symmetry is broken the superpartners in the chiral and gauge supermultiplets don't necessarily correspond to mass eigenstates of the theory. There are now eight real scalar degrees

Table 3.3: The mass eigenstates of supersymmetric particles resulting from the mixing of gauge eigenstates in the MSSM.

Gauge eigenstates	Mass eigenstates	Names
$\tilde{B}^0$, $\tilde{W}^0$, $\tilde{H}_u^0$, $\tilde{H}_d^0$	$\tilde{\chi}_1^0$, $\tilde{\chi}_2^0$, $\tilde{\chi}_3^0$, $\tilde{\chi}_4^0$	Neutralinos
$\tilde{W}^+$, $\tilde{W}^-$, $\tilde{H}_u^+$, $\tilde{H}_d^-$	$\tilde{\chi}_1^\pm$, $\tilde{\chi}_2^\pm$	Charginos
$\tilde{t}_\mathrm{L}$, $\tilde{t}_\mathrm{R}$	$\tilde{t}_1$, $\tilde{t}_2$	Stops
$\tilde{b}_\mathrm{L}$, $\tilde{b}_\mathrm{R}$	$\tilde{b}_1$, $\tilde{b}_2$	Sbottoms
$\tilde{\tau}_\mathrm{L}$, $\tilde{\tau}_\mathrm{R}$	$\tilde{\tau}_1$, $\tilde{\tau}_2$	Staus

of freedom from the Higgs doublets, with three Nambu-Goldstone bosons becoming the longitudinal modes of the massive vector bosons. The remaining mass eigenstates are two CP-even neutral h^0 and H^0, a CP-odd neutral A^0, and two charged $H^\pm$ Higgs scalars. The SM-like Higgs is taken to be the h^0, with a further 4 Higgs bosons presumed to exist.

Electroweakinos are linear combinations of the fermionic partners of the gauge bosons and the two Higgs fields. Neutral Higgsinos and gauginos mix to form four mass eigenstates called *neutralinos* ($\tilde{\chi}_i^0$ with $i = 1, 2, 3, 4$ and the charged winos and Higgsinos form two mass eigenstates called *charginos* ($\tilde{\chi}_i^\pm$ with $i = 1, 2$). The relative proportions of the Higgsino and gauginos in these mixed mass eigenstates is important in determining the decay properties, along with couplings to SM particles. If in a particular mixing scenario the Higgsinos dominate then the decays will preferentially be via the SM-like Higgs, with the charged particles still decaying via W if $m_{W^\pm} < m_{H^\pm}$ as is largely assumed in many models. Otherwise if the gauginos dominate then the decays will largely be via Z and W for the neutral and charged electroweakinos respectively.

In the scalar sector the mixing is proportional to the SM partner mass, so is heavily skewed to the third generation. The left and right-handed stops mix to form two mass eigenstates $\tilde{t}_1$ and $\tilde{t}_2$, as do the sbottom and stau. Other gauge eigenstates correspond to mass eigenstates assuming negligible mixing. The $\tilde{t}_1$ is typically the lightest squark and predominantly right-handed. The mixing is shown in Table 3.3.

3.4 Simplified models

For the purposes of phenomenology 105 additional free parameters are too extensive to scan over, and varying the renormalisation behaviour of mSUGRA leads to vastly different behaviour. To be able to make realistic and easy to characterise predictions for new physics *simplified models* are defined, utilising effective Lagrangians to describe a small number of particles assuming a single production process and decay channel with 100% branching ratio. In addition certain types of mixing, especially between the Higgsinos and gauginos of the electroweakino sector, are fixed at certain values. This alters the decays of these electroweakinos. In the analyses presented in this work charginos and higher mass neutralinos are assumed to be wino dominated, decaying via W and Z bosons to bino-like LSPs.

4 The ATLAS Experiment

This chapter describes the Large Hadron Collider (LHC), and the ATLAS Experiment, the experimental apparatus used to collect the data for the results presented. To study the properties of the standard model and to search for new physics at high energies, a robust collider with high luminosity is required. A large area detector with the ability to identify and measure a variety of particles with high bandwidth and precise timing is also required. The LHC and ATLAS form such a combination.

4.1 The LHC

The LHC is a circular proton collider of nearly 27 km circumference located approximately 100m under the France-Switzerland border near Geneva [30]. Hydrogen gas is ionised and the separated protons are injected through a chain of accelerators, beginning with the 50 MeV Linac 2, then the Proton Synchrotron Booster (1.4 GeV), followed by the 25 GeV Proton Synchrotron and 450 GeV Super Proton Synchrotron. Finally, in the configuration used for 2015-2018 data taking (known as Run 2), the protons are injected into the LHC to form two counter-rotating beams of 6.5 TeV, giving a total centre of mass energy of 13 TeV. There are four main experiments at collision points around the ring; two general-purpose detectors, ATLAS and CMS; LHCb, an experiment dedicated to flavour physics, and ALICE, a heavy ion detector. The LHC utilises 1232 superconducting dipole magnets keep the proton beams on a circular path, while beam focusing is handled by 392 quadrupole magnets. The protons are arranged in *bunches*, and the bunches themselves are arranged in *trains*. The tunability of the beams leads to a variety of bunch and train configurations and

beam collision parameters, along with the ability to run with heavier ions such as lead and xenon.

4.1.1 Luminosity and pileup

The *instantaneous luminosity* of the LHC (measured in units $\text{cm}^{-2}\text{s}^{-1}$) can be determined by

$$L = \frac{N_B^2 n_b f_{rev} \gamma_b}{4\pi\epsilon_n \beta*} F, \tag{4.1}$$

where N_B is the number of particles per bunch, n_b the number of bunches per beam, f_{rev} the revolution frequency, γ_b the relativistic gamma factor, ϵ_n the normalised transverse beam emittance, $\beta*$ the beta function at the collision point[1], and F a geometric reduction factor taking into account the non-zero crossing angle of the beams at the interaction point. The LHC was designed to achieve luminosities in the range of 10^{34} $\text{cm}^{-2}\text{s}^{-1}$, and indeed surpassed its design luminosity during Run 2, with 2.06×10^{34} $\text{cm}^{-2}\text{s}^{-1}$ measured in 2017. The bunch crossing scheme was initially 50 ns during Run 1 (20 MHz), and moved to 25 ns (40 MHz) during Run 2. The number of collisions over some time period is known as *integrated luminosity*, $\mathcal{L} = \int L dt$ and is measured in units of inverse cross section.

To be able to probe low cross section processes high luminosity is usually maintained by having large numbers of proton bunches and close bunch spacing. This increases the number of interactions per bunch crossing, known as *pile-up*. Experiments need to be able to discern between the myriad interactions in the bunch crossing. This is known as *in-time pile-up*, while the effect of successive bunch crossings on the detector components is *out-of-time pile-up*. Pile-up is either measured as the number of primary vertices (N_{PV}), or as the average number of interactions per bunch crossing ($\langle\mu\rangle$). N_{PV} does not consider out-of-time pile-up and is derived from reconstructed vertices, $\langle\mu\rangle$ is calculated from measured luminosity. Figure 4.1 shows the distribution of $\langle\mu\rangle$ at the ATLAS detector for the four years of Run 2.

[1] The β function is related to the transverse size of the particle beam along its trajectory, viz. $\sigma(s) = \sqrt{\epsilon\beta(s)}$ where s is the location along the beam trajectory, the beam is assumed to be a Gaussian in the transverse direction with $\sigma(s)$ being the width and ϵ the RMS beam emission. The value of the

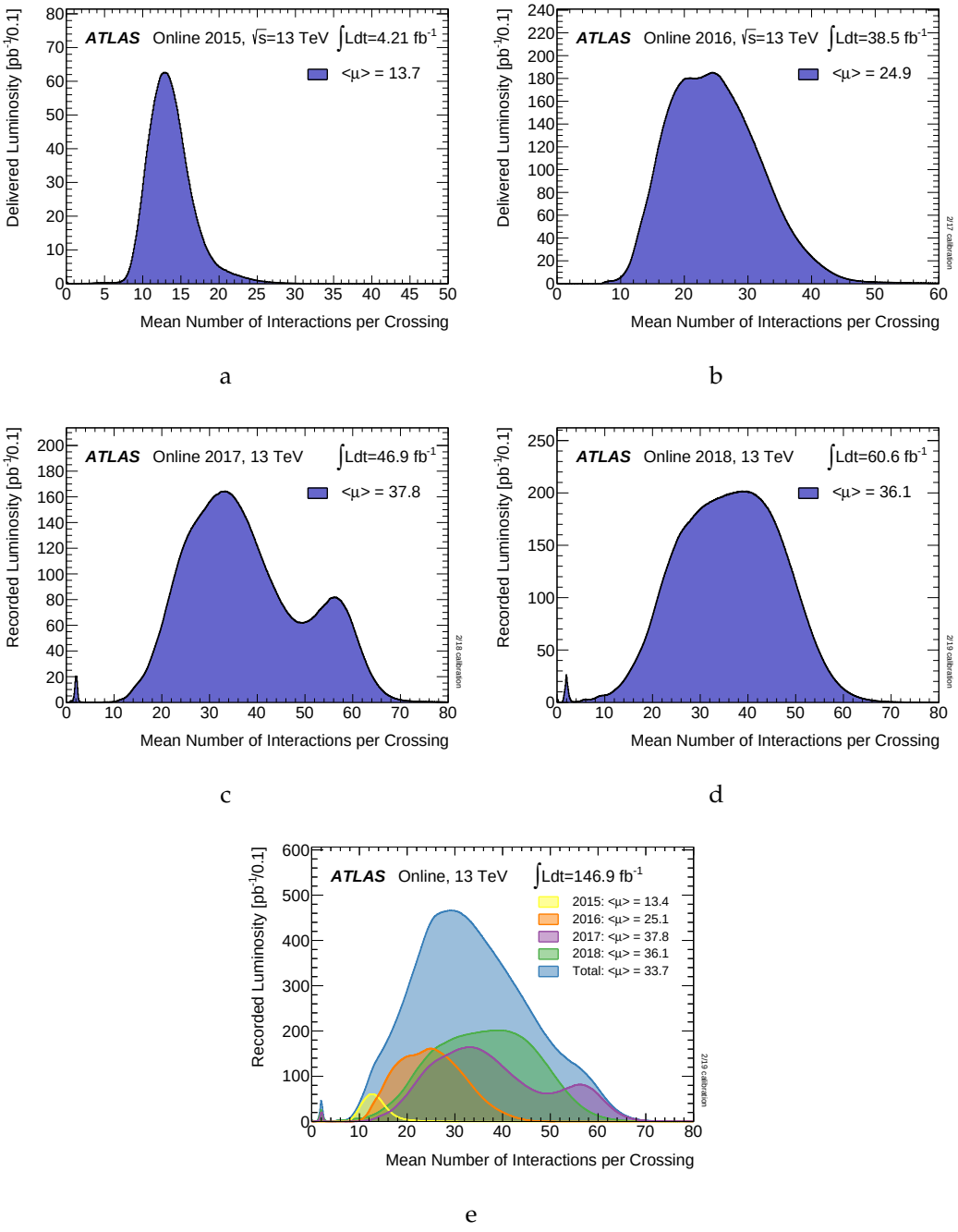

Figure 4.1: ATLAS pile-up profiles of 2015-2018 data passing data quality criteria are shown in Figures 4.1a to 4.1d. The overall profile for all data (before data quality selections) collected in Run 2 is shown in Figure 4.1e.

4.1.2 Proton collisions and their products

Protons are not elementary particles: they consist of quarks and gluons, known generally as partons in high energy collisions. At LHC energy protons behave as collections of unbound massless partons, with the valence quarks being the two up and one down quark along with a "sea" of quarks and gluons due to the QCD interactions. In a typical proton-proton collision, two partons will interact in a hard scattering process with the remainder of the partonic material interacting with lower energy or being scattered away from the interaction point. The energy fraction carried by a particular parton is modelled using the *parton distribution function* or PDF, which is determined at some fixed momentum transfer. This leads to situations across the whole energy range of the LHC where the hard partonic interaction, the one that produces a Higgs boson, top quark pair, or sparticle pairs, is shrouded in other processes like initial and final state radiation, multiple parton interactions and so on. Each proton-proton interaction has the potential to have a wide variety of decay products associated with it, and as detailed in Section 4.1.1 a number of these proton-proton interactions can happen every 25 ns interval bunch crossing. The sheer rate of particles produced raises a number of questions for any prospective detector, and the design of a multipurpose detector starts with this in mind.

4.2 The ATLAS detector

Studying collision products and determining their characteristics allows for the reconstruction of the underlying physics processes responsible. When a particle interacts with a material it loses energy in one (or more) of the following ways: the material itself becomes ionised, or excited, or the particle emits radiation. Particle detectors convert this lost energy into an electronic signal which can then be analysed. Tracking detectors fix a spatial position of the traversing particle, and with successive measurements can build a trajectory (*track*). An applied magnetic field can be used to determine momentum and electric charge. Calorimeters measure deposited energy.

beta function at the interaction point is $\beta*$

To run a varied and impactful physics program there are a few requirements for detectors at the LHC:

- Fast, radiation resistant sensors and electronics with high granularity due to the busy environment.
- Good momentum resolution and reconstruction for charged particles in the inner tracker, especially for τ-leptons and b-jets.
- An excellent calorimetry system, both electromagnetic (EM) and hadronic, to identify and measure electrons, photons, jets and missing energy with high accuracy.
- Muon identification, momentum resolution, and importantly charge determination at high momenta.
- Efficient triggering at low momentum coupled with good background rejection.
- Maximal area coverage.

ATLAS (A Toroidal LHC ApparatuS) is a general-purpose detector located underground at Point 1 on the LHC ring [31, 32]. It fulfils the criteria for effective LHC detectors outlined above; a forward-backward symmetric detector with near 4π coverage, with a thin superconducting solenoid around the inner detector, and three superconducting toroids (barrel and two endcaps) arranged with eightfold azimuthal symmetry around the calorimeters.

4.2.1 The ATLAS coordinate system

ATLAS uses a right-handed coordinate system with the origin being at the nominal interaction point of the detector. Positive x is defined from the interaction point to the centre of the LHC ring, positive y from the interaction point upwards to the surface. The beam line defines the z axis, with side-A of the detector being positive z and side-C negative z. Given the shape of the detector it is wise to use cylindrical coordinates. The azimuthal angle ϕ is measured around the beam axis, and the polar angle θ is

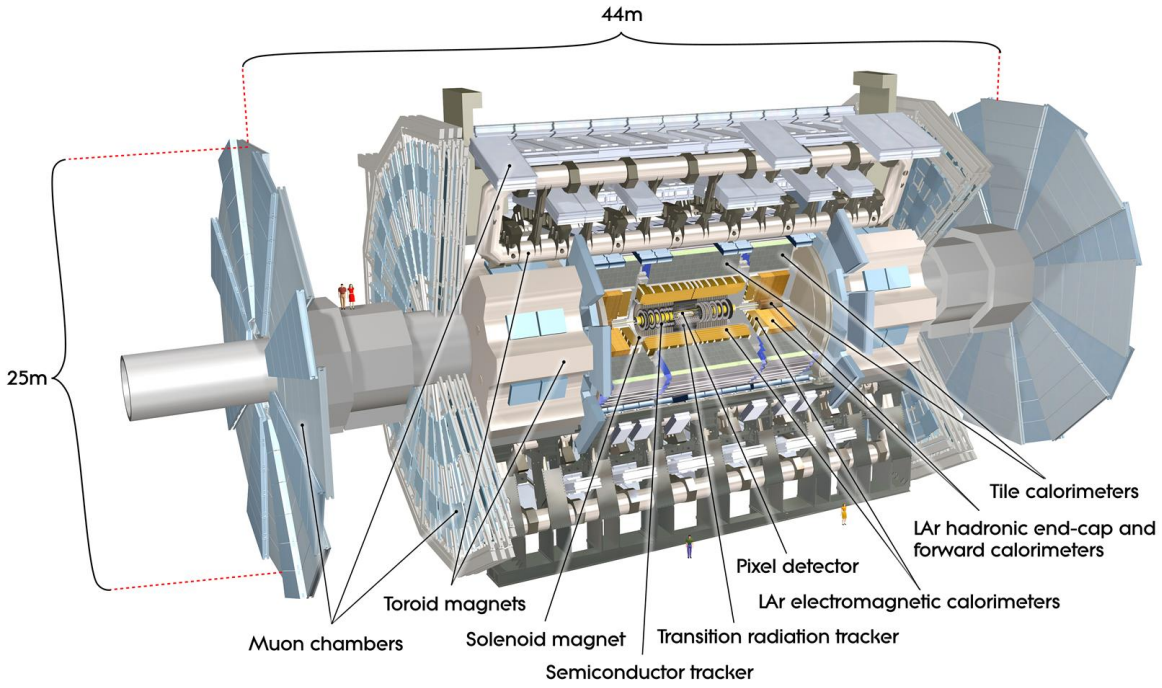

Figure 4.2: A cutaway diagram showing the ATLAS detector [33].

the angle from the beam axis. The polar angle is more conveniently parameterised as *pseudorapidity* $\eta = -ln\tan(\theta/2)$ (or for massive objects the rapidity $y = 1/2ln[(E + p_z)/(E - p_z)]$ is more common). Transverse momentum p_T, transverse energy E_T, and missing transverse energy $\vec{E}_T^{miss}$ are defined in the $x - y$ plane. A distance $\Delta R = \sqrt{\Delta\eta^2 + \Delta\phi^2}$ can be defined in the pseudorapidity-azimuthal angle space. The transverse impact parameter d_0 is defined in the $x - y$ direction perpendicular to the beam axis.

4.2.2 Inner tracker

Hundreds of tracks emerge from the interaction point at every bunch crossing. To measure vertices and momenta high-precision measurements need to be made with fine granularity. The ATLAS inner tracking system, illustrated in Figure 4.3, consists

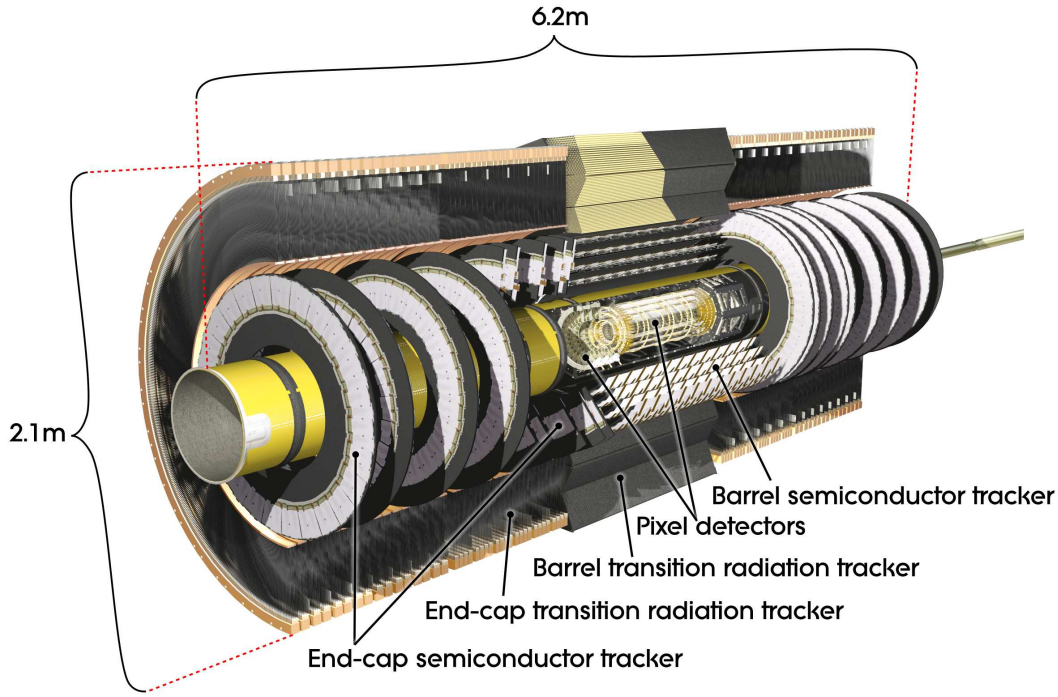

Figure 4.3: A cut-away diagram of the ATLAS inner detector

of silicon pixel and strip (SCT) detectors and the Transition Radiation Tracker (TRT), constructed of straw tubes.

The inner detector is subject to a 2 T magnetic field from the central solenoid 5.3 m long and 2.5 m in diameter. The silicon pixel and SCT precision tracking covers $|\eta| < 2.5$, and are arranged in concentric circles around the beam axis in the barrel and disks perpendicular to the beam line in the end-caps. The highest granularity is required in the vertex regions close to the beamline, where the silicon pixel detectors are situated. Closest to the beam pipe is the pixel insertable B-layer (IBL) at a radius of 33 mm, installed between Run 1 and Run 2, and much improving tracking performance and b-tagging [34]. The remaining pixel layers are segmented in $R - \phi$ and z with typically 3 layers being crossed by each track. All pixel sensors have a minimum pixel size $50 \times 400 \mu\text{m}^2$ ($R - \phi \times z$) and are identical. The pixel detector has around 86 million readout channels.

The SCT has eight strip layers, with a typical track crossing four spatial points. In

the barrel small-angle (40 mrad) stereo strips are used to measure both coordinates ($R-\phi$), with a set of strips parallel to the beam consisting of two 6.4 cm long daisy-chained sensors with strip pitch of 80 μm. In the end-cap regions the detectors have strips running radially and a set of stereo strips at an angle of 40 mrad, with mean strip pitch also being 80 μm. There are approximately 6.3 million readout channels in the SCT.

The TRT typically provides 36 hits per track, with an array of 4 mm diameter straw tubes allowing for tracking-following within $|\eta| < 2.0$ providing only $R-\phi$ information. In the barrel the straws are parallel to the beam axis and are 144 cm long, with the wires split in two around $\eta = 0$. In the end-cap the straws are 37 cm long and are arranged radially in wheels. There are around 351, 000 TRT readout channels.

In concert, the high granularity of the silicon layers and the large radius of the TRT leads to reliable and accurate pattern recognition, and high precision in both $R-\phi$ and z directions. Momentum resolution is also improved with longer track measurement distances.

4.2.3 Calorimetry

The calorimeters in ATLAS (shown in Figure 4.4) cover the range $|\eta| < 4.9$, using a variety of techniques over the large pseudorapidity range. In the η range matching the coverage of the inner detector, the fine granularity of the EM calorimeter is useful in measuring electrons and photons, while the rest of the calorimetry system is optimised for jet and $E_{\mathrm{T}}^{\mathrm{miss}}$ reconstruction.

The calorimeters must be able to contain the EM and hadronic showers completely, avoiding punch-through into the muon system, so the depths of the calorimeter systems is important. The EM calorimeter has thickness > 22 radiation lengths (X_0) in the barrel and $> 24\mathrm{X}_0$ in the end-caps.

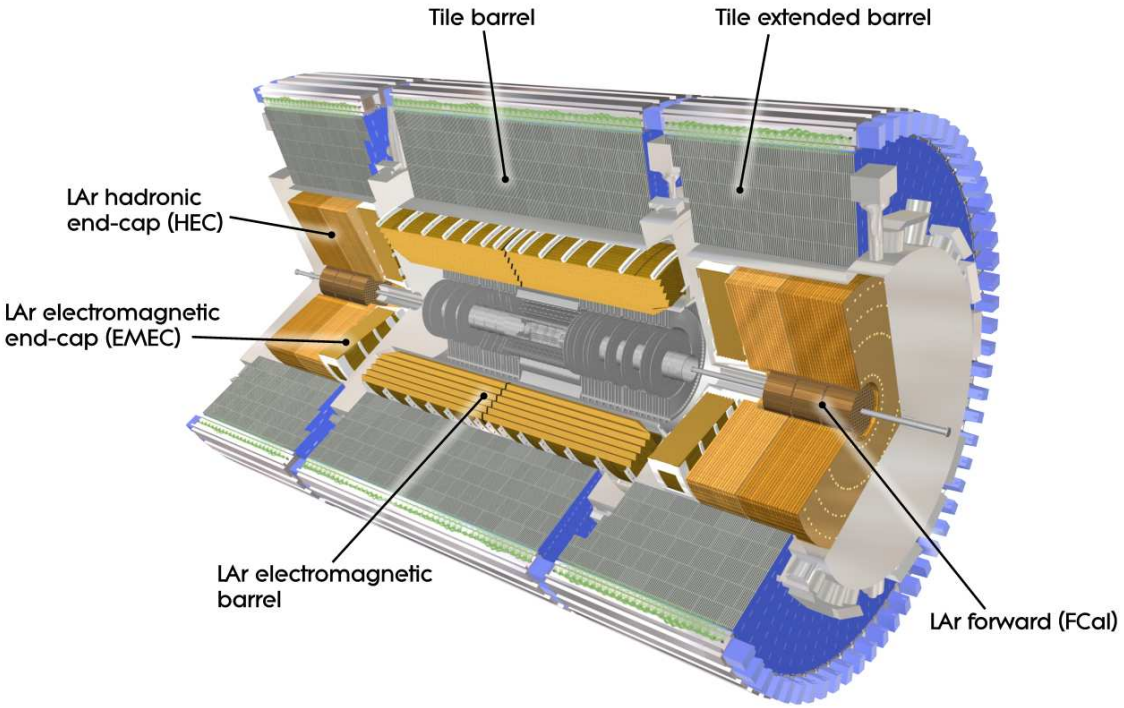

Figure 4.4: A cut-away diagram of the ATLAS calorimeters.

Electromagnetic calorimeter

The EM calorimeter is divided into barrel ($|\eta| < 1.475$) and two end-cap components ($1.375 < |\eta| < 3.2$), housed in individual cryostats. The central portion of the calorimeter is housed in the same vacuum vessel as the adjoining solenoid for material budgeting reasons. The barrel calorimeter contains two identical halves, with a small gap (4 mm) at $z = 0$. The end-cap calorimeters are divided into two coaxial wheels, the outer covering $1.375 < |\eta| < 2.5$ and the inner covering $2.5 < |\eta| < 3.2$. The EM calorimeter is a lead-Liquid Argon (LAr) detector with accordion-shaped kapton electrodes and lead absorber plates. The accordion geometry provides complete ϕ coverage, and the lead plate thickness varies as a function of η to optimise energy resolution performance. The central region ($|\eta| < 2.5$) the EM calorimeter is three sections deep, and in the inner end-cap wheel is segmented two sections deep with coarser lateral granularity than other regions. In the region $|\eta| < 1.8$ a

presampler is used to correct for the energy lost by electrons and photons before reaching calorimetry.

Hadronic calorimeter

The tile calorimeter is situated directly outside the EM calorimeter, covering the region $|\eta| < 1.0$ with two extended barrels in $0.8 < |\eta| < 1.7$. It is a sampling calorimeter with steel absorbers and scintillating tiles as the active material. The barrel and extended barrels are divided azimuthally into 64 modules. The radius ranges from 2.28 m to 4.25 m. Two sides of the scintillating tiles are read out by wavelength shifting fibres into two photomultiplier tubes. The readout cells built by grouping fibres into the photomultipliers are divided in η.

The LAr Hadronic End-cap Calorimeter (HEC) has two independent wheels per end-cap, directly behind the end-cap EM calorimeter and sharing the same LAr cryostats. To minimise the drop in material density at the transition between the end-cap and the forward calorimeter (around $|\eta| = 3.1$) the HEC extends to $|\eta| < 3.2$, overlapping with the forward calorimeter. It also overlaps with the tile calorimeter on the other side of the η range, at $|\eta| = 1.5$. Each wheel is built from 32 wedge-shaped modules, fixed around the outer edge and in the centre, with each wheel divided in two segments in depth for a total of four layers per end-cap. The two wheels are made from copper plates, 25 mm closer to the interaction point, and 50 mm for the outer. These plates are interleaved with 8.5 mm LAr gaps acting as the active medium.

The LAr forward calorimeter (FCal) is integrated into the end-cap cryostats for uniform calorimeter coverage, with the added benefit of less radiation in the muon spectrometer. To reduce the neutron albedo in the inner detector, the front of the FCAL is recessed by 1.2 m compared to the EM calorimeter face. This reduces the allowable depth of the calorimeter, which must be high density. The FCAL is 10 interaction lengths deep, and is made of three modules: one copper module for EM measurements, and the other two made of tungsten optimised for hadronic interactions. Each of these modules consists of a metal matrix with regular longitudinal channels filled with the electrodes of concentric rods and tubes parallel to the

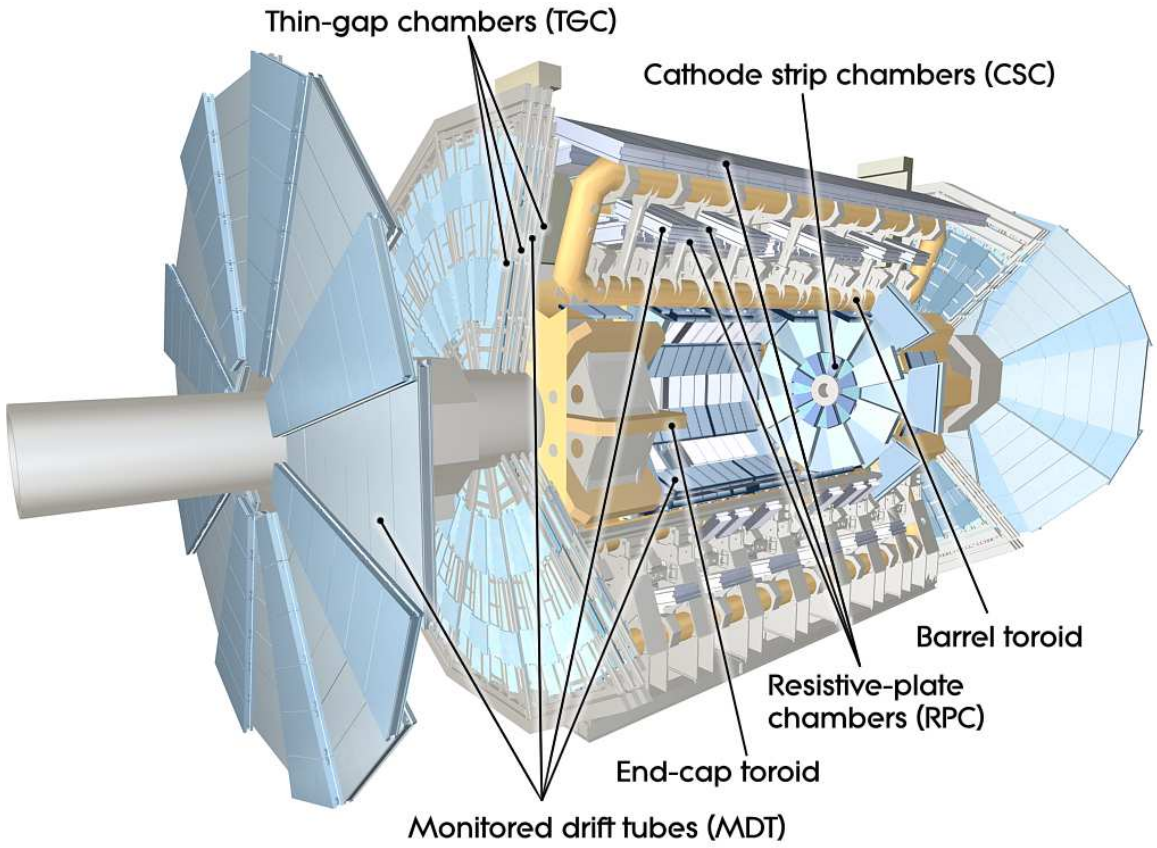

Figure 4.5: A cut-away diagram of the ATLAS muon system.

beam axis. In the gap between the rods and tubes LAr forms the sensitive medium. This design allows for fine control of the gaps to minimise problems due to ion buildup.

4.2.4 Muon spectrometer (MS)

The ATLAS muon system is laid out in Figure 4.5, and is based on the magnetic deflection of muons in the superconducting air-core toroid magnets with integrated trigger and high precision tracking chambers. Within $|\eta| < 1.4$ the magnetic bending is applied by the large barrel toroid, while in $1.6 < |\eta| < 2.7$ tracks are bent by smaller end-cap magnets inserted into the barrel toroid. For $1.4 < |\eta| < 1.6$, known

as the transition region, the magnetic field is supplied by both the barrel and end-cap magnets. This magnetic field configuration provides a mostly orthogonal magnetic field to muon trajectories while minimising resolution degradation from multiple scattering. In the barrel tracks are measured in cylindrical chambers three layers deep, while in the end-caps there are also three layers but in planes perpendicular to the beam.

There are three large air-core toroids generating the magnetic field for the muon spectrometer, two end-cap toroids and one barrel toroid. Each of these toroids is constructed of eight coils assembled radially and symmetrically around the beam axis. The end-cap toroids are rotated 22.5° to the barrel to provide radial overlap and to optimise bending in the transition region. The barrel toroids are housed in individual cryostats linked together for stability. The end-cap toroids are constructed with eight coils in an aluminium housing. Each end-cap coil has two double-pancake windings, and are assembled as a single mass housed in a single cryostat. The bending power of the magnets is given by the field integral $\int Bdl$, where B is the field component normal to the muon direction and the integral is calculated along an infinite-momentum muon trajectory from the innermost to the outer muon-chamber planes. The barrel toroid provides 1.5 to 5.5 Tm of bending power in $0 < |\eta| < 1.4$, the end-caps 1 to 7.5 Tm in $1.6 < |\eta| < 2.7$, with lower power in the transition region due.

Monitored Drift Tubes (MDT's) provide precision track coordinate measurements over most of muon spectrometer η range. The isolation of each wire from its neighbours allows for robust operation. At large pseudorapidities ($2 < |\eta| < 2.7$) Cathode Strip Chambers (CSC's), multiwire proportional chambers with cathodes segmented into strips, are used due to high rate and background conditions. The integration and alignment requirements of these subsystems requires both precision assembly techniques and optical alignment systems.
The muon trigger system covers the central region $|\eta| < 2.4$ with three main functions: bunch crossing identification, defined p_{T} thresholds, and to measure the muon in the direction orthogonal to the other tracking chambers. Resistive Plate Chambers (RPC's) are used in the barrel and Thin Gap Chambers (TGC's) are used in the end-caps.

4.2.5 Forward detectors

There are three small detectors in the forward regions of ATLAS. The first two, LUCID (LUminosity measurement using Cerenkov Integrating Detector) and ALFA (Absolute Luminosity For ATLAS) are dedicated to measuring the luminosity delivered to ATLAS. LUCID is located ± 17 m from the interaction point, detecting inelastic $p - p$ scattering in the forward direction and is the main online relative-luminosity monitor for ATLAS. ALFA is located ± 240 m from the interaction point and is made of scintillating fibres inside Roman pots designed to approach up to 1 mm from the beam. The third system is the Zero-Degree Calorimeter (ZDC), which is used for measuring the centrality of heavy-ion collisions. It is located at ± 140 m from the interaction point, beyond the where the common vacuum-pipe divides back into two individual pipes. The ZDC consists of alternating quartz rods and tungsten plates which measure neutral particles at $|\eta| \geq 8.2$.

4.2.6 Data acquisition and triggering

The Trigger and Data Acquisition (TDAQ) systems, the timing- and trigger-control functions, and the Detector Control System (DCS) are usually split into subsystems associated with various subdetectors, while sharing similar logic. The function of these systems is to read out event information in a cohesive way from all the sub-detectors, and to apply selections to save events of physics interest.

In Run 1 the ATLAS trigger had three levels: L1, L2, and the event filter. To cope with the higher collision energies and increase in instantaneous luminosity upgrades of the trigger system began prior to Run 2 (known as Phase-I TDAQ Upgrade [35]), including a shift from L2 and event filter to an integrated High-Level Trigger (HLT) setup. A schematic overview of the TDAQ system in Run 2 is shown in Figure 4.2.6. In addition the new Topological Processor for Level-1 trigger (L1Topo) was introduced into the L1 trigger hardware. L1Topo allows for the geometric comparison of multiple L1 trigger objects, and selections based on kinematic variables such as H_{T} and M_{eff}. These trigger levels act sequentially and refine decisions made by previous levels and apply additional selection criteria. The data acquisition system receives

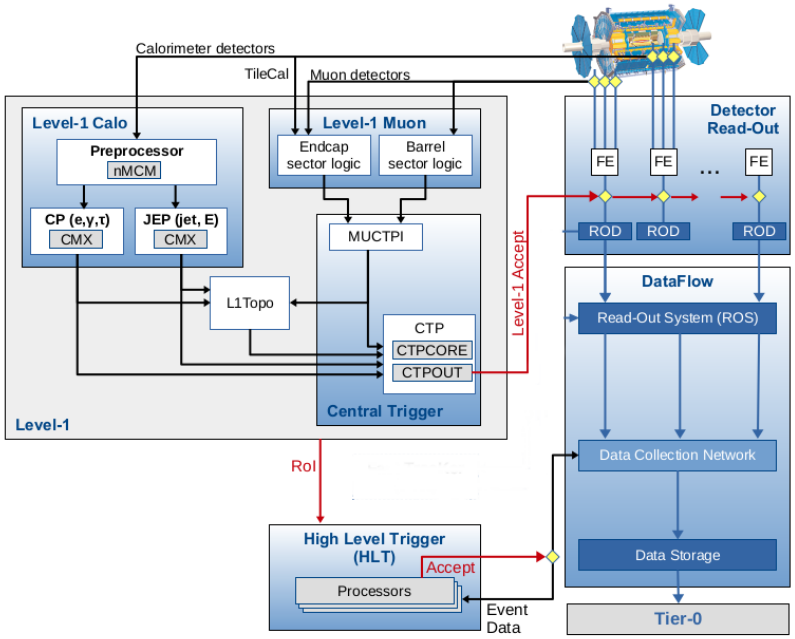

Figure 4.6: A schematic representation of the TDAQ system in Run 2.

event data from the individual detector subsystem electronics at the L1 trigger accept rate. This first level uses a small amount of detector information to make a fast decision, less than 2.5 μs, reducing the rate to about 100 kHz. The higher layers use more detector information to reduce the rate further to a more manageable 1000 Hz (about 2.4 GB/s write rate). This includes 25 kHz of Level-2 requests and a 6.5 kHz event building rate.

Trigger system

The L1 trigger looks for interesting objects such as high transverse-momentum muons, electrons, photons, jets, and hadronically decaying τ-leptons, as well as

event-wide variables such as large missing or total transverse energy. This selection is based on a subset of the full suite of detectors. High transverse-momentum muons are identified using the trigger chambers in the barrel and end-cap regions of the spectrometer. Calorimeter selections are based on coarse outputs from the various calorimeters. These L1 triggers are then parsed by the central trigger system, containing the Central Trigger Processor (CTP), the Muon-to-CTP-Interface (MUCTPI), and the Level-1 Topological Processor (L1Topo), which implements a trigger "menu" made up of different trigger combinations. This menu can vary according to luminosity and other background conditions, and triggers can be pre-scaled, allowing for flexible use of the available bandwidth. The topological aspect of this trigger allows for complex object multiplicity or H_{T} and invariant mass based triggers. Events which pass the L1 triggers are passed along to the next stage of specific readout electronics for the particular detectors.

The High-Level Trigger is software based, operating on a large server farm, and executing chains of reconstruction and signature algorithms, including on event level inputs such as primary vertex position and number of primary vertices. The HLT step is limited not by readout rate but by the computing resources required to execute the various functions. HLT selections can be made on single- and multi-lepton triggers, hadronic triggers like jets (with or without b-tags) and the important $E_{\mathrm{T}}^{\mathrm{miss}}$, photons, τ-leptons, and combinations thereof. A wide array of specialised triggers are also used, ranging from B-physics and VBF, to exotics and long-lived particles (LLP), to triggers used for combined performance work such as lepton tag-and-probe.

4.3 Object reconstruction and definitions

The outputs of the various detector subsystems, collected and organised by the trigger and data acquisition system, are then reconstructed into objects for physics analysis. These objects constitute the building blocks of any analysis and accurate, robust object definitions are vital to maximising the reach of searches for new physics, or improving the accuracy of SM measurements. During the course of LHC Run 2, updates and improvements to object reconstruction, identification, and isolation

were implemented in ATLAS software Release 21, an improvement on the previous Release 20 software derived largely from simulations of 13 TeV collisions.

4.3.1 Tracks and vertices

The primary vertex is required to be close to the nominal interaction point in both z and in d_0 significance, and needs to have at least two associated tracks with $p_{\mathrm{T}} > 400$ MeV [36]. When more than one vertex satisfies these conditions, the vertex with the largest Σp_{T}^2 of the associated tracks us chosen.

4.3.2 Muons

Muon candidates are formed by combining inner tracking and muon spectrometer information, along with calorimetry information in the small coverage gap around $\eta = 0$ [37]. Track segments are built within each layer of the MS and then combined into tracks throughout the full system. These are combined with ID tracks to form a suite of muon types: *standalone muons* are based on MS track extrapolation to a primary vertex, *combined muons* are based on both MS and inner detector tracks, *segment-tagged muons* have an ID track that is extrapolated to the MS and is matched to an energy deposit in at least one MS segment. Calorimeter-tagged muons have an ID track associated with a minimally ionising calorimeter deposit, not involving the MS. Combined muons are have the cleanest There are a set of muon identification benchmark points *Loose*, *Medium* and *Tight*, with increasing strictness on the quality and precision of the hits in the various detector subsystems.

4.3.3 Electrons

In the early part of Run 2 electrons were formed from inner detector tracks matched to electromagnetic calorimeter inputs passing energy and shower shape criteria [38]. The energy deposits were measured in sliding windows of 3×5 in $\eta \times \phi$ for the depth of the calorimeters (known as towers), with a minimum threshold of 2.5 GeV. Later

on in Run 2 the sliding window methodlogy is replaced with *superclusters* of variable size to maximise separation between electron and photon candidates [39]. The energy deposits are then close matched in $\eta \times \phi$ space with tracks that are reconstructed in the inner detector from χ^2 pattern matching and fitting, after accounting for bremsstrahlung from material interactions and including experimental noise with Gaussians. There are three benchmark identification points *Loose* + *b-layer*, *Medium*, *Tight*, all with d_0 significance and z_0 selections applied.

4.3.4 Photons

Photon candidates are made from either electromagnetic calorimeter deposits without associated tracks, or EM calorimeter deposits matched to a conversion vertex (or vertices) in the inner detector [39]. At low η around 20% of photons will convert in the inner detector, with the conversion rate increasing to around 65% at $\eta \approx 2.3$. Photons have *Loose* and *Tight* working points.

4.3.5 Jets

Due to the confining nature of QCD, quarks and gluons produced in interactions do not interact directly with the detector. Instead they will hadronise repeatedly in a collimated spray of particles known as a jet.

Candidate jets are constructed with topo-cluster input from calorimetry and passed through the anti-k_t algorithm [40].[2] Topo-clusters are groups of noise-suppressed calorimeter cells can be the basic EM-scale or fully calibrated and corrected hadronic scale [41]. To reconstruct jets tracks, topo-clusters, or a combination of the two are used. Track jets are defined within $|\eta| < 2.5$ due to inner detector coverage and calorimeter dependent jets can be reconstructed up to $|\eta| < 4.5$. Pileup mitigation

[2] There are other jet reconstruction methods that are used in specialised cases. Additionally Particle Flow algorithms are becoming increasingly common and will soon be the default reconstruction method.

techniques are applied before the jets are even constructed to avoid selecting extra objects in the event of interest [42].

4.3.6 Jets from *b*- and *c*-hadrons

Jets originating from b-quarks are unique among jets with the majority of the energy carried by a b-hadron of a large mass (from 5 to 10 GeV) and are more long-lived than jets from lighter quarks or gluons. This leads to displaced vertices and altered jet shape, allowing for discrimination between b-jets and jets from other sources, known as b-tagging. b-tagging at ATLAS is done using the MV2c10 algorithm [43], a boosted decision tree (BDT) developed to exploit the long lifetime of b-hadrons and the increased tracking capability of the IBL [44]. The inputs include transverse and longitudinal impact parameter significances; secondary vertex properties; b-hadron reconstruction with a Kalman filter to find commonality between the primary vertex and subsequent decay vertices; jet p_{T} and η. The performance of b-tagging is measured by the tagging efficiency as well as the background (consisting of light jets and charm jets) rejection efficiency, shown in Figure 4.7. The BDT score can be used as an input into analyses, or jets can be classified as either originating from a b or not at some efficiency working point such as 77% of 85%.

Jets originating from charm quarks are difficult to discriminate from light jets and b-jets due to the charms intermediate mass and the varying lifetimes of charmed hadrons. Thus charm tagged jets are used in specific analyses where c quarks are vital, such as $H \to c\bar{c}$ [45]. Boosted decision trees are used to determine two discriminants, separating c-jets from light and b-jets, using the same variables as for b-tagging [44]. Given the multivariate discriminant, instead of a single selection on BDT output a surface of efficiency can be chosen to optimise light jet versus b-jet rejection [46]. For the aforementioned $H \to c\bar{c}$, the efficiency surface is shown in Figure 4.8.

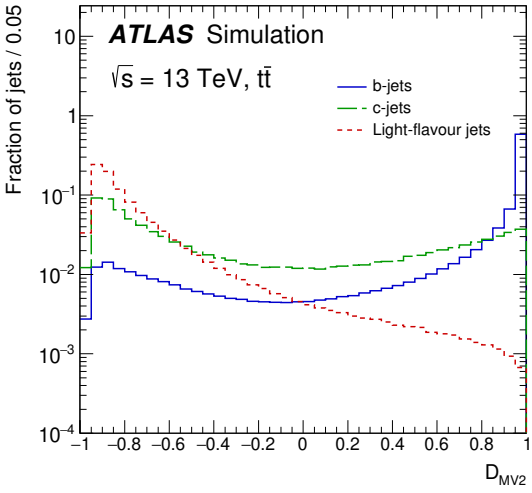

a

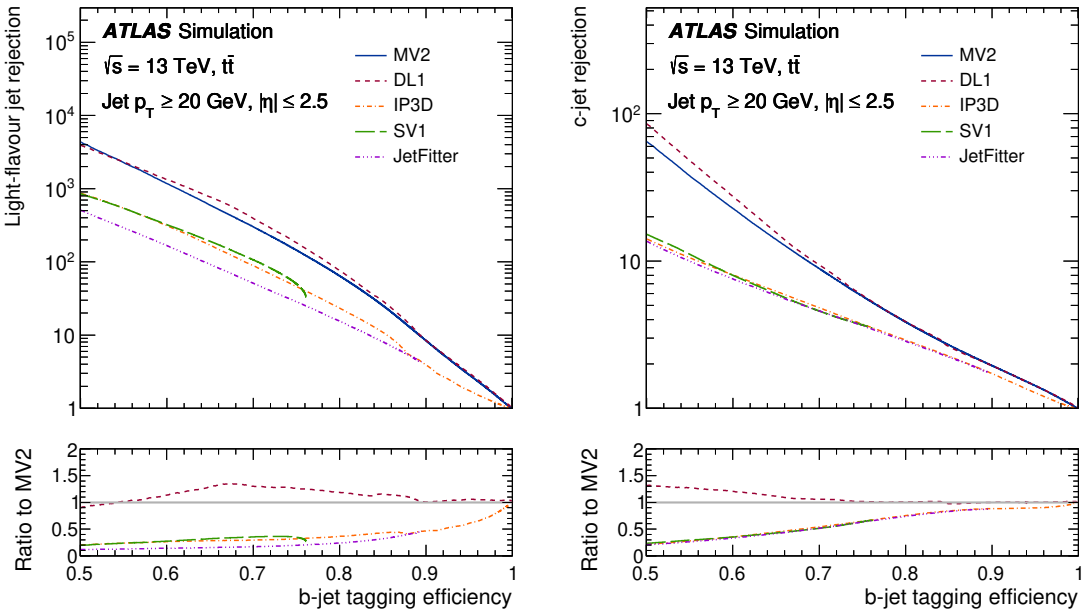

b c

Figure 4.7: (a) the output of the MV2C10 algorithm for *b*-, *c*- and light jets. The light (b) and *c*-jet (c) rejection factors are plotted as functions of the *b*-tagging efficiency [44]

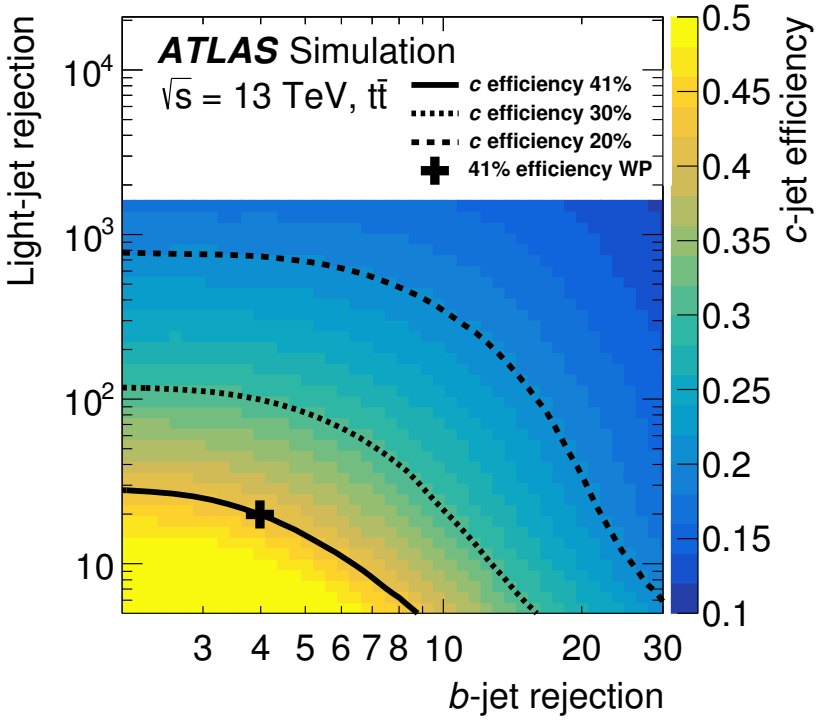

Figure 4.8: The *c*-jet efficiency is shown as the colour scale as a function of both the light jet and *b*-jet rejection [45].

4.3.7 Tau leptons

Leptonic τ decays are covered by the electron and muon reconstructions, and hadronic τ decays (known as τ_{had} in shorthand) are seeded by jets of down to 10 GeV in transverse momentum [47]. A τ vertex is chosen as the candidate vertex with the largest fraction of momentum from tracks within $R < 0.2$ of the jet. The tracks must pass quality and minimum momentum thresholds as outlined in Section 4.3.1, along with impact parameter and beamline proximity selections to ensure clean τ candidates. The tracks are then associated to *core* and *isolation* regions of ranges $0 < \Delta R < 0.2$ and $0.2 < \Delta R < 0.4$ respectively around the tau candidate. The tau candidate is defined to be massless and has a direction given by vector summing the Topo-clusters in the core of the candidate. There is then an energy calibration applied to correct measured energy deposits, and three benchmark ID points are available, *Loose*, *Medium* and *Tight*.

4.3.8 Missing transverse energy

Missing transverse momentum $\vec{E}_{\mathrm{T}}^{\mathrm{miss}}$ (and its magnitude missing transverse energy $E_{\mathrm{T}}^{\mathrm{miss}}$) are constructed by taking advantage of the initial beam conditions: $p_{\mathrm{T}} = 0$. This condition means that the final state particles must be balanced transverse to the beam axis, and the missing transverse momentum vector $\vec{E}_{\mathrm{T}}^{\mathrm{miss}}$ is calculated with:

$$E_{x,y}^{\mathrm{miss}} = E_{x,y}^{\mathrm{miss},\mu} + E_{x,y}^{\mathrm{miss},e} + E_{x,y}^{\mathrm{miss},\gamma} + E_{x,y}^{\mathrm{miss},\tau} + E_{x,y}^{\mathrm{miss,jets}} + E_{x,y}^{\mathrm{miss,soft}}, \tag{4.2}$$

where each of the terms is the negative vector sum of the transverse momenta of energy deposits or trajectories of charged particles. To avoid double counting first reconstructed objects are added (known as the *hard term*, and then the remainder of the energy deposits are taken together as the *soft term*. In ATLAS $\vec{E}_{\mathrm{T}}^{\mathrm{miss}}$ is calculated with jets of up to $|\eta| = 4.5$ and with other objects at their maximal coverages [48]. There are a number of operating points for the $E_{\mathrm{T}}^{\mathrm{miss}}$ calculation, which largely have to do with the type of jets allowed into the calculations with a view to minimising the number of pile-up origin jets. To facilitate the identification and rejection of these jets the jet vertex tagging algorithm (JVT), which results in a likelihood discriminant that can be selected on [49]. A more specific use case of this algorithm is forward jet vertex tagging (fJVT) specifically targeting jets which have no tracking information to constrain them to a vertex [50]. The *Loose* operating point for instance requires central jets ($|\eta| < 2.4$) of less than 60 GeV to pass JVT> 0.59 while *Tight* requires forward jets to be greater than 30 GeV to be included in calculations.

4.4 Simulation of SM and BSM processes

Simulation is vital at all stages of particle physics: from the development of signatures for SM and BSM processes, to prototyping detectors, understanding and constraining backgrounds, and guiding optimisation of searches and measurements. In particle physics, simulations almost exclusively take the form of Monte Carlo.

4.4.1 Monte Carlo generators

Since there are vast numbers of particles produced in hadron collisions, with momenta ranging from TeV to MeV, simulating events is a difficult task, especially at lower energies where QCD is non-perturbative. The procedure for generating these simulated events is performed in several steps. The matrix element for the hard scattering between the two incident protons is calculated from perturbation theory to some order; for example if the calculation is done to leading order (LO), then the next-to-leading-order (NLO) effects can be parameterised by the k-factor, the ratio of the NLO to LO calculation in a particular kinematic regime. The *parton distribution function* (PDF) is a major input into the hard scattering calculation describing the constituents of the protons: sea and valence quarks, and gluons, and their momentum fractions as a function of the total momentum transfer. In addition the factorisation scale, which is the transition point between perturbative and non-perturbative regimes, and the renormalisation scale describing the running coupling of the strong interaction both need to be fixed. These scales are unphysical and their effects on results are lessened with additional orders of perturbation theory.

From the highly energetic and clean hard process, the event evolves down to lower energy scales and higher object multiplicities to the confinement scale, described by parton shower algorithms based on DGLAP [51–53] evolution. The incoming and outgoing partons shower, radiating off other partons or splitting repeatedly. The parton shower accounts for other effects not found in the original fixed order calculation for the underlying process. The hadronisation step where the partons finally decay into colourless bound states is based on phenomenological models such like the *colour string model* [54]. The parameters of these models are not dependent on the initial hard process, but instead can be derived for a representative dataset and then applied to other situations. In addition *underlying event activity*, consisting of multiple parton interactions alongside the main process, must be considered. These interactions are included by overlaying the simulated event with some general pp collision events.

Given the complex multi-step nature of simulating the full range of SM and BSM processes at hadron colliders, a variety of MC generator programs have been de-

veloped with different parameters and tunings to provide maximal phase space coverage, as well as robust modelling of key kinematic properties.

4.4.2 Detector simulation

Once the events have been simulated, the decay products must be propagated through a detector simulation to get a suitable comparison to real data. To this end the ATLAS detector, including support structures, is simulated using *GEANT* [55, 56] to derive energy deposits and track behaviour for each simulated particle. Then the various detector subsystem specific digitisation software converts these simulated signals into the same format as signals received by real events, and reconstruction is carried out in the same way.

In the *full simulation* procedure described above, the detector simulation component is very computationally expensive and takes several minutes per event, largely due to the calorimeter response in *GEANT*4. A *fast simulation* procedure Atlfast-II (AFII) [57] has been developed, utilising parameterised calorimeter response with lookup tables, and is used where the full calorimeter response is not required.

4.4.3 Event weighting

MC generators are tuned to replicate certain important observables such as object momenta and direction, object multiplicities, $\vec{E}_{\mathrm{T}}^{\mathrm{miss}}$, and relative abundances of decay products. To achieve this, and to increase statistics and therefore reduce uncertainties, events are weighted according to the position in the phase space considered. This means that the sample is normalised to some benchmark integrated luminosity, usually 1 fb^{-1}, using the sum of weights instead of the number of events. 1 fb^{-1} is chosen due to the simulation being produced prior to data taking, so that when comparing to data they can be easily weighted by the integrated luminosity.

5 Electron ID Efficiency at Low Energies

This section presents work that was done in combined performance for low energy electron identification (ID) efficiency using J/ψ decays, based on the method described in [58] and presented in [38]. Electrons from isolated sources are vital to both SM measurements and searches for new physics, but corrections to the experimentally determined electrons are required. Various selection efficiencies, relating to triggers, isolation, identification, and reconstruction, must be taken into account before measurements can be made. The efficiencies can be taken directly from data using *tag-and-probe* methods. The total efficiency can be written as a product of different efficiency terms

$$\epsilon_{\text{total}} = \epsilon_{\text{EMclus}} \times \epsilon_{\text{reco}} \times \epsilon_{\text{id}} \times \epsilon_{\text{trig}} = \left(\frac{N_{\text{cluster}}}{N_{\text{all}}}\right) \times \left(\frac{N_{\text{reco}}}{N_{\text{cluster}}}\right) \times \left(\frac{N_{\text{id}}}{N_{\text{reco}}}\right) \times \left(\frac{N_{\text{iso}}}{N_{\text{id}}}\right) \times \left(\frac{N_{\text{trig}}}{N_{\text{iso}}}\right), \quad 5.1$$

where each are determined successively from all energy deposits to events passing triggers. The identification efficiency is the number of reconstructed electrons which pass some identification criteria. Importantly there is difference in the response of simulation and real data at each of the stages of reconstruction that needs to be accounted for and corrected. Efficiency studies are used to find these multiplicative correction factors.

5.1 The basics of electron identification

Electrons in the central region of ATLAS ($|\eta| < 2.47$) are selected using likelihood based (LH) identification methods. The inputs into the LH are from tracking, calori-

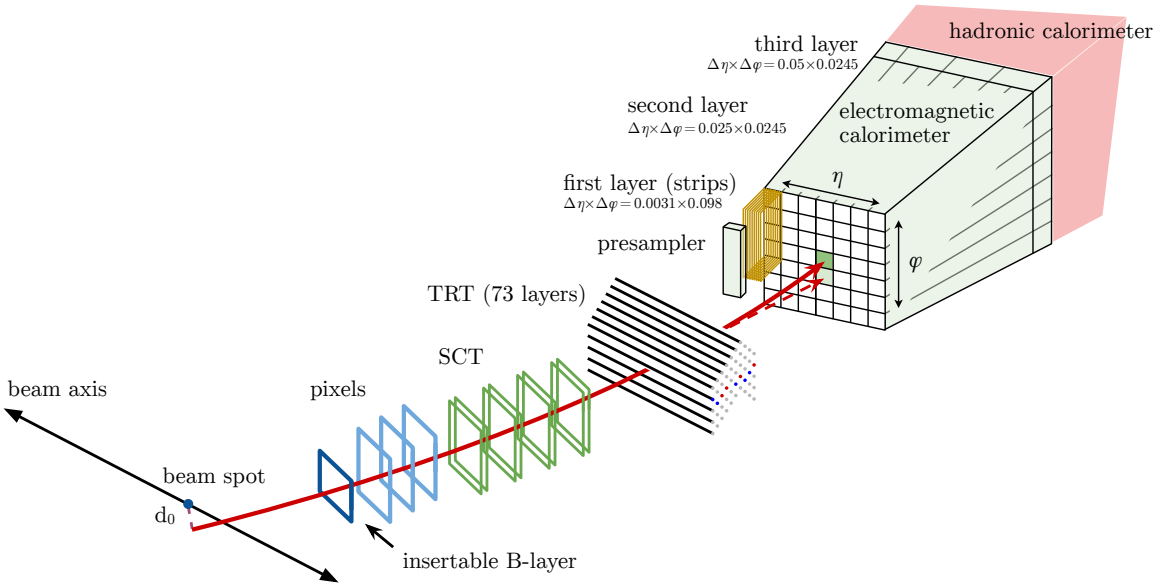

Figure 5.1: A schematic of the path of an electron candidate (red trajectory) through the detector [38].

metry, and some secondary quantities constructed from both tracks and calorimetry. These inputs are listed in Table 5.1, and a schematic of the path of an electron through the detector is illustrated in Figure 5.1.

The electron LH is based on the products of signal (L_s), and background (L_B) of n pdfs, P:

$$L_{S(B)}(\mathbf{x}) = \prod_{i=1}^{n} P_{S(B),i}(x_i), \tag{5.2}$$

where $\mathbf{x}$ is a vector of the variables listed in Table 5.1, $P_{S,i}(x_i)$ is the signal pdf value at x_i and $P_{B,i}(x_i)$ is the background pdf for the same variable. The signal is prompt electrons, while the backgrounds can range from jets faking prompt electrons, photon conversions in the detector, non-prompt electrons from heavy flavour (c and b) hadrons. Any correlations in the quantities are neglected.

Before Run 2 the conditions at 13 TeV had to be simulated instead of being derived from data, with the probability density functions (pdfs) being reweighted to match data. This procedure was refined through Run 2 and likelihoods based on data were

developed.

A discriminant d_L is constructed for each electron candidate:

$$d_L = \frac{L_S}{L_S + L_B}, \tag{5.3}$$

the electron LH is based on this. d_L has sharp peaks at 0 and 1 for background and signal respectively: the peaking structure can lead to issues with selecting operating points due to fine binning. To change the behaviour and range of the discriminant, an inverse sigmoid function is used:

$$d'_L = -\tau^{-1} log(d_L^{-1} - 1), \tag{5.4}$$

where τ is fixed at 15. For each operating point a value of this inverted discriminant is chosen: electrons with d'_L larger are signal.

There are some advantages to using a LH based selection for electrons when compared to more standard selections ("cut-based" methods): prompt electrons can fail ID by not satisfying a single selection while they can be kept in the LH, and the range of discriminating variables that are used in LH methods can be wider than in cut-based methods where certain variables cannot be used without large losses in efficiency.

The pdfs are derived in bins of electron candidate E_{T} and η using finely binned histograms of the various quantities, with some smoothing applied to avoid unphysical fluctuations arising from low statistics. Due to differences in the detector response between simulation and data some of the quantities used in LH calculation need to be corrected. The differences manifest as either shifts in distributions or changes in width quantified by full-width at half-maximum (FWHM) in the distributions. f_1, f_3, R_η, $w_{\eta 2}$ and R_θ have η-dependent shifts, while f_1, f_3, R_{had}, $\Delta\eta_1$ and $\Delta\theta_{\mathrm{res}}$ have FWHM differences in 2015-16. In later years of Run 2 the corrections are less required due to the availability of data to base likelihoods on. The corrections are applied as η-dependent shifts and multiplicative factors on distributions, the values of which are determined by χ^2 minimisation of compared data and simulation distributions. For low E_{T} pdfs ($4.5 < E_{\mathrm{T}} < 15$ GeV) $J/\psi \to ee$ Monte Carlo is used, and for higher energies (> 15 GeV) $Z \to ee$ MC is used.

Table 5.1: Quantities used for electron identification. These are broken into type based on detector component and the "Rejects" column describes whether the variable discriminates electrons from light flavour (LF) jets, photons (γ), and/or heavy flavour (HF) jets.

Type	Description	Name	Rejects			Usage
			LF	γ	HF	
Hadronic leakage	Ratio of E_T in the first layer of the hadronic calorimeter to E_T of the EM cluster (used over the range $\lvert\eta\rvert < 0.8$ or $\lvert\eta\rvert > 1.37$)	R_{had1}	x	x		LH
	Ratio of E_T in the hadronic calorimeter to E_T of the EM cluster (used over the range $0.8 < \lvert\eta\rvert < 1.37$)	R_{had}	x	x		LH
Third layer of EM calorimeter	Ratio of the energy in the third layer to the total energy in the EM calorimeter. This variable is only used for $E_T < 80$ GeV, due to inefficiencies at high E_T, and is also removed from the LH for $\lvert\eta\rvert > 2.37$, where it is poorly modelled by the simulation.	f_3	x			LH
Second layer of EM calorimeter	Lateral shower width, $\sqrt{(\Sigma E_i \eta_i^2)/(\Sigma E_i) - ((\Sigma E_i \eta_i)/(\Sigma E_i))^2}$, where E_i is the energy and η_i is the pseudorapidity of cell i and the sum is calculated within a window of 3×5 cells	$w_{\eta 2}$	x	x		LH
	Ratio of the energy in 3×3 cells over the energy in 3×7 cells centred at the electron cluster position	R_ϕ	x	x		LH
	Ratio of the energy in 3×7 cells over the energy in 7×7 cells centred at the electron cluster position	R_η	x	x	x	LH
First layer of EM calorimeter	Shower width, $\sqrt{(\Sigma E_i (i - i_{max})^2)/(\Sigma E_i)}$, where i runs over all strips in a window of $\Delta\eta \times \Delta\phi \approx 0.0625 \times 0.2$, corresponding typically to 20 strips in η, and i_{max} is the index of the highest-energy strip, used for $E_T > 150$ GeV only	w_{stot}	x	x	x	C
	Ratio of the energy difference between the maximum energy deposit and the energy deposit in a secondary maximum in the cluster to the sum of these energies	E_{ratio}	x	x		LH
	Ratio of the energy in the first layer to the total energy in the EM calorimeter	f_1	x			LH
Track conditions	Number of hits in the innermost pixel layer	n_{Blayer}		x		C
	Number of hits in the pixel detector	n_{Pixel}		x		C
	Total number of hits in the pixel and SCT detectors	n_{Si}		x		C
	Transverse impact parameter relative to the beam-line	d_0		x	x	LH
	Significance of transverse impact parameter defined as the ratio of d_0 to its uncertainty	$\lvert d_0/\sigma(d_0)\rvert$		x	x	LH
	Momentum lost by the track between the perigee and the last measurement point divided by the momentum at perigee	$\Delta p/p$	x			LH
TRT	Likelihood probability based on transition radiation in the TRT	eProbabilityHT	x			LH
Track–cluster matching	$\Delta\eta$ between the cluster position in the first layer and the extrapolated track	$\Delta\eta_1$	x	x		LH
	$\Delta\phi$ between the cluster position in the second layer of the EM calorimeter and the momentum-rescaled track, extrapolated from the perigee, times the charge q	$\Delta\phi_{res}$	x	x		LH
	Ratio of the cluster energy to the track momentum, used for $E_T > 150$ GeV only	E/p	x	x		C

Table 5.2: Boundaries in absolute cluster η used for LH pdf and LH discriminants.

Bin boundaries in $\lvert\eta\rvert$									
0.0	0.6	0.8	1.15	1.37	1.52	1.81	2.01	2.37	2.47

Table 5.3: Boundaries in transverse electron energy used for LH pdf and discriminants.

Bin boundaries in E_{T} [GeV]													
pdfs	4.5	7	10	15	20		30		40				∞
Discriminant	4.5	7	10	15	20	25	30	35	40	45	80	150	∞

To cover the varying prompt-electron needs of ATLAS, there are four values of the LH discriminant used as benchmark operating points. These are referred to as VeryLoose, Loose, Medium, and Tight in order of increasing LH thresholds and hence signal selection reduction and increased background rejection. The identification is split in bins of absolute η and E_{T}, as shown in Table 5.2 and Table 5.3, with the $|\eta|$ bins being chosen to reflect the detector geometry and composition, along with the change in pdfs as a function of energy. The background sources and rates also vary with η and E_{T}. The discriminant is binned finer than the pdfs to smooth out the variation across E_{T}, and the pdf values and discriminants are linearly interpolated between the centres of two adjacent bins. The operating points have some fixed tracking quality requirements. Loose (LLH), Medium (MLH), and Tight (TLH) operating points require at least seven hits in the inner detector, with at least two of those being in the pixel. For Medium and Tight this requirement is further tightened to require the innermost pixel layer to record a hit to avoid photon conversions. A variation on Loose is LooseAndBLayer (LLHBL), which involves the additional requirement of a hit in the innermost pixel layer. VeryLoose does not require this innermost layer hit, indeed only requiring a single hit in the pixel detector, allowing for background studies. Each of these likelihoods can also be calculated with a $d_0 - z_0$ significance cut. Some of the pdfs are dependent on pileup conditions, especially R_{had} and R_η which are affected by extra activity in the calorimeters. To mitigate these changes each E_{T}-η bin of the d_L' is adjusted with a linear variation in n_{vtx}, the number of primary vertices per collision. The background efficiency is constrained to be approximately constant with n_{vtx}, resulting in a slight

($\leq 5\%$) decrease in signal efficiency at high n_{vtx}.

To measure the efficiency of these LH working points and to derive corrections to be applied to simulation for a range of electron transverse energies across the entire detector, there are a number of methods relying on either Z bosons or J/ψ mesons depending on the energy range probed. One of the two low E_{T} methods is known as the τ-fit method.

5.2 τ-fit method

The τ-fit method is a way of determining the efficiencies of LH based identification based on the tag-and-probe paradigm. From a known resonance, in this case the J/ψ meson (mass 3.1 GeV), unbiased *probes* are selected by applying strict criteria on the other object (*tags*) from the decay. Events are selected based on fitting the dielectron invariant mass (m_{ee}), and then signal like events are further separated into prompt and non-prompt components using pseudo-proper time fits. In contrast the other method is τ-cut, where as the name suggests, the non-prompt component is largely cut out with the remainder being estimated using results from $J/\psi \to \mu\mu$.

5.2.1 Triggers and dataset requirements

The dataset consists of events passing a set dedicated triggers with E_{T} ranging from 4 to 14 GeV, where one electron candidate (or *leg*) passes strict criteria and the other has some loose E_{T} selection and lower ID thresholds. In 2017 the triggers were moved to L1Topo, with a dielectron invariant mass window of $1 < m_{ee} < 5$ GeV. Due to the large rates of low mass resonances the triggers are prescaled depending on E_{T} and luminosity conditions, and need to be unprescaled before the events can be used. The tag must be outside the calorimeter transition region ($1.37 < |\eta| < 1.52$, known as the "crack" region), and must associated to the Tight trigger leg. The other leg must be matched to the probe, and if both electrons pass the tag requirements then there are two probes in the event. Due to the challenging environment with both prompt and non-prompt signal components, along with considerable background

processes requires some isolation requirements on the tag and probe electrons. The probe electrons have only very relaxed isolation requirements to avoid biasing the ID efficiency measurement. The tag and probe electrons also need to be separated with $\Delta R > 0.15$.

Simulation is used for signal like J/ψ mesons and background b-hadrons decaying to J/ψ, with continuum backgrounds being estimated with same-sign events from data. Due to the reduced statistics of the samples compared to those for the other ID methods based on Z decays, the $E_{\mathrm{T}} - |\eta|$ binning of the probe electrons needs to be both coarser and binned in absolute η, shown in Table 5.4 and Table 5.5.

Table 5.4: The $|\eta|$ binning scheme used in the τ-fit method. The bins reflect detector geometry.

Bin boundaries in $\lvert\eta\rvert$ in τ-fit.						
0.0	0.1	0.8	1.37	1.52	2.01	2.47

Table 5.5: The E_{T} binning scheme used in the τ-fit method. The 15-20 GeV bin is only used for overlap studies with the Z based methods.

Bin boundaries of E_{T} (GeV) in τ-fit.				
4.5	7	10	15	(20)

5.2.2 Mass fits

Events which pass the basic selections are passed into a fit on m_{ee}, where the main J/ψ and smaller $\psi(2S)$ peaks are fit with MC using Gaussians convolved with Crystal Ball functions to account for resolution effects, and backgrounds are estimated using same-sign events fit with a second-order Chebyshev polynomial. In $E_{\mathrm{T}} - \eta$ bins where χ_c, another $c\bar{c}$ resonance, is significant another Gaussian and Crystal Ball fit can be made. The treatment of same-sign contributions has varied throughout Run 2, depending on reconstruction changes and data taking configurations. The original method is to subtract the same-sign events from the total, reweighting the

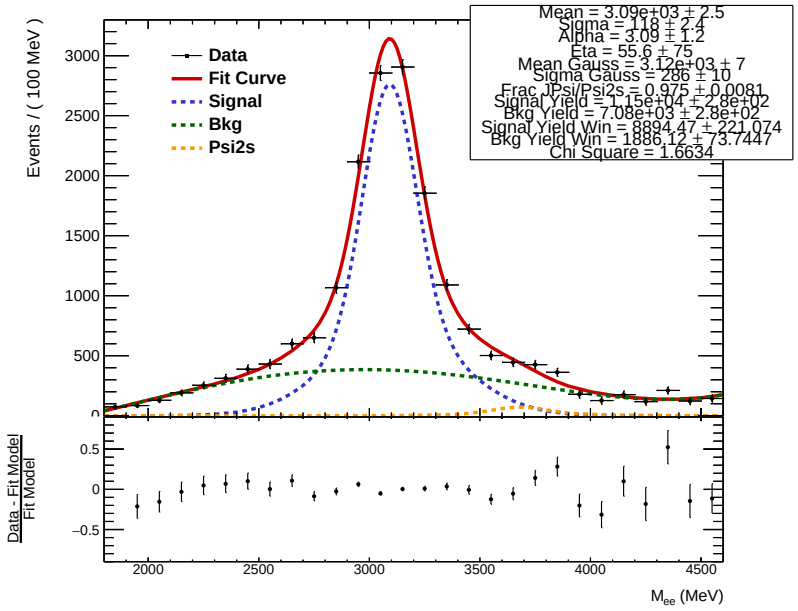

Figure 5.2: The mass fit result for the $E_{\mathrm{T}} - |\eta|$ bin $7 < E_{\mathrm{T}}$ GeV < 10, $0.1 < |\eta| < 0.8$.

m_{ee} distribution, and there is also the option of fitting the same-sign contribution explicitly. The fit range is $1.8 < m_{ee} < 4.6$ GeV.

5.2.3 Time fits

The extracted signal J/ψ mesons consist of those produced in primary vertices or radiative decays of heavier charmonium states (prompt) and those from decays of b-hadrons (non-prompt). The non-prompt J/ψ decay products are often not isolated in the same way as electrons that are used for physics analysis, being embedded in hadronic activity. To separate the two components the long lifetime of b-hadrons can be exploited via the pseudo-proper time

$$\tau = \frac{L_{xy} \times m_{\mathrm{PDG}}^{J/\psi}}{p_{\mathrm{T}}^{J/\psi}}, \tag{5.5}$$

where L_{xy} is the transverse distance from the primary vertex to the J/ψ vertex, $m_{\mathrm{PDG}}^{J/\psi}$ is the mass of the J/ψ, and $p_{\mathrm{T}}^{J/\psi}$ is the transverse momentum of the J/ψ. The pseudo-proper time is typically measured in the range $-1 < \tau\,(\mathrm{ps}) < 3$, though

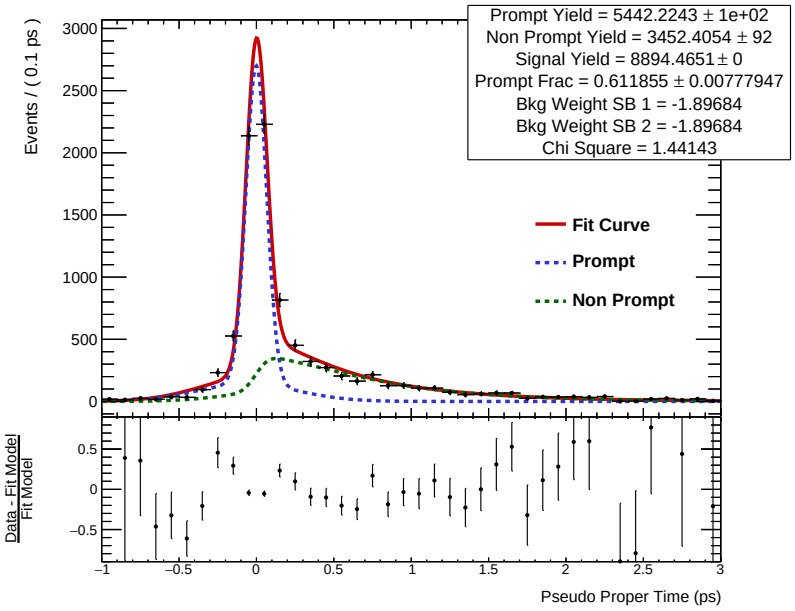

Figure 5.3: The time fit result for the $E_{\mathrm{T}} - |\eta|$ bin $7 < E_{\mathrm{T}}\mathrm{GeV} < 10$, $0.1 < |\eta| < 0.8$.

depending on the statistics populating the high tail of the distribution the range can be shortened. The prompt peak was initially fit with a double Gaussian, and later with a Gaussian and Crystal Ball functions. The non-prompt tail is modelled with a Gaussian convolved with an exponential function. The remnant background contribution is estimated with sidebands of the mass fit which is then subtracted from the J/ψ component before the time fit is done. Thus the fit itself is purely separating the prompt and non-prompt signal components. A typical time fit result is shown in Figure 5.3.

5.2.4 Efficiencies and scale factors

Once a reliable sample of prompt J/ψ mesons has been extracted from the data and MC simulation, the efficiency calculations can be carried out. There are two axes on which the efficiencies can be measured: data or MC, prompt or non-prompt. The non-prompt efficiencies are not applicable to physics analyses, but the prompt efficiencies are important for determining the effect of LH selections on the probe

electrons.

The mass and time fits for each E_T-$|\eta|$ segment are done with four LH selections: no selection (known as the container), LooseAndBLayer, Medium, and Tight, each with the $d_0 - z_0$ significance cut applied. For each of these LH selections data and MC efficiencies are derived (Figure 5.4), with the ratio of data/MC being the scale factor (SF) that is supplied to analyses to account for the differences in LH response between data and simulation (Figure 5.5).

5.2.5 Systematic uncertainties

There are a systematic uncertainties from a number of sources: the isolation requirements applied to the tag and probe electrons, the functions used to fit both mass and time, along with fit ranges for sidebands and signal peaks. These uncertainties are evaluated by independent variations of the selection of input events (in the case of isolation), or of the parameters in the mass/time fits. Any correlations between the variations are neglected. The full chain of mass and time fits are carried out for each variation, and are added in quadrature during the efficiency and SF calculations.

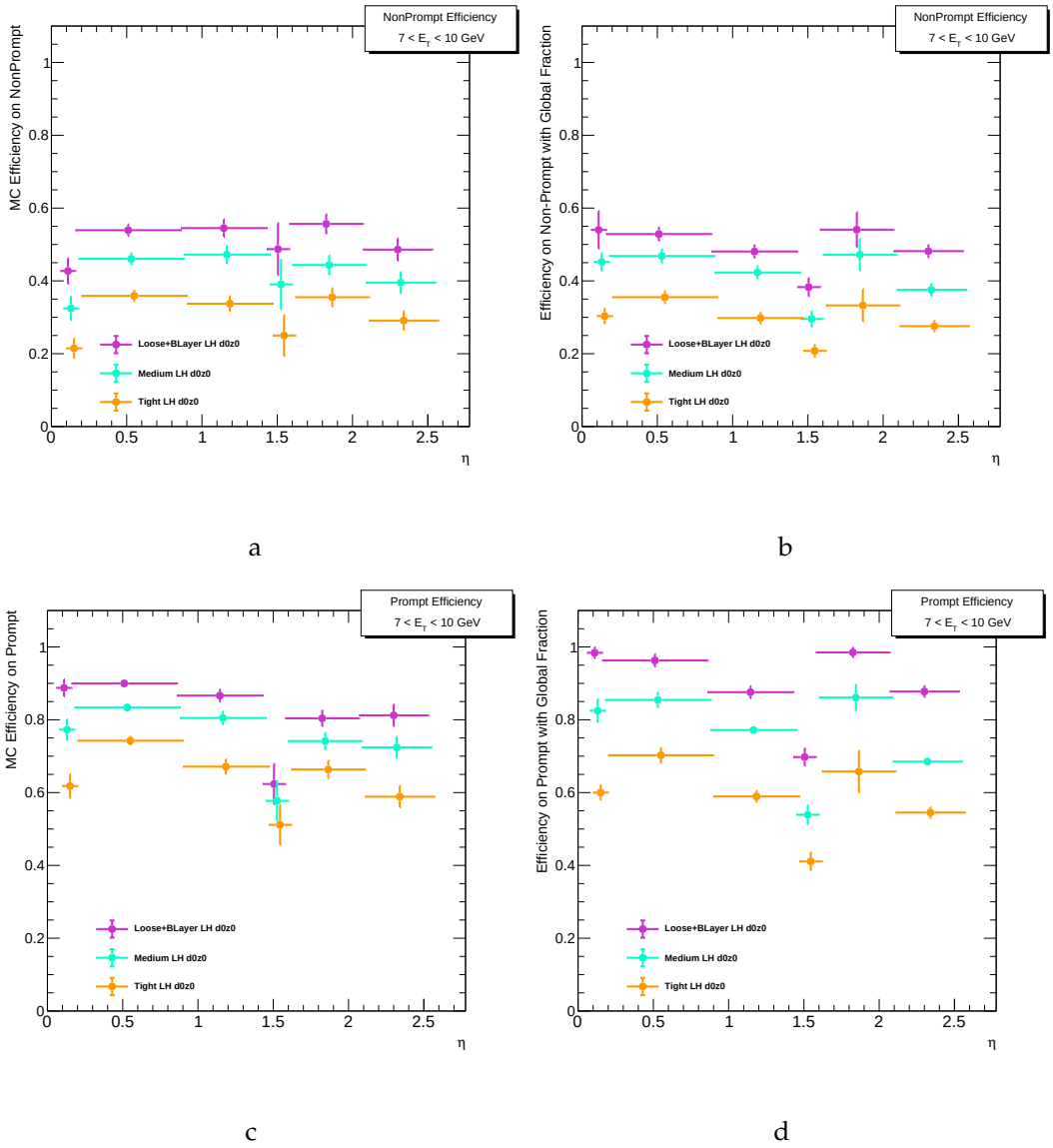

Figure 5.4: Efficiencies for all LH working points in $7 < E_{\mathrm{T}} < 10$ GeV for: (Figure 5.4a) non-prompt MC, (Figure 5.4b) non-prompt data, (Figure 5.4c) prompt MC, and (Figure 5.4d) prompt data.

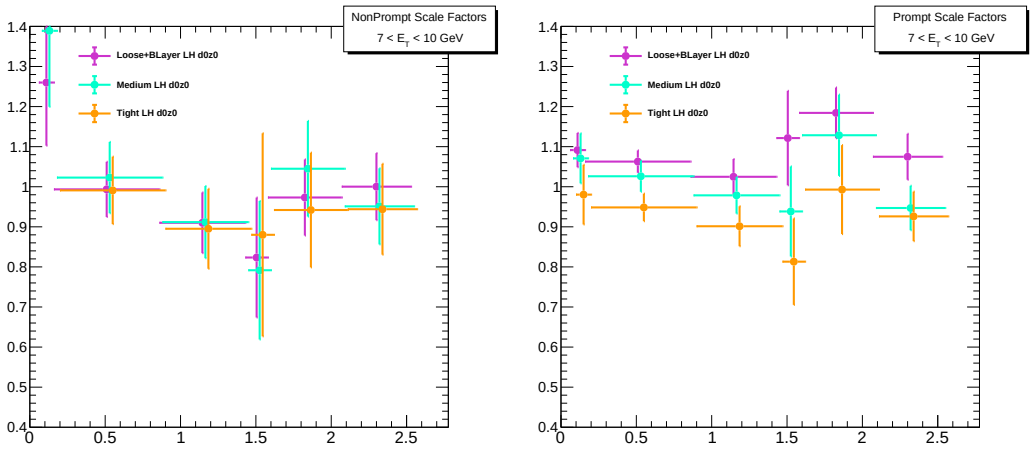

a b

Figure 5.5: Scale factors for all LH working points in $7 < E_{\mathrm{T}} < 10$ GeV for: (Figure 5.5a) non-prompt, and (Figure 5.5b) prompt.

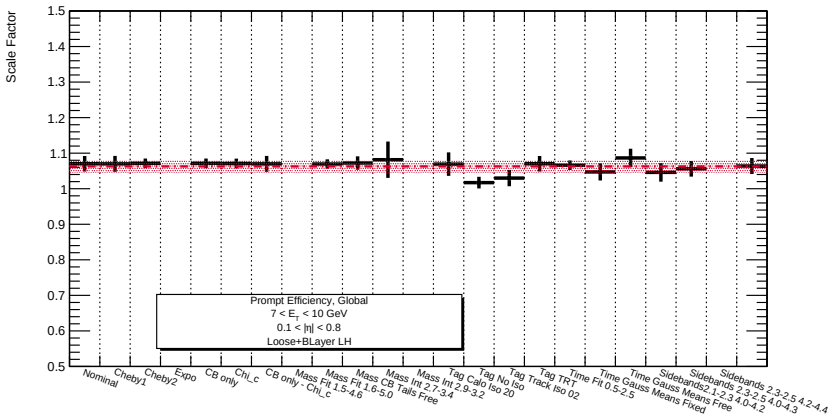

a

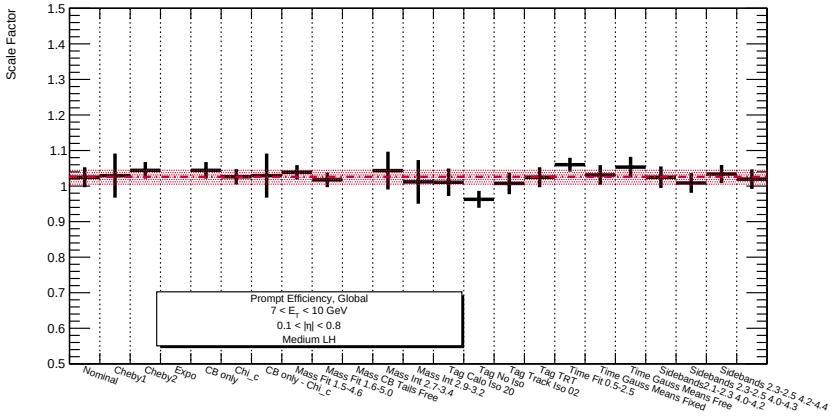

b

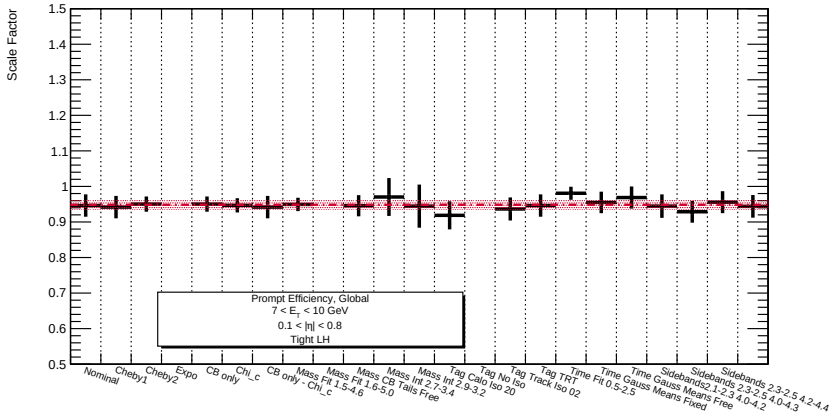

c

Figure 5.6: Systematic variation effects in SFs for $7 < E_{\mathrm{T}} < 10$ GeV, $0.1 < |\eta| < 0.8$: (Figure 5.6a) LLHBL, (Figure 5.6b) MLH, (Figure 5.6c) TLH. Not all the variations are applicable for all $|\eta|$ ranges and so do not appear.

5.3 Pushing the boundaries: electrons at $E_T = 4.5$ GeV

Motivated in part by searches for supersymmetric particles with compressed mass spectra, lowering the E_T threshold of electrons was made a priority in Run 2. The question of what lower bound is achievable depends largely on the triggers that are used to collect J/ψ data, with 4 GeV being the minimum probe leg E_T. A study on the behaviour of the probe E_T (Figure 5.7) showed that the trigger plateau, where there are enough statistics and reliable behaviour from the triggers, was reached at 4.5 GeV. Once the range is fixed, a new E_T bin from 4.5-7 GeV was added to efficiency measurements. The background shapes and fitting functions were adjusted

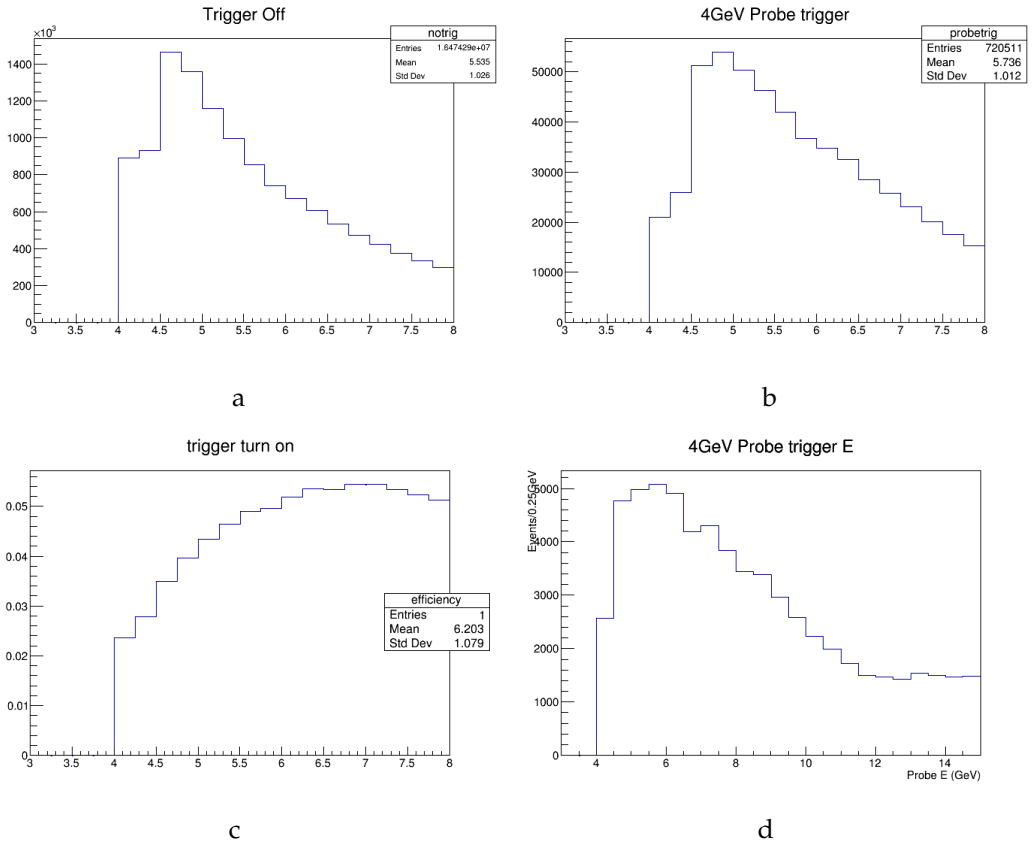

Figure 5.7: Trigger behaviour in data of the probe E_T: (Figure 5.7a) without triggers, (Figure 5.7b) probe trigger matching applied, (Figure 5.7c) the efficiency of the probe trigger leg, (Figure 5.7d) the probe E_T after applying trigger requirements to both tag and probe legs. The turn-on at 4.5 GeV determines the minimum probe energy achievable.

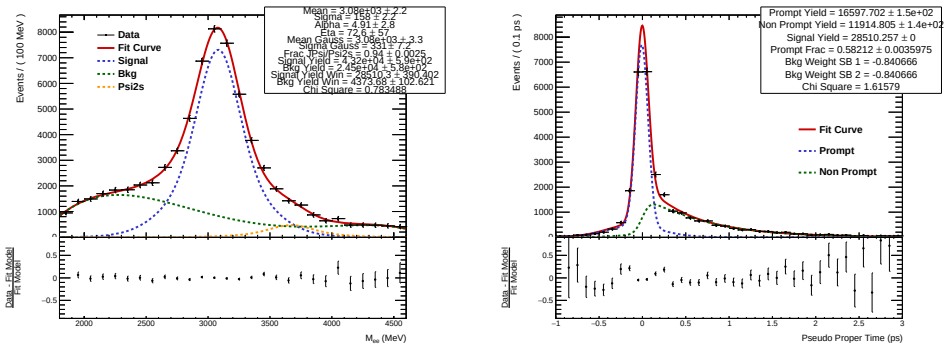

a b

Figure 5.8: $4.5 < E_T < 7$ GeV mass (Figure 5.8a) and time (Figure 5.8b) fits over the full $|\eta|$ range.

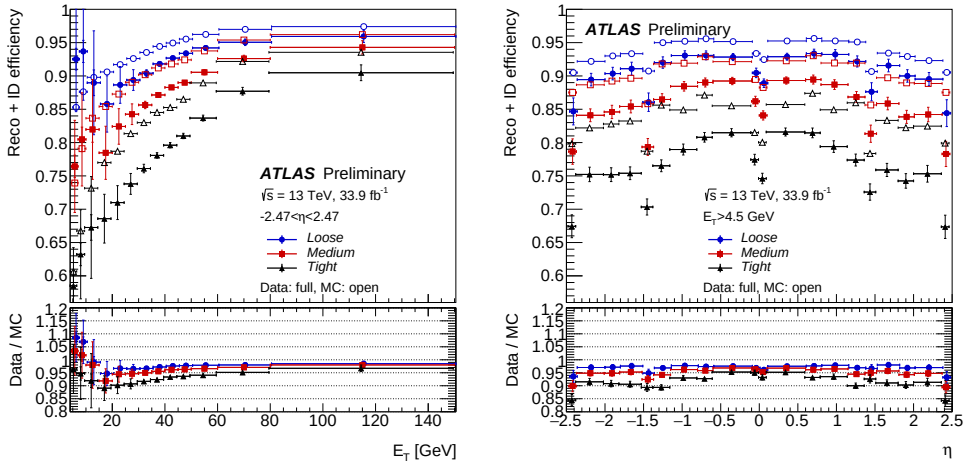

a b

Figure 5.9: Electron efficiency measurements in 2016 data are shown in energy in Figure 5.9a and η in Figure 5.9b [59].

to account for the continuum distributions. Third order Chebyshev polynomials covered the abundance of events low m_{ee} well, and the existing signal functions worked well, as seen in Figures 5.8a and 5.8b. There were also enough events spread through the bins of $|\eta|$ to allow for the calculation of scale factors, shown in the first bin of Figure 5.9a and incorporated in the η distribution of Figure 5.9b. This remains the lowest energy for electron reconstruction and identification at ATLAS.

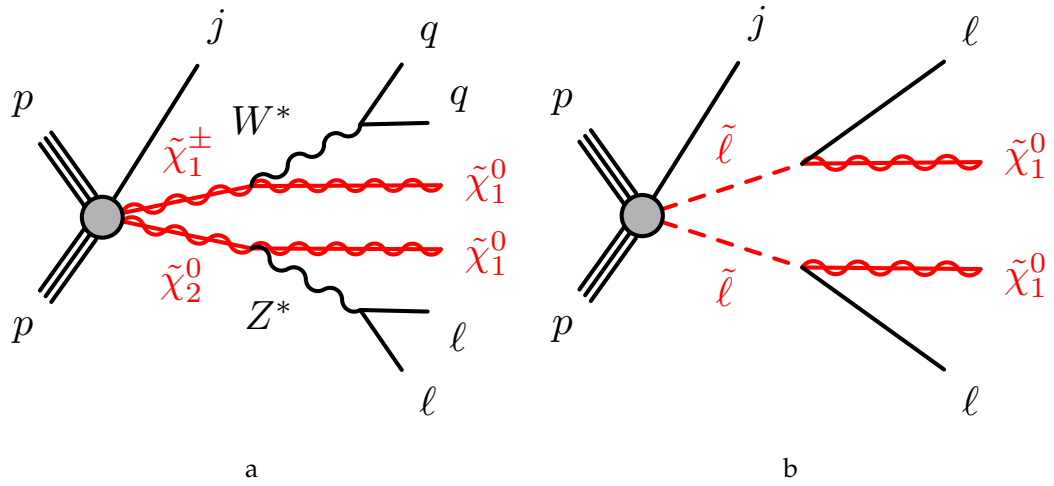

Figure 5.10: The processes considered with $\tilde{\chi}_2^0\,\tilde{\chi}_1^{\pm}$ (Figure 5.10a), and $\tilde{\ell}\,\tilde{\ell}$ (Figure 5.10b).

5.4 An application: compressed electroweak SUSY

The first application of the new lower electron E_{T}, along with similar developments to low momentum muons, is in a compressed (small sparticle mass splitting) electroweak SUSY search with leptons and jets in the final state boosted with ISR jets [60]. The processes searches for are chargino-neutralino production with decays to LSPs via W and Z bosons, and slepton decays to LSPs with leptonic final states, with diagrams shown in Figure 5.10. The chargino-neutralino process is further divided into Higgsino or wino/bino dominated decays with different final state characteristics, and the slepton pair decay can also be interpreted in terms of di-chargino production decaying via W bosons.

The leading lepton p_{T} requirement is 5 GeV, subleading lepton is 4.5 GeV with events being triggered on $E_{\mathrm{T}}^{\mathrm{miss}}$. Major backgrounds consist of top quark processes, $Z \rightarrow \tau\tau$+jets, and diboson events, along reducible backgrounds from fake and non-prompt leptons or poorly reconstructed $E_{\mathrm{T}}^{\mathrm{miss}}$. The first two backgrounds are constrained in control regions, dibosons are estimated directly from MC, and fake and non-prompt leptons are estimated from data using the Fake Factor (FF) method. $E_{\mathrm{T}}^{\mathrm{miss}}$ effects are studied with MC and are found to be negligible. Suitable validation regions binned in some discriminating variables such as $m_{\ell\ell}$ and m_{T2} are used to

check the effectiveness of the background estimations (shown in Figure 5.11). Signal regions also binned in $m_{\ell\ell}$ and m_{T2} are constructed from a common signal region (SR), with results and representative lepton distributions shown in Figure 5.12.

Strong limits are set on the Higgsino and wino/bino chargino-neutralino production with $2 < \Delta m < 25/30$ GeV up to $\tilde{\chi}_2^0$ masses of 175 GeV, and for sleptons for Δm of up to about 15 GeV (Figure 5.13). These limits are a great improvement from ATLAS Run 1 limits for all models considered, and could only be achieved with improvements in low momentum lepton ID.

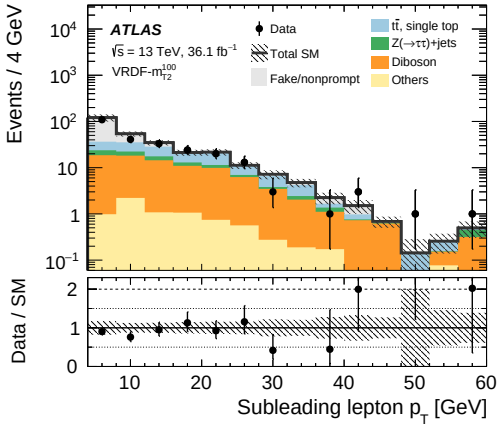

a

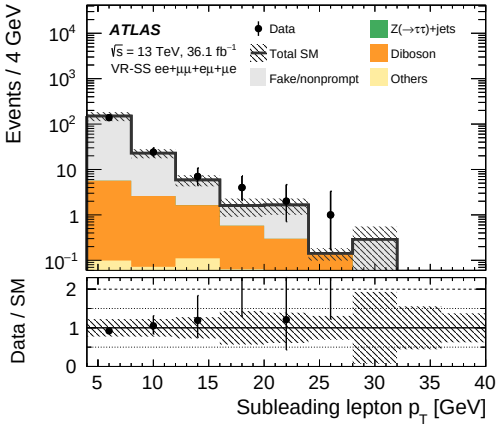

b

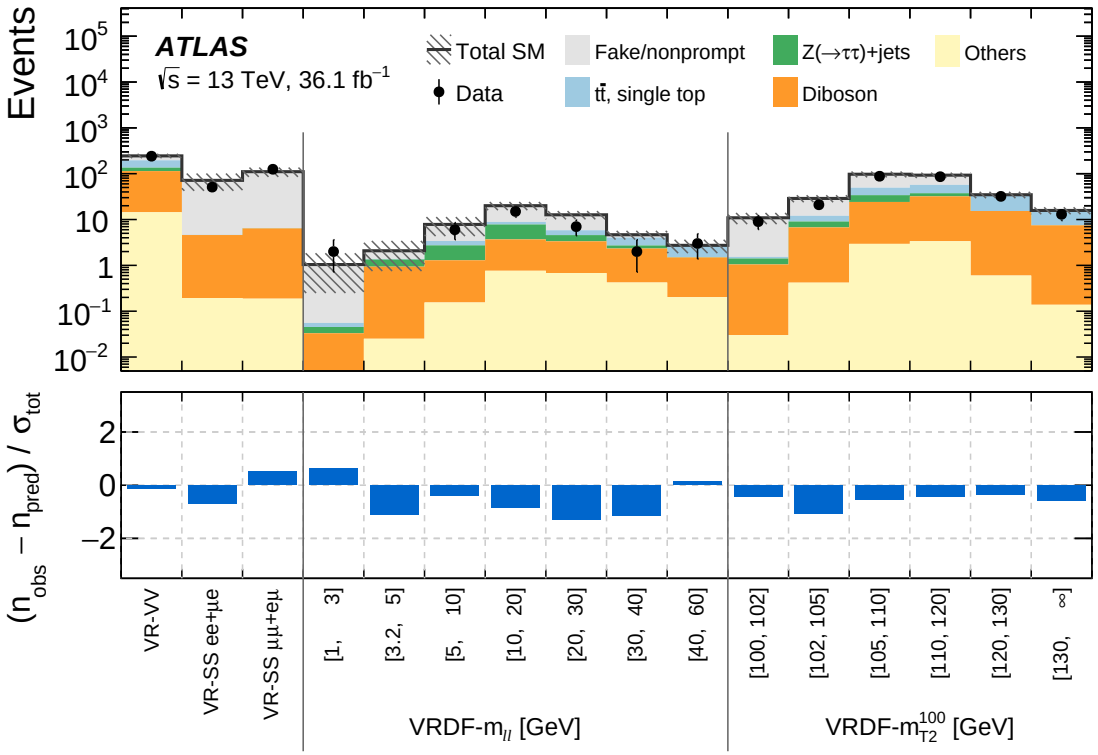

c

Figure 5.11: Distributions of sub-leading lepton p_{T} in validation regions (Figure 5.11c), (Figure 5.11b), and validation region summary (Figure 5.11c).

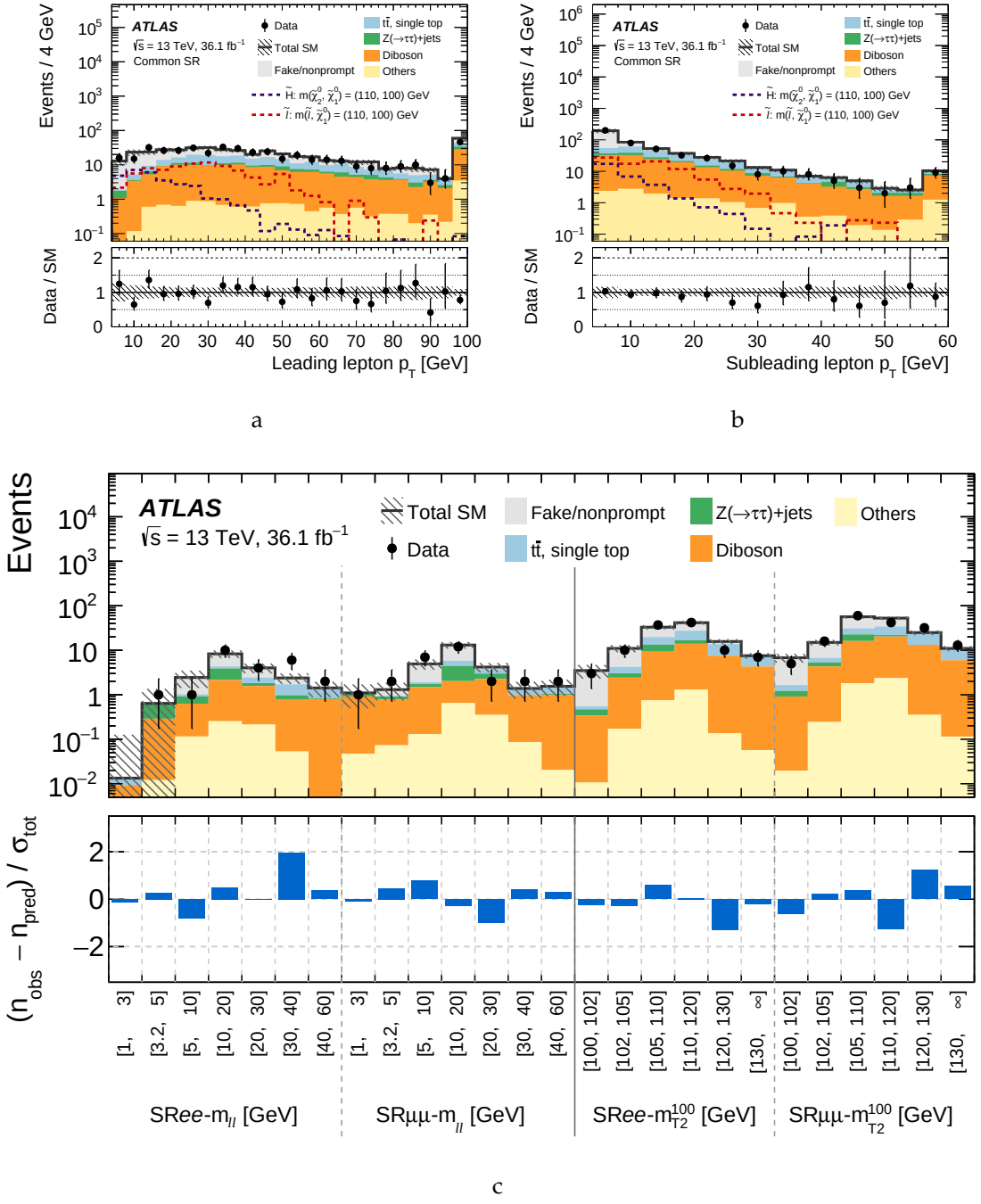

Figure 5.12: Distributions of leading (Figure 5.12a), and sub-leading lepton (Figure 5.12b) p_{T} in the common SR, and signal region summary (Figure 5.12c).

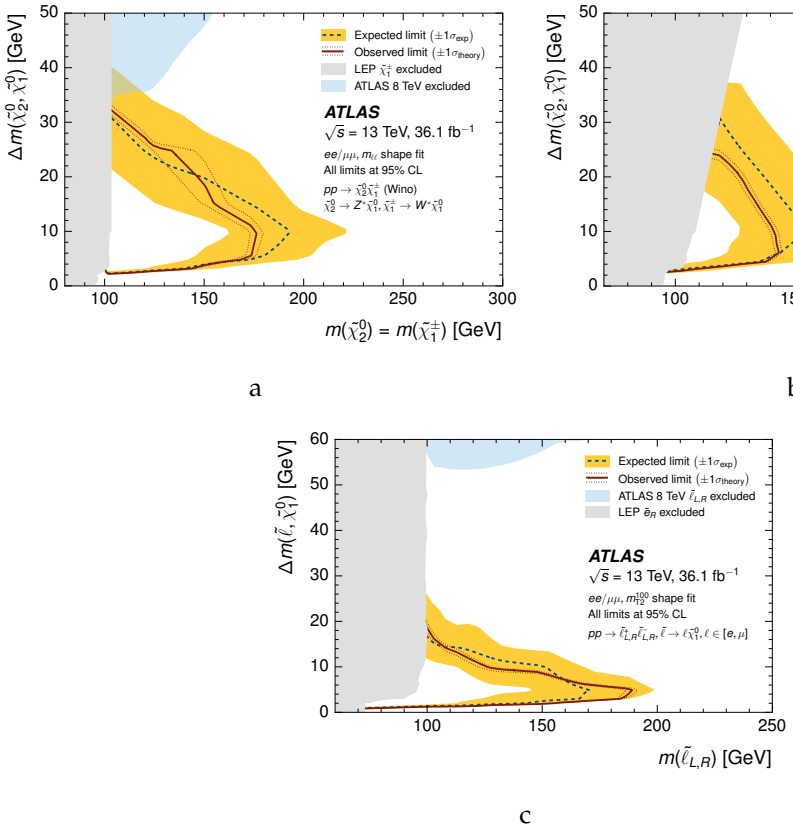

Figure 5.13: Wino (Figure 5.13a), Higgsino (Figure 5.13b), and slepton (Figure 5.13c) exclusions.

5.5 Improving τ-fit for the full Run 2 dataset

With improvements in particle reconstruction software for full Run 2 data analysis, the electron ID methods also require improvements to cope with the change in conditions. Of particular importance for fit-based methods is the improved background rejection at reconstruction level, which along with data-driven LH estimations lead to a lack of statistics for both mass and time. The former underlying continuum contribution that reduced fluctuations and allowed for easy fit convergence is greatly reduced, especially with the same-sign event subtraction and reweighting that is normally performed. To counteract this instability, the same-sign contribution can be restored to provide more statistics. In addition the objects that are reconstructed can have different properties, meaning that a review of the mass and time fitting

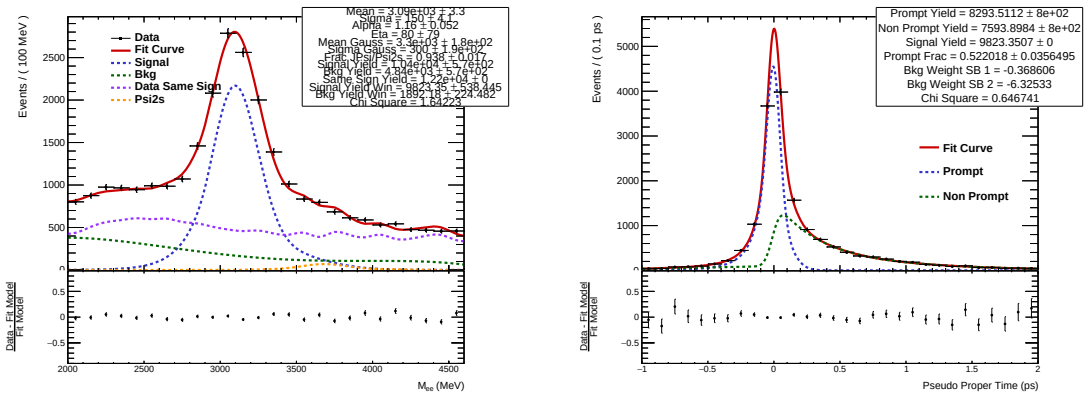

a b

Figure 5.14: An example of a mass (Figure 5.14a) and time (Figure 5.14b) fit with the inclusion of same-charge electron pairs.

functions themselves is needed to ensure accurate peak modelling. Another effect of the increased background rejection is the reduction of events with high τ values, signifying better knowledge of electrons resulting from b-hadron decays. The former time range of $-1 < \tau < 3$ ps is no longer required, and is shortened to $-1 < \tau < 2$ ps.

6 Recursive Jigsaw Reconstruction

There are a number of limitations of collider experiments when it comes to analysing data: reconstructing the processes leading to particular final states, combinatoric difficulties with identical particles and multiple interactions, and at hadron colliders, the fundamental lack of knowledge of initial parton momenta. To combat these shortcomings, an industry of kinematic variables has developed to maximise signal sensitivity, minimise (or at least control) backgrounds, and to provide meaningful descriptions of processes. While many analyses rely on a handful of kinematic variables, often with large correlations, ideally a *basis* of variables is more desirable to maximise sensitivity to the process being studied. It is with this in mind that *Recursive Jigsaw Reconstruction* (RJR) [61] was developed.

6.1 Kinematic variables: A brief overview

Whether undertaking a SM measurement or a BSM search carefully determined and validated variables are important. At the detector level observables such as p_{T}, η, and ϕ of objects, along with transverse momentum conservation ($E_{\mathrm{T}}^{\mathrm{miss}}$ and its direction), and counting the numbers of objects such as jets and leptons are all commonly used. In addition, combinations of these observables such as invariant masses (m_{ij}), summing the momenta in various ways such as m_{eff} and H_{T}, or angular separation between objects are also common. For example taking the invariant mass spectrum of same flavour opposite sign lepton pairs shows numerous resonances from the J/ψ and Υ mesons, up to the Z boson at higher values.

Once these basic variables have exhausted their applications, particularly when dealing with resonances with missing energy from neutrinos or hypothesised BSM

particles, then some higher level constructs are required. The archetype for such processes is $W \to \ell\nu$ at hadron colliders, where there is a missing degree of freedom from the longitudinal component of the neutrino that escapes the detector. The canonical way of dealing with this issue to restrict the reconstruction to the transverse plane with the transverse mass,

$$M_{\mathrm{T}}^2 = (E_{\mathrm{T},1} + E_{\mathrm{T},2})^2 - (\vec{p}_{\mathrm{T},1} + p_{\mathrm{T},2})^2, \tag{6.1}$$

which in the limit where the objects are massless (as is often assumed in hadron colliders), reduces to,

$$M_{\mathrm{T}}^2 = 2p_{\mathrm{T},1}p_{\mathrm{T},2}(1 - cos\phi_{12}), \tag{6.2}$$

having the useful property of being invariant under transverse boosts. For the case of the leptonically decaying W one of the inputs is the $E_{\mathrm{T}}^{\mathrm{miss}}$ vector, and was the method used to set a lower bound on the mass of the W boson at the time of its discovery [62].

From this point, it is natural to ask how to reconstruct parent particles when there is more than one source of missing momentum in a process. For example $WW \to \ell\nu\ell\nu$, $H \to WW \to \ell\nu\ell\nu$, or any R-parity conserving SUSY process will have two sources of $E_{\mathrm{T}}^{\mathrm{miss}}$, often of similar magnitudes. The case of pair produced SUSY particles, the parent being P and the LSP referred to as χ, have inspired a range of variables designed to decouple them from the SM backgrounds in the tails of mass distributions, most notably m_{T2} [63], the *stransverse mass* which splits the objects in the event into two hemispheres and attempts to constrain the missing degree of freedom using minimisation. This process also requires the input of a test mass m_χ for the LSP. M_{T2} is defined

$$M_{\mathrm{T2}}^2(m_\chi) = \underset{\vec{p}_{\mathrm{T}}^{\chi_1} + \vec{p}_{\mathrm{T}}^{\chi_2} = E_{\mathrm{T}}^{\mathrm{miss}}}{min} \{max[M_{\mathrm{T1}}^2, M_{\mathrm{T2}}^2]\}, \tag{6.3}$$

where

$$M_{\mathrm{T}}^2\left(m_\chi, \vec{p}_{\mathrm{T}}^{V_{1(2)}}, \vec{p}_{\mathrm{T}}^{\chi_{1(2)}}\right) = m_\chi^2 + 2\left(E_T^{V_{1(2)}} E_{\mathrm{T}}^{\chi_{1(2)}} - \vec{p}_{\mathrm{T}}^{V_{1(2)}} \cdot \vec{p}_{\mathrm{T}}^{\mathrm{X}_1(2)}\right). \tag{6.4}$$

By varying the test mass appropriately the variable has a kinematic endpoint at the parent mass m_P, while if the test mass is zero then the mass splitting can be probed: $M_{\mathrm{T2}}(0) = M_\Delta = \frac{m_P^2 - m_\chi^2}{m_P}$.

From the example of M_{T2} a number of related variables can be introduced, such as M_{CT} (the *contrasverse mass*) defined with an opposite sign to the transverse mass, or extending to longer chains that are commonly hypothesised SUSY decays. A system of variables sensitive to mass splittings can also be defined, with the *razor variables* [64] being a well used example:

$$\begin{aligned} R &= \frac{M_{\mathrm{T}}^R}{M_R} \\ M_R^2 &= \left(E^{V_1} + E^{V_2}\right)^2 - \left(p_z^{V_1} + p_z^{V_2}\right)^2 \\ M_{\mathrm{T}}^R &= \frac{\sqrt{E_{\mathrm{T}}^{\mathrm{miss}}\left[p_{\mathrm{T}}^{V_1} + p_{\mathrm{T}}^{V_2}\right]^2 - E_{\mathrm{T}}^{\mathrm{miss}} \cdot \left[\vec{p}_{\mathrm{T}}^{V_1} + \vec{p}_{\mathrm{T}}^{J_2}\right]^2}}{4} \end{aligned} \quad . \tag{6.5}$$

The razor variable system can be extended to final states with > 2 visible objects by defining "mega-objects" which are vector sums of the individual objects in the two assumed hemispheres associated with the decays of the parent particles. The endpoint of M_{T}^R and the peak of M_R are at M_Δ, separating them from backgrounds with little to no $E_{\mathrm{T}}^{\mathrm{miss}}$ which populate low values of R. The *super-razor* variable M_Δ^R [65] can be added as an extension with a boost applied to get an estimation of the CM frame.

Variables can be combined in various ways to try to resolve specific information about events. For example $E_{\mathrm{T}}^{\mathrm{miss}}/m_{\mathrm{eff}}$ can be used to test how much of the energy in an event is taken by the $E_{\mathrm{T}}^{\mathrm{miss}}$.

These approaches are largely designed around pair produced particles and are sensitive to new physics beyond the SM scale, which manifest in the tails of distributions in the derived variables. Heavy optimisation on signal models is often needed to get sensitivity, and new physics at scales similar to the SM is very difficult to decouple from backgrounds. The question becomes: How can the optimal set of variables be derived for any process that needs to be studied?

6.2 Introduction to RJR

RJR is a technique for dealing with final states with combinatoric and/or kinematics ambiguities at collider experiments, as well as an analysis methodology for the

reconstructed particles. The method begins with imposing a decay tree onto the event corresponding to the signal topology in question, and then for each event finding the (approximate) inertial frames of reference for that tree. These reference frames are *reconstructed* using a set of *jigsaw* rules. The rules are specified from frame-to-frame by the degrees of freedom required by the Lorentz transformation between them. These rules are applied *recursively* up the decay chain from the lab frame through each intermediate frame in the tree, and RJR is a library of the jigsaw rules together with the methods for assembling them to reconstruct any process.

As an example of how RJR works for a simple system, consider $W \to \ell\nu$ once again. As shown in Equation 6.1 and its limiting case in Equation 6.2, along with not knowing the true centre of mass energy for the production of the W at a hadron collider there are two missing degrees of freedom from the neutrino: the energy and longitudinal component of the momentum. What *is* calculated is a $E_{\mathrm{T}}^{\mathrm{miss}}$ vector which together with the measured lepton four-vector forms the lab frame kinematic basis.

What RJR does is to parametrise the unknown degrees of freedom as unknown components of the velocity relating the lab frame to the W rest frame, $\vec{\beta}_W^{\mathrm{lab}}$ [1], where specifying this vector is equivalent to choosing values for the neutrino longitudinal momentum $p_{\nu,z}^{\mathrm{lab}}$ and m_ν, and hence being able to calculate the approximate rest frame of the W. The boost $\vec{\beta}_W^{\mathrm{lab}}$ can be broken into two parts: the longitudinal component $\beta_{W,z}^{\mathrm{lab}}$, and the transverse component $\beta_{W,\mathrm{T}}^{\mathrm{lab}}$. Instead of looking for accurate estimation of the longitudinal momentum, a value can be chosen so that any quantities derived are independent of the true value. This is equivalent to choosing $\beta_{W,z}^{\mathrm{lab}}$

$$\frac{\partial E_\ell^{\vec{\mathrm{lab}},z}\left(\beta_{W,z}^{\vec{\mathrm{lab}}}\right)}{\partial \beta_{W,z}^{\vec{\mathrm{lab}}}} = 0, \tag{6.6}$$

where $\beta_{W,z}^{\mathrm{lab}} = p_{\ell,z}^{\mathrm{lab}} / E_\ell^{\mathrm{lab}}$. This is also sets the rapidity of the neutrino equal to that of the visible lepton, a jigsaw rule that can be generalised to other decay processes. Now that the longitudinal component has been estimated the transverse component, which depends on m_ν, needs to be guessed. The complication here is that choosing $\beta_{W,\mathrm{T}}^{\mathrm{lab}}$ in a similar way to Equation 6.6, say minimising m_W, can lead to tachyonic

[1] $\vec{\beta}_W^{\mathrm{lab}}$ is the velocity (in units of c) of the W frame evaluated in the lab frame.

neutrinos. This is in general true for other systems with invisible particles too, so making the mass the smallest Lorentz invariant value must be done to ensure a viable event reconstruction. This is another jigsaw rule, which in this example means setting $m_\nu = 0$ as the neutrino mass is much smaller than the scale considered ($\approx m_W$). In addition to re-deriving M_T with the W mass estimation in the lab frame:

$$M_\mathrm{W}^2 = m_\ell^2 + 2\left(\left|\vec{p}_{\nu,\mathrm{T}}^{\,\vec{\mathrm{lab}}}\right|\sqrt{m_\ell^2 + \left|\vec{p}_{\ell,\mathrm{T}}^{\,\vec{\mathrm{lab}}}\right|^2} - \vec{p}_{\ell,\mathrm{T}}^{\,\vec{\mathrm{lab}}}\cdot\vec{p}_{\nu,\mathrm{T}}^{\,\vec{\mathrm{lab}}}\right) \tag{6.7}$$

more information such as the azimuthal decay angle of the W ϕ_W can be obtained. These handles are nearly independent from each other and only very weakly depend on the true momentum of the W in the lab frame. These quantities are also nearly independent of the transverse momentum of the W along with being explicitly invariant under longitudinal boosts. So a useful basis of variables can be derived, free from correlation.

Figure 6.1 shows a schematic of the decay tree, the W mass estimate compared to the true distribution, and the resilience of the reconstructed variables to to transverse momentum of the W. The results shown in Figure 6.1 are obtained using RestFrames [66], a package for implementing RJR including a suite of jigsaw rules as well as an inbuilt event generator.

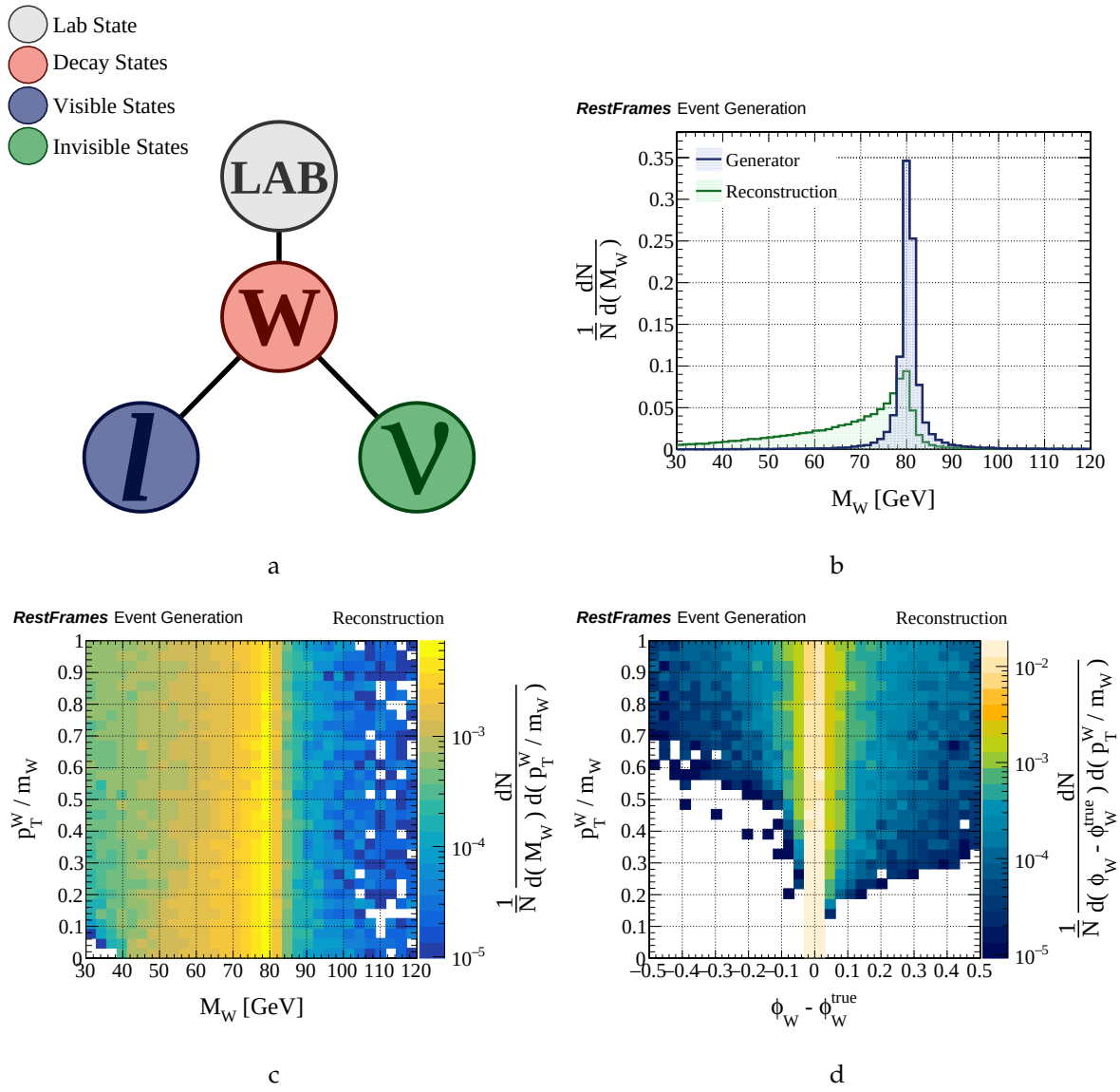

Figure 6.1: For the process $W \to \ell\nu$: (a) the reconstruction tree, (b) the comparison of the generator mass with the reconstruction, (c) M_W compared to p_T^W / m_W, and (d) $\Delta\phi_W$ compared to p_T^W / m_W. Event generation, reconstruction and plotting done with RestFrames [66].

6.3 Discerning the invisible: hemispheres and $\mathbb{Z}_2$ symmetry

For many SM and BSM processes of interest, most notably for all R-parity conserving SUSY scenarios with a $\mathbb{Z}_2$ symmetry, there are multiple sources of $E_{\mathrm{T}}^{\mathrm{miss}}$ which leads to further ambiguity to the partitioning of the momentum between the invisible particles. To be able to reconstruct the event in a similar way to $W \to \ell\nu$, the additional missing degrees of freedom need to be accounted for. Taking a classic simple SUSY decay scenario of pair produced $\tilde{q} \to q\tilde{\chi}_1^0$, there is one visible jet and an invisible $\tilde{\chi}_1^0$ for each side of the decay. The two $\tilde{\chi}_1^0$ transverse momenta form the measured $\vec{E}_{\mathrm{T}}^{\mathrm{miss}}$, leading to six missing degrees of freedom. To constrain these missing degrees of freedom, the $\mathbb{Z}_2$ symmetry can be exploited by noting that in some frame PP the squarks are back to back, along with the rapidity rule used for the W decay case, shown in Figure 6.2. Again the unknown parameters can be parameterised in the boosts relating the two squark rest frames P_a and P_b to the PP frame, and again it is helpful to have the derived variables being independent of the true velocities. To evaluate this another constraint needs to be added: the two squarks having the same mass, a reasonable choice for many pair produced particle systems. This choice allows for a single vector description of both the squark velocities:

$$\vec{\beta}_{\mathrm{PP}} = \vec{\beta}_{\mathrm{P}_a}^{\mathrm{PP}} = -\vec{\beta}_{\mathrm{P}_b}^{\mathrm{PP}}, \tag{6.8}$$

and a minimisation can be done over this common vector. Choosing $\vec{\beta}_{\mathrm{PP}}$ to satisfy

$$\frac{\partial(E_{q_a}^{\mathrm{P}_a} + E_{q_b}^{\mathrm{P}_b})}{\partial\vec{\beta}_{\mathrm{PP}}}, \tag{6.9}$$

where q_a and q_b are the measured jets coming from the quarks. The solution is

$$\beta_{\mathrm{PP}} = \frac{\vec{p}_{q_a}^{\mathrm{PP}} - \vec{p}_{q_b}^{\mathrm{PP}}}{E_{q_a}^{\mathrm{PP}} - E_{q_b}^{\mathrm{PP}}}. \tag{6.10}$$

With this choice, the estimated quantities are *contra-boost invariant*, also known as

Euclidean mass:

$$M_c^2\left(\mathbf{p}_{q_a}^{\mathrm{PP}},\mathbf{p}_{q_b}^{\mathrm{PP}}\right)=2\left(E_{q_a}^{\mathrm{PP}}E_{q_b}^{\mathrm{PP}}+\vec{p}_{q_a}^{\mathrm{PP}}\cdot\vec{p}_{q_b}^{\mathrm{PP}}\right), \tag{6.11}$$

where M_c^2 is the inner product of two Euclidean vectors, and is invariant under any boost for any two four-vectors. The invisible mass rule used in the W decay case can also be extended to more particles by requiring that the mass of an invisible vector can be chosen to the smallest Lorentz invariant function of visible four-vectors, while being large enough to allow splitting into other invisibles. The choice of $\vec{\beta}_c$ is also a jigsaw rule: if the degrees of freedom for splitting one invisible particle I into two $\{\mathrm{I}_a,\mathrm{I}_b\}$ are unknown then they can be specified by choosing a pair of visible particles $\mathrm{V}=\{\mathrm{V}_a,\mathrm{V}_b\}$ and applying the constraint $M_{\mathrm{V}_a,\mathrm{I}_a}=M_{\mathrm{V}_b,\mathrm{I}_b}$. The visible four-vectors need to be known in the centre-of-mass frame along with the combined invisible vector, and a system of equations can be solved to find the individual invisible four-vectors. This topic is discussed in great detail in [67], along with the case where P_a and P_b are not of equal mass. The decay trees with (nearly) fully resolved intermediate states, often with a notable $\mathbb{Z}_2$ symmetry, are known as "Standard" trees.

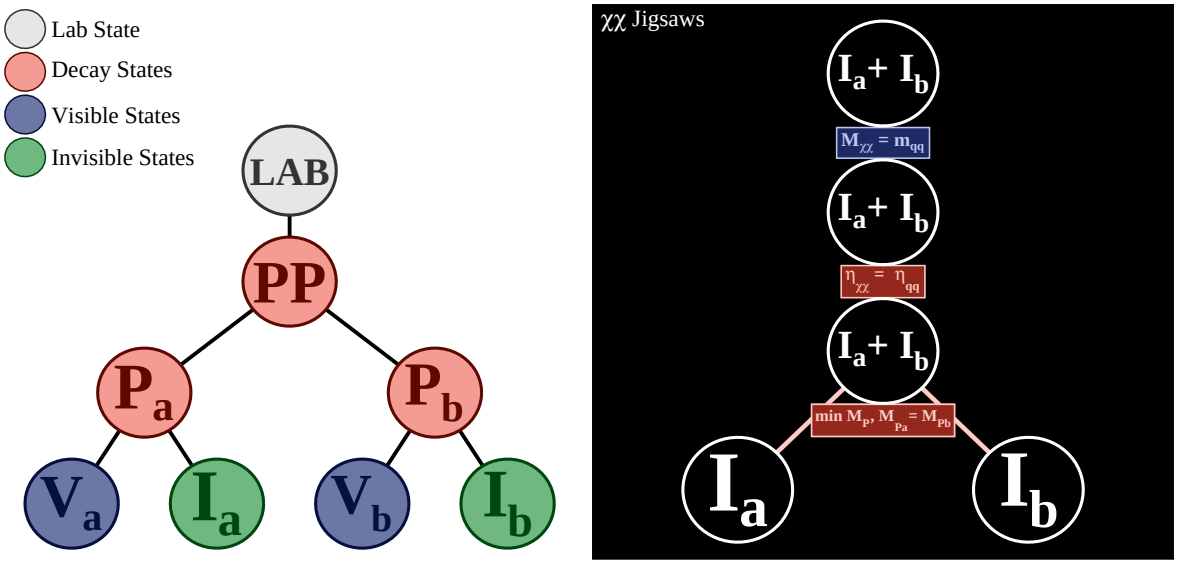

a b

Figure 6.2: For $\tilde{q} \to q\tilde{\chi}_1^0$ the (a) decay tree, and (b) treatment of the invisible vectors. Images are generated using RestFrames [66].

6.4 Compressed spectra

A area of SUSY searches where RJR has been particularly applicable is in compressed spectra scenarios, where the mass difference between the parent sparticle and the LSP is small. This region of phase space is difficult to probe as the SM resonances that often provide the means for reconstructing the events are likely off-shell and provide little scope for separating signal from background. The final state visible objects themselves likely have little momentum compared to those in the bulk of phase space, and indeed the $E_{\mathrm{T}}^{\mathrm{miss}}$ is often also reduced. The reduction in object momenta also affects the trigger acceptance rate for these events.

For example $\tilde{t} \to t\tilde{\chi}_1^0$ is typically considered with decays to an on-shell top, but as the masses become more compressed the top is off-shell, leading to a three body $Wb\tilde{\chi}_1^0$ state. Compressing further, the W can also be off-shell leading to a four body state $jj(\ell\nu)b\tilde{\chi}_1^0$. These changes in kinematic regimes can be easily seen in limits set by collider experiments, like that shown for the $\tilde{t} \to t\tilde{\chi}_1^0$ in Figure 6.3, where the boundaries correspond to a reduction in sensitivity.

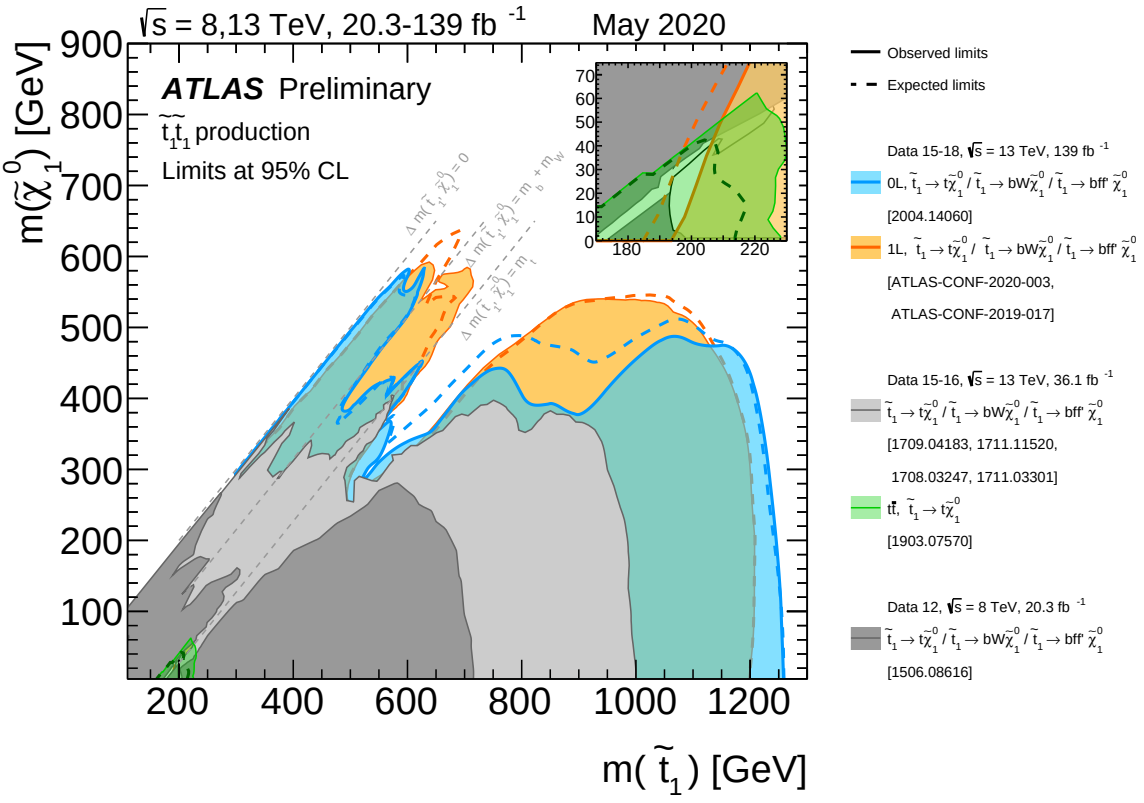

Figure 6.3: Summary of the ATLAS top squark searches [68], with decays to $\tilde{\chi}_1^0$ LSP. The dashed grey lines show the changes between resolved top quarks, three body decays and four body decays as the mass splitting is reduced.

The main way to mitigate many of the limitations of compressed spectra is to use events with energetic initial state radiation (ISR) jet(s) to boost the SUSY system, increasing the measured object momenta and $E_{\mathrm{T}}^{\mathrm{miss}}$. However this leads to a new issue with decoupling the SUSY system from the ISR, a combinatoric ambiguity, along with the usual $\vec{E}_{\mathrm{T}}^{\mathrm{miss}}$ splitting issue. The normal method is to assume the most energetic jet will be from the ISR, but this breaks down if there are multiple jets in the event.

Recursive jigsaw reconstruction can be applied to this case in a specific manner outlined in [69, 70], with the relationship between the ISR system and the $\vec{E}_{\mathrm{T}}^{\mathrm{miss}}$ in events allowing for estimation of the mass splitting of the sparticles. If the LSPs

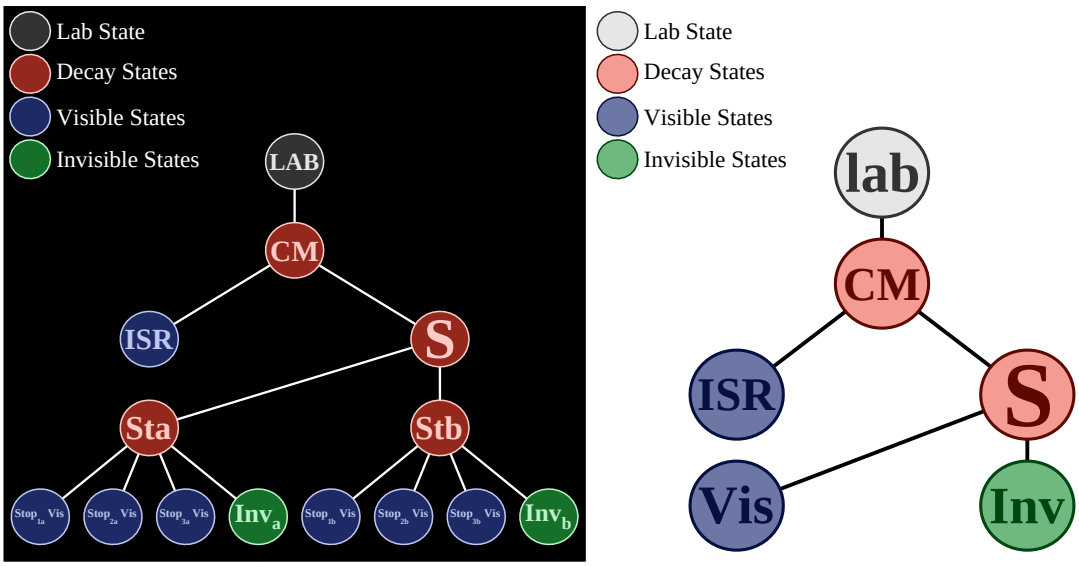

a b

Figure 6.4: For the process $\tilde{t} \to t\tilde{\chi}_1^0, t \to bjj$ with ISR, the (a) full event decay tree, and (b) the simplified ISR decay tree. Images generated with RestFrames [66].

receive no momentum from the parent decays any $E_{\mathrm{T}}^{\mathrm{miss}}$ results purely from the recoil against the ISR, leading to the following:

$$\vec{E}_{\mathrm{T}}^{\mathrm{miss}} \approx -p_{\mathrm{T}}^{\mathrm{ISR}} \times \frac{m_{\tilde{\chi}}}{m_{\tilde{P}}}, \tag{6.12}$$

where the $\tilde{\chi}$ and $\tilde{P}$ are the LSP and parent sparticle respectively and $p_{\mathrm{T}}^{\mathrm{ISR}}$ is the total transverse momentum of the ISR system. In traditional analyses [71, 72], some higher level variable such as $|\vec{E}_{\mathrm{T}}^{\mathrm{miss}}| / |p_{\mathrm{T}}^{leadjet}|$ can be used to estimate the relationship between the ISR system and the $\vec{E}_{\mathrm{T}}^{\mathrm{miss}}$. But if the ISR system is not dominated by a single high momentum jet then these methods will not be applicable. Instead a simplified recursive jigsaw reconstruction decay tree can be imposed on the event, breaking it up into ISR and sparticle (S) frames, with the sparticle frame being made of a Visible (V) and an Invisible (I) frame. Here each of the frames can contain multiple objects, and each event is considered in the transverse plane only. For example fully hadronic stop decays, a difficult final state with multiple jets, reduces to the three frames ISR, V, and I as shown in Figure 6.4.

Now for this final state the question of where to put the jets arises, and is where another class of jigsaw rule can assist: the combinatoric rules. As with previous jigsaw rules there is some physics input to handle the ambiguities, typically that the desired assignment of visible particles is one that minimises the mass of the set of visible particles (in this case the jets J) in the centre-of-mass frame, which is also dependent on the invisible system I. This is done by noting that in that CM frame $\vec{p}^{\,\mathrm{CM}}_{\mathrm{ISR}} = -\vec{p}^{\,\mathrm{CM}}_{\mathrm{V}}$, and that the overall invariant mass of J m_J is invariant

$$m_J = \sqrt{|\vec{p}^{\,\mathrm{CM}}_{\mathrm{ISR}}|^2 + m^2_{\mathrm{ISR}}} + \sqrt{|\vec{p}^{\,\mathrm{CM}}_{\mathrm{V}}|^2 + m^2_{\mathrm{V}}}, \tag{6.13}$$

and that maximising the momentum $\vec{p}^{\,\mathrm{CM}}_{\mathrm{ISR}}$ is equivalent to minimising the mass. Whatever partitioning of J = ISR + V satisfies this constraint is what will be used to get the kinematic basis in the event.

An aside: although the combinatoric rules have been introduced in terms of compressed scenarios, they are applicable to a wide range of problems. For instance determining what the energetically favourable b-jet assignment is in dileptonic top pair decays, or lepton assignments in triboson production. A useful feature of combinatoric assignment is that other criteria such as b-tag scores and lepton charge and flavour can be applied afterwards to maximise separation of signal and backgrounds.

6.5 Designing RJ variables

While RJR can derive a kinematic basis according to the decay tree and jigsaw rules imposed on an event, being able to translate that into separation between signal and background is another matter. Different decay topologies will have different features such as resonance structure, angular properties, or other kinematic properties. Instead of mandating a single discriminating variable such as m_{T2} variables can be constructed with objects evaluated in natural frames, such as the estimated centre-of-mass frame. In addition variables can be calculated in any frame, and the relationship between difference rest frames can be explored using the boosts between them.

This section will provide an overview of the different classes of variables, split between the standard decay tree and the ISR tree: scale variables, ratios and angles.

6.5.1 Standard trees

The standard tree is usually defined in the fullest way possible with as many intermediate states as possible being reconstructed. This allows for measurement of the overall scale of the event, as well as the amount of energy taken up by particular particles in the decay and the relationship between particles, particularly when considering processes with $\mathbb{Z}_2$ symmetry.

Scale variables

The most obvious (and Lorentz invariant) quantity to calculate is the mass of a particular frame F, denoted in the usual way with m_{F}. This quantity can correspond to a single particle or can be from a collection of particles. For instance for a SUSY system the mass of the di-sparticle system PP can be calculated. The energy or three momentum of a frame can also be calculated either in the same frame or in another frame.

Object momenta evaluated in a particular non-lab frame can be evaluated, and in principle used as selection criteria, but this is not usually done as trigger and object definition thresholds are dependent on the lab frame.

Using the momentum information of particles in a frame F, the H variables can be constructed according to

$$H^{\mathrm{F}}_{n,m} = \sum_{i=1}^{n} \left|\vec{p}^{\,\mathrm{F}}_{\mathrm{vis},i}\right| + \sum_{j=1}^{m} \left|\vec{p}^{\,\mathrm{F}}_{\mathrm{inv},j}\right|, \tag{6.14}$$

where the visible and invisible four-momenta are dependent on the process under study. Common combinations are $H^{\mathrm{F}}_{1,1}$ where the visible and invisible vectors are individually vector summed then scalar summed, and $H^{\mathrm{F}}_{n,1}$ where the visible vectors are scalar summed, the invisibles vector summed, and then both components are vector summed. These are akin to $E_{\mathrm{T}}^{\mathrm{miss}}$ and m_{eff} respectively. Considering the

example of squark pair production in Section 6.3, in the PP frame there are four H variables possible $H^{\mathrm{PP}}_{1,1}$, $H^{\mathrm{PP}}_{2,1}$, $H^{\mathrm{PP}}_{1,2}$, and $H^{\mathrm{PP}}_{2,2}$. Due to the implementation of the jigsaw rules and the underlying symmetry of the event, there will be some correlation between the variables so a subset of these variables will typically be used in an analysis. Moving to either one of the squark rest frames $\mathrm{P_a}$ and $\mathrm{P_b}$, a single $H^{\mathrm{P_a(P_b)}}_{1,1}$ can also be calculated and compared to see the balance of the event.

The H variables can also be calculated with transverse variables, denoted with the usual subscript $_{\mathrm{T}}$.

Ratio variables

Calculated scale variables can be used in ratio to probe some important properties of events. $\frac{H^{\mathrm{F}}_{\mathrm{T}n,m}}{H^{\mathrm{F}}_{n,m}}$ can be used to determine the transversity of an event, noting that processes with high momentum transfer are normally more transverse than softer background processes.

$\frac{H^{\mathrm{F}}_{1,1}}{H^{\mathrm{F}}_{n,1}}$ is akin to the $\frac{E^{\mathrm{miss}}_{\mathrm{T}}}{m_{\mathrm{eff}}}$ in measuring the fraction of the overall event energy that can be attributed to the $E^{\mathrm{miss}}_{\mathrm{T}}$, however if F is not the lab frame but instead the centre-of-mass or PP frame then the variable is nearly independent of boosts applied to the event.

Two halves of a decay can be balanced against each other to determine whether there is an energy or boost imbalance. One useful variable is

$$\frac{\min\left(H^{\mathrm{P}_a}_{1,1}, H^{\mathrm{P}_b}_{1,1}\right)}{\min\left(H^{\mathrm{P}_a}_{k,1}, H^{\mathrm{P}_b}_{k,1}\right)}, \tag{6.15}$$

where the k represents the number of visible vectors associated with either half. This variable is not effective for the simple squark case considered until now, but for any situation where there are more visible than invisible parts to each half of the decay it provides good discrimination.

There are two related ratios that are used to test for boosts in the z and transverse directions:

$$R_{p_z} = \frac{p^{\text{lab}}_{\text{PP},z}}{\left(p^{\text{lab}}_{\text{PP},z} + H^{\text{PP}}_{\text{T}\,n,m}\right)}, \tag{6.16}$$

$$R_{p_\text{T}} = \frac{p^{\text{lab}}_{\text{PP,T}}}{\left(p^{\text{lab}}_{\text{PP,T}} + H^{\text{PP}}_{\text{T}\,n,m}\right)}, \tag{6.17}$$

which measures the z(T) momentum of the PP frame measured in the lab frame modulated with the overall transverse scale $H^{\text{PP}}_{\text{T}n,m}$. R_{p_T} is especially useful as it provides a measure of how well the event is reconstructed in the transverse plane, where there is a useful momentum conservation relationship, and is normally close to zero for well resolved events.

Angular variables

With knowledge of the frames and the boosts between the frames a number of angles can be calculated. In addition to the usual set of angles between certain objects of interest, now calculable in any frame, some cross-frame angles can be evaluated to leverage boosting.

$\Delta\phi^{\text{P}}_V$ is the azimuthal angle between the visible system V in frame P and the direction of the boost from PP to P, evaluated in the PP frame. For backgrounds which don't obey the signal topology variable will be close to 0 or π, while for signal-like events it is flat.

Similarly $\Delta\phi^{\text{PP}}_V$ is angle between the boost from the lab to the PP frame and the visible system in the PP frame, again evaluated in the PP frame.

6.5.2 ISR trees

For ISR boosted decays the scale of event is set by magnitude of the ISR system and thus the majority of variables are based on the relationship between the ISR system and recoiling S system. Using combinatoric jigsaw rules the number of jets (and c- or b-jets) can be determined in either of the two visible frames, allowing for

easy selection based on jet criteria. In the compressed hadronic stop decay case, a large number of jets in the ISR system is not desirable, nor are any b-jets, both being signatures of top quark processes. Without explicitly forcing jets into a particular part of the decay and instead letting the mass minimisation assign the sets of jets certain backgrounds can be filtered out, or indeed used as control and validation samples.

Scale variables

Commonly the first variable chosen is $p_{\mathrm{T}\,ISR}^{\mathrm{CM}}$ which is the ISR momentum in the CM frame. Selecting on this variable allows for selecting appropriately energetic ISR systems.

H variables constructed with the S system will be in general be correlated with the ISR momentum, and thus are not preferred in these reconstructions. $p_{\mathrm{T\,S}}^{\mathrm{CM}}$ runs into similar issues, though it has been used effectively in [73].

The transverse mass of the S system $m_{\mathrm{T}}^{\mathrm{S}}$ can be used to probe situations where the mass splitting is not necessarily very low.

$p_{\mathrm{T,I}}^{\mathrm{CM}}$ is effectively the boost corrected $E_{\mathrm{T}}^{\mathrm{miss}}$ which is a good indicator of how genuine the missing energy is.

To measure how successful the mass minimisation combinatoric procedure is, a cleaning variable $p_{\mathrm{T}}^{\mathrm{CM}}$ can be used. This variable is the transverse drift of the CM frame evaluated in the lab frame and is small for well reconstructed events. In the hadronic stop case there can be assignment of jets from $t\bar{t}$ events into the ISR system which results in a poorly constructed CM frame.

Ratio variables

The major ratio variable, and indeed one the most discriminating variables for ISR based compressed searches is R_{ISR}. This variable, constructed in the CM frame,

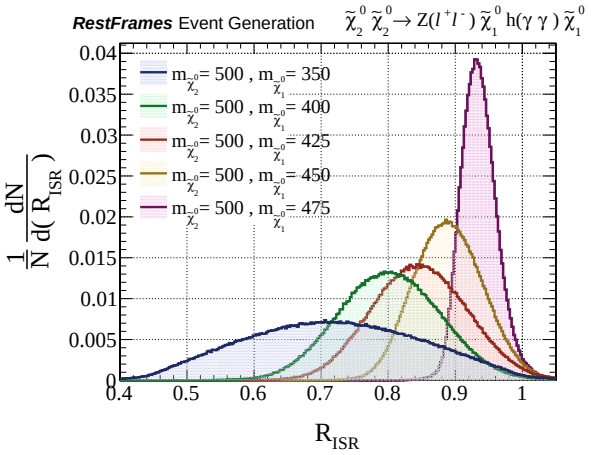

Figure 6.5: R_{ISR} for different $\tilde{\chi}_1^0$ mass values in $\tilde{\chi}_2^0\tilde{\chi}_2^0 \to Z(\ell^+\ell^-)\tilde{\chi}_1^0 h(\gamma\gamma)\tilde{\chi}_1^0$ decays, for $m(\tilde{\chi}_2^0) = 500\,\text{GeV}$ [69]. As the mass difference between the two sparticles decreases, R_{ISR} has a sharper peak.

utilises the observation made in Equation 6.12 that the mass splitting of $\mathbb{Z}_2$ symmetric processes can be accessed by using the $E_{\text{T}}^{\text{miss}}$ and $p_{\text{TISR}}^{\text{CM}}$:

$$R_{\text{ISR}} \equiv \frac{|\vec{p}_{\text{I T}}^{\,\text{CM}} \cdot \hat{p}_{\text{ISR T}}^{\,\text{CM}}|}{|\vec{p}_{\text{ISR T}|}^{\,\text{CM}}|}, \tag{6.18}$$

which describes the amount of missing energy along the ISR system axis, normalised by the magnitude of the ISR. This variable peaks strongly as the masses of parent sparticles and LSPs become close to each other, indicating that the majority of the missing energy in the system originates from the mass of the LSP. The effect for different mass splittings in an electroweak SUSY $\tilde{\chi}_2^0\tilde{\chi}_2^0$ decay is shown in Figure 6.5.

An upgraded version of p_{T}^{CM} can be constructed in a similar method to R_{ISR} normalising the drift of the CM frame with the ISR system:

$$R_{\text{CM}} \equiv \frac{|\vec{p}_{\text{T}}^{\,\text{CM}} \cdot \hat{p}_{\text{ISR T}}^{\,\text{CM}}|}{|\vec{p}_{\text{ISR T}|}^{\,\text{CM}}|}, \tag{6.19}$$

where $\vec{p}_{\text{T}}^{\,\text{CM}}$ is the transverse vector of the CM frame evaluated in the lab frame.

Angular variables

A vital question in ISR analyses is "how can one be sure that the ISR is actually boosting the S system?" Normally in addition to criteria on the momentum of the ISR system, the angle between the ISR and the S system is also cut on. In the RJ methodology this angle $\Delta\phi^{\mathrm{CM}}_{\mathrm{ISR,I}}$ is measured in the CM frame, both to negate any transverse boosts and to keep in line with other quantities calculated.

Angular information can also be used to measure the relationship between the visible and invisible components of the S system with $\Delta\phi^{\mathrm{CM}}_{\mathrm{V,I}}$ to determine whether the missing energy can be associated with the S system, or is a result from other processes or mismeasurement.

6.6 Designing analyses with RJR

Compared to analysis techniques relying on a small number of discriminating variables, recursive jigsaw reconstruction allows for flexibility in targeting certain kinematic regimes by relying on scale versus angular and ratio variables more or less.

Returning to the example of stop pair production: in the 2D mass plane on which analyses and exclusions are parametrised there are mass splittings ranging from nearly 0 GeV to near 1 TeV, with major changes in reconstruction of the visible decay products from fully resolved top quarks to 4-body decays where neither the top nor the W boson are on-shell. The ideal would be to have an analysis methodology that could cover the whole mass plane with the same set of variables, but in practice this is difficult to achieve. With recursive jigsaw a cohesive set of variables can be defined whereby high mass sensitivity can be found by cutting hard on scale variables, knowing that it is difficult for SM backgrounds to be produced with such high momentum, and then relaxing those scale variables in the intermediate and lower mass splitting regions by selecting on the angular and ratio variables which have more power when the background and signal are only subtly different.

A similar approach can be taken for ISR boosted final states with low mass splittings, or for mass splittings in troublesome kinematic regions. Here the ISR system itself determines the scale of the event, and most variables are defined with reference to direction and/or magnitude of the ISR system. This means that some care needs to be taken to minimise correlations in the basis of variables used.

7 A search for electroweakinos in 2 and 3 lepton final states with 2015-16 data

This chapter describes a search [74] for electroweakinos ($\tilde{\chi}_2^0\,\tilde{\chi}_1^\pm$) with 2 and 3 lepton final states performed using recursive jigsaw reconstruction with ATLAS 2015-16 $\sqrt{13}$ TeV proton-proton collision data.

7.1 Motivation and analysis scope

The flagship SUSY searches at the LHC are dedicated to inclusive production of strongly coupled sparticles due their larger predicted production cross sections, driven in part by their colour charge. So far these searches have yielded null results, with excluded masses reaching to the TeV range. If the masses of the coloured sparticles are beyond the reach of the LHC, alternative SUSY search targets and strategies are needed. Electroweak SUSY states, despite having lower production cross sections (Figure 7.1), often have benefits of clean final states and are increasingly favoured as probes for SUSY at LHC energies. The most abundant electroweak SUSY production is predicted to be of the electroweakinos, fermionic partners of the electroweak bosons, with pair produced electroweakinos ($\tilde{\chi}_2^0\,\tilde{\chi}_1^\pm$) decaying to $\tilde{\chi}_1^0$ and Z and W respectively.

Two multi-leptonic final states can be considered: the first where the Z decays

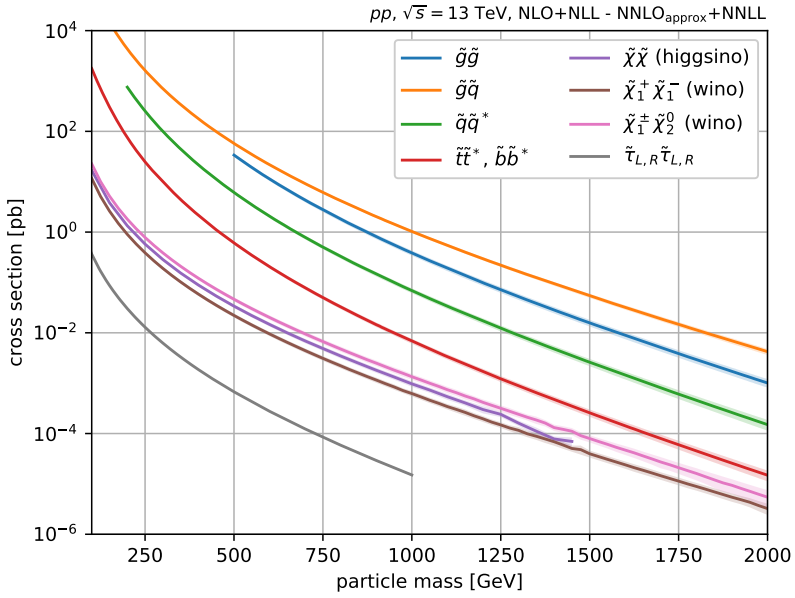

Figure 7.1: The $\sqrt{s} = 13$ TeV LHC SUSY production cross sections for squarks, gluons, electroweakinos and sleptons [75].

leptonically [1] and the W decays hadronically Figure 7.2 (2ℓ) (a), and the second where both the Z and W decay leptonically Figure 7.2 (3ℓ) (b). In addition both of the states can be ISR boosted Figure 7.2 (c) and (d), useful for when the mass splitting between the $\tilde{\chi}_2^0/\tilde{\chi}_1^\pm$ and $\tilde{\chi}_1^0$ is near m_Z.

Previous searches from both ATLAS [76–79] and CMS [80–82] have put 95% confidence level (CL) constraints on $\tilde{\chi}_2^0/\tilde{\chi}_1^\pm$ masses of up to 570 GeV for massless $\tilde{\chi}_1^0$, but tend to struggle in the regime where the mass splittings reduce to around the Z mass.

[1] Here leptonically refers to either electron or muons.

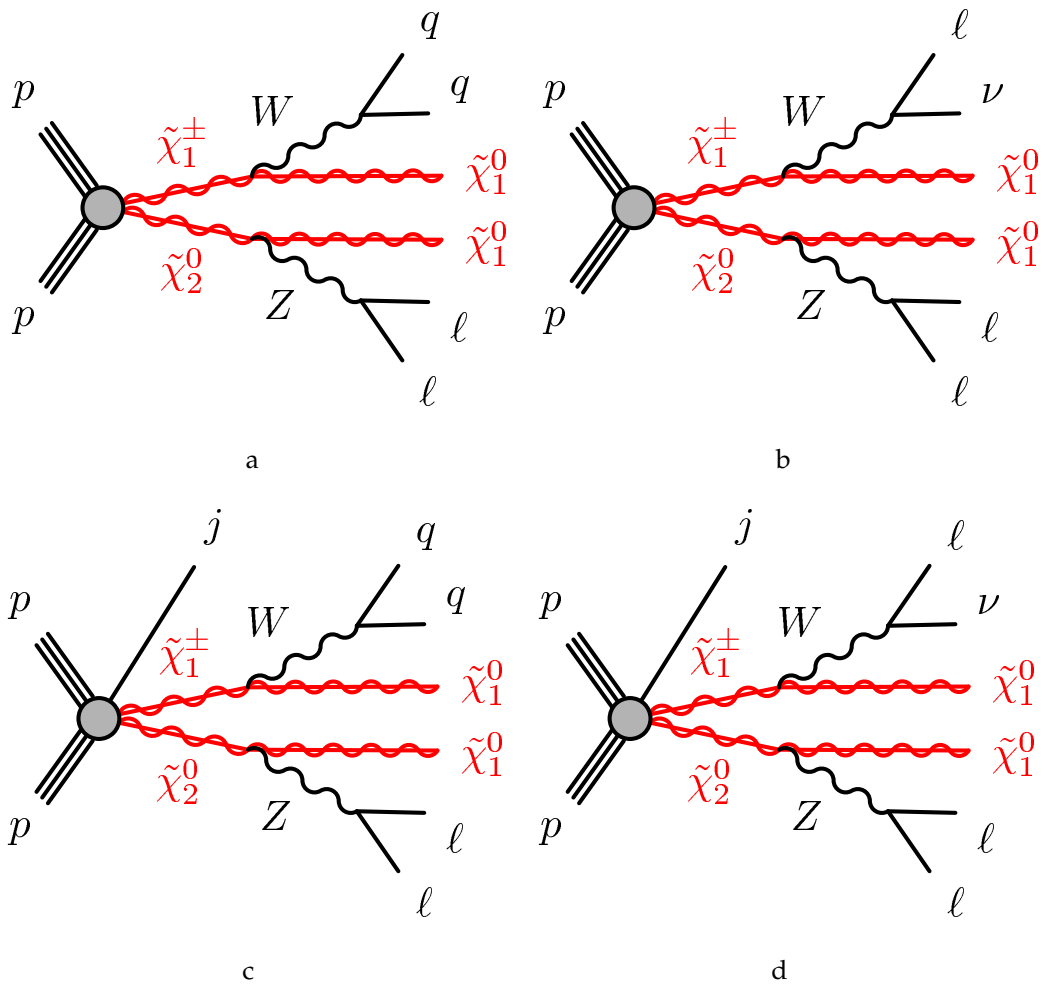

Figure 7.2: Diagrams for the four final states: (a) $\tilde{\chi}_1^{\pm}\tilde{\chi}_2^0$ with decays to two-lepton plus two-jet plus $E_{\mathrm{T}}^{\mathrm{miss}}$ final states through a hadronically decaying W boson and a leptonically decaying Z boson, (b) $\tilde{\chi}_1^{\pm}\tilde{\chi}_2^0$ with decays with leptonically decaying W and Z bosons, (c) $\tilde{\chi}_1^{\pm}\tilde{\chi}_2^0$ production in association with an initial state radiation jet with decays to two-lepton plus two-jet plus $E_{\mathrm{T}}^{\mathrm{miss}}$ final states through a hadronically decaying W boson and a leptonically decaying Z boson and (d) $\tilde{\chi}_1^{\pm}\tilde{\chi}_2^0$ production in association with an initial state radiation jet (labeled 'j' in the figure) with decays with leptonically decaying W and Z bosons [74].

7.2 Data and Monte Carlo samples

The data were collected with the ATLAS detector during 2015 with peak $L = 5.2 \times 10^{33}\text{cm}^{-2}\text{s}^{-1}$, and during 2016 with maximum luminosity $L = 1.37 \times 10^{34}\text{cm}^{-2}\text{s}^{-1}$. The pileup distributions of 2015 and 2016 data taking is shown in 4.1. The collected data has various beam, detector, and quality criteria gives a final analysis-ready integrated luminosity of 36.1fb^{-1}, with uncertainty of ± 2.1 %, derived from beam scans done at the start of each run year using methodology derived in [83].

Monte Carlo background samples are listed in Table 7.1, and are used to define selection criteria and estimate sensitivity to the signal models considered.

The production of Z bosons in association with jets [84] was performed with the SHERPA 2.2.1 generator [85]. The NNPDF3.0NNLO [86] parton distribution function (PDF) was used in conjunction with dedicated parton shower tuning developed by the SHERPA authors. The matrix elements (ME) were calculated for up to two partons at next-to-leading order (NLO) and with up to two additional partons at leading order (LO) using the COMIX [87] and OPEN LOOPS [88] matrix-element generators, and merged with the SHERPA parton shower (PS) [89] using the ME+PS@NLO prescription [90]. For MC closure studies of the data-driven Z+jets background estimate, γ+jets events were generated at LO with up to four additional partons using the SHERPA 2.1.1 generator with CT10 [91] PDF set.

Diboson processes (WW, WZ, ZZ) [92] were simulated using the SHERPA 2.2.1 generator and contain off-shell contributions. For processes with four charged leptons (4ℓ), three charged leptons and a neutrino (3ℓ+1ν) or two charged leptons and two neutrinos (2ℓ+2ν), the matrix elements contain all diagrams with four electroweak couplings, and were calculated for up to one (4ℓ, 2ℓ+2ν) or no extra partons (3ℓ+1ν) at NLO. All diboson samples were also simulated with up to three additional partons at LO using the COMIX and OPENLOOPS matrix-element generators, and were merged with the SHERPA parton shower using the ME+PS@NLO prescription. The diboson events were normalised to their NLO cross sections [93, 94]. Additional MC simulation samples of events with a leptonically decaying vector boson and photon, $V\gamma$, were generated at LO using Sherpa 2.1.1 [85]. Matrix elements including all diagrams with three electroweak couplings were calculated with up to three partons

at LO and merged with the Sherpa parton shower [95] according to the ME+PS@LO prescription [96]. The CT10 PDF set is used in conjunction with dedicated parton shower tuning developed by the Sherpa authors.

The POWHEG-BOX v2 [97] generator was used for the generation of $t\bar{t}$ and single-top-quark processes in the Wt- and s-channels [98], while t-channel single-top production was modeled using POWHEG-BOX v1 [99]. For the latter process, the decay of the top quark was simulated using MadSpin [100] preserving all spin correlations. For all processes the CT10 [91] PDF set was used for the matrix element, while the parton shower, fragmentation, and the underlying event were generated using PYTHIA 6.428 [101] with the CTEQ6L1 [102] PDF set and a set of tuned parameters called the Perugia 2012 tune [103]. The top-quark mass in all samples was set to 172.5 GeV. The $t\bar{t}$ and the Wt-channel single-top events were normalised to cross sections calculated at next-to-next-to-leading-order plus next-to-next-to-leading-logarithm (NNLO+NNLL) [104–107] accuracy, while s- and t-channel single-top-quark events were normalised to the NLO cross sections [108, 109]. The production of Zt events was generated with the MG5_aMC@NLO 2.2.1 [110] generator at LO with the CTEQ6L1 PDF set.

The MG5_aMC@NLO 2.2.2 (2.2.3 for $t\bar{t} + Z/\gamma^*$) generator at LO, interfaced to the PYTHIA 8.186 [111] parton-shower model, was used for the generation of $t\bar{t}$ + EW processes ($t\bar{t} + W/Z/WW$) [112], with up to two ($t\bar{t} + W$, $t\bar{t} + Z(\to \nu\nu/qq)$), one ($t\bar{t} + Z(\to \ell\ell)$ [2]) or no ($t\bar{t} + WW$) extra partons included in the matrix element. The events were normalised to their respective NLO cross sections [113, 114].

Triboson processes (WWW, WWZ, WZZ and ZZZ) were simulated with the SHERPA 2.2.1 generator with matrix elements calculated at LO with up to one additional parton. The triboson events were normalised to their LO cross sections [115].

Higgs-boson production processes (including gluon–gluon fusion, associated vector-boson production, VH,[3] and vector-boson fusion, VBF) were generated using POWHEG v2 [98] + PYTHIA 8.186 and normalised to cross sections calculated at

[2] The letter ℓ stands for the charged leptons (electrons, muons and taus). While the contributions from tau leptons are included in all the Monte Carlo samples, in the next sections the symbol ℓ refers to electrons and muons only.

[3] The letter V represents the W or Z gauge boson.

Table 7.1: The SUSY signals and the Standard Model background Monte Carlo samples for this analysis. The generators, the order in α_s of cross section calculations used for yield normalisation, PDF sets, parton showers and parameter tunes used for the underlying event are shown [74].

Physics process	Generator	Cross section normalisation	PDF set	Parton shower	Tune
SUSY processes	MADGRAPH v2.2.3	NLO+NLL	NNPDF2.3LO	PYTHIA 8.186	A14
$Z/\gamma^*(\to \ell\bar{\ell})$ + jets	SHERPA 2.2.1	NNLO	NNPDF3.0NNLO	SHERPA	SHERPA default
γ + jets	SHERPA 2.1.1	LO	CT10	SHERPA	SHERPA default
$H(\to \tau\tau)$, $H(\to WW)$	POWHEG-BOX v2	NLO	CTEQ6L1	PYTHIA 8.186	A14
HW, HZ	MG5_aMC@NLO 2.2.2	NLO	NNPDF2.3LO	PYTHIA 8.186	A14
$t\bar{t}+H$	MG5_aMC@NLO 2.2.2	NLO	CTEQ6L1	HERWIG 2.7.1	A14
$t\bar{t}$	POWHEG-BOX v2	NNLO+NNLL	CT10	PYTHIA 6.428	Perugia2012
Single top (Wt-channel)	POWHEG-BOX v2	NNLO+NNLL	CT10	PYTHIA 6.428	Perugia2012
Single top (s-channel)	POWHEG-BOX v2	NLO	CT10	PYTHIA 6.428	Perugia2012
Single top (t-channel)	POWHEG-BOX v1	NLO	CT10f4	PYTHIA 6.428	Perugia2012
Single top (Zt-channel)	MG5_aMC@NLO 2.2.1	LO	CTEQ6L1	PYTHIA 6.428	Perugia2012
$t\bar{t}+W/WW$	MG5_aMC@NLO 2.2.2	NLO	NNPDF2.3LO	PYTHIA 8.186	A14
$t\bar{t}+Z$	MG5_aMC@NLO 2.2.3	NLO	NNPDF2.3LO	PYTHIA 8.186	A14
WW, WZ, ZZ	SHERPA 2.2.1	NLO	NNPDF30NNLO	SHERPA	SHERPA default
$V\gamma$	SHERPA 2.1.1	LO	CT10	SHERPA	SHERPA default
Triboson	SHERPA 2.2.1	NLO	NNPDF30NNLO	SHERPA	SHERPA default

NNLO with soft gluon emission effects added at NNLL accuracy, whilst $t\bar{t}H$ events were produced using aMC@NLO 2.2.2 + HERWIG 2.7.1 [116] and normalised to the NLO cross section [117]. All samples assume a Higgs boson mass of 125 GeV.

Signal samples are produced using simplified models [118] as outlined in Section 3.4, with an effective Lagrangian and fixed production and decay mechanisms. The MC signal samples were generated from leading-order matrix elements with up to two extra partons using MADGRAPH v2.2.3 [119] interfaced to PYTHIA version 8.186, with the A14 parameter tune [120], for the modeling of the SUSY decay chain, parton showering, hadronisation and the description of the underlying event. Parton luminosities were provided by the NNPDF23LO PDF set [91]. Jet–parton matching follows the CKKW–L prescription [121], with a matching scale set to one quarter of the $\tilde{\chi}_1^\pm/\tilde{\chi}_2^0$ mass. Signal cross sections were calculated at NLO in the strong coupling constant, with soft gluon emission effects added at next-to-leading-logarithm (NLL) accuracy [122–126]. The nominal cross section and the uncertainty were taken from

an envelope of cross section predictions using different PDF sets and factorisation and renormalisation scales, as described in Ref. [127]. For $\tilde{\chi}_1^{\pm}$ and $\tilde{\chi}_2^0$ with a mass of 500 GeV, the production cross section is 46 ± 4 fb at $\sqrt{s} = 13$ TeV.

7.3 Objects

This analysis uses electrons, muons, jets (with b-jets being vetoed in signal regions and accepted for top quark backgrounds), $E_{\mathrm{T}}^{\mathrm{miss}}$, along with photons for data-driven background estimation in the 2ℓ regions.

7.3.1 Electrons

Electrons are reconstructed using the Egamma algorithm and are required to reside within $|\eta| < 2.47$. At baseline level, electrons must have $p_{\mathrm{T}} > 10$ GeV and satisfy the `LooseAndBLayerLLH` quality criteria. Signal electrons must have $p_{\mathrm{T}} > 10$ GeV and be isolated with respect to other high-p_{T} charged particles, satisfying the `GradientLoose` isolation criteria and additionally passing `MediumLLH` quality criteria. Signal electron candidates must also satisfy the IP conditions: $d_0/\sigma_{d_0} < 5$ and $z_0 \sin\theta < 0.5$ mm. The electron selection is summarised in Table 7.2.

7.3.2 Muons

Muons used in this analysis must have $p_{\mathrm{T}} > 10$ GeV and reside within $|\eta| < 2.4$. Baseline muons must pass `Medium` quality requirements. Signal muons must have $p_{\mathrm{T}} > 10$ GeV and be isolated with respect to other high-p_{T} charged particles, satisfying the `GradientLoose` isolation criteria and additionally having $|d_0/\sigma_{d_0}| < 3$ and $z_0 \sin\theta < 0.5$ mm constrains on the IP.

The muon selection criteria are summarised in Table 7.3.

Table 7.2: Summary of the electron selection criteria. The signal selection requirements are applied on top of the baseline selection and after Overlap Removal.

Cut	Value/description
Baseline Electron	
Acceptance	$p_{\mathrm{T}} > 10$ GeV, $\lvert\eta^{\mathrm{clust}}\rvert < 2.47$
PID Quality	`LooseAndBLayerLLH`
Signal Electron	
Acceptance	$p_{\mathrm{T}} > 10$ GeV, $\lvert\eta^{\mathrm{cluster}}\rvert < 2.47$
PID Quality	`LLHMedium`
Isolation	`GradientLoose`
Impact parameter	$\lvert z_0 \sin\theta\rvert < 0.5$ mm
	$\lvert d_0/\sigma_{d_0}\rvert < 5$

Table 7.3: Summary of the muon selection criteria. The signal selection requirements are applied on top of the baseline selection after Overlap Removal.

Cut	Value/description
Baseline Muon	
Acceptance	$p_{\mathrm{T}} > 10$ GeV, $\lvert\eta\rvert < 2.4$
PID Quality	`Medium`
Signal Muon	
Acceptance	$p_{\mathrm{T}} > 10$ GeV, $\lvert\eta\rvert < 2.4$
PIDQuality	`Medium`
Isolation	`GradientLoose`
Impact parameter	$\lvert z_0 \sin\theta\rvert < 0.5$ mm
	$\lvert d_0/\sigma_{d_0}\rvert < 3$

Table 7.4: Summary of the jet and b-jet selection criteria. The signal selection requirements are applied on top of the baseline requirements after Overlap Removal has been performed.

Cut	Value/description
	Baseline jet
Collection	`AntiKt4EMTopo`
Acceptance	$p_{\mathrm{T}} > 20$ GeV , $\lvert\eta\rvert < 4.5$
	Signal jet
JVT	$\lvert\mathrm{JVT}\rvert > 0.59$ for jets with $p_{\mathrm{T}} < 60$ GeV and $\lvert\eta\rvert < 2.4$
Acceptance	$p_{\mathrm{T}} > 20$ GeV , $\lvert\eta\rvert < 2.4$
	Signal b-jet
b-tagger Algorithm	MV2c10
Efficiency	77 %
Acceptance	$p_{\mathrm{T}} > 20$ GeV , $\lvert\eta\rvert < 2.4$

7.3.3 Jets

This analysis used `EMTopo` jets [41] reconstructed using the Anti-kt algorithm [40] with distance parameter $D = 0.4$. At baseline level these jets are required to have $p_{\mathrm{T}} > 20$ GeV and fulfill the pseudorapidity requirement of $|\eta| < 4.5$. Signal jets are further required to pass a JVT cut (JVT >0.59) if the jet p_{T} is less than 60 GeV and it resides within $|\eta| < 2.4$. The jet selection criteria are summarised in Table 7.4.

7.3.4 Missing transverse energy

The missing transverse energy is built from the transverse momenta of all physics objects considered in the analysis (jets, muons and electrons), as well as photons and all tracks matched to the primary vertex not associated with these objects. The $E_{\mathrm{T}}^{\mathrm{miss}}$ is rebuilt from the calibrated electron, muon, photon and jet objects. Objects entering the MET are required to satisfy the 'baseline' selection criteria defined above. Jets are required to be tagged as originating from the hard scatter, using the Jet Vertex Tagger.

Table 7.5: Summary of photon definitions as used for the photon template Z+jets estimation.

Cut	Value/Description
Signal photon	
Acceptance	$p_{\mathrm{T}} > 35$ GeV, $\lvert\eta\rvert < 2.47$
PID	`Tight`
Isolation	Track and calorimeter

7.3.5 Photons

Photons are required to estimate the Z+jets backgrounds in the 2ℓ regions, with single photon+jets events being reweighted to be Z-like. Photons between 35 and 100 GeV are recorded with prescaled triggers, and are suitably unprescaled using factors provided centrally by ATLAS Data Preparation, while the lowest unprescaled photon trigger is at 140 GeV. The photon criteria are listed in Table 7.5. For the measurement of Z+jets backgrounds in the 2ℓ regions, the MC is not sufficient to reproduce the $\vec{E}_{\mathrm{T}}^{\mathrm{miss}}$ distributions due to the difficulty in simulating the effect of jet mismeasurement and the presence of MC events with large weights both positive and negative. This leads to unreliable estimations in the signal regions especially. To resolve this issue the data-drive photon template method is used in the analysis. This method takes photon+jets events from data and reweights the photon to behave like a Z, complete with splitting into two pseudo-leptons which then can be used as a regular 2ℓ event.

7.3.6 Triggers

The trigger logic used to collect the data used in this analysis is accepting events with two electrons, two muons, or an electron and a muon. The lepton transverse momentum thresholds range from 8 to 22 GeV depending on flavour and data taking period, and the offline lepton momentum thresholds are greater than the trigger

Table 7.6: Summary of Trigger strategy. Offline pt thresholds on the leading and sub-leading leptons are also highlighted in the first column and, in cases where there are three leptons in the event, the subsub-leading p_{T} offline requirement is relaxed to 20 GeV.

Lepton p_T	Trigger	
	Data15	Data16
Di-electron channel		
$p_T(e_{1(2)}) > 25$ GeV	HLT_2e12_lhloose_L12EM10VH	HLT_2e17_lhvloose_nod0
Di-muon channel		
$p_T(\mu_{1(2)}) > 25$ GeV	HLT_mu18_mu8noL1	HLT_mu22_mu8noL1
Electron-muon channel		
$p_T(e) > 25$ GeV and $p_T(\mu) > 25$ GeV	HLT_e17_lhloose_mu14	HLT_e17_lhloose_nod0_mu14

lepton p_{T} to stay on the plateau. For the entire dataset the trigger strategy is to take the logical OR of the triggers listed in Table 7.6.

7.3.7 Overlap removal

To remove any ambiguity between jets of $|\eta| < 4.5$ and baseline leptons, the following procedure is followed:

1. Any electron that shares an ID track with a muon is removed.
2. If an 85% efficiency b-jet is within $\Delta R = 0.2$ of an electron, then the electron rejected as originating from a semileptonic b-hadron decay. If there is a non-b-tagged jet within $\Delta R = 0.2$ then the electron is kept as the jet is usually due to an electron-induced shower.
3. Electrons within $\Delta R = 0.4$ of other jet candidates are rejected due to their likely origins from semileptonic b- and c-hadron decays.
4. If a jet has fewer than three associated tracks, and has a nearby muon which carries a large fraction of the transverse momentum of the jet, $p_{\mathrm{T}}^{\mu} > 0.7\Sigma p_{\mathrm{T}}^{\text{jet tracks}}$ are discarded if the muon is within $\Delta R = 0.2$ or if the muon is track matched to the jet.

5. Muons within $\Delta R = 0.4$ of any remaining jet candidates are discarded to mitigate muons from semileptonic c- and b-hadron decays.

7.4 Analysis strategy

To search for the prospective signal models across a wide range of kinematic regimes a set of signal regions (SRs) are designed using MC of both the SUSY process and SM backgrounds. The aim is to maximise the expected exclusion sensitivity for the signal models. The major SM backgrounds are estimated using control regions (CRs) defined orthogonal but close in parameters to their respective SRs. These CRs are enriched in a particular type of background and used to normalise the background MC contribution. The CRs are optimised to have low to no signal contamination, and are useful in minimising the systematic uncertainties from the extrapolation from the CR to the SR. To confirm the efficacy of the CR background normalisations validation regions (VRs) are used, orthogonal to both the CRs and SRs, where the CR normalisation is applied to the background considered and the closure is checked. The VRs also have low signal contamination.

The final results are obtained by using three types of likelihood fits implemented in the HistFitter framework [128]: background-only, model-independent, and model-dependent. All fits are performed using the total number of events in each region. Background-only fits are used to obtain background predictions and to derive fit parameters independent of the SRs, which are removed from the fit and signal contributions are neglected. The normalisation factors (NFs) are derived from the normalisation of the major background components in the CRs, and are propagated into the associated SRs. The SM yield expected in the SRs is derived from MC corrected by the CR fits, along with data derived contributions for Z+jets in the 2ℓ regions and Matrix Method fake and non-prompt lepton estimations for all regions (defined in Section 7.6). The MC statistical and systematic uncertainties appear in the fit as nuisance parameters constrained by Poisson distributions and Gaussians with widths given by the size of the uncertainty respectively. The derived CR normalisation factors are applied to the VRs in the background-only fit as well.

Model-independent fits quantify the level of agreement between observed data yields and the SM background predictions to determine the number of possible BSM signal events in the SRs. This fit behaves much like the background-only fits discussed previously, with the addition of the number of observed events in the SRs as input along with a BSM signal strength (constrained to be non-negative). The expected (S^{85}_{exp}) and observed (S^{95}_{obs}) upper limits are derived at 95% confidence level (CL) using the CL_s prescription [129]. This procedure neglects signal contamination in the CRs. When the upper limits are normalised to the integrated luminosity of data taken can be converted into upper limits on the visible cross sections of BSM processes ($\langle \epsilon\sigma \rangle^{95}_{obs}$), where the visible cross section is defined as the product of the production cross section filtered by the analysis acceptance and detector efficiency. The one-sided p-value of the background-only hypothesis (p_0) can also be computed using the model-independent fits, quantifying the statistical significance of an excess[4].

The simplified model(s) considered in the analysis are constrained using a model-dependent fit, with a view to set exclusion limits on the signal cross sections. The fits themselves proceed in the same way as the model-independent variety, but with the yields in both CRs and SRs taken into account. In this case systematics and statistical impacts on the signal yields are also considered, along with the theoretical signal acceptance. Correlations in systematic uncertainties between signal and backgrounds are also considered. The cross section upper limits can be mapped to sparticle mass limits in the two-dimensional simplified model mass plane.

7.5 Event selection and region definition

The analysis is split by final state: 2ℓ for hadronic W decays, and 3ℓ for leptonic W decays. Each final state is also split further into two regimes: one SR at lower mass splitting ($\Delta m = m_{\tilde{\chi}^{\pm}_1/\tilde{\chi}^0_2} - m_{\tilde{\chi}^0_1}$) which relies on an ISR jet system, and another three SRs which work on fuller reconstruction of events. These eight SRs are defined using Recursive Jigsaw Reconstruction, discussed in detail in Chapter 6, which for each

[4] p_0 cannot exceed 0.5.

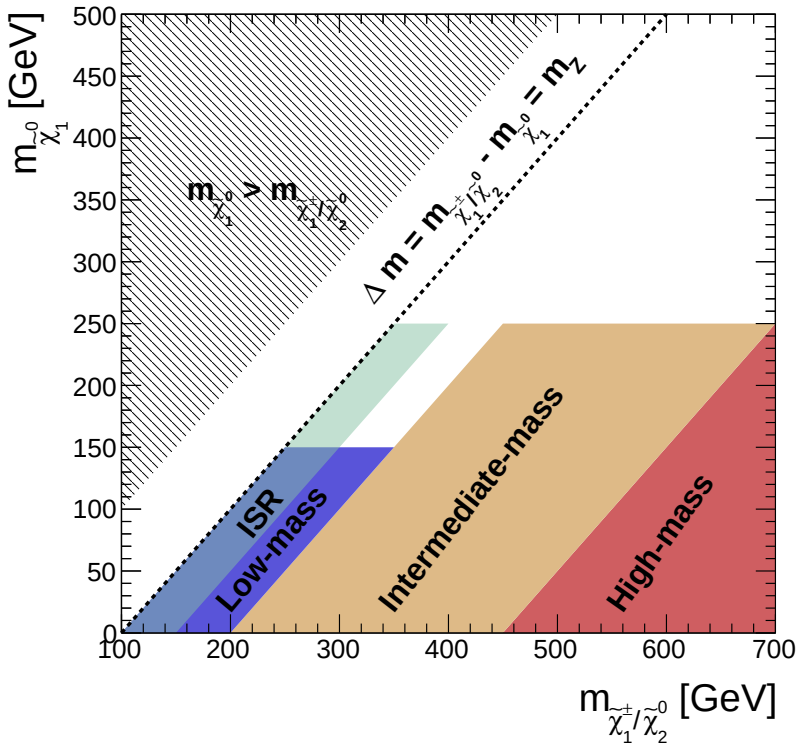

Figure 7.3: The areas of the two dimensional mass plane $m_{\tilde{\chi}_1^\pm/\tilde{\chi}_2^0} - m_{\tilde{\chi}_1^0}$ that are probed by the four SRs [74].

event takes in object four(three)-vectors: jets, electrons, muons, $\vec{E}_{\mathrm{T}}^{\mathrm{miss}}$, and applies either the standard or ISR decay tree and jigsaw rules.

Both 2ℓ and 3ℓ regions are constructed in a similar fashion: a high mass region probing large mass splittings ($\Delta m \gtrsim 400$ GeV), an intermediate mass region covering ($\Delta m \gtrsim 200$ GeV), and complementary low mass and ISR regions ($\Delta m \gtrsim 100$ GeV). The latter two mutually exclusive regions target an area of the two dimensional mass plane that is kinematically difficult as the LSPs carry little momentum with the W and Z bosons being produced close to rest. A schematic representation of the SR layout on the two dimensional SUSY simplified model mass plane is shown in Figure 7.3. For the purposes of testing the expected sensitivities of the SRs some benchmark signal points are used: $(m_{\tilde{\chi}_2^0}, m_{\tilde{\chi}_1^\pm})$ = (600,0), (400,200), (200,100) GeV for the high mass, intermediate mass, and low mass & ISR regions respectively.

7.5.1 Event selection in the 2ℓ regions

The 2ℓ channel regions defined with the standard decay tree are three SRs, two CRs for VV (where V is W or Z) and top quark processes (the sum of $Wt + t\bar{t}$) and four VRs validating the VV, top, and Z+jets background estimates. The preselection criteria for the standard decay tree regions is listed in Table 7.7, and include selections on object multiplicity (n_{leptons}), the jet multiplicity (n_{jets}), the b-tag jet multiplicity ($n_{b\text{-tag}}$), the transverse momenta of the leading ($p_{\text{T}}^{\ell_1}$, $p_{\text{T}}^{j_1}$) and subleading ($p_{\text{T}}^{\ell_2}$, $p_{\text{T}}^{j_2}$) leptons and jets and the invariant mass of the dilepton ($m_{\ell\ell}$) and dijet (m_{jj}) system. Most of the regions are defined with exactly two opposite-charge, same-flavour leptons with transverse momentum greater than 25 GeV and an invariant mass consistent with arising from a Z boson. Exceptions to this are the diboson CR (CR2ℓ-VV) and top VR (VR2ℓ-Top). The CR2ℓ-VV requires three or four leptons, which helps to select a sample enriched in diboson events as well as to ensure orthogonality with the SRs. The lepton pair is selected by choosing the opposite-charge, same-flavour pair closest to the Z mass, while the remaining lepton(s) are treated as invisible objects contributing to $\vec{p}_{\text{T}}^{\,\text{miss}}$. The additional requirement on m_{T}^{W}, which is applied only in the events containing exactly three charged leptons, ensures orthogonality with the 3ℓ regions described in Section 7.5.2. Both the top CR (CR2ℓ-Top) and VR (VR2ℓ-Top) are defined with a b-tag jet requirement while orthogonality with each other is ensured by inverting the dilepton invariant mass requirement. In all regions the dijet invariant mass is formed using the two leading jets in p_{T}. The SRs require the m_{jj} to be consistent with a W boson while the Z+jets (VR2ℓ_High-Zjets and VR2ℓ_Low-Zjets) and diboson (VR2ℓ-VV) VRs select events outside of the W mass window.

In addition to the preselection criteria, further selection requirements are applied in each region according to the parameter space probed, including some variables constructed according to the principles outlined in Section 6.5:

- $H_{4,1}^{\text{PP}}$, constructed with the two leptons, two leading jets and the $\vec{E}_{\text{T}}^{\,\text{miss}}$.
- $H_{1,1}^{\text{PP}}$, with the same inputs as above, but with a vector sum of visible objects.
- $p_{\text{T PP}}^{\text{lab}}/(p_{\text{T PP}}^{\text{lab}} + H_{\text{T}\,n,1}^{\text{PP}})$, testing for significant transverse boosts.

Table 7.7: Preselection criteria for the three standard-decay-tree 2ℓ SRs and the associated CRs and VRs [74]. The variables are defined in the text.

Region	n_{leptons}	n_{jets}	$n_{b\text{-tag}}$	$p_{\text{T}}^{\ell_1,\ell_2}$ [GeV]	$p_{\text{T}}^{j_1,j_2}$ [GeV]	$m_{\ell\ell}$ [GeV]	m_{jj} [GeV]	m_{T}^{W} [GeV]
CR2ℓ-VV	$\in [3,4]$	≥ 2	=0	> 25	> 30	$\in (80,100)$	> 20	$\in (70,100)$ if $n_{\text{leptons}} = 3$
CR2ℓ-Top	$= 2$	≥ 2	=1	> 25	> 30	$\in (80,100)$	$\in (40,250)$	–
VR2ℓ-VV	$= 2$	≥ 2	=0	> 25	> 30	$\in (80,100)$	$\in (40,70)$	–
							or $\in (90,500)$	–
VR2ℓ-Top	$= 2$	≥ 2	=1	> 25	> 30	$\in (20,80)$	$\in (40,250)$	–
						or > 100		–
VR2ℓ_High-Zjets	$= 2$	≥ 2	$= 0$	> 25	> 30	$\in (80,100)$	$\in (0,60)$	–
							or $\in (100,180)$	–
VR2ℓ_Low-Zjets	$= 2$	$= 2$	$= 0$	> 25	> 30	$\in (80,100)$	$\in (0,60)$	–
							or $\in (100,180)$	–
SR2ℓ_High	$= 2$	≥ 2	$= 0$	> 25	> 30	$\in (80,100)$	$\in (60,100)$	–
SR2ℓ_Int	$= 2$	≥ 2	$= 0$	> 25	> 30	$\in (80,100)$	$\in (60,100)$	–
SR2ℓ_Low	$= 2$	$= 2$	$= 0$	> 25	> 30	$\in (80,100)$	$\in (70,90)$	–

- $\min(H_{1,1}^{\text{P}_\text{a}}, H_{1,1}^{\text{P}_\text{b}})/\min(H_{2,1}^{\text{P}_\text{a}}, H_{2,1}^{\text{P}_\text{b}})$, comparing the scale of one visible object and $E_{\text{T}}^{\text{miss}}$ in their respective production frames, to two visible objects and $E_{\text{T}}^{\text{miss}}$ in the same frame.

- $H_{1,1}^{\text{PP}}/H_{4,1}^{\text{PP}}$, tests for unbalanced events where one object (visible or invisible) takes a large part of the total event scale.

- $\Delta\phi_{\text{V}}^{\text{P}}$, the azimuthal angle between the visible system in frame P and the direction of the boost from PP to P.

These selection requirements are shown in Table 7.8. The $\min\Delta\phi(j_1/j_2, \vec{p}_{\text{T}}^{\text{miss}})$ variable corresponds to the minimum azimuthal angle between the jets and $\vec{p}_{\text{T}}^{\text{miss}}$ and is applied only in SR2ℓ_Low to further suppress the Z+jets contribution. The selection criteria applied in VR2ℓ_High-Zjets and VR2ℓ_Low-Zjets differ so as to be closer and orthogonal to their respective SRs. As such the $0.35 < H_{1,1}^{\text{PP}}/H_{4,1}^{\text{PP}} < 0.6$ requirement is retained only for VR2ℓ_Low-Zjets. VR2ℓ-VV is the only region with an $H_{1,1}^{\text{PP}}$ requirement, but one that is necessary since it further suppresses the Z+jets background while keeping the VRs close to the SRs.

The ISR regions are defined with at least three jets and using the compressed decay tree, leaving SR2ℓ_ISR orthogonal to SR2ℓ_Low. The lepton and jet multiplicities

Table 7.8: Selection criteria for the three standard-decay-tree 2ℓ SRs and the associated CRs and VRs [74]. The variables are defined in the text

Region	$H_{4,1}^{\mathrm{PP}}$ [GeV]	$H_{1,1}^{\mathrm{PP}}$ [GeV]	$\frac{p_{\mathrm{T}}^{\mathrm{lab}}{}_{\mathrm{PP}}}{p_{\mathrm{T}}^{\mathrm{lab}}{}_{\mathrm{PP}}+H_{\mathrm{T}}^{\mathrm{PP}}{}_{4,1}}$	$\frac{\min(H_{1,1}^{\mathrm{Pa}},H_{1,1}^{\mathrm{Pb}})}{\min(H_{2,1}^{\mathrm{Pa}},H_{2,1}^{\mathrm{Pb}})}$	$\frac{H_{1,1}^{\mathrm{PP}}}{H_{4,1}^{\mathrm{PP}}}$	$\Delta\phi_{\mathrm{V}}^{\mathrm{P}}$	$\min\Delta\phi(j_1/j_2, \vec{p}_{\mathrm{T}}^{\,\mathrm{miss}})$
CR2ℓ-VV	> 200	–	< 0.05	> 0.2	–	$\in (0.3, 2.8)$	–
CR2ℓ-Top	> 400	–	< 0.05	> 0.5	–	$\in (0.3, 2.8)$	–
VR2ℓ-VV	> 400	> 250	< 0.05	$\in (0.4, 0.8)$	–	$\in (0.3, 2.8)$	–
VR2ℓ-Top	> 400	–	< 0.05	> 0.5	–	$\in (0.3, 2.8)$	–
VR2ℓ_High-Zjets	> 600	–	< 0.05	> 0.4	–	$\in (0.3, 2.8)$	–
VR2ℓ_Low-Zjets	> 400	–	< 0.05	–	$\in (0.35, 0.60)$	–	–
SR2ℓ_High	> 800	–	< 0.05	> 0.8	–	$\in (0.3, 2.8)$	–
SR2ℓ_Int	> 600	–	< 0.05	> 0.8	–	$\in (0.6, 2.6)$	–
SR2ℓ_Low	> 400	–	< 0.05	–	$\in (0.35, 0.60)$	–	> 2.4

Table 7.9: Preselection criteria for the compressed-decay-tree 2ℓ SR and the associated CRs and VRs [74]. The variables are defined in the text.

Region	n_{leptons}	$N_{\mathrm{jet}}^{\mathrm{ISR}}$	$N_{\mathrm{jet}}^{\mathrm{S}}$	n_{jets}	$n_{b\text{-tag}}$	$p_{\mathrm{T}}^{\ell_1,\ell_2}$ [GeV]	$p_{\mathrm{T}}^{j_1,j_2}$ [GeV]
CR2ℓ_ISR-VV	$\in [3,4]$	≥ 1	≥ 2	> 2	$= 0$	> 25	> 30
CR2ℓ_ISR-Top	$= 2$	≥ 1	$= 2$	$\in [3,4]$	$= 1$	> 25	> 30
VR2ℓ_ISR-VV	$\in [3,4]$	≥ 1	≥ 2	≥ 3	$= 0$	> 25	> 20
VR2ℓ_ISR-Top	$= 2$	≥ 1	$= 2$	$\in [3,4]$	$= 1$	> 25	> 30
VR2ℓ_ISR-Zjets	$= 2$	≥ 1	≥ 1	$\in [3,5]$	$= 0$	> 25	> 30
SR2ℓ_ISR	$= 2$	≥ 1	$= 2$	$\in [3,4]$	$= 0$	> 25	> 30

and other preselection criteria are defined in Table 7.9. All ISR regions require at least one jet assigned to the ISR system by combinatoric mass minimisation of all jets in an event, with a further two jets being assigned to the S system. The VV control and validation regions are constructed with 3 and 4 lepton events as in the standard tree case, with VR2ℓ_ISR-VV having a lowered 20 GeV jet p_{T} threshold to increase the number of events in the region.

Additional requirements are placed on the regions using variables derived from the compressed decay tree, relying on the recoil of the S system against ISR, listed in Table 7.10. Most of these variables have been defined and described in Section 6.5.2:

- m_Z, the mass of the dilepton pair.
- m_J, the mass of the jet system assigned to the S system.

Table 7.10: Selection criteria for the compressed-decay-tree 2ℓ SR and the associated CRs and VRs [74]. The variables are defined in the text.

Region	m_Z [GeV]	m_J [GeV]	$\Delta\phi^{\mathrm{CM}}_{\mathrm{ISR,I}}$	R_{ISR}	$p^{\mathrm{CM}}_{\mathrm{T\,ISR}}$ [GeV]	$p^{\mathrm{CM}}_{\mathrm{T\,I}}$ [GeV]	$p^{\mathrm{CM}}_{\mathrm{T}}$ [GeV]
CR2ℓ_ISR-VV	$\in (80,100)$	> 20	> 2.0	$\in (0.0,0.5)$	> 50	> 50	< 30
CR2ℓ_ISR-Top	$\in (50,200)$	$\in (50,200)$	> 2.8	$\in (0.4,0.75)$	> 180	> 100	< 20
VR2ℓ_ISR-VV	$\in (20,80)$ or > 100	> 20	> 2.0	$\in (0.0,1.0)$	> 70	> 70	< 30
VR2ℓ_ISR-Top	$\in (50,200)$	$\in (50,200)$	> 2.8	$\in (0.4,0.75)$	> 180	> 100	> 20
VR2ℓ_ISR-Zjets	$\in (80,100)$	< 50 or > 110	–	–	> 180	> 100	< 20
SR2ℓ_ISR	$\in (80,100)$	$\in (50,110)$	> 2.8	$\in (0.4,0.75)$	> 180	> 100	< 20

- $p^{\mathrm{CM}}_{\mathrm{T\,ISR}}$, the magnitude of the vector summed transverse momenta of all the jets assigned to the ISR system.

- $p^{\mathrm{CM}}_{\mathrm{T\,I}}$, the magnitude of the missing transverse momenta of the invisible system. This behaves like boost-corrected $E^{\mathrm{miss}}_{\mathrm{T}}$.

- p^{CM}_{T}, the magnitude of the vector summed transverse momenta of the CM system. This measures the transverse momentum of the CM frame itself, useful for diagnosing misreconstruction of the CM frame.

- R_{ISR}, serving as an estimate of the mass splitting of the NLSP and LSP.

- $N^{\mathrm{S}}_{\mathrm{jet}}$, the number of jets assigned to the S system by combinatoric mass minimisation.

- $N^{\mathrm{ISR}}_{\mathrm{jet}}$, the number of jets assigned to the ISR system by combinatoric mass minimisation.

- $\Delta\phi^{\mathrm{CM}}_{\mathrm{ISR,I}}$, the azimuthal angle between the ISR and I vectors in the CM frame.

CR2ℓ_ISR-VV and VR2ℓ_ISR-VV are orthogonal due to inverted m_Z requirements, the top CR and VR are defined with a b-tag requirement and expanded m_Z and m_J windows as there are no W and Z peaks in top-enriched leptonic final states. The top regions are made orthogonal by inverting the $p^{\mathrm{CM}}_{\mathrm{T}}$ selection. Additionally a Z+jets VR is constructed with orthogonality ensured by m_J being outside of the expected vector boson decay range.

Distributions of the RJR derived variables in some loose preselection regions are shown in Figure 7.4, CR distributions are shown in Figure 7.5, and VR distributions are shown in Figure 7.6. The background component labelled "Others" includes SM Higgs, $V\gamma$, VVV, $t\bar{t}V$ production, along with the fake and non-prompt leptons.

7.5.2 Event selection in the 3ℓ regions

The 3ℓ regions are considerably simpler than the 2ℓ regions and are fewer in number as a result, with the major background being VV events comprised almost entirely of WZ trileptonic decays. The leptons are assigned according to the following recipe: the same-flavour opposite-sign pair with invariant mass closest to m_Z is assigned to the Z with the other being assigned to the W. This unpaired lepton is used in conjunction with the $E_{\mathrm{T}}^{\mathrm{miss}}$ to construct a common variable to both the standard and ISR trees:

$$m_{\mathrm{T}}^{W} = \sqrt{2p_{\mathrm{T}}^{\ell}E_{\mathrm{T}}^{\mathrm{miss}}(1-\cos\Delta\phi)}, \tag{7.1}$$

with ϕ being the azimuthal angle between the unpaired lepton and the $\vec{E}_{\mathrm{T}}^{\mathrm{miss}}$.

The 3ℓ standard tree regions are three SRs (SR3ℓ_High, SR3ℓ_Int, SR3ℓ_Low), a CR for VV, and a VR to test the normalisation of the diboson. The transverse momenta of the three leptons are required to be higher than those in the 2ℓ selections with $p_{\mathrm{T}}^{\ell_3} > 30$ GeV, and there is a requirement for low jet activity (zero jets for SR3ℓ_Low). The preselection criteria for the regions are described in Table 7.11. The variables that define the regions in Table 7.12 are:

- $H_{3,1}^{\mathrm{PP}}$, the scale variable constructed with 3 visible objects.
- $H_{\mathrm{T}\,3,1}^{\mathrm{PP}}/H_{3,1}^{\mathrm{PP}}$, measuring how transverse the event is.
- $p_{\mathrm{T}\,\mathrm{PP}}^{\mathrm{lab}}/(p_{\mathrm{T}\,\mathrm{PP}}^{\mathrm{lab}} + H_{\mathrm{T}\,3,1}^{\mathrm{PP}})$, testing for significant transverse boosts.
- $\min(H_{1,1}^{\mathrm{P_a}}, H_{1,1}^{\mathrm{P_b}})/\min(H_{2,1}^{\mathrm{P_a}}, H_{2,1}^{\mathrm{P_b}})$ reduces to $H_{1,1}^{\mathrm{P_b}}/H_{2,1}^{\mathrm{P_b}}$, comparing the scale of one visible object and $E_{\mathrm{T}}^{\mathrm{miss}}$, to two visible objects and $E_{\mathrm{T}}^{\mathrm{miss}}$ in the frame with the Z boson.

Table 7.11: Preselection criteria for the 3ℓ CR, VR and SR with the standard decay tree [74]. The variables are defined in the text.

Region	n_{leptons}	n_{jets}	$n_{b\text{-tag}}$	$p_{\text{T}}^{\ell_1}$ [GeV]	$p_{\text{T}}^{\ell_2}$ [GeV]	$p_{\text{T}}^{\ell_3}$ [GeV]
CR3ℓ-VV	$= 3$	< 3	$= 0$	> 60	> 40	> 30
VR3ℓ-VV	$= 3$	< 3	$= 0$	> 60	> 40	> 30
SR3ℓ_High	$= 3$	< 3	$= 0$	> 60	> 60	> 40
SR3ℓ_Int	$= 3$	< 3	$= 0$	> 60	> 50	> 30
SR3ℓ_Low	$= 3$	$= 0$	$= 0$	> 60	> 40	> 30

Table 7.12: Selection criteria for the 3ℓ CR, VR and SR with the standard decay tree [74]. The variables are defined in the text.

Region	$m_{\ell\ell}$ [GeV]	m_{T}^{W} [GeV]	$H_{3,1}^{\text{PP}}$ [GeV]	$\frac{p_{\text{T PP}}^{\text{lab}}}{p_{\text{T PP}}^{\text{lab}}+H_{\text{T }3,1}^{\text{PP}}}$	$\frac{H_{\text{T }3,1}^{\text{PP}}}{H_{3,1}^{\text{PP}}}$	$\frac{H_{1,1}^{\text{P}_\text{b}}}{H_{2,1}^{\text{P}_\text{b}}}$
CR3ℓ-VV	$\in (75, 105)$	$\in (0, 70)$	> 250	< 0.2	> 0.75	–
VR3ℓ-VV	$\in (75, 105)$	$\in (70, 100)$	> 250	< 0.2	> 0.75	–
SR3ℓ_High	$\in (75, 105)$	> 150	> 550	< 0.2	> 0.75	> 0.8
SR3ℓ_Int	$\in (75, 105)$	> 130	> 450	< 0.15	> 0.8	> 0.75
SR3ℓ_Low	$\in (75, 105)$	> 100	> 250	< 0.05	> 0.9	–

Table 7.13: Preselection criteria for the 3ℓ CR, VR and SR with the compressed decay tree [74]. The variables are defined in the text.

Region	n_{leptons}	n_{jets}	$n_{b\text{-tag}}$	$p_{\text{T}}^{\ell_1}$ [GeV]	$p_{\text{T}}^{\ell_2}$ [GeV]	$p_{\text{T}}^{\ell_3}$ [GeV]
CR3ℓ_ISR-VV	$= 3$	≥ 1	$= 0$	> 25	> 25	> 20
VR3ℓ_ISR-VV	$= 3$	≥ 1	$= 0$	> 25	> 25	> 20
SR3ℓ_ISR	$= 3$	$\in [1, 3]$	$= 0$	> 25	> 25	> 20

In the high mass region the scale variable $H_{3,1}^{\text{PP}}$ is required to be large, and when transitioning to the intermediate and lower mass regions the ratio variables are more discriminating. For the low mass region the visible decay products behave almost exactly like SM WZ decays.

The ISR regions are defined similarly to their 2ℓ equivalents, with SR3ℓ_ISR, CR3ℓ_ISR-VV, and VR3ℓ_ISR-VV. Each of these regions requires at least one jet to make an ISR system, with the SR having an upper bound to reduce some of the backgrounds with higher object multiplicity. The lepton momenta thresholds are also lower than the standard tree, with 25, 25, 20 GeV for the leading, sub-leading and third lepton respectively. The preselection criteria are outlined in Table 7.13.

Table 7.14: Selection criteria for the 3ℓ CR, VR and SR with the compressed decay tree [74]. The variables are defined in the text.

Region	$m_{\ell\ell}$ [GeV]	m_{T}^{W} [GeV]	$\Delta\phi_{\mathrm{ISR,I}}^{\mathrm{CM}}$	R_{ISR}	$p_{\mathrm{T\,ISR}}^{\mathrm{CM}}$ [GeV]	$p_{\mathrm{T\,I}}^{\mathrm{CM}}$ [GeV]	$p_{\mathrm{T}}^{\mathrm{CM}}$ [GeV]
CR3ℓ_ISR-VV	$\in (75, 105)$	< 100	> 2.0	$\in (0.55, 1.0)$	> 80	> 60	< 25
VR3ℓ_ISR-VV	$\in (75, 105)$	> 60	> 2.0	$\in (0.55, 1.0)$	> 80	> 60	> 25
SR3ℓ_ISR	$\in (75, 105)$	> 100	> 2.0	$\in (0.55, 1.0)$	> 100	> 80	< 25

The lepton assignment is inherited from that used in the standard tree and the m_{T}^{W} is defined in the same way. The full selection criteria are defined in Table 7.14, with the following variables constructed in an equivalent way to the 2ℓ ISR regions:

- $p_{\mathrm{T\,ISR}}^{\mathrm{CM}}$, the magnitude of the vector summed transverse momenta of all the jets assigned to the ISR system.
- $p_{\mathrm{T\,I}}^{\mathrm{CM}}$, the magnitude of the missing transverse momenta of the invisible system. This behaves like boost-corrected $E_{\mathrm{T}}^{\mathrm{miss}}$.
- p_{T}^{CM}, the magnitude of the vector summed transverse momenta of the CM system. This measures the transverse momentum of the CM frame itself, useful for diagnosing misreconstruction of the CM frame.
- R_{ISR}, serving as an estimate of the mass splitting of the NLSP and LSP.
- $\Delta\phi_{\mathrm{ISR,I}}^{\mathrm{CM}}$, the azimuthal angle between the ISR and I vectors in the CM frame.

The control region is defined with an inverted m_{T}^{W} and the VR is defined with an inverted $p_{\mathrm{T}}^{\mathrm{CM}}$ an relaxed m_{T}^{W} for allow more events in the region.

Distributions of the RJR derived variables in some loose preselection regions are shown in Figure 7.7, CR distributions are shown in Figure 7.8, and VR distributions are shown in Figure 7.9. The background contribution labelled "Others" contains Higgs, $t\bar{t}V$ and fake and non-prompt leptons.

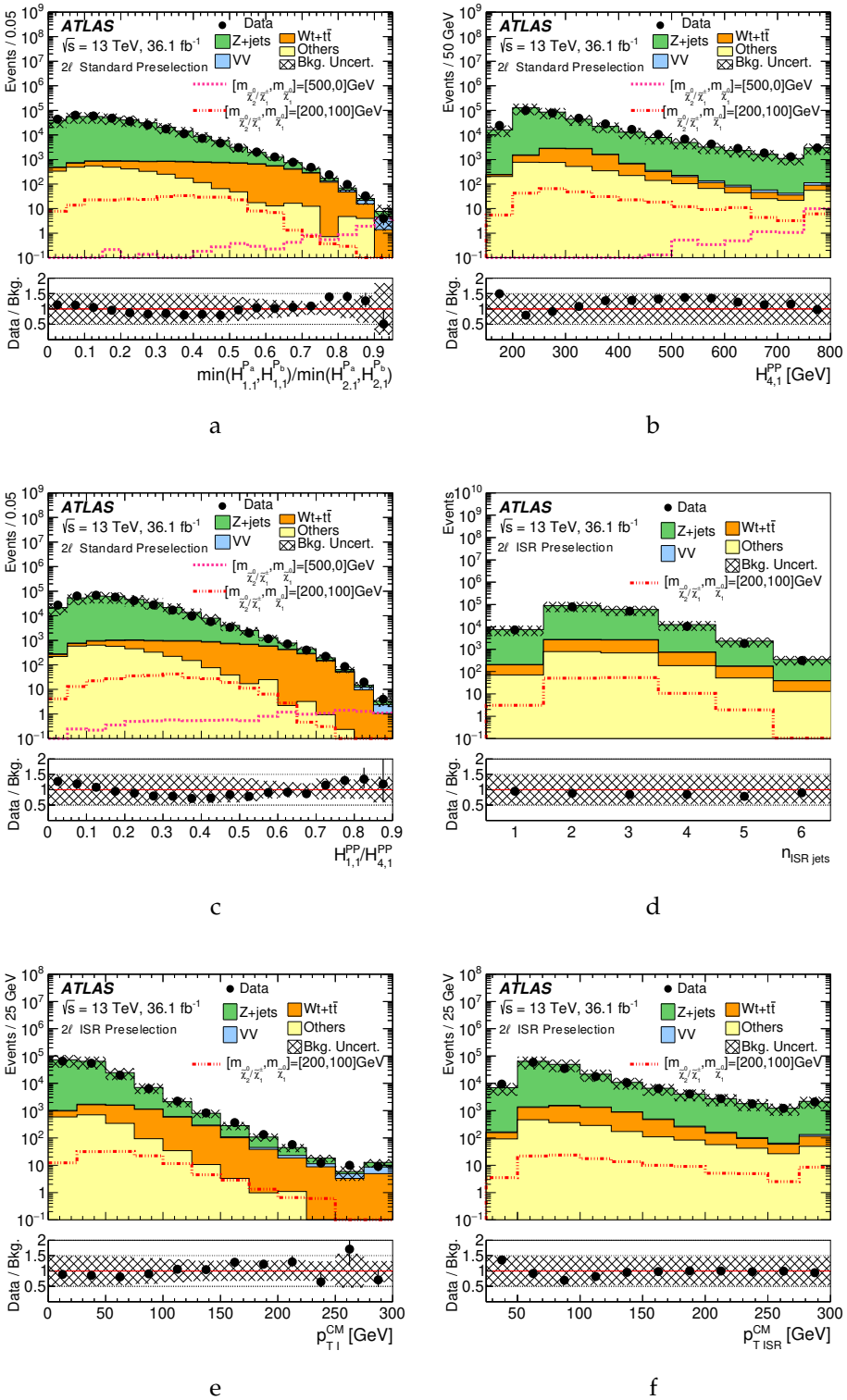

Figure 7.4: Kinematic variables at preselection level for the 2ℓ channel [74]. The last bin includes the overflow. Distributions for the (a) $\min(H^{P_a}_{1,1}, H^{P_b}_{1,1})/\min(H^{P_a}_{2,1}, H^{P_b}_{2,1})$, (b) $H^{PP}_{4,1}$, (c) $H^{PP}_{1,1}/H^{PP}_{4,1}$, (d) N^{ISR}_{jet}, and (e) $p^{CM}_{T\,I}$, and (f) $p^{CM}_{T\,ISR}$ are plotted.

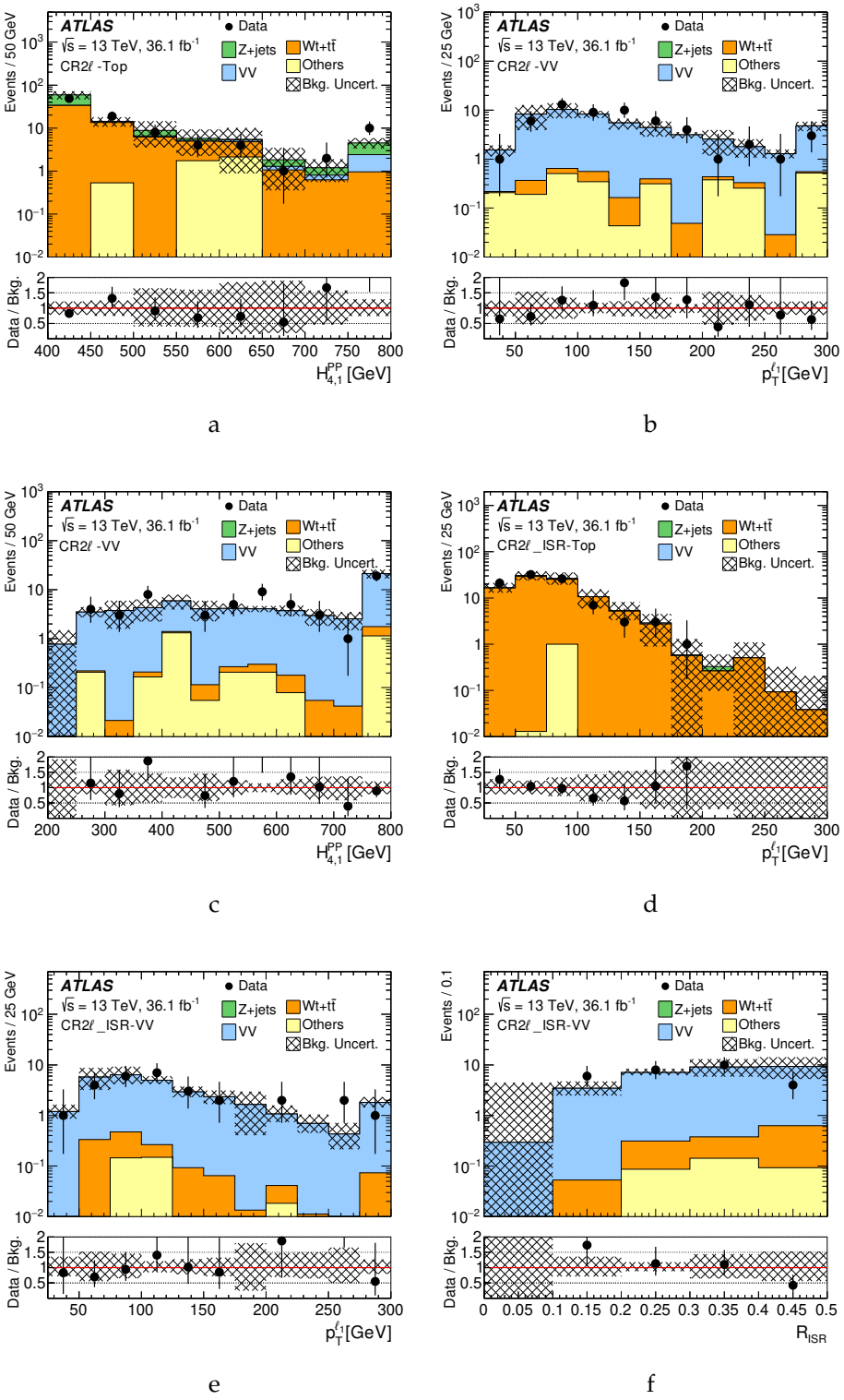

Figure 7.5: Distributions of kinematic variables in the control regions for the 2ℓ channel after applying all selection requirements in Tables 7.8 or 7.10 [74]. Distributions for the (a) $H_{4,1}^{\mathrm{PP}}$ in CR2ℓ-Top, (b) $p_{\mathrm{T}}^{\ell_1}$ and (c) $H_{4,1}^{\mathrm{PP}}$ for CR2ℓ-VV, (d) $p_{\mathrm{T}}^{\ell_1}$ in CR2ℓ_ISR-Top, and (e) $p_{\mathrm{T}}^{\ell_1}$ and (f) R_{ISR} for CR2ℓ_ISR-VV are plotted.

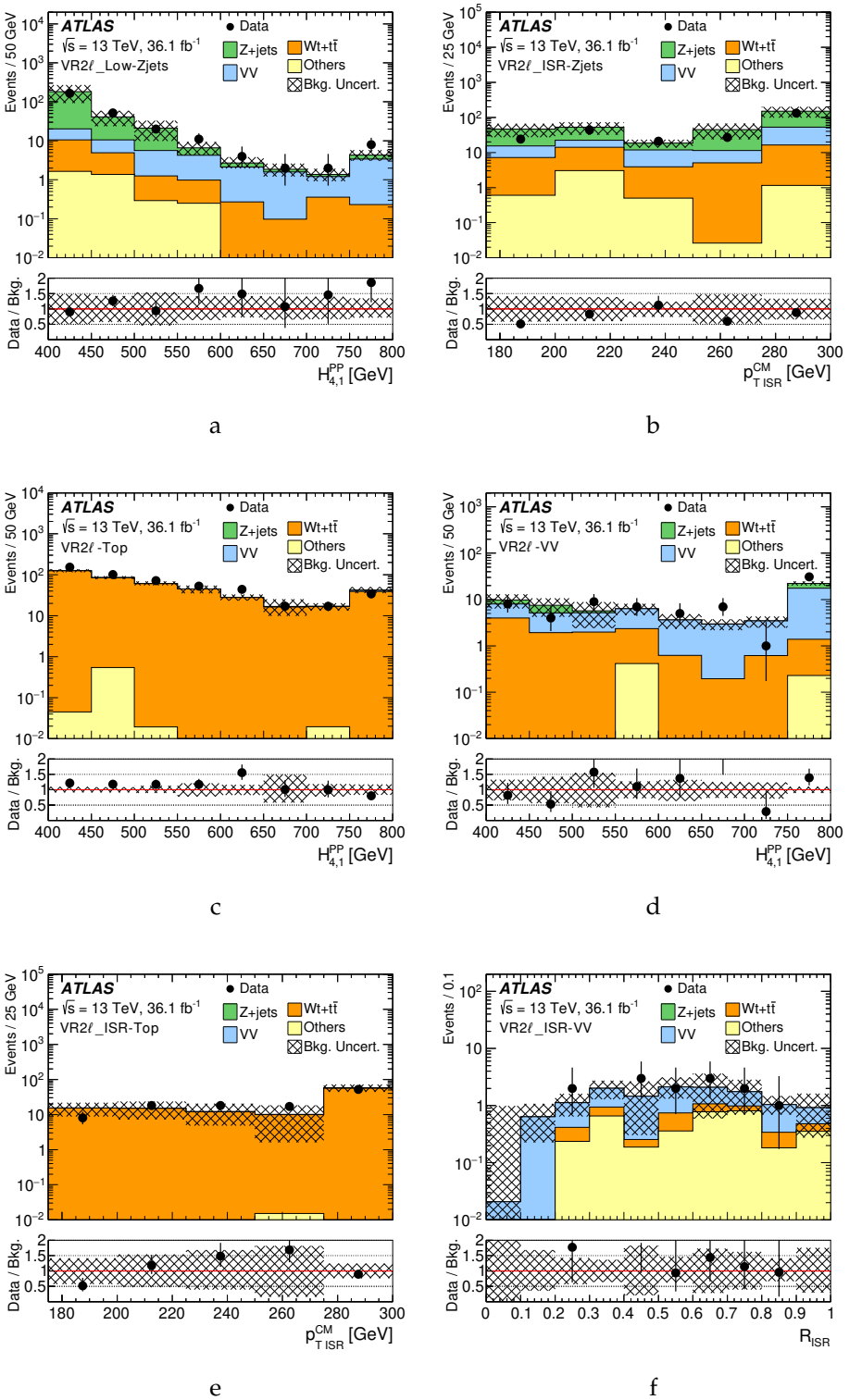

Figure 7.6: Distributions of kinematic variables in the validation regions for the 2ℓ channel after applying all selection requirements in Tables 7.8 or 7.10 [74]. Plots show (a) $H_{4,1}^{\mathrm{PP}}$ and (b) $p_{\mathrm{T\,ISR}}^{\mathrm{CM}}$ in VR2ℓ-Zjets and VR2ℓ_ISR-Zjets respectively; (c) $H_{4,1}^{\mathrm{PP}}$ in VR2ℓ-Top and (d) $H_{4,1}^{\mathrm{PP}}$ in VR2ℓ-VV; (e) $p_{\mathrm{T\,ISR}}^{\mathrm{CM}}$ in VR2ℓ_ISR-Top, and (f) R_{ISR} in VR2ℓ_ISR-VV.

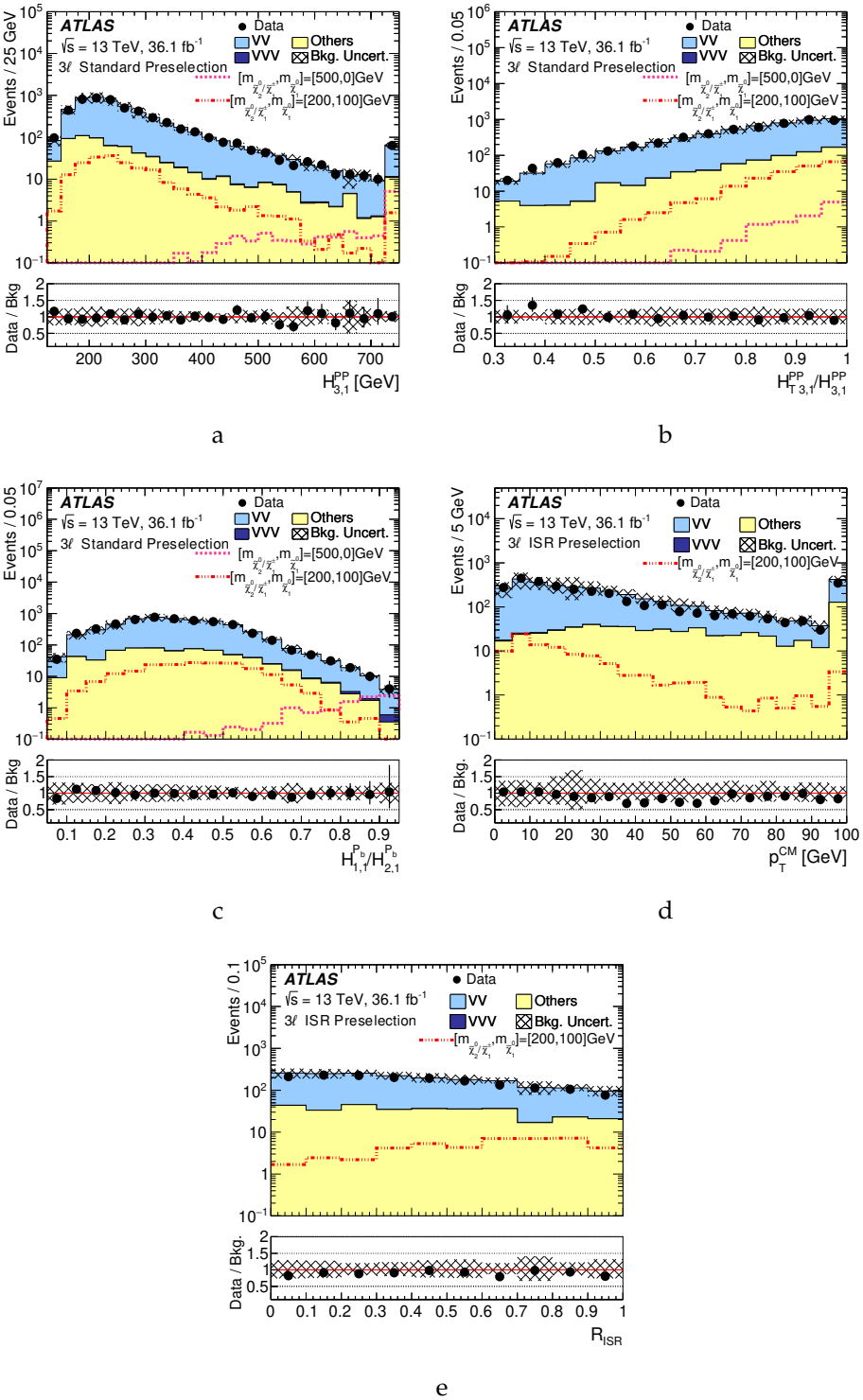

Figure 7.7: Distributions of kinematic variables at preselection level for the 3ℓ channel [74]. The last bin includes the overflow. Distributions for the (a) $H_{3,1}^{\mathrm{PP}}$, (b) $H_{\mathrm{T}\,3,1}^{\mathrm{PP}}/H_{3,1}^{\mathrm{PP}}$, (c) $H_{1,1}^{\mathrm{P_b}}/H_{2,1}^{\mathrm{P_b}}$, and (d) $p_{\mathrm{T}}^{\mathrm{CM}}$ and (e) R_{ISR} are plotted. The hatched error bands indicate the combined theoretical, experimental and MC statistical uncertainties.

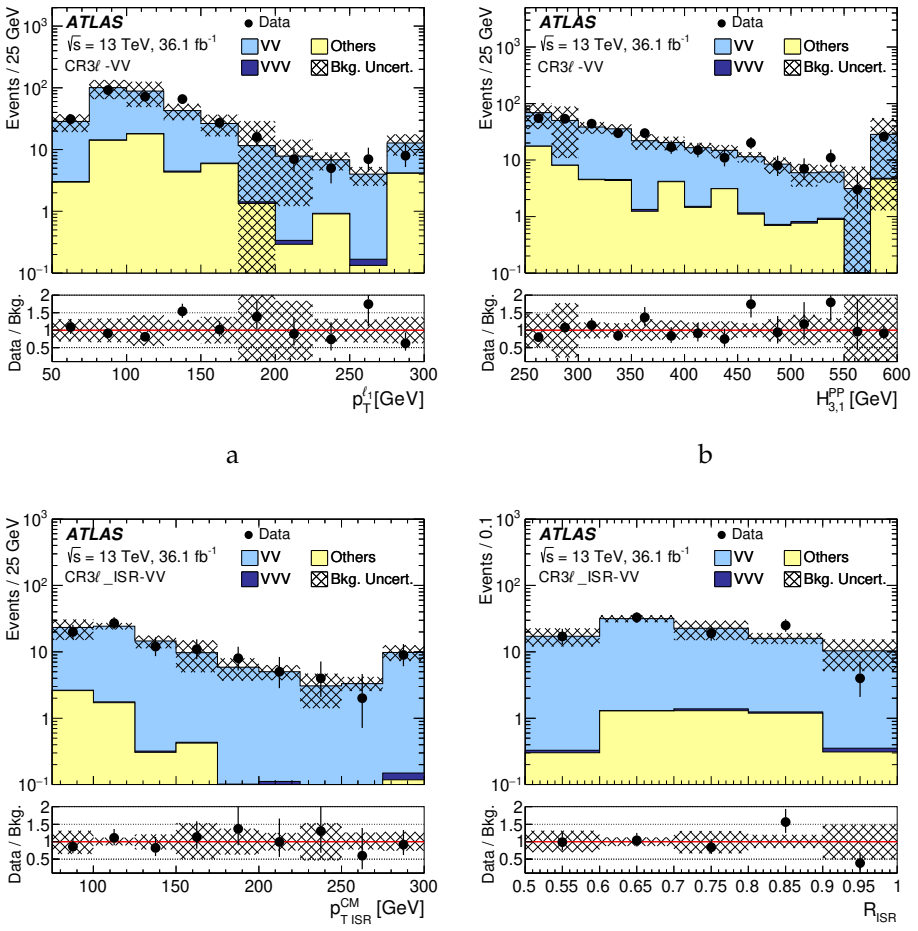

Figure 7.8: Distributions of kinematic variables in the control regions for the 3ℓ channel after applying all selection criteria described in Tables 7.12 or 7.14 [74]. The histograms show the post-fit MC background predictions. The FNP contribution is estimated from a data-driven technique and is included in the category "Others". The last bin includes the overflow. Plots show (a) $p_{\mathrm{T}}^{\ell_1}$ and (b) $H_{3,1}^{\mathrm{PP}}$ for the diboson CR in the standard decay tree, (c) $p_{\mathrm{T\,ISR}}^{\mathrm{CM}}$ and (d) R_{ISR} for the diboson CR in the compressed decay tree. The hatched error bands indicate the combined theoretical, experimental and MC statistical uncertainties.

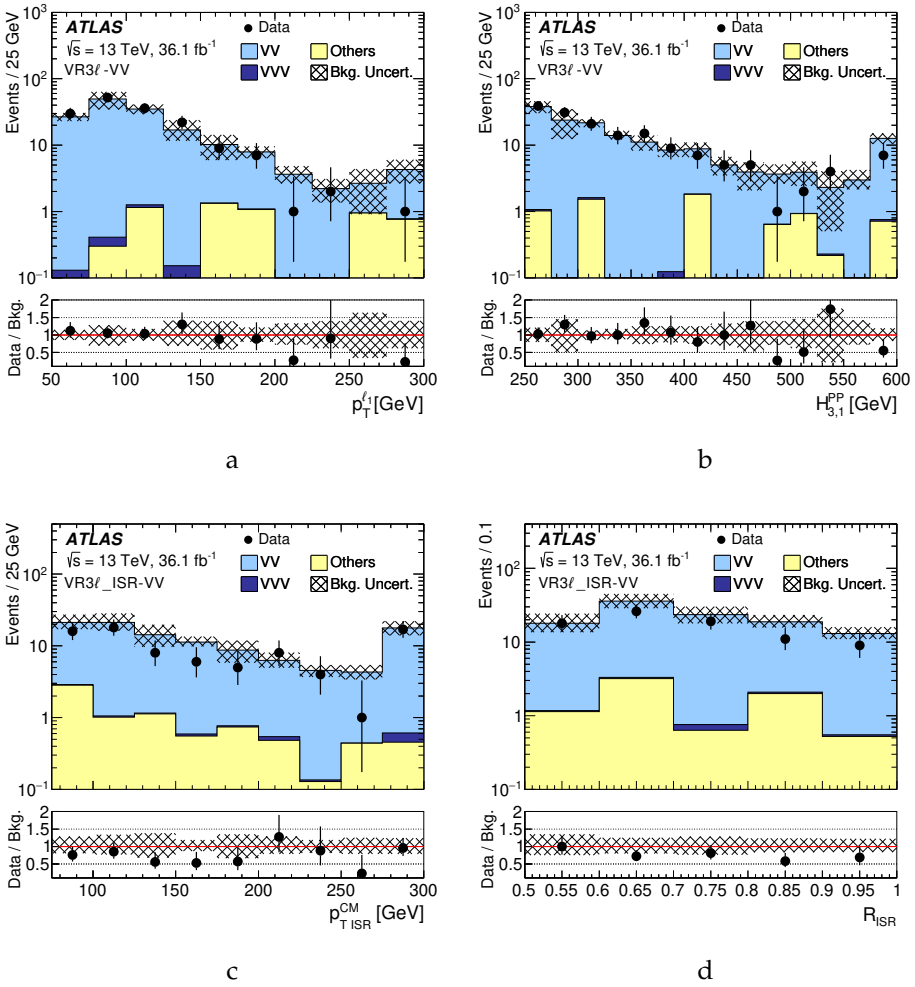

Figure 7.9: Distributions of kinematic variables in the validation regions for the 3ℓ channel after applying all selection criteria in Tables 7.12 or 7.14 [74]. The histograms show the post-fit MC background predictions. The FNP contribution is estimated from a data-driven technique and is included in the category "Others". The last bin includes the overflow. Plots show (a) $p_{\mathrm{T}}^{\ell_1}$ and (b) $H_{3,1}^{\mathrm{PP}}$ for the standard decay tree, (c) $p_{\mathrm{T\,ISR}}^{\mathrm{CM}}$ and (d) R_{ISR} for the compressed decay tree. The hatched error bands indicate the combined theoretical, experimental and MC statistical uncertainties.

7.6 Background estimation

A number of backgrounds need estimation in the SRs, with dibosons and Z+jets being the major contributors, along with lesser contributions from Higgs processes, $t\bar{t}$ and single top, tribosons and $t\bar{t}V$. The backgrounds can be split into two types: irreducible backgrounds with prompt and isolated leptons and real $E_{\mathrm{T}}^{\mathrm{miss}}$, and reducible backgrounds containing at least one fake or non-prompt (FNP) lepton or where detector and reconstruction effects (such as jet reconstruction or overlap removal issues) lead to improperly calculated $E_{\mathrm{T}}^{\mathrm{miss}}$.

Fake and non-prompt leptons can come from semileptonic decays of b- or c-hadrons, decays of light hadrons, jet misidentification, or photon conversions. The two analysis channels have different sources of FNP leptons, for the 2ℓ regions multijets, W+jets, single top and $t\bar{t}$, while in 3ℓ Z+jets and WW can appear as well, along with any other process where there are fewer than three isolated and prompt leptons. These FNP contributions are estimated from data using the Matrix Method, outlined in [130]. The matrix method uses two lepton identification criteria, a looser baseline selection and a more stringent signal selection corresponding to the definitions in 7.3. The numbers of observed events with baseline-baseline, baseline-signal, signal-baseline and signal-signal p_{T} ordered leptons pairs are used. For the 3ℓ channel the highest momentum lepton (electron or muon) is taken to be real, an assumption which holds more than 95% of the time. Once the probabilities for real and FNP leptons are extracted in some loose regions, the fraction of baseline leptons passing signal selection can be used to determined the expected rate of the FNP background from the data itself. This estimate is binned in lepton momentum and pseudorapidity to provide appropriate distributions as well as the overall background contribution.

7.6.1 Backgrounds in the 2ℓ channel

In the 2ℓ final state Z+jets is a major background contributor, with two real leptons, jets and $E_{\mathrm{T}}^{\mathrm{miss}}$ that largely comes from jet sources: semileptonic decays of b- and c-hadrons or jet mismeasurement. These effects are difficult to include in simulation,

and MC is often unreliable with large event weights and badly modelled kinematic distributions away from the bulk phase space. Instead γ+jets events in data are used to extract the $E_{\mathrm{T}}^{\mathrm{miss}}$ shape in Z+jets events. This procedure has been used in other ATLAS [131] and CMS [132, 133]. The $E_{\mathrm{T}}^{\mathrm{miss}}$ shape is extracted from a control sample which has similar properties to Z+jets events and are recorded using single photon triggers. Events from prescaled triggers correspond to $p_{\mathrm{T}} < 140$ GeV and are weighted with the appropriate trigger scale factor. These photons are then corrected for momentum distribution and momentum resolution factors for electrons, muons and photons are applied. This sample still contains contributions from $W\gamma$ and $Z\gamma$ which have genuine $E_{\mathrm{T}}^{\mathrm{miss}}$ from neutrinos. These are subtracted using MC normalised in a photon+lepton control region. This $V\gamma$ normalisation factor is 0.79.

Further steps are required to be able to replicate the behaviour of $Z \to \ell\ell$ with photons. First an $m_{\ell\ell}$ is assigned to each γ+jets event by sampling from $m_{\ell\ell}$ distributions parametrised as a function of boson p_{T} and the component of $E_{\mathrm{T}}^{\mathrm{miss}}$ that is parallel to the boson p_{T}, derived from Z+jets MC. Then each photon is boosted to the rest frame of the Z candidate and is split into two psuedo-leptons. The angular distributions of these assume isotropic decays in the rest frame. For SR2ℓ_High, SR2ℓ_Int, and SR2ℓ_ISR the Z+jets background is directly estimated from the weighted yield of events passing the SR selections. In SR2ℓ_Low there is a statistical issue relating to the prescaling of the photon triggers for the lower momentum events that enter the region. In this case the high-$p_{\mathrm{T}}^{\ell\ell}$component entering SR2$\ell$_Low is estimated directly and the shape is transferred to the low-$p_{\mathrm{T}}^{\ell\ell}$using a normalisation factor, the ratio of low-$p_{\mathrm{T}}^{\ell\ell}$to high-$p_{\mathrm{T}}^{\ell\ell}$events in an orthogonal sample with inverted $H_{4,1}^{\mathrm{PP}}$.

To validate the method, as well as to check the modeling of other SM backgrounds, validation regions are defined for each SR. The definitions of these regions (VR2ℓ-VV, VR2ℓ-Top, VR2ℓ_High-Zjets and VR2ℓ_Low-Zjets) are given for the standard decay tree in Table 7.8 and (VR2ℓ_ISR-VV, VR2ℓ_ISR-Top and VR2ℓ_ISR-Zjets) for the compressed decay tree in Table 7.10. The VRs targeting the validation of the Z+jets background estimation have an inverted dijet mass requirement with respect to the corresponding SR definitions as well as having some other selection criteria relaxed. In this way a potential signal contribution is rejected while the regions remain close but orthogonal to the SR selections.

As described in Section 7.5.1, the background contributions from $Wt + t\bar{t}$ and VV are normalised to data in dedicated CRs and the extracted normalisation factors from the fit are validated in orthogonal regions. The VV process in the SRs has contributions from all diboson processes producing at least two leptons in the final state. The dominant diboson process in SR2ℓ_High and SR2ℓ_Int is $ZZ \to \ell\ell\nu\nu$ with a smaller contribution from $WZ \to \ell\nu\ell\ell$. The picture changes with lower $\tilde{\chi}_1^{\pm}/\tilde{\chi}_2^0$ masses and smaller mass-splitting; in SR2ℓ_Low the dominant component is $WW \to \ell\nu\ell\nu$ followed by $WZ \to \ell\nu\ell\ell$ while in SR2ℓ_ISR the dominant contribution is from $WZ \to \ell\nu\ell\ell$ and to a lesser extent from $ZZ \to \ell\ell\nu\nu$. The semihadronic decays of dibosons, for example $ZV \to \ell\ell qq$, are accounted for by the γ+jets template since they do not lead to genuine $E_{\mathrm{T}}^{\mathrm{miss}}$ in the event. The CRs are designed to have compositions, in terms of diboson processes, similar to their respective SRs.

The two-lepton diboson and top CRs defined with the standard decay tree do not contain an explicit selection to make them orthogonal to their respective compressed CRs. However, the two decay trees of the RJR method, by construction, probe different event topologies, hence they select events where the overlap is designed to be insignificant. For the top CR the overlap is less than 1% while for the diboson CR it is smaller than 3%. Since the impact of this effect is negligible in comparison with the background uncertainties, it is not considered in the remainder of the analysis.

The normalisation factors obtained from the background-only fit for $Wt + t\bar{t}$ and VV for the selections applied to the standard (compressed) decay tree are 0.91 ± 0.23 and 0.91 ± 0.13 (0.99 ± 0.12 and 0.94 ± 0.18), respectively, where the uncertainties are dominated by the statistical uncertainty. The background fit results are summarised in Tables 7.15 and 7.16 for the CRs and VRs, respectively. The data are consistent with the expected background in all validation regions.

7.6.2 Backgrounds in the 3ℓ channel

The main background in the 3ℓ channel is the irreducible WZ diboson production. MC describes the shape of this distribution well and the normalisation is derived in dedicated CRs. The normalisation factors are 1.09 ± 0.10 for the standard tree CR3ℓ-VV and 1.13 ± 0.13 for the ISR tree CR3ℓ_ISR-VV. As with the 2ℓ regions

Table 7.15: Background fit results for the 2ℓ CRs [74]. The normalisation factors for $Wt + t\bar{t}$ and VV for the standard and compressed decay trees are different and are extracted from separate fits. The nominal predictions from MC simulation are given for comparison for the $Wt + t\bar{t}$ and VV backgrounds. The "Other" category contains the contributions from Higgs boson processes, $V\gamma$, VVV, $t\bar{t}V$ and non-prompt and non-isolated lepton production. The dashes indicate that these backgrounds are negligible and are included in the category "Other". Combined statistical and systematic uncertainties are given. The individual uncertainties can be correlated and do not necessarily add in quadrature to the total systematic uncertainty.

Region	CR2ℓ-VV	CR2ℓ-Top	CR2ℓ_ISR-VV	CR2ℓ_ISR-Top
Observed events	60	97	28	93
Total (post-fit) SM events	60 ± 8	97 ± 10	28 ± 5	93 ± 10
Other	3.5 ± 0.3	1.4 ± 0.3	0.72 ± 0.31	0.50 ± 0.15
Fit output, $Wt + t\bar{t}$	–	60 ± 11	–	90 ± 10
Fit output, VV	57 ± 8	4.0 ± 1.0	27 ± 5	0.99 ± 0.31
Z+jets	–	31 ± 15	–	2.1 ± 1.0
Fit input, $Wt + t\bar{t}$	–	66	–	91
Fit input, VV	62	4.4	29	1.1

the backgrounds are validated in dedicated VRs, with sub-dominant backgrounds from VVV, $t\bar{t}V$ and Higgs processes being taken directly from simulation. The background fit results are summarised in Table 7.17.

Similar to the two-lepton CR design, the three-lepton diboson CR defined with the standard decay tree does not contain an explicit selection to make it orthogonal to its respective compressed CR. The overlap is less than 0.5%. Since the impact of this effect is negligible in comparison with the background uncertainties, it is not considered in the remainder of the analysis.

Table 7.16: Expected and observed yields from the background fit for the 2ℓ VRs [74]. The nominal predictions from MC simulation are given for comparison for the $Wt + t\bar{t}$ and VV backgrounds. The "Other" category contains the contributions from Higgs boson processes, $V\gamma$, VVV, $t\bar{t}V$ and non-prompt and non-isolated lepton production. The dashes indicate that these backgrounds are negligible and are included in the category "Other". Combined statistical and systematic uncertainties are given. The individual uncertainties can be correlated and do not necessarily add in quadrature to the total systematic uncertainty.

Region	VR2ℓ_Low-Zjets	VR2ℓ_High-Zjets	VR2ℓ-VV	VR2ℓ-Top	VR2ℓ_ISR-VV	VR2ℓ_ISR-Top	VR2ℓ_ISR-Zjets
Observed events	263	77	72	491	13	113	248
Total (post-fit) SM events	261 ± 130	69 ± 26	61 ± 13	423 ± 105	12 ± 4	110 ± 18	310 ± 100
Other	3.5 ± 1.5	$0.25^{+0.62}_{-0.25}$	0.80 ± 0.09	2.3 ± 0.4	4.2 ± 0.5	0.68 ± 0.22	3.0 ± 0.6
Fit output, $Wt + t\bar{t}$	15 ± 5	1.7 ± 0.7	12 ± 4	415 ± 105	–	107 ± 18	40 ± 8
Fit output, VV	30 ± 7	16 ± 3	40 ± 13	3.7 ± 0.9	7.9 ± 3.6	0.97 ± 0.25	67 ± 15
Z+jets	210 ± 130	51 ± 25	8.4 ± 4.1	2.4 ± 1.2	–	1.6 ± 0.8	200 ± 100
Fit input, $Wt + t\bar{t}$	16	1.9	13	455	–	108	41
Fit input, VV	33	17	43	4.1	8.4	1.1	71

Table 7.17: Expected and observed yields from the background fit for the 3ℓ CRs and VRs [74]. The normalisation factors for VV for the standard and compressed decay trees are different and are extracted from separate fits. The nominal predictions from MC simulation are given for comparison for the VV background. The "Other" category contains the contributions from Higgs boson processes, $t\bar{t}V$ and non-prompt and non-isolated lepton production. Combined statistical and systematic uncertainties are given. The individual uncertainties can be correlated and do not necessarily add in quadrature to the total systematic uncertainty.

Region	CR3ℓ-VV	VR3ℓ-VV	CR3ℓ_ISR-VV	VR3ℓ_ISR-VV
Observed events	331	160	98	83
Total (post-fit) SM events	331 ± 18	159 ± 38	98 ± 10	109 ± 24
Other	52 ± 2	5.6 ± 1.2	4.4 ± 1.2	7.1 ± 1.6
Tribosons	1.1 ± 0.1	0.44 ± 0.03	0.22 ± 0.14	0.42 ± 0.04
Fit output, VV	278 ± 18	153 ± 38	93 ± 10	102 ± 24
Fit input, VV	255	140	83	90

7.7 Statistical and systematics treatment

In this analysis, theoretical and experimental uncertainties are considered in the SM background estimates and signal models considered, and are included in the profile likelihoods used for the fits outlined in Section 7.4. Diboson modelling theoretical systematics are estimated by varying the renormalisation, factorisation and merging scales, along with the choice of PDF. The experimental systematics considered relate to the jet energy scale and resolution, $E_{\mathrm{T}}^{\mathrm{miss}}$ modelling in the simulation, and lepton reconstruction and identification. The data-driven matrix method and γ+jets background estimation methods also have systematics derived. For the normalised top and VV background predictions, with the normalisation being extracted from dedicated control regions, the systematic uncertainties only affect the extrapolation to the SRs. The statistical uncertainty for the MC samples is also included (sum of weights). Additionally the pileup reweighting systematics is also considered and is found to be negligible.

The jet energy scale and resolution uncertainties are derived as a function of the p_{T} and η of the jet, as well as of the pileup conditions and the jet flavour composition of the selected jet sample. They are determined using a combination of simulated events and data samples, through measurements of the jet response balance in multijet, Z+jets and γ+jets events [41].

The systematic uncertainties related to the modeling of $E_{\mathrm{T}}^{\mathrm{miss}}$ in the simulation are estimated by propagating the uncertainties in the energy and momentum scale of each of the physics objects, as well as the uncertainties in the soft-term resolution and scale [134].

The remaining detector-related systematic uncertainties, such as those in the lepton reconstruction efficiency, b-tagging efficiency [135, 136], lepton energy scale, energy resolution and in the modeling of the trigger [37, 58], are included but are found to be negligible in all channels.

In the 2ℓ channel, uncertainties in the data-driven Z+jets estimate are calculated following the methodology used in Ref. [131]. An additional uncertainty is based on the difference between the expected background yield from the nominal method

(which produces 6.3 events in SR2ℓ_Low and 0.1 events in SR2ℓ_ISR) and from a second method implemented as a cross-check, which extracts the dijet mass shape from data validation regions, normalises the shape to the sideband regions of the SRs, and extrapolates the background into the W mass region. The Z+jets background estimations obtained from the sideband method are 5.9 and 0.2 events for SR2ℓ_Low and SR2ℓ_ISR, respectively. Moreover, a 100% uncertainty in the $V\gamma$ normalisation factor is included. To cover any statistical limitations on the Z+jets estimate that may be present in SR2ℓ_ISR, an upper limit on the Z+jets estimate is considered as an additional systematic uncertainty. The upper limit is calculated by multiplying the sum of the nominal Z+jets background estimate, adding the statistical uncertainty, with the ratio of low-$p_{\mathrm{T}}^{\ell\ell}$ to high-$p_{\mathrm{T}}^{\ell\ell}$ events calculated with a looser requirement on $p_{\mathrm{T\,I}}^{\mathrm{CM}}$. This is the dominant uncertainty in the ISR region and accounts for 95% of the total uncertainty in the Z+jets estimate.

Systematic uncertainties are also assigned to the estimated background from FNP leptons in both the 2ℓ and 3ℓ channels to account for potentially different compositions (heavy flavour, light flavour or conversions) between the signal and control regions. An additional uncertainty is associated with the subtraction of prompt leptons from this CR using simulation.

A summary of the dominant uncertainties in the 2ℓ SRs is shown in Table 7.18. The uncertainties with the largest impact in these SRs are those in the data-driven Z+jets estimate, followed by the VV modeling uncertainties, the statistical uncertainties in the MC background samples and the uncertainty in the fitted normalisation factor for VV related to the number of events in the corresponding CRs.

A similar summary of the systematic uncertainties impacting the 3ℓ SRs is given in Table 7.19. These are dominated by the statistical uncertainties in the MC background samples, the modeling uncertainties in the VV processes and the uncertainties related to the fitted normalisation factors for VV.

Table 7.18: Summary of the main systematic uncertainties and their impact (in %) on the total SM background prediction in each of the 2ℓ SRs [74]. The total systematic uncertainty can be different from the sum in quadrature of individual sources due to the correlations between them resulting from the fit to the data.

Signal Region	SR2ℓ_High	SR2ℓ_Int	SR2ℓ_Low	SR2ℓ_ISR
Total uncertainty [%]	42	38	70	103
Z+jets data-driven estimate	42	31	69	96
VV theoretical uncertainties	28	27	6	34
MC statistical uncertainties	16	12	5	9
VV fitted normalisation	13	14	2	16
FNP leptons	-	5	13	12
Jet energy resolution	5	10	4	3
Jet energy scale	1	2	< 1	3
$E_{\mathrm{T}}^{\mathrm{miss}}$ modeling	3	4	< 1	< 1
$t\bar{t}$ fitted normalisation	< 1	< 1	2	2
Lepton reconstruction / identification	< 1	< 1	< 1	< 1

Table 7.19: Summary of the main systematic uncertainties and their impact (in %) on the total SM background prediction in each of the 3ℓ SRs [74]. The total systematic uncertainty can be different from the sum in quadrature of individual sources due to the correlations between them resulting from the fit to the data.

Signal Region	SR3ℓ_High	SR3ℓ_Int	SR3ℓ_Low	SR3ℓ_ISR
Total uncertainty [%]	44	22	19	26
VV theoretical uncertainties	18	9	12	19
MC statistical uncertainties	37	17	8	10
VV fitted normalisation	8	7	9	11
FNP leptons	7	< 1	3	5
Jet energy resolution	4	< 1	7	3
Jet energy scale	7	< 1	2	3
$E_{\mathrm{T}}^{\mathrm{miss}}$ modeling	2	< 1	1	4
Lepton reconstruction / identification	3	4	2	2

7.8 Results

The observed number of events in the 2ℓ SRs are compared to the expected background yields in Table 7.20 and graphically in Figure 7.10. The 3ℓ channel results are shown in Table 7.21 and Figure 7.11. For both channels there are no significant excesses above the SM in the intermediate and high mass signal regions. In each of the four orthogonal regions targeting low mass splittings there are excesses seen above the expected backgrounds. A model independent fit of all regions is done to show the level of agreement with the SM, shown in Table 7.22.

As seen in Table 7.22 the excesses in SR2ℓ_Low, SR2ℓ_ISR, SR3ℓ_Low, and SR3ℓ_ISR are 1.39, 1.99, 2.13, and 3.02 standard deviations from the background only hypothesis. Some kinematic distributions are also shown in Figure 7.12 and Figure 7.13 for the 2ℓ and 3ℓ SRs respectively. The signal model shown for the SRs is a simplified model with $m_{\tilde{\chi}_2^0/\tilde{\chi}_1^\pm} = 200$ GeV and $m_{\tilde{\chi}_1^0} = 100$ GeV, used for optimising the regions.

Table 7.20: Expected and observed yields from the background-only fit for the 2ℓ SRs [74]. The errors shown are the statistical plus systematic uncertainties. Uncertainties in the predicted background event yields are quoted as symmetric, except where the negative error reaches down to zero predicted events, in which case the negative error is truncated.

Signal region	SR2ℓ_High	SR2ℓ_Int	SR2ℓ_Low	SR2ℓ_ISR
Total observed events	0	1	19	11
Total background events	1.9 ± 0.8	2.4 ± 0.9	8.4 ± 5.8	$2.7^{+2.8}_{-2.7}$
Other	0.02 ± 0.01	$0.05^{+0.12}_{-0.05}$	$0.02^{+1.07}_{-0.02}$	$0.06^{+0.33}_{-0.06}$
Fit output, $Wt + t\bar{t}$	0.00 ± 0.00	0.00 ± 0.00	0.57 ± 0.20	$0.28^{+0.34}_{-0.28}$
Fit output, VV	1.8 ± 0.7	2.4 ± 0.8	1.5 ± 0.9	2.3 ± 1.1
Z+jets	$0.07^{+0.78}_{-0.07}$	$0.00^{+0.74}_{-0.00}$	6.3 ± 5.8	$0.10^{+2.58}_{-0.10}$
Fit input, $Wt + t\bar{t}$	0.00	0.00	0.63	0.28
Fit input, VV	1.9	2.6	1.6	2.4

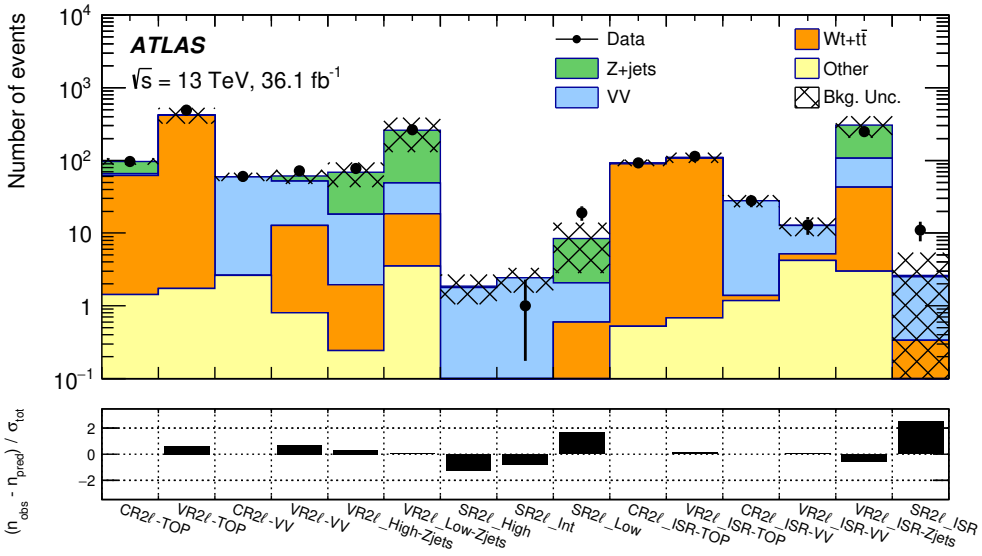

Figure 7.10: The observed and expected SM background yields in the CRs, VRs and SRs considered in the 2ℓ channel [74]. The statistical uncertainties in the background prediction are included in the uncertainty band, as well as the experimental and theoretical uncertainties. The bottom panel shows the difference in standard deviations between the observed and expected yields.

Table 7.21: Expected and observed yields from the background-only fit for the 3ℓ SRs [74]. The errors shown are the statistical plus systematic uncertainties. Uncertainties in the predicted background event yields are quoted as symmetric, except where the negative error reaches down to zero predicted events, in which case the negative error is truncated.

Signal region	SR3ℓ_High	SR3ℓ_Int	SR3ℓ_Low	SR3ℓ_ISR
Total observed events	2	1	20	12
Total background events	1.1 ± 0.5	2.3 ± 0.5	10 ± 2	3.9 ± 1.0
Other	$0.03^{+0.07}_{-0.03}$	0.04 ± 0.02	$0.02^{+0.34}_{-0.02}$	$0.06^{+0.19}_{-0.06}$
Triboson	0.19 ± 0.07	0.32 ± 0.06	0.25 ± 0.03	0.08 ± 0.04
Fit output, VV	0.83 ± 0.39	1.9 ± 0.5	10 ± 2	3.8 ± 1.0
Fit input, VV	0.76	1.8	9.2	3.4

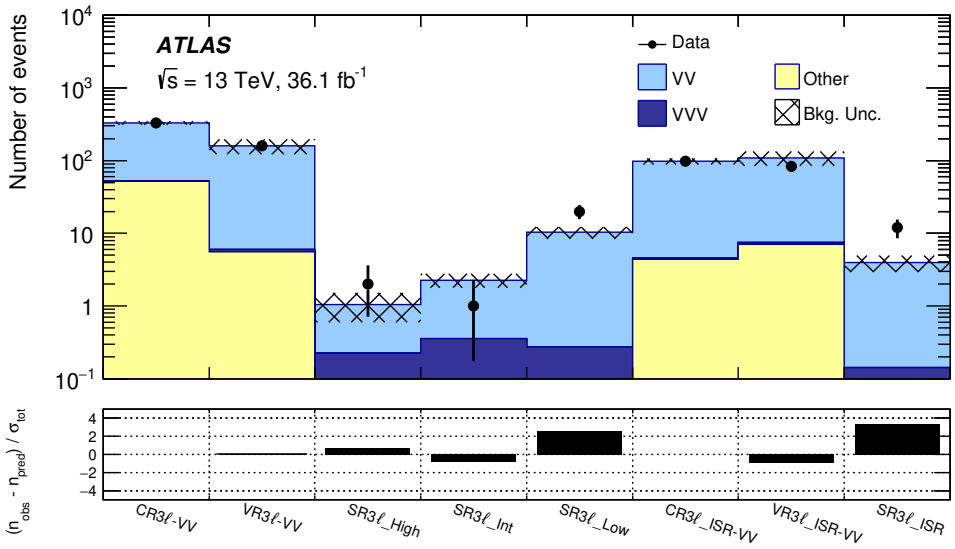

Figure 7.11: The observed and expected SM background yields in the CRs, VRs and SRs considered in the 3ℓ channel [74]. The statistical uncertainties in the background prediction are included in the uncertainty band, as well as the experimental and theoretical uncertainties. The bottom panel shows the difference in standard deviations between the observed and expected yields.

Table 7.22: Model-independent fit results for all SRs [74]. The first column shows the SRs, the second and third columns show the 95% CL upper limits on the visible cross section ($\langle\epsilon\sigma\rangle^{95}_{\text{obs}}$) and on the number of signal events (S^{95}_{obs}). The fourth column (S^{95}_{exp}) shows the 95% CL upper limit on the number of signal events, given the expected number (and $\pm 1\sigma$ excursions of the expectation) of background events. The last column indicates the discovery p_0-value and its associated significance (Z).

Signal region	$\langle\epsilon\sigma\rangle^{95}_{\text{obs}}$[fb]	S^{95}_{obs}	S^{95}_{exp}	p_0 (Z)
SR3ℓ_ISR	0.42	15.3	$6.9^{+3.1}_{-2.2}$	0.001 (3.02)
SR2ℓ_ISR	0.43	15.4	$9.7^{+3.6}_{-2.5}$	0.02 (1.99)
SR3ℓ_Low	0.53	19.1	$9.5^{+4.2}_{-1.8}$	0.016 (2.13)
SR2ℓ_Low	0.66	23.7	$16.1^{+6.3}_{-4.3}$	0.08 (1.39)
SR3ℓ_Int	0.09	3.3	$4.4^{+2.5}_{-1.5}$	0.50 (0.00)
SR2ℓ_Int	0.09	3.3	$4.6^{+2.6}_{-1.5}$	0.50 (0.00)
SR3ℓ_High	0.14	5.0	$3.9^{+2.2}_{-1.3}$	0.23 (0.73)
SR2ℓ_High	0.09	3.2	$4.0^{+2.3}_{-1.2}$	0.50 (0.00)

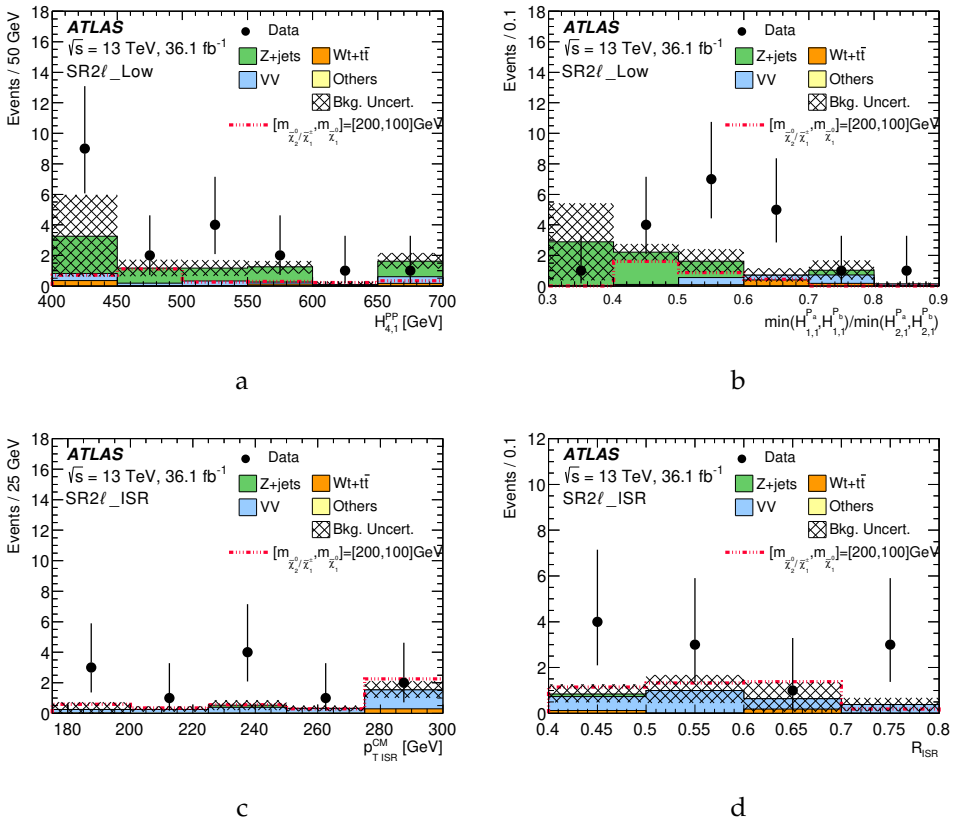

Figure 7.12: Distributions of kinematic variables in the signal regions for the 2ℓ channels after applying all selection requirements [74]. The histograms show the post-fit background predictions. The last bin includes the overflow. Distributions for (a) $H_{4,1}^{\mathrm{PP}}$ and (b) $\min(H_{1,1}^{\mathrm{P_a}}, H_{1,1}^{\mathrm{P_b}})/\min(H_{2,1}^{\mathrm{P_a}}, H_{2,1}^{\mathrm{P_b}})$ in SR2ℓ_Low, (c) $p_{\mathrm{T\,ISR}}^{\mathrm{CM}}$ and (d) R_{ISR} in SR2ℓ_ISR are plotted.

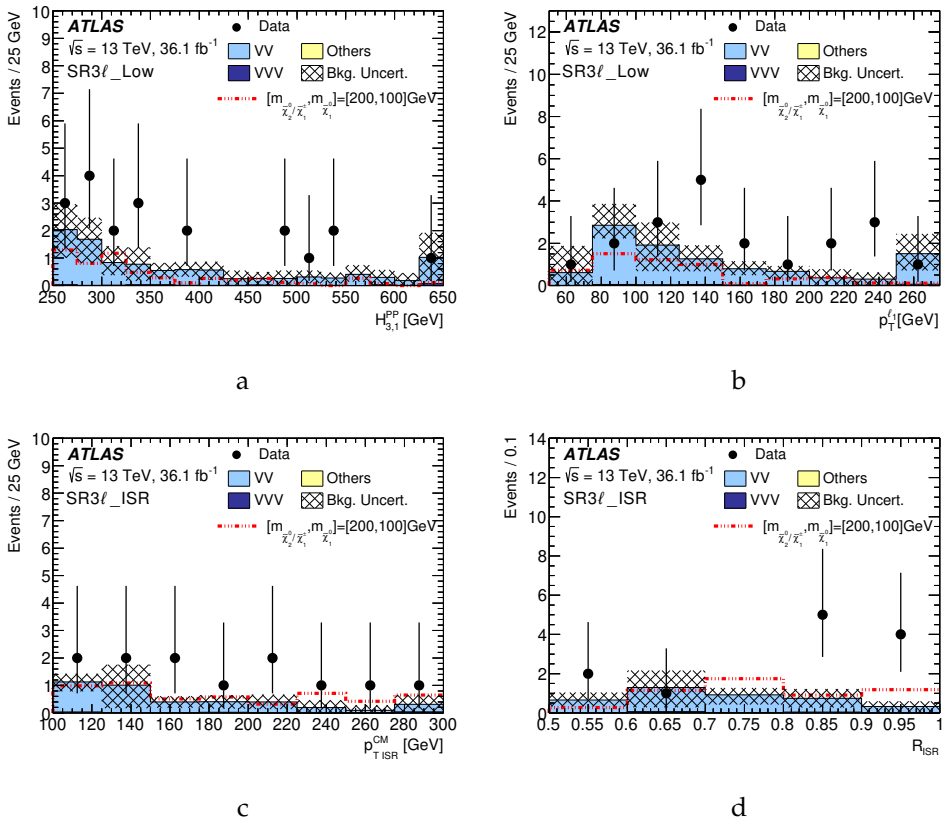

Figure 7.13: Distributions of kinematic variables in the signal regions for the 3ℓ channels after applying all selection requirements [74]. The histograms show the post-fit background predictions. The last bin includes the overflow. Distributions for (a) $H_{3,1}^{\mathrm{PP}}$ and (b) $p_{\mathrm{T}}^{\ell_1}$ in SR3ℓ_Low, (c) $p_{\mathrm{T\,ISR}}^{\mathrm{CM}}$ and (d) R_{ISR} in SR3ℓ_ISR are plotted.

7.9 Interpretation

Exclusion limits on the simplified models, where the $\tilde{\chi}_2^0 \tilde{\chi}_1^\pm$ pairs decay exclusively to W/Z bosons and $\tilde{\chi}_1^0$ are shown in Figure 7.14. The exclusions for the 2ℓ and 3ℓ channels are shown in Figure 7.14a and Figure 7.14b respectively, where the limits are obtained by selecting the SR with the highest expected sensitivity for each signal point. Here the orthogonal low mass and ISR regions are statistically combined. Figure 7.14c is the combination of both channels. This is done by statistically combining the two corresponding regions which target the same part of parameter space. For example the signal point $(m_{\tilde{\chi}_2^0/\tilde{\chi}_1^\pm}, m_{\tilde{\chi}_1^0}) = (600, 0)$ GeV will be covered by SR2ℓ_High and SR3ℓ_High, which contain mutually exclusive events. Then the combined region with the best CL_S value for each model is chosen, since the low, intermediate and high mass SRs are not explicitly orthogonal. The ISR SRs are orthogonal with the low mass SRs and so can be combined without issue. Figure 7.14d compares expected and observed exclusion limits from this analysis and the analysis described in [79], which uses a different analysis methodology but with similar expected significance in the lower mass splitting region of phase space. The exclusions in the high and intermediate mass ranges are extended from the previous analyses, with the lower mass regions ($\Delta m \simeq 100$ GeV unable to be excluded due to the excesses.

Since the low and ISR SRs are complementary for both channels it is interesting to study commonalities between low and ISR regions. For the 2ℓ this is not really feasible since there is no common variable to both the 2ℓ trees, as well as larger uncertainty on the Z+jets estimates, but m_{T}^W allows for a direct comparison between events passing the two regions with the common selection $m_{\mathrm{T}}^W > 100$ GeV. Figure 7.15 shows the "N-1" distributions, with every SR selection applied except for the variable being plotted, of SR3ℓ_Low (Figure 7.15a), SR3ℓ_ISR (Figure 7.15b), and of events entering either region (logical OR, Figure 7.15c). There is good agreement between data and backgrounds outside of the signal selection.

This analysis and that presented in [79] (hereafter referred to as the conventional analysis or CA) are uniquely placed to address some subtleties of optimising analyses on a 2D simplified model mass plane, having used the same dataset and benchmark models. The CA regions use different methodologies to tackle the 2ℓ and 3ℓ channels

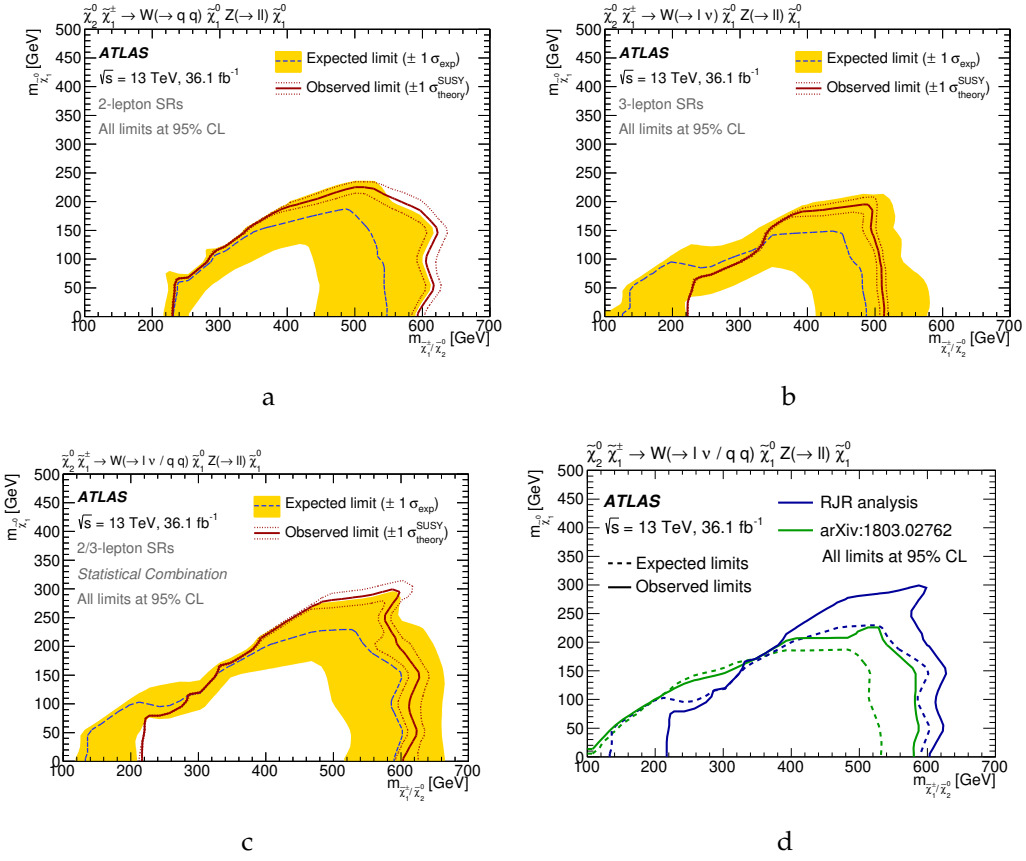

Figure 7.14: Exclusion limits at 95% CL on the masses of $\tilde{\chi}_1^{\pm}/\tilde{\chi}_2^0$ and $\tilde{\chi}_1^0$ from the analysis of 36.1 fb^{-1} of 13 TeV pp collision data obtained from the (a) 2ℓ search, (b) the 3ℓ search, (c) the statistical combination of the 2ℓ and 3ℓ search channels, assuming 100% branching ratio of the sparticles to decay to SM W/Z bosons and $\tilde{\chi}_1^0$ [74]. The dashed line and the shaded band are the expected limit and its $\pm 1\sigma$ uncertainty, respectively. The thick solid line is the observed limit for the central value of the signal cross section. The dotted lines around the observed limit illustrate the change in the observed limit as the nominal signal cross section is scaled up and down by the theoretical uncertainty and (d) comparison between the exclusion limits from this analysis and Ref. [79].

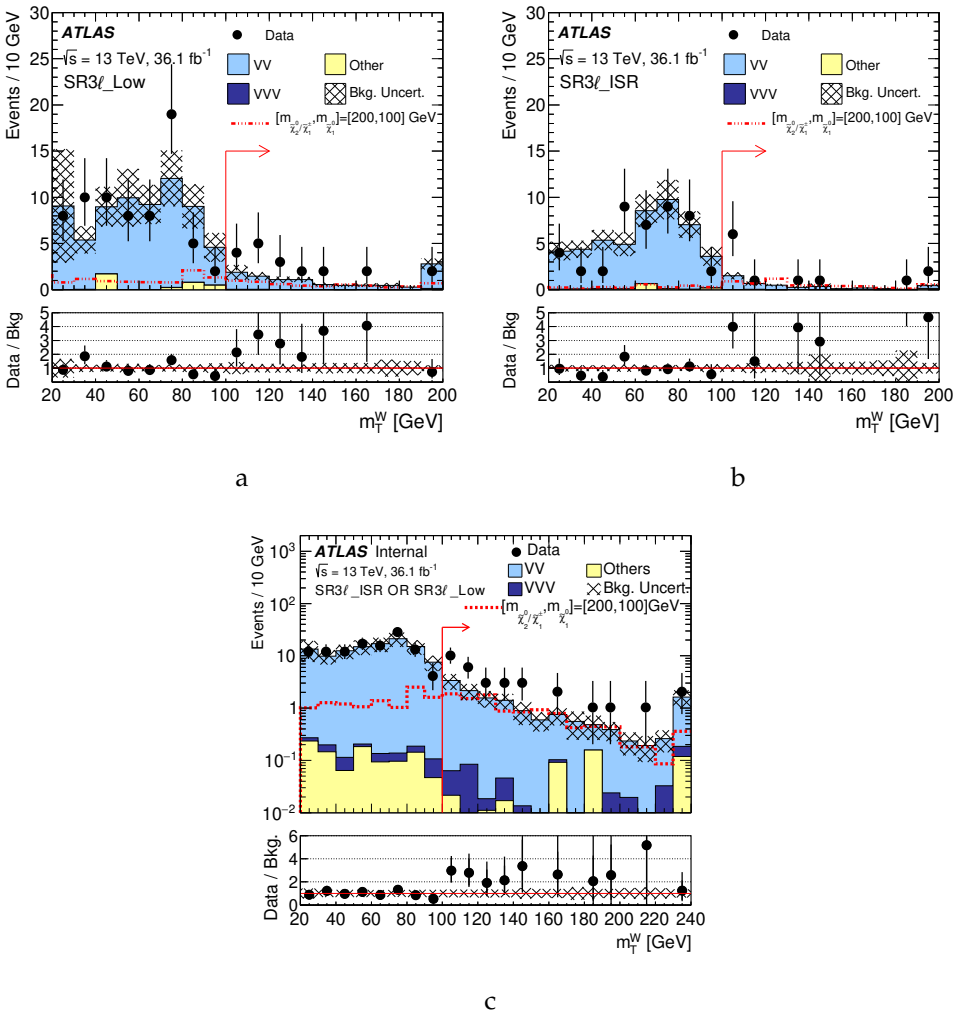

Figure 7.15: The transverse mass of the unpaired lepton for events falling in either (a) SR3ℓ_Low or (b) SR3ℓ_ISR, or (c) both regions prior to the selection placed on this variable [74]. The solid red line and arrow indicates the requirement defining these SRs. The last bin includes the overflow.

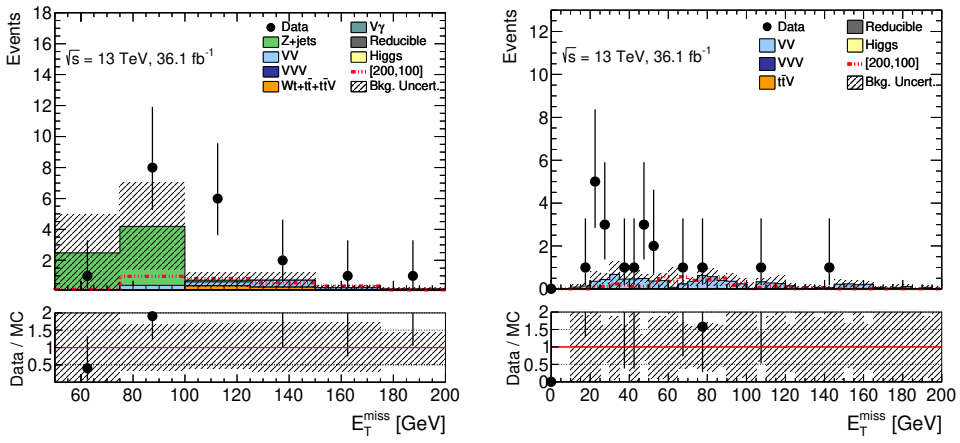

a b

Figure 7.16: The $E_{\mathrm{T}}^{\mathrm{miss}}$ distributions (a) SR2ℓ_Low and (b) SR3ℓ_Low.

but are notable for selecting on $E_{\mathrm{T}}^{\mathrm{miss}}$, at least 100 GeV for the 2ℓ channels and at least 60 GeV for the 3ℓ channels, with most regions requiring more. This is in contrast to the RJR selections which don't select on $E_{\mathrm{T}}^{\mathrm{miss}}$ in the standard trees at all and on the CM frame variable $p_{\mathrm{TI}}^{\mathrm{CM}}$ in the ISR trees. $E_{\mathrm{T}}^{\mathrm{miss}}$ does enter into the calculations of the rest frames and of the variables derived from that basis but there is no strict selection on $E_{\mathrm{T}}^{\mathrm{miss}}$ as an input variable, shown in Figure 7.16. This feature alters the type of events entering the SRs of both methods, and other selections sculpt the kinematics of the regions. For example in the CA 3ℓ channel the choice of which lepton pair is assigned to the Z is based on which same-flavour opposite-sign pair minimises m_{T}^{W}, useful for rejecting diboson backgrounds.

To quantify how complementary the SRs in the RJR and CA analyses are some overlap studies were done on data yields as well as the benchmark signal points. These are shown in Figure 7.17 and Figure 7.18 for the 2ℓ and 3ℓ regions respectively. From Figure 7.17 it is clear that the high and intermediate mass regions of both analyses target many of the same signal events, due to the lower production cross section of higher mass states. For the $(m_{\tilde{\chi}_2^0/\tilde{\chi}_1^\pm}, m_{\tilde{\chi}_1^0}) = (200, 100)$ GeV point there is around 50% overlap in the two low mass regions requiring exactly two jets, while in the data the same two regions had the only significant overlap with around 30%. The 3ℓ channel in Figure 7.18 has less overlap than the 2ℓ regions with the intermediate SR, a region with low statistics, having around 30% overlap.

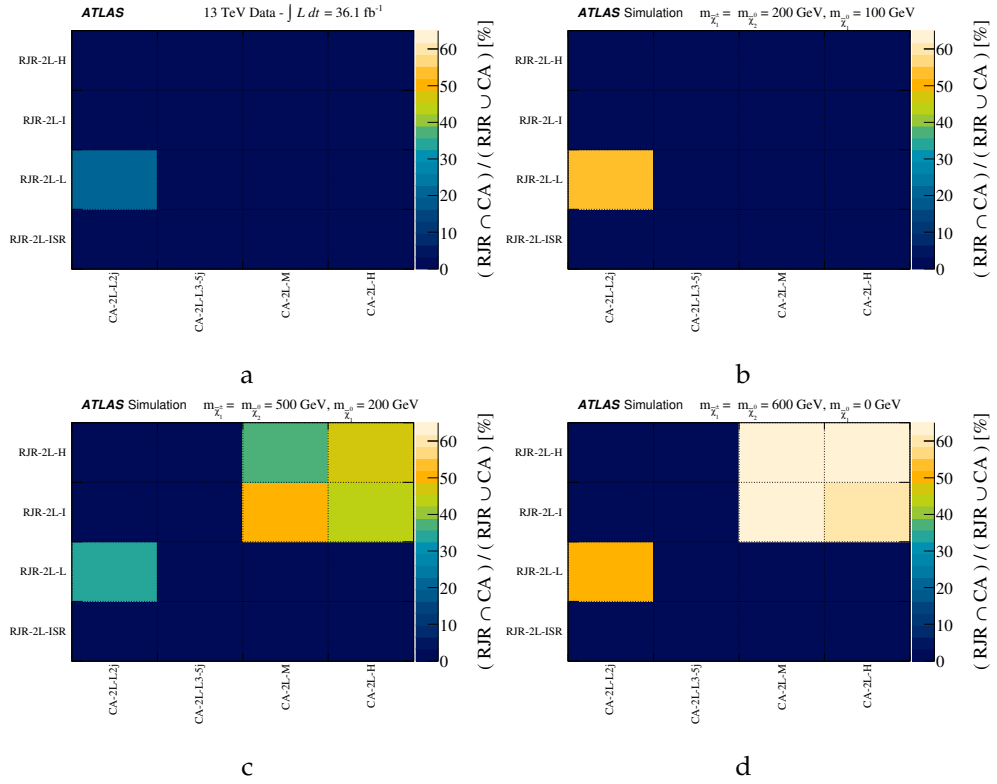

Figure 7.17: Fractional overlap in the 2ℓ channel SRs of data events (a) and signal MC events (b, c and d), selected in the RJR-based SRs and those from the CA [74]. The CA SRs are listed along the x-axis with RJR-based regions on the y-axis. The intersection events falling in each pair of regions, normalised by the union, is shown on the z-axis.

Further investigations including using alternative diboson MC, using alternative FNP estimates for the 3ℓ channel, and checking for detector or pileup related effects show no issues with the data quality or background estimation. For SR3ℓ_Low another validation region with SR-like selections except for inverted $H_{3,1}^{\mathrm{PP}}$ has good agreement with some important distributions shown in Figure 7.19. A similar VR with inverted $p_{\mathrm{T}}^{\mathrm{CM}}$ is constructed for SR3ℓ_ISR which also shows good agreement between data and the background prediction (Figure 7.20).

Another point of interest is the flavour breakdown of the leptons in the SRs, shown in Table 7.23. All regions require a same-flavour opposite-sign pair of leptons close to the Z mass, so there are two possible 2ℓ combinations and four possible 3ℓ configurations. For SR2ℓ_ISR there are more muon pairs than expected, even taking

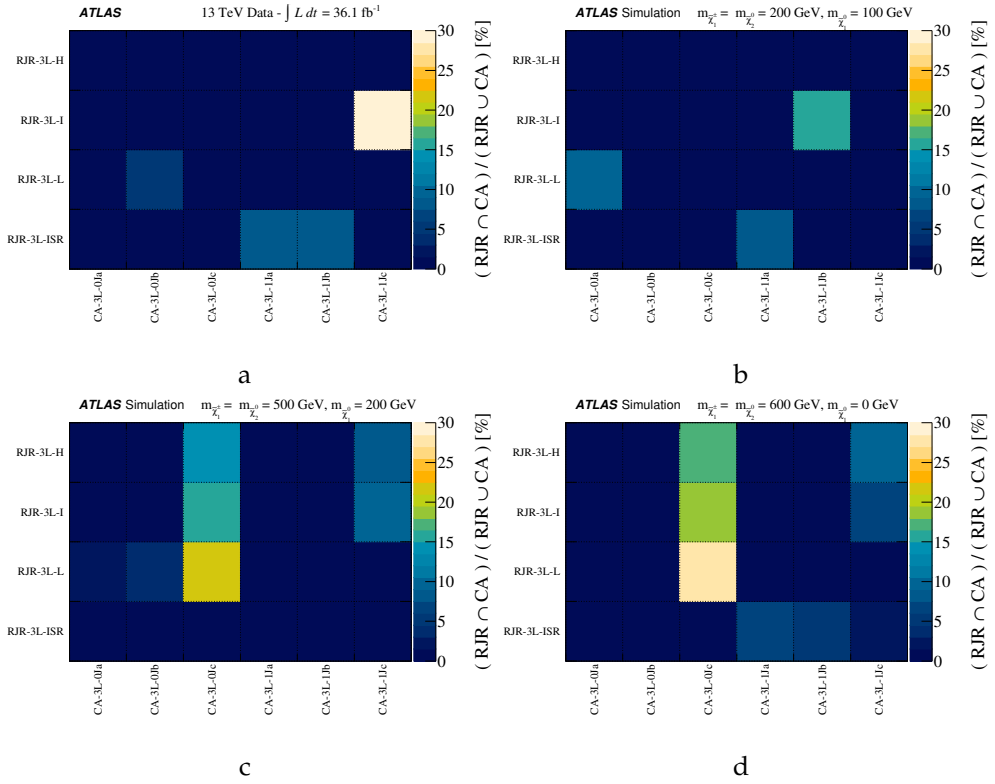

Figure 7.18: Fractional overlap in the 3ℓ channel SRs of data events (a) and signal MC events (b, c and d), selected in the RJR-based SRs and the CA SRs [74]. The CA SRs are listed along the x-axis with RJR-based regions on the y-axis. The intersection events falling in each pair of regions, normalised by the union, is shown on the z-axis.

into account the higher efficiency of muons compared to electrons. There is some evidence for this feature continuing in the 3ℓ regions with the $\mu\mu\mu$ configuration having the highest yield for both SR3ℓ_Low and SR3ℓ_ISR. The charge of these leptons can also be considered: with an opposite sign pair requirement there will an odd charge in the 3ℓ final states. For a logical OR of the low mass and ISR regions the sum of charges is shown in Figure 7.21, with the unpaired lepton being more likely to be positively charged. Adding the flavour component in, 11 being the PDG ID for electrons and 13 the PDG ID for muons, the control and validation regions have good good data/background agreement for all the unpaired leptons but both SR3ℓ_Low (Figure 7.22) and SR3ℓ_ISR (Figure 7.23) show a preference for μ^+ as the unpaired lepton.

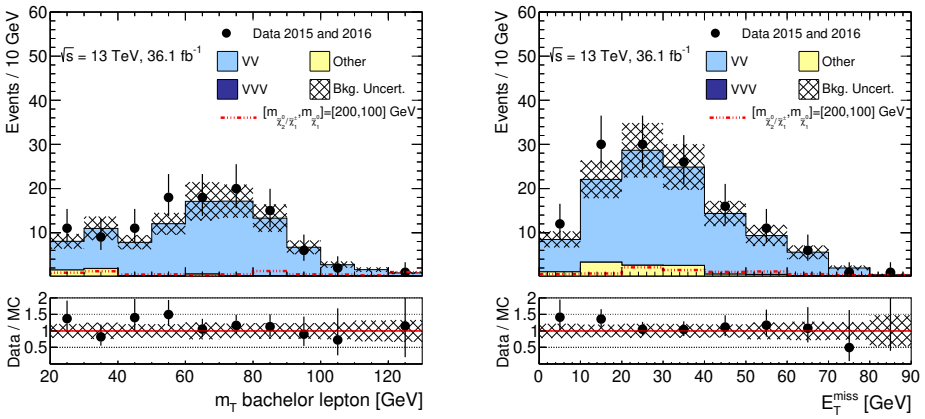

a m_T^W with an inverted $H_{3,1}^{\mathrm{PP}}$ selection. b $E_{\mathrm{T}}^{\mathrm{miss}}$ with an inverted $H_{3,1}^{\mathrm{PP}}$ selection.

Figure 7.19: Study of the $E_{\mathrm{T}}^{\mathrm{miss}}$ resolution with an inverted $H_{3,1}^{\mathrm{PP}}$ selection. The rest of the cuts defining this VR are exactly the same as in $SR3\ell$_Low.

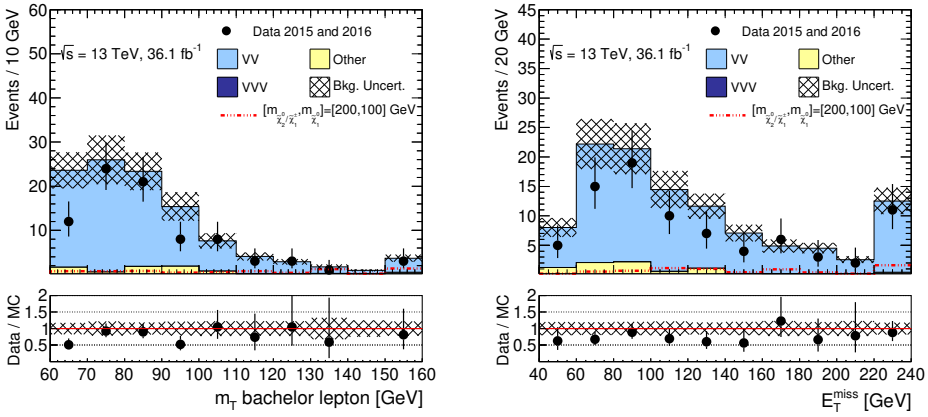

a m_T^{W} with an inverted $p_{\mathrm{T}}^{\mathrm{CM}}$ selection. b $E_{\mathrm{T}}^{\mathrm{miss}}$ with an inverted $p_{\mathrm{T}}^{\mathrm{CM}}$ selection.

Figure 7.20: Study of the $E_{\mathrm{T}}^{\mathrm{miss}}$ resolution with an inverted $p_{\mathrm{T}}^{\mathrm{CM}}$ selection. This region is kinematically similar to VR3ℓ_ISR-VV.

Table 7.23: Breakdown of the observed and expected (in parentheses) number of events in terms of flavour composition in the SRs with an excess.

Signal region	SR2ℓ_Low	SR2ℓ_ISR
ee	9 (4.5±3.9)	3 (1.2±1.2)
$\mu\mu$	10 (3.9±2.6)	8 (1.5±1.5)
Signal region	SR3ℓ_Low	SR3ℓ_ISR
eee	6 (3.5±0.7)	3 (1.1±0.3)
$ee\mu$	6 (2.0±0.4)	3 (0.9±0.3)
$\mu\mu\mu$	7 (2.7±0.6)	4 (1.5±0.4)
$\mu\mu e$	1 (1.9±0.4)	2 (0.4±0.1)

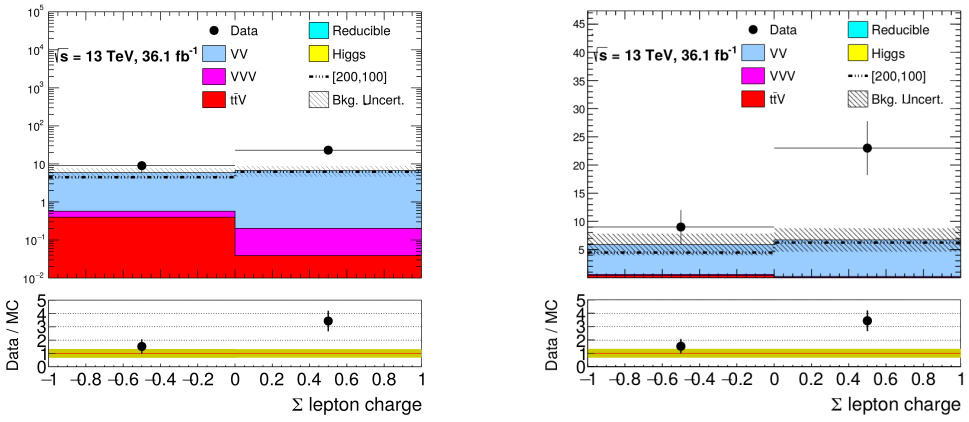

a b

Figure 7.21: The sum of the lepton charges for the three lepton signal regions for Low mass OR'ed with the compressed region. The charge of the two leptons associated with the Z cancel. This is shown both on log (a) and linear (b) scales.

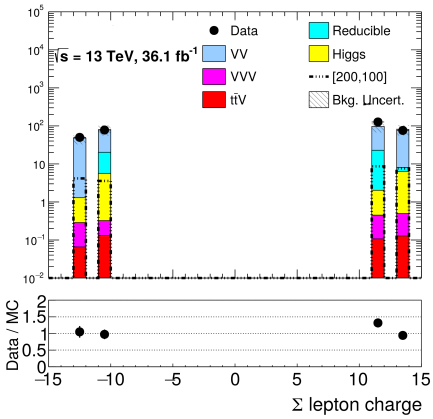

a CR3ℓ-VV lone lepton PDG ID

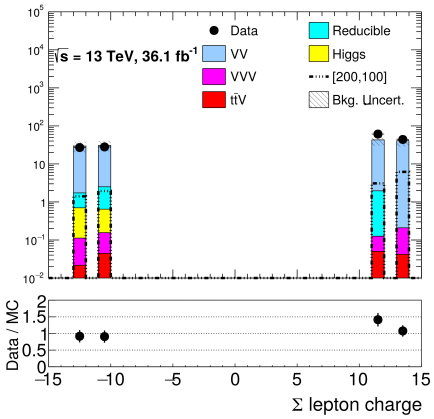

b VR3ℓ-VV lone lepton PDG ID

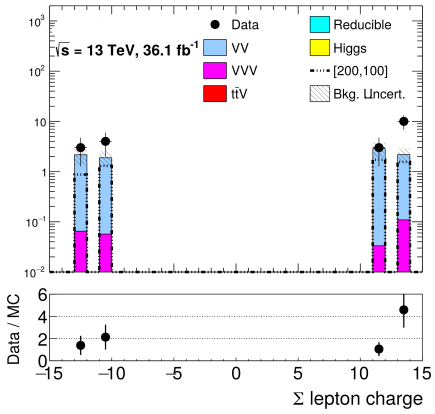

c SR3ℓ_Lowlone lepton PDG ID

Figure 7.22: The PDG ID for the lone lepton in CR3ℓ-VV, VR3ℓ-VV and SR3ℓ_Low. The charge and PDG ID of the two leptons associated with the Z cancel.

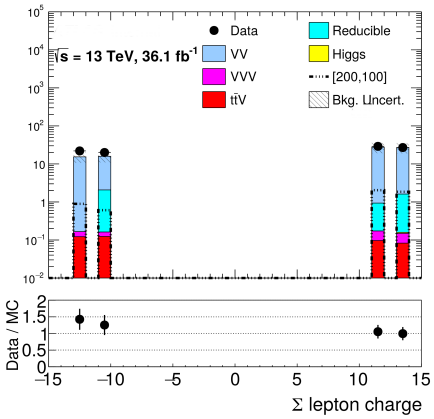

a CR3ℓ_ISR-VV lone lepton PDG ID

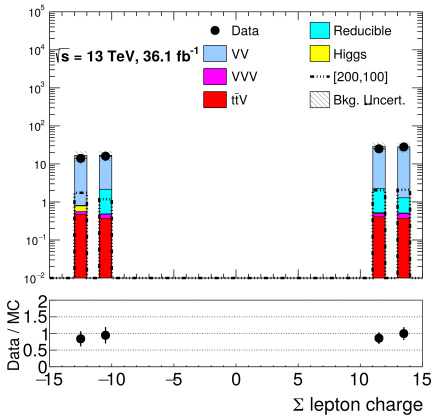

b VR3ℓ_ISR-VV lone lepton PDG ID

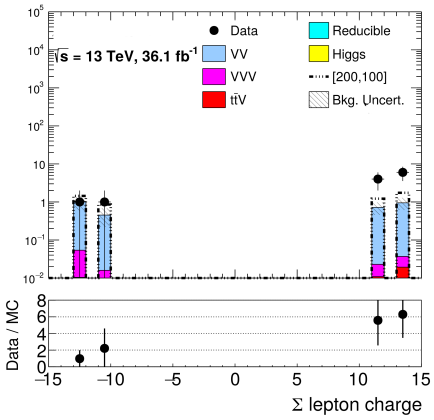

c SR3ℓ_ISRlone lepton PDG ID

Figure 7.23: The PDG ID for the lone lepton in the ISR regions. The charge and PDG ID of the leptons associated with the Z cancel.

In discussing the excesses in terms of SUSY models, it is natural to ask how closely they match any of the signal points considered in the optimisation. The four lower mass splitting regions have been optimised on the $(m_{\tilde{\chi}_2^0}, m_{\tilde{\chi}_1^\pm}) = (200,100)$ GeV point. Revisiting the distributions in Figure 7.12 and Figure 7.13 it is clear that the benchmark signal point does not describe the shape nor yield of the data. Other signal points targeting similar mass splittings also fail to match the data. This is not unexpected due to the construction of the simplified models: many fixed masses and parameters. The limitations of simplified models leads to the question "how can one use this analysis (along with others) to infer realistic electroweak SUSY parameters and models?"

7.10 GAMBIT global statistical fit on the electroweakino sector

A way forward to combine and analyse electroweak SUSY using the large number of electroweak analyses at the LHC, along with other constraints such as LEP results and electroweak decays, is using statistical fits. This section describes a detailed global fit conducted by the GAMBIT collaboration [137] using the eponymous analysis framework to derive a likely electroweakino spectrum for a scenario where they are the only light sparticles.

7.10.1 Model and fitting

The electroweakino sector of the MSSM, as outlined in 3.3.1, can be described using the parameters M_1, M_2, μ and $tan\beta$. An electroweakino EFT is constructed with the interactions between the SM fermions, gauge boson and an SM-like Higgs boson. Gauge and Yukawa couplings are fixed from data and the Higgs parameters are fixed in the same fashion, including $m_H = 125.09$ GeV. Instead of doing the calculations within the EFT it is easier to use an MSSM model where other states (squarks etc) are very heavy to allow for use of robust MSSM calculation tools. The nominal GAMBIT MSSM model has 63 parameters which are dependent on some soft SUSY

Table 7.24: Parameters, ranges and priors adopted in the scans. The "hybrid" prior is flat where $|x| < 10$GeV, and logarithmic elsewhere. All other soft SUSY-breaking parameters are decoupled.

Parameter	Minimum	Maximum	Priors
$M_1(Q)$	-2 TeV	2 TeV	hybrid, flat
$M_2(Q)$	0 TeV	2 TeV	hybrid, flat
$\mu(Q)$	-2TeV	2TeV	hybrid, flat
$\tan\beta(m_Z)$	1	70	flat
Q	3 TeV		fixed
$\alpha_s^{\overline{MS}}(m_Z)$	0.1181		fixed
Top quark pole mass	171.06GeV		fixed

breaking scale. After first setting the scale of SUSY breaking Q to be at 3 TeV, the sfermion mass matrices are taken to be diagonal and the pseudoscalar Higgs A and the gluino mass parameter M_3 have masses set to 5 TeV. In short all other sparticles are effectively decoupled from the electroweakinos. The resultant parameters are shown in Table 7.24.

This model also assumes R-parity is conserved or is broken in such a way that the LSP, a neutralino, is stable on detector lifetimes. Any parameter set that does not have a neutralino LSP is discarded.

The fitting is done using GAMBIT (Global And Modular BSM Inference Tool) [138–143] 1.2.0. Collider constraints from the LHC and LEP come from ColliderBit [139] with invisible widths being provided by DecayBit [143]. The inherit from calculations made by SpecBit [143] and sampling handled by ScannerBit [142]. The dark matter implications of parameter sets are explored using DarkBit [140]. The parameters listed in Table 7.24 can be varied beyond LHC reach and the parameter space is sampled using Diver.

A major limitation in scanning the electroweak parameter space, and for electroweak SUSY searches in general, is the granularity and number of MC events. This is due to the stricter kinematic selections required to separate signal from background. The

availability of MC after applying selections can greatly change the best sensitivity point. To remedy this issue the initial scan is done with 100 000 generated events per parameter point, and two other targeted scans with $|\mu| < 500$ GeV and $M_2 < 500$ GeV are done with 500 000 events per point. Furthermore a sequential post-processing step is done for the preferred regions of the fit. This ensures 4 million generated events for points inside the 2σ region, 16 million generated events for points within the 1σ region, and 64 million events for the 500 highest likelihood points.

7.10.2 Observables and likelihoods

The analyses considered are direct searches for charginos and neutralinos from OPAL and L3 at LEP, and ATLAS and CMS at the LHC, along with Higgs and Z invisible widths. The searches are numerous and have decays to W, Z, h and final states from all hadronic to all leptonic, including ISR boosted final states. Notably both the analysis presented earlier in the chapter and [79] (CA) are included, giving an opportunity to test how the complementary analyses fare in the parameter space. There is an possible issue with including both analyses as independent contributions to the likelihood scan, however as seen in Figure 7.17 and Figure 7.18 there are few enough events that it does not affect the results of the scan.

All the searches are added to the ColliderBit module, which implements LHC constraints by doing MC simulations of sparticle production at the 13 TeV LHC each parameter point in the scan, using PYTHIA8 [111, 144]. These events are then passed through a custom fast parameterisation of the ATLAS and CMS detectors, and analysis cuts are applied, giving the expected yield of signal events in a particular analysis. These defined Poisson likelihood terms (including statistical and systematic uncertainties) for the region with the best expected exclusion. Likelihoods for different analyses are treated as independent and are multiplied. PYTHIAleading order (LO) and leading log (LL) cross-sections are used to lessen the computing cost of event generations, something that needs to be considered in discussing the results.

Cut-flow matching for various benchmark points supplied with the original analyses provide a good avenue to validate the MC generation.The comparisons are generally good, however for certain points and final states the discrepancy can be up to 40%. As additional validation the exclusion contours for the RJR and CA are reproduced, shown in Figure 7.24. For the CMS analysis targeting similar processes [80], exclusion contours are more difficult to reproduce due to the exclusion power in these analyses coming from a combination of many bins for which covariance information has not been provided. Additionally many electroweak analyses require ISR jets to boost signal systems, something that the PYTHIAsimulations employed do not have at matrix element level. This should lead to smaller signal efficiencies for GAMBIT in these regions. Jet kinematics comparisons for chargino-neutralino pair of mass 200 GeV, similar to the benchmark points for both the RJR and CA analyses, are shown in Figure 7.25. These show that the spectra for the GAMBIT implementation are softer than in a more complete MC simulation, but the shapes are similar. These effects should pull the high likelihood points toward lower mass (higher production cross section) points.

7.10.3 Results

The first thing to examine is the exclusion power of the analyses for the electroweakinos, assuming that any excesses are purely statistical and that there is no electroweak sparticle production at the LHC. This is done using a capped likelihood

$$\mathcal{L}_{\text{cap}} = \min\left[\mathcal{L}_{\text{LHC}}(s+\boldsymbol{b}), \mathcal{L}_{\text{LHC}}(\boldsymbol{b})\right] \tag{7.2}$$

where $\mathcal{L}_{LHC}$ is the combined likelihood from all the simulated 13 TeV searches. No parameter point can achieve a likelihood higher than the background only expectation. The capping is done only on the final likelihood for all the analyses, so that the potential for multiple analyses to exclude points is retained. The profile likelihood ratio is taken with respect to the best possible value, $\mathcal{L}_{cap}/\mathcal{L}_{cap}^{max} \equiv \mathcal{L}_{cap}/\mathcal{L}_{LHC}(\mathbf{b})$ and so measures how much worse a point in the parameter space does in fitting the data than the SM. A likelihood ratio less than 1 means the SM fits the data better than the SUSY point, while greater than 1 indicates that the parameter point is doing better than the SM. To get 1 either no analyses are sensitive ($\mathbf{s} = 0$) or the sensitivity

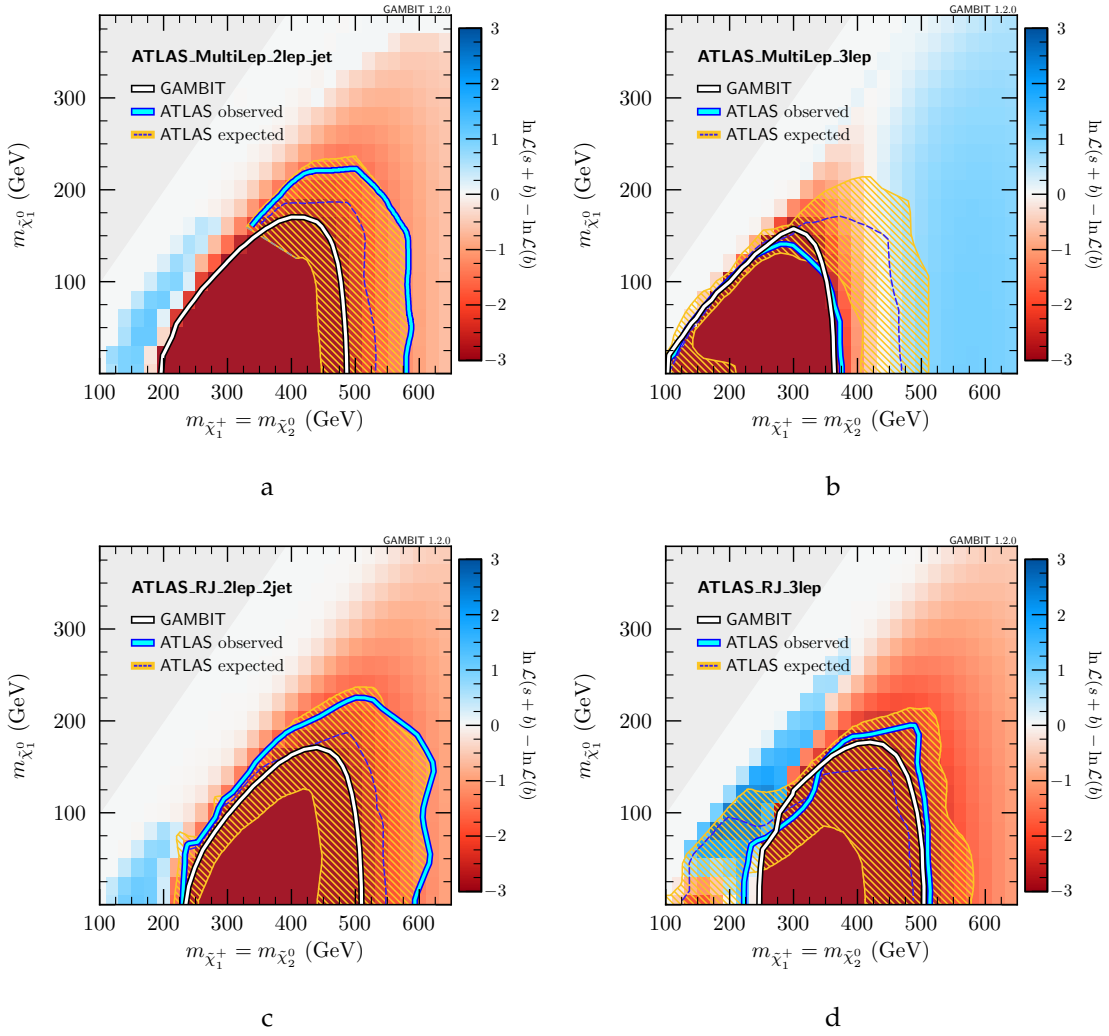

Figure 7.24: GAMBIT reproductions of 95% CL ATLAS exclusion limits for a simplified model of wino production. CA and the recursive jigsaw analysis are shown in the top and bottom rows, respectively. In both cases results are given separately for 2-lepton (left) and 3-lepton (right) signal regions. The ATLAS observed (light blue) and expected (dashed, dark blue) limits, along with the $\pm 1\sigma$ uncertainty band (hatched, yellow) on the expected limit, are obtained from the published auxiliary materials. The underlying heatmap depicts the full log-likelihood function obtained from the GAMBIT simulations.

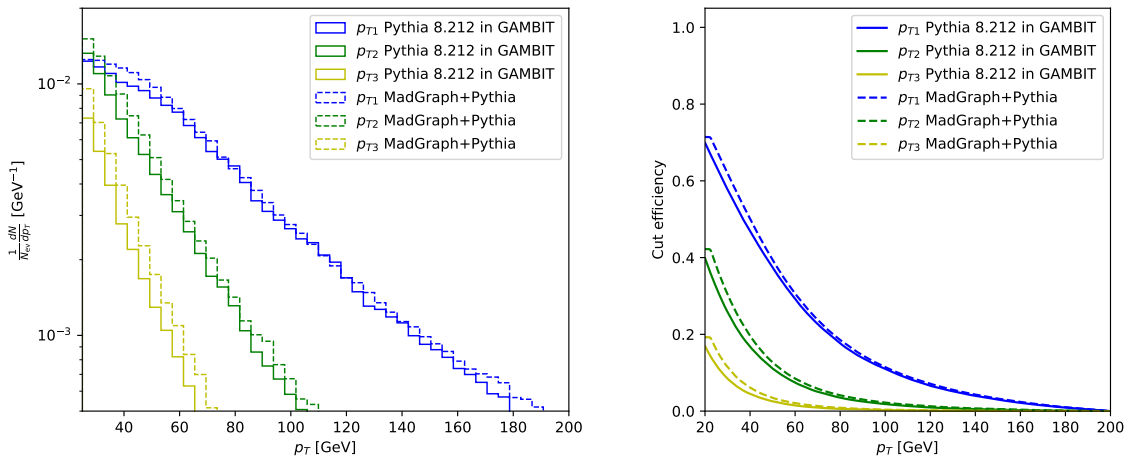

a b

Figure 7.25: p_{T} distributions (a) for the three hardest jets in a benchmark model with production of chargino–neutralino pairs with $m_{\tilde{\chi}_2^0,\tilde{\chi}_1^\pm} = 200$ GeV, as well as the corresponding cut-efficiencies (b).

of multiple analyses have cancelled out. The profile likelihood ratio for the $\tilde{\chi}_1^\pm$-$\tilde{\chi}_1^0$ plane is shown in Figure 7.26, indicating that there is no significant constraint on the electroweakino masses. This is reconciled with the experimental results by noting that experimental searches use idealised simplified models and that the full electroweakino sector has features which can certainly explain this lack of exclusion. For instance if $\tilde{\chi}_2^0/\tilde{\chi}_2^\pm$ pairs are not wino dominated the the production cross section is lower than pure wino. It is also noted that due to computing constraints the scan resulting in Equation 7.2 includes points with 500 000 events generated instead of the 4 million for other results in this analysis. The result is therefore a conservative estimate of the constraining power of the combined analyses.

Now a full uncapped likelihood with the possibility of sparticle production and detection is considered.

The profile likelihoods in various electroweak mass planes are shown in Figure 7.27. There is a preference in $(m_{\tilde{\chi}_1^\pm}, m_{\tilde{\chi}_1^0})$ (Figure 7.27a) for lower masses and mass splittings of 100 GeV, with the best fit point being $m_{\tilde{\chi}_1^\pm} \approx 100$ GeV and $m_{\tilde{\chi}_1^0} \approx 50$ GeV. In general

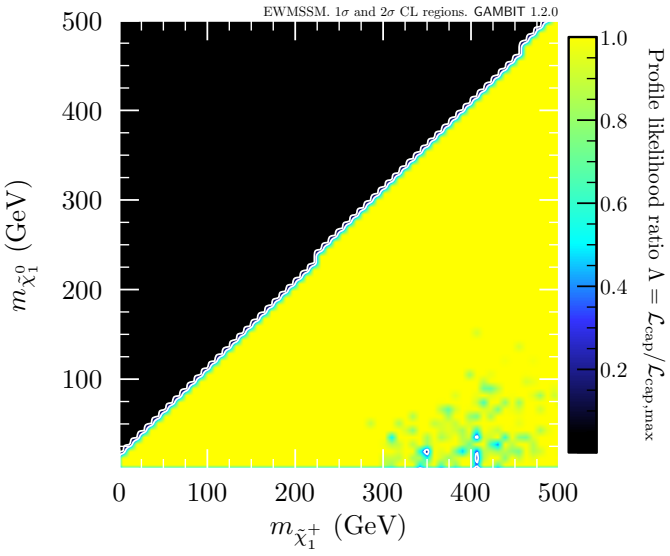

Figure 7.26: Capped profile likelihood in the $(m_{\tilde{\chi}_1^\pm}, m_{\tilde{\chi}_1^0})$ plane. The capped likelihood function Equation 7.2 is based solely on the joint likelihood for the 13 TeV LHC direct SUSY searches. The contour lines show the 1σ and 2σ confidence regions.

the masses for this plane are preferred to be lower than 300 GeV. This is driven by the excesses in the analysis described in this chapter and some other small excesses from CMS. The larger mass splitting indicates a predominantly bino LSP.

Figure 7.27b shows that $m_{\tilde{\chi}_1^\pm} \approx m_{\tilde{\chi}_2^0}$ which indicates that they are composed of Higgsinos, winos or some combination thereof. Again there is a preference for masses below 300 GeV at 2σ.

In Figure 7.27c the $(m_{\tilde{\chi}_2^0}, m_{\tilde{\chi}_3^0})$ plane again has $m_{\tilde{\chi}_2^0}$ <300 GeV and $m_{\tilde{\chi}_3^0}$ <700 GeV. The mass splitting range shows a wider spread of $\tilde{\chi}_3^0$ masses for $m_{\tilde{\chi}_2^0}$ <300 GeV. The position of the best fit point suggests that the winos are lighter than the Higgsinos, and the opposite scenario with lighter Higgsinos has points within the 1σ range for higher $m_{\tilde{\chi}_2^0}$.

Finally Figure 7.27d shows the heaviest neutralinos $\tilde{\chi}_3^0$ and $\tilde{\chi}_4^0$ which are 2σ bounded less than 700 GeV. The likelihood flattens out beyond the 2σ point so heavier electroweakinos are not constrained by current LHC results, but the best fit points remain light. $\tilde{\chi}_2^\pm$ is near degenerate in mass with $\tilde{\chi}_4^0$ for the entire 2σ contour.

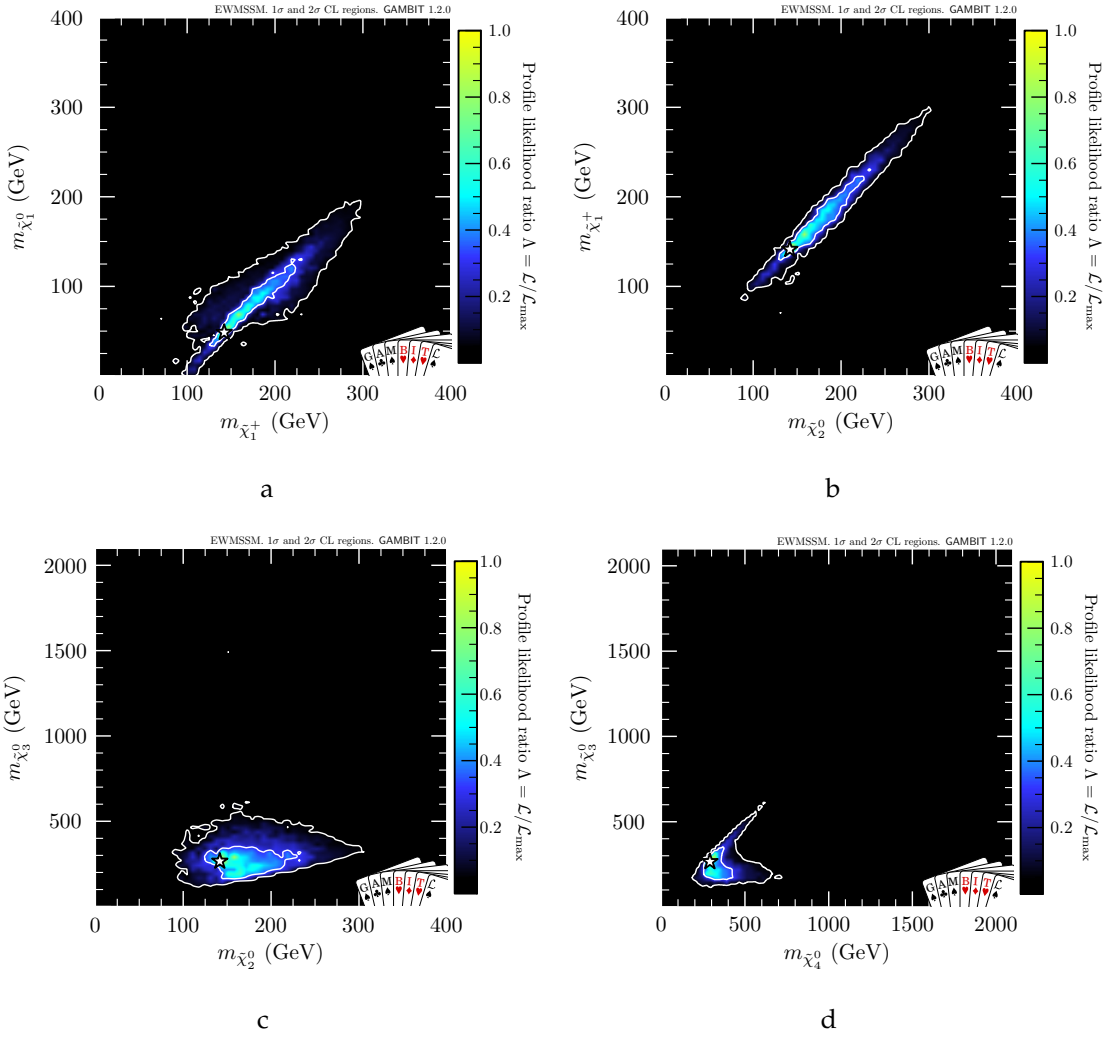

Figure 7.27: Profile likelihood in the $(m_{\tilde{\chi}_1^\pm}, m_{\tilde{\chi}_1^0})$ plane (a), the $(m_{\tilde{\chi}_2^0}, m_{\tilde{\chi}_1^\pm})$ plane (b), the $(m_{\tilde{\chi}_2^0}, m_{\tilde{\chi}_3^0})$ plane (c) and the $(m_{\tilde{\chi}_4^0}, m_{\tilde{\chi}_3^0})$ plane (d). The contour lines show the 1σ and 2σ confidence regions. The best-fit point is marked by the white star.

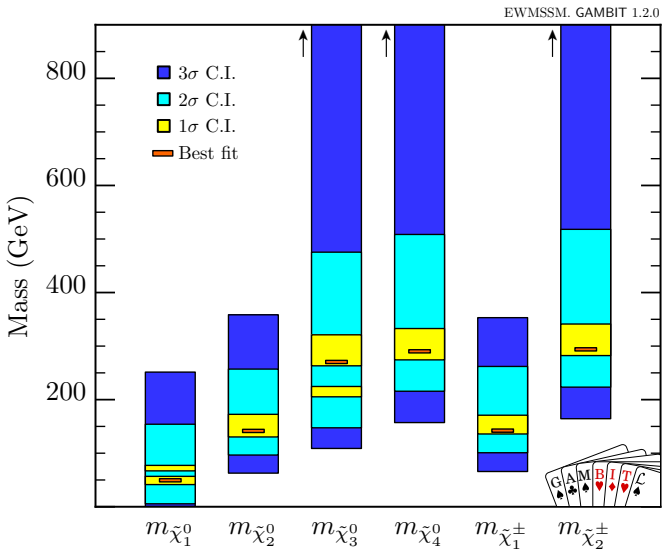

Figure 7.28: Summary of the one-dimensional 1σ, 2σ and 3σ confidence intervals for the neutralino and chargino masses. The orange lines mark the best-fit values. For $m_{\tilde{\chi}_3^0}$, $m_{\tilde{\chi}_4^0}$ and $m_{\tilde{\chi}_2^\pm}$, the 3σ confidence intervals extend up to the 2 TeV upper limit on the mass parameters in our scan.

The best fit points for the electroweakino masses are shown in Figure 7.28, where the 1, 2, and 3σ bands for each mass. The 3σ band is spans the entire parameter range for the higher mass electroweakinos.

The most likely mass points to a preference for mass splitting between the NLSP and LSP of around 100 GeV, exactly where the RJR and CA both had dedicated signal regions. Moreover, the production cross section dictates that the masses are relatively light. In terms of mass parameters Figure 7.29 shows the profile likelihoods of the bino (Figures 7.29a, 7.29d, 7.29g and 7.29j), wino (Figures 7.29b, 7.29e, 7.29h and 7.29k), and Higgsino (Figures 7.29b, 7.29e, 7.29h and 7.29k) content of the neutralinos plotted against the mass of that neutralino. The LSP is shown to be mostly bino, with more Higgsino allowed for the remainder compared to wino. For $\tilde{\chi}_2^0$ and $\tilde{\chi}_4^0$ there is no real preference between wino and Higgsino with best fit points preferring bino for the former and Higgsino for the latter. $\tilde{\chi}_3^0$ is mostly Higgsino. The charginos are not shown as there is no preference for any particular composistion, which is consistent with the observation that any wino-Higgsino mixture is allowed

for the $\tilde{\chi}_2^0$ and the $\tilde{\chi}_2^0$ and $\tilde{\chi}_1^\pm$ are basically mass degenerate.

Returning to the topic of excesses seen in the RJR compared to the CA, the relative contributions of the various analyses to the overall likelihood can be examined. This is interesting to reconcile the analyses with excesses with others with null results. While the focus will be on the RJR and the CA, it is important to note that the ATLAS four lepton analysis [145] which largely focuses on RPV scenarios and only considers gravitino LSPs in RPC models, also sees some local excesses (the largest being 2.3σ) and favours signals. Aside from the RJR, CA and ATLAS four lepton, other analyses generally do not have a large effect on the likelihood. Looking at the four individual channels in the RJR and CA for the $\tilde{\chi}_1^\pm$-$\tilde{\chi}_1^0$ plane in Figure 7.30, the z-axis represents the contribution to the likelihood: red being negative and blue positive. The CA 2ℓ+jets regions (Figure 7.30a) have a weak positive contribution for mass splittings slightly greater than 100 GeV, matched somewhat by the RJR regions in Figure 7.30c. The 3ℓ regions, CA in Figure 7.30b has some positive regions and other negative regions, with the best fit point being very close to the boundary between the regions. The RJR 3ℓ (Figure 7.30d) has a rather strong positive contribution, especially near the best fit point.

Furthermore examining the more massive neutralinos in addition to those present in the simplified model used for optimisation and exclusion in the input analyses (Figure 7.31), a preference for lower mass $\tilde{\chi}_3^0$ and $\tilde{\chi}_4^0$ is seen. This indicates that other light neutralinos can have an effect on evading limits set with simplified models. Models near the best fit point have $\tilde{\chi}_3^0$, $\tilde{\chi}_4^0$ and $\tilde{\chi}_2^\pm$ production alongside the lighter particles, with additional gauge bosons in the decay chains. Some example decays include:

- $\tilde{\chi}_2^0\,\tilde{\chi}_3^0$ production with decays
  $\tilde{\chi}_2^0 \to Z + \tilde{\chi}_1^0, \tilde{\chi}_3^0 \to W^\mp + \tilde{\chi}_1^\pm \to W^\mp + W^\pm + \tilde{\chi}_1^0$

- $\tilde{\chi}_2^\pm\tilde{\chi}_2^\mp$ production, with decays
  $\tilde{\chi}_2^\pm \to W^\pm + \tilde{\chi}_2^0 \to W^\pm + Z + \tilde{\chi}_1^0$

- ...

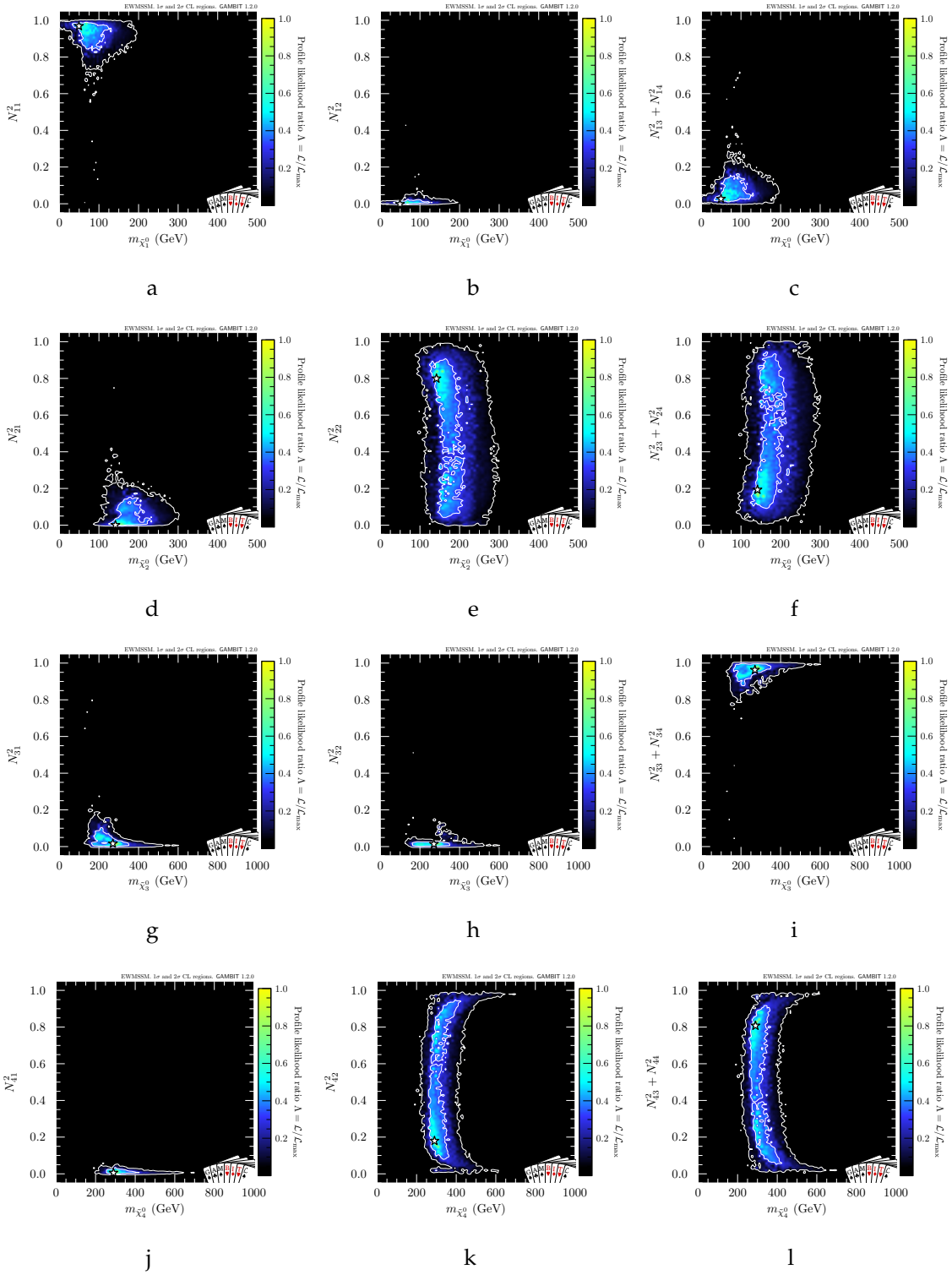

Figure 7.29: Profile likelihood of the bino (left), wino (middle) and Higgsino (right) content of the four neutralinos (starting from the lightest in the top row), plotted against the mass of the respective neutralino. Contour lines show the 1σ and 2σ confidence regions. The best-fit point is marked by the white star.

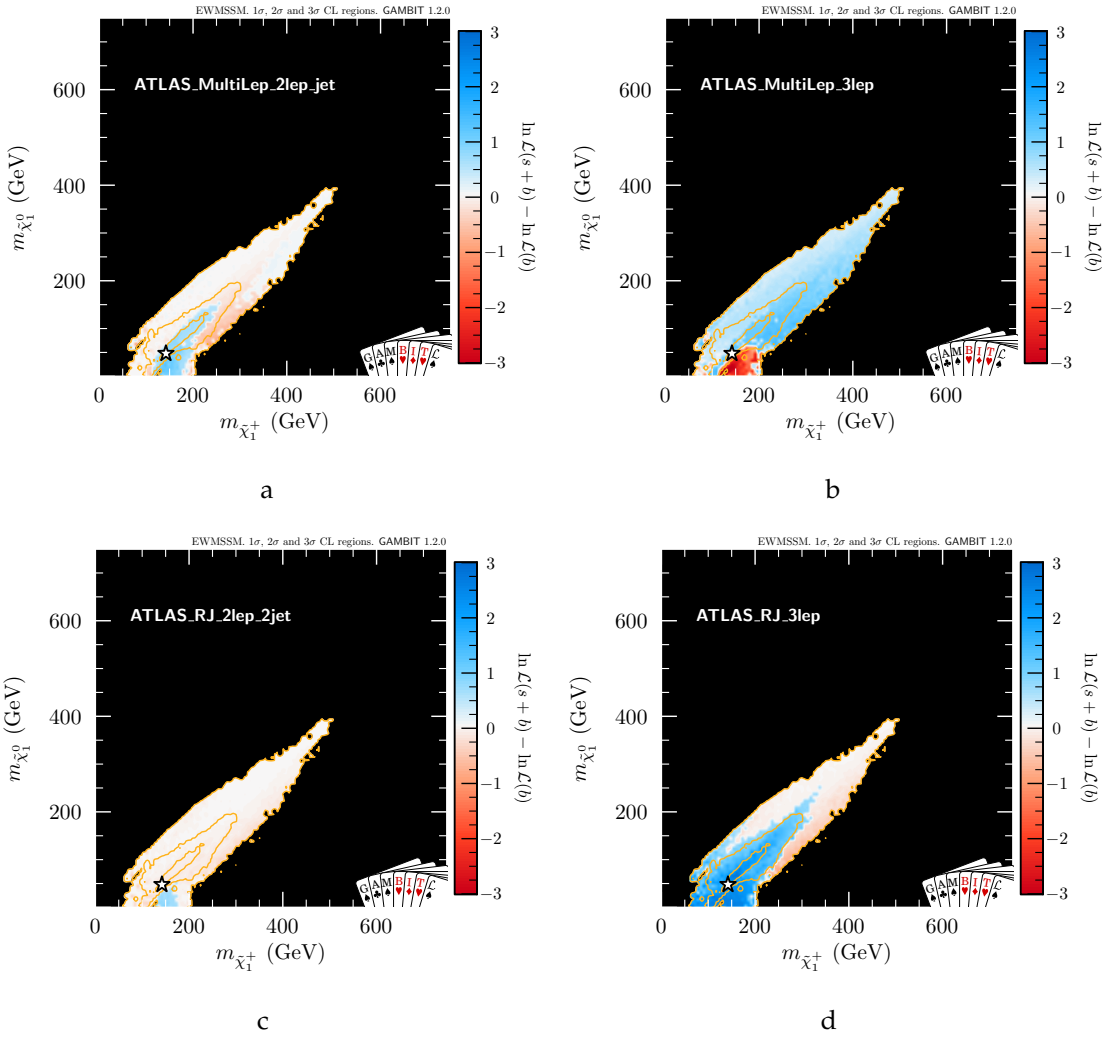

Figure 7.30: The 1σ, 2σ and 3σ regions (orange lines) preferred by CA and RJR analyses in the $(m_{\tilde{\chi}_1^0}, m_{\tilde{\chi}_1^\pm})$ plane. For each of the twelve panels, the colours (where present) show the contribution to the total log-likelihood from a different search (white text). Blue indicates that the signal improves the fit to that search and red that it worsens it.

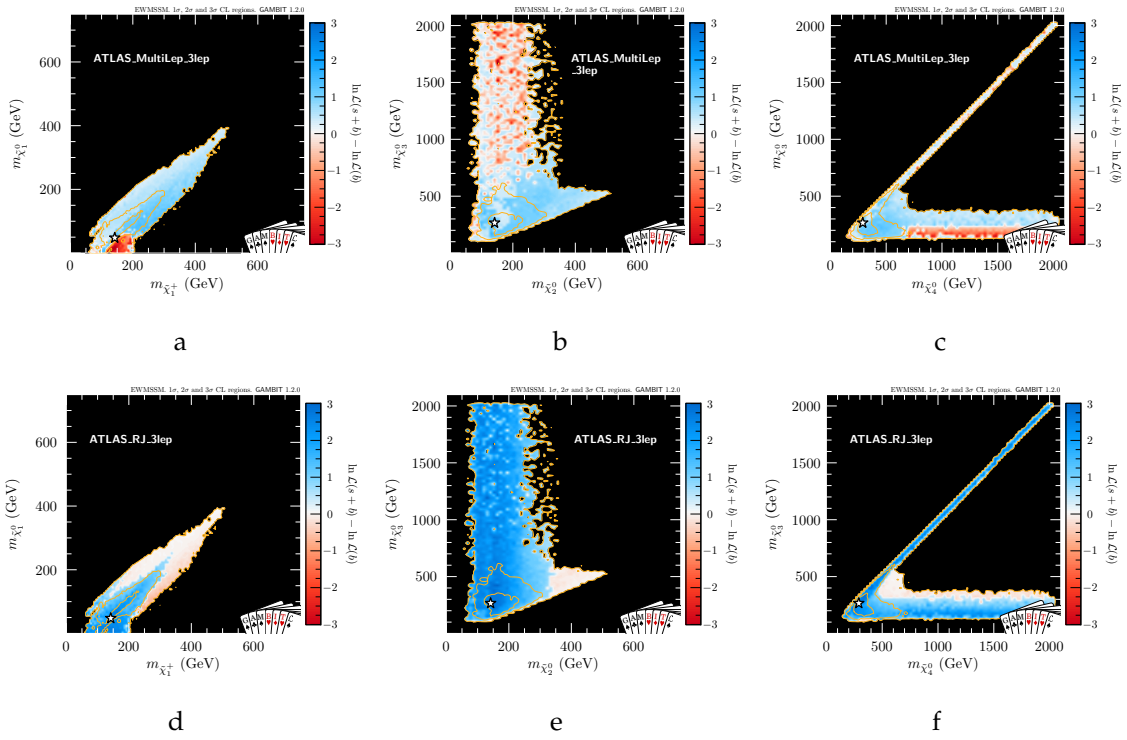

Figure 7.31: The 1σ, 2σ and 3σ regions (orange lines) preferred by the combination of searches in the $\tilde{\chi}_1^{\pm}$ versus $\tilde{\chi}_1^0$ (left), $\tilde{\chi}_2^0$ versus $\tilde{\chi}_3^0$ (middle) and $\tilde{\chi}_4^0$ versus $\tilde{\chi}_3^0$ (right) mass planes. The colours (where present) show the contribution to the total log-likelihood from the 3ℓ CA (first row), and 3ℓ RJR (second row) searches. Blue indicates that the signal improves the fit to that search and red that it worsens the fit.

These decays often satisfy the object selection criteria of two/three leptons and can also have considerable jet activity, but in general will not fit into decay tree structures defined with RJR. Four interesting points, including the best fit point and others with heavier winos or electroweakino masses, as well as the point with the best collider and dark matter likelihood, are shown in Table 7.25. The best fit point has $\tilde{\chi}_1^0$ mass of around 50 GeV and near degenerate $\tilde{\chi}_2^0/\tilde{\chi}_1^{\pm}$ mass of near 142 GeV.

The best fit point is used to generate signal MC for injection into the replicated analyses to see if it matches the data in the RJR regions. For the 2ℓ regions (Figure 7.32) the signal does not particularly match the data distribution shown, especially for the SR2ℓ_Low variable $\frac{\min(H_{1,1}^{\mathrm{Pa}}, H_{1,1}^{\mathrm{Pb}})}{\min(H_{2,1}^{\mathrm{Pa}}, H_{2,1}^{\mathrm{Pb}})}$ (Figure 7.32b). The SR2ℓ_ISR yields match more

Table 7.25: Parameter values and sparticle masses for a variety of benchmark points. Point #1 is the best-fit model, for which the Higgsinos are heavier than the winos. Point #2 is a solution with the winos heavier than the Higgsinos with similar likelihood. Point #3 is the point within the 1σ region with the highest LSP mass. Point #4 has the best combined DM and collider likelihood.

Parameter	#1 Best fit	#2 Heavy winos	#3 Highest mass	#4 DM
$M_1(Q)$	-50.6 GeV	-79.2 GeV	133.4 GeV	-45.6 GeV
$M_2(Q)$	149.3 GeV	263.0 GeV	243.5 GeV	143.7 GeV
$\mu(Q)$	252.7 GeV	-187.3 GeV	-293.2 GeV	260.8 GeV
$\tan\beta(m_Z)$	28.7	40.4	41.5	16.4
$m_{\tilde{\chi}_1^0}$	-49.4 GeV	-73.9 GeV	129.4 GeV	-45.1 GeV
$m_{\tilde{\chi}_2^0}$	141.6 GeV	165.7 GeV	230.6 GeV	136.5 GeV
$m_{\tilde{\chi}_3^0}$	-270.3 GeV	-208.5 GeV	-308.8 GeV	-277.8 GeV
$m_{\tilde{\chi}_4^0}$	290.2 GeV	292.6 GeV	344.6 GeV	297.2 GeV
$m_{\tilde{\chi}_1^\pm}$	142.1 GeV	168.7 GeV	230.2 GeV	136.8 GeV
$m_{\tilde{\chi}_2^\pm}$	293.9 GeV	294.2 GeV	345.8 GeV	300.5 GeV
Collider log-likelihood	10.8	10.3	9.7	10.4

closely with the caveat that the ISR jet treatment in GAMBIT has higher uncertainties. The 3ℓ regions are similar, with $H_{1,1}^{\mathrm{P_b}}/H_{2,1}^{\mathrm{P_b}}$ (Figure 7.33c) not matching in SR3ℓ_Low and R_{ISR} (Figure 7.33e) peaking at higher values in data for SR3ℓ_ISR. So, while the highest likelihood point gives a compelling mass profile, the kinematic behaviour does not match the data. Some part of this must come from fast treatment of the signal event generation and will benefit from a more careful full simulation with full parton showering and complete detector simulation.

The GAMBIT treatment of the two $2/3\ell$ analyses shows that there is much to be gained from implementing a program of varied analyses in searching for electroweak SUSY. These global fits summarise the state of the art in searches for electroweak SUSY with only a quarter of the data integrated in LHC Run 2, with analyses with the full dataset being completed in the period between Run 2 and Run 3. The follow-up to the RJR $2/3\ell$ analysis is one such analysis.

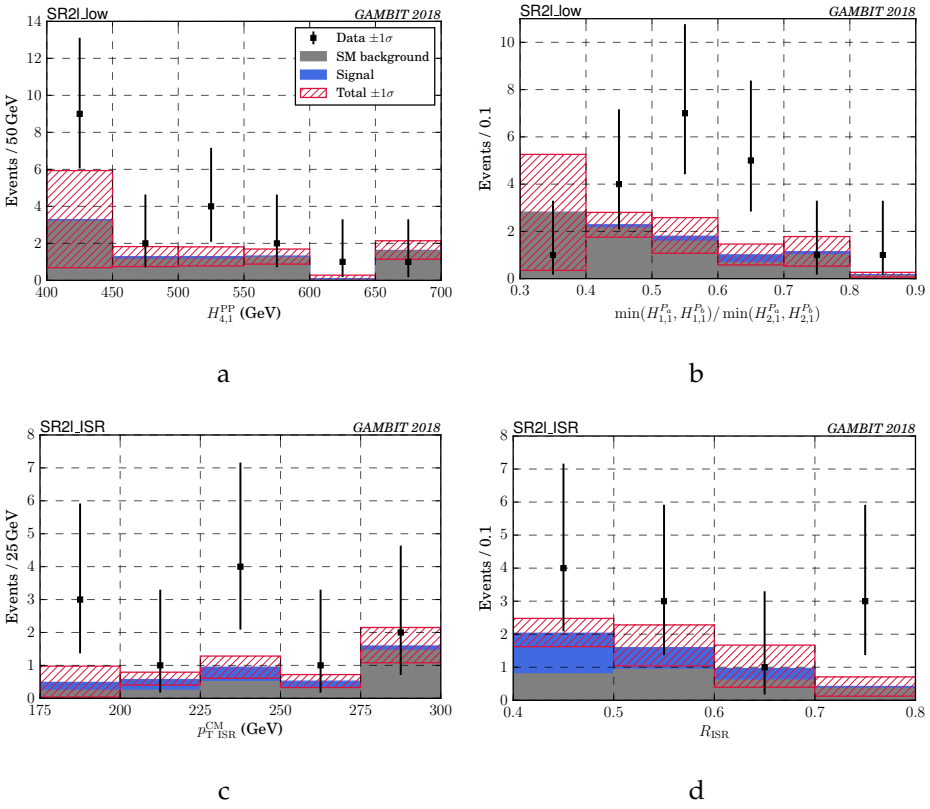

Figure 7.32: Distribution of kinematic variables in the 2 lepton signal regions for the ATLAS RJ analysis, after applying all selection requirements. The grey bars show the total SM background and the stacked blue bars show the signal for the best-fit point. The hatched red bands show the 1σ uncertainty on the total number of expected events, found by summing in quadrature the background uncertainty and the signal statistical uncertainty for the best-fit point. The black points show the ATLAS data.

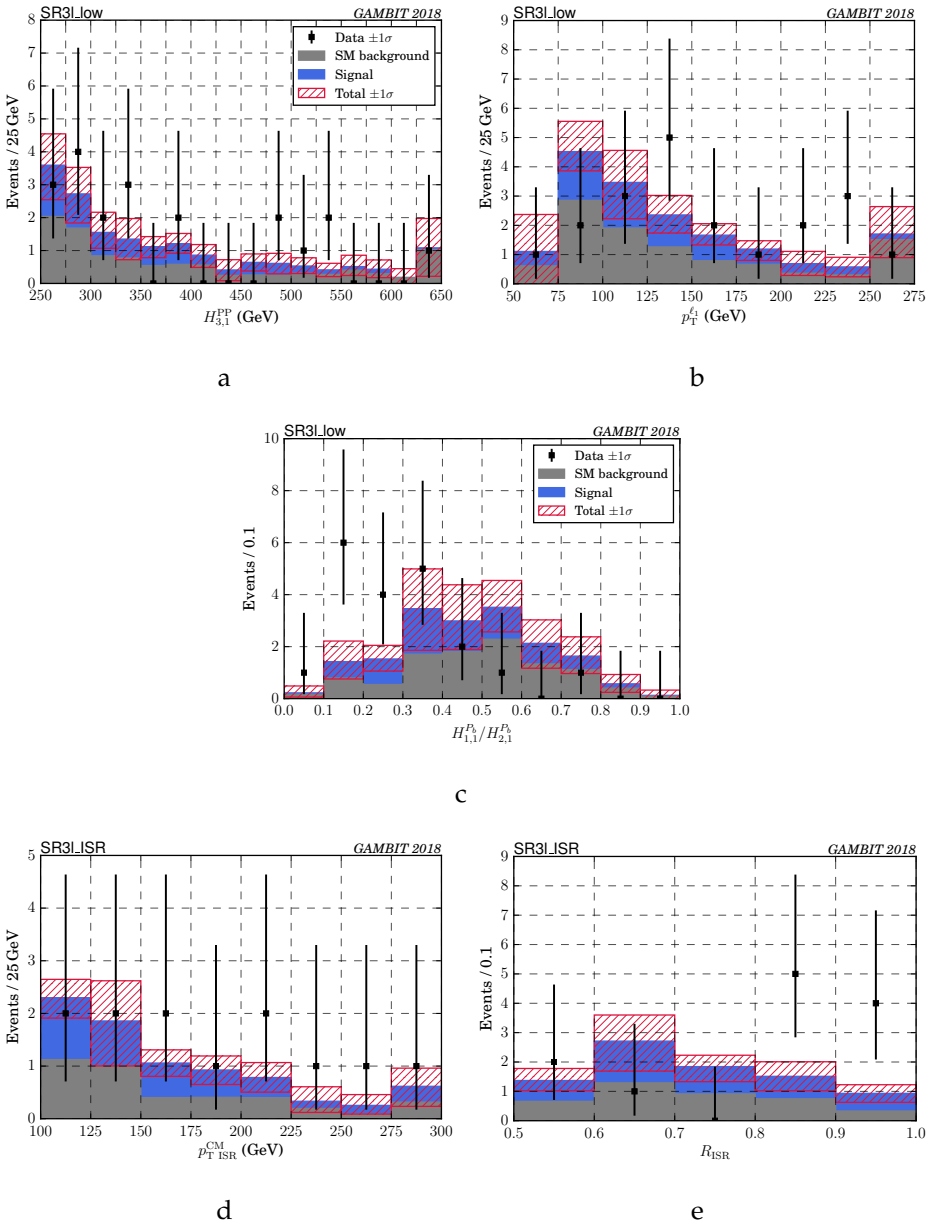

Figure 7.33: Distribution of kinematic variables in the 3 lepton signal regions for the ATLAS RJ analysis, after applying all selection requirements. The grey bars show the total SM background and the stacked blue bars show the signal for the best-fit point. The hatched red bands show the 1σ uncertainty on the total number of expected events, found by summing in quadrature the background uncertainty and the signal statistical uncertainty for the best-fit point. The black points show the ATLAS data.

8 Electroweakino follow-up with full Run 2 data

This chapter describes the follow-up to the RJR $2/3\ell$ analysis presented in Chapter 7, where the focus is on the four regions, SR2ℓ_Low, SR2ℓ_ISR, SR3ℓ_Low, and SR3ℓ_ISR, targeting low mass splittings. To summarise:

- There were a set of excesses in SR3ℓ_ISR (3.0σ), SR3ℓ_Low (2.1σ), SR2ℓ_ISR (2.0σ), and SR2ℓ_Low (1.4σ).
- The 2ℓ signal regions were heavily affected by the systematics on the photon template Z+jets estimation.
- The data distributions and yields did not match the simplified model signal.

Naturally, continuing this analysis with the full Run 2 ATLAS dataset is important to see whether the excesses grow with more integrated luminosity. The signal model used previously is also not considered: instead only model-independent exclusions are calculated.

8.1 Analysis overview and region definitions

The analysis proceeds in a very similar fashion to that presented in Chapter 7, with some changes in the background estimation method for Z+jets in the 2ℓ channel and the definitions of CR3ℓ-VV and VR3ℓ-VV. The definitions of objects recommended for use in physics analysis have also changed from the previous analysis, and so validation of these is outlined in Section 8.4.

In terms of background estimation techniques the only change has come from the Z+jets estimation changing from the photon template to using an ABCD method for deriving the expected yields in the two SRs directly from data. This is to reduce the systematic uncertainties associated with the photon template method at low $E_{\mathrm{T}}^{\mathrm{miss}}$ and $p_{\mathrm{T}}^{\ell\ell}$ which lead to reduced sensitivity in the previous analysis. The ABCD method uses two (largely) uncorrelated variables used in the SR to define regions where the expected number of Z+jets events can be extracted, which is then propagated into the SR itself to obtain an expected value there. For SR2ℓ_Low the ABCD variables are m_{jj} and $\frac{H_{1,1}^{\mathrm{PP}}}{H_{4,1}^{\mathrm{PP}}}$, and for SR2$\ell$_ISR the two variables are m_J and $p_{\mathrm{TI}}^{\mathrm{CM}}$.

8.1.1 2ℓ regions

The definitions for the control and validation regions for VV and top quark processes is the same as the previous analysis (Section 7.5.1), with the major change being the removal of the validation regions for previous photon template Z+jets estimate. The VV contributions in both the standard and ISR SRs are normalised in regions with three and four leptons. The region definitions for the standard tree CRs, VRs, and SR2ℓ_Low are shown in Tables 8.1 and 8.2). The ISR regions are defined in Tables 8.3 and 8.4.

Table 8.1: Preselection criteria for the standard-decay-tree SR2ℓ_Low and the associated CRs and VRs. The variables are defined in the text.

Region	n_{leptons}	n_{jets}	$n_{b\text{-tag}}$	$p_{\mathrm{T}}^{\ell_1,\ell_2}$ [GeV]	$p_{\mathrm{T}}^{j_1,j_2}$ [GeV]	$m_{\ell\ell}$ [GeV]	m_{jj} [GeV]	m_{T}^{W} [GeV]
CR2ℓ-VV	$\in [3,4]$	≥ 2	=0	> 25	> 30	$\in (80,100)$	> 20	$\in (70,100)$ if $n_{\text{leptons}} = 3$
CR2ℓ-Top	$= 2$	≥ 2	=1	> 25	> 30	$\in (20,80)$	$\in (40,250)$	–
						or > 100		–
VR2ℓ-VV	$= 2$	≥ 2	=0	> 25	> 30	$\in (80,100)$	$\in (40,70)$	–
							or $\in (90,500)$	–
VR2ℓ-Top	$= 2$	≥ 2	=1	> 25	> 30	$\in (80,100)$	$\in (40,250)$	–
SR2ℓ_Low	$= 2$	$= 2$	$= 0$	> 25	> 30	$\in (80,100)$	$\in (70,90)$	–

Table 8.2: Selection criteria for the standard-decay-tree SR2ℓ_Low and the associated CRs and VRs. The variables are defined in the text

Region	$H_{4,1}^{\mathrm{PP}}$ [GeV]	$H_{1,1}^{\mathrm{PP}}$ [GeV]	$\frac{p_{\mathrm{T\ PP}}^{\mathrm{lab}}}{p_{\mathrm{T\ PP}}^{\mathrm{lab}}+H_{\mathrm{T}\ 4,1}^{\mathrm{PP}}}$	$\frac{\min(H_{1,1}^{\mathrm{Pa}},H_{1,1}^{\mathrm{Pb}})}{\min(H_{2,1}^{\mathrm{Pa}},H_{2,1}^{\mathrm{Pb}})}$	$\frac{H_{1,1}^{\mathrm{PP}}}{H_{4,1}^{\mathrm{PP}}}$	$\Delta\phi_{\mathrm{V}}^{\mathrm{P}}$	$\min\Delta\phi(j_1/j_2, \vec{p}_{\mathrm{T}}^{\,\mathrm{miss}})$
CR2ℓ-VV	> 200	–	< 0.05	> 0.2	–	$\in (0.3, 2.8)$	–
CR2ℓ-Top	> 400	–	< 0.05	> 0.5	–	$\in (0.3, 2.8)$	–
VR2ℓ-VV	> 400	> 250	< 0.05	$\in (0.4, 0.8)$	–	$\in (0.3, 2.8)$	–
VR2ℓ-Top	> 400	–	< 0.05	> 0.5	–	$\in (0.3, 2.8)$	–
SR2ℓ_Low	> 400	–	< 0.05	–	$\in (0.35, 0.60)$	–	> 2.4

Table 8.3: Preselection criteria for the compressed-decay-tree 2ℓ SR and the associated CRs and VRs. The variables are defined in the text.

Region	n_{leptons}	$N_{\mathrm{jet}}^{\mathrm{ISR}}$	$N_{\mathrm{jet}}^{\mathrm{S}}$	n_{jets}	$n_{b\text{-tag}}$	$p_{\mathrm{T}}^{\ell_1,\ell_2}$ [GeV]	$p_{\mathrm{T}}^{j_1,j_2}$ [GeV]
CR2ℓ_ISR-VV	$\in [3, 4]$	≥ 1	≥ 2	> 2	$= 0$	> 25	> 30
CR2ℓ_ISR-Top	$= 2$	≥ 1	$= 2$	$\in [3, 4]$	$= 1$	> 25	> 30
VR2ℓ_ISR-VV	$\in [3, 4]$	≥ 1	≥ 2	≥ 3	$= 0$	> 25	> 20
VR2ℓ_ISR-Top	$= 2$	≥ 1	$= 2$	$\in [3, 4]$	$= 1$	> 25	> 30
SR2ℓ_ISR	$= 2$	≥ 1	$= 2$	$\in [3, 4]$	$= 0$	> 25	> 30

Table 8.4: Selection criteria for the compressed-decay-tree 2ℓ SR and the associated CRs and VRs. The variables are defined in the text.

Region	m_Z [GeV]	m_J [GeV]	$\Delta\phi_{\mathrm{ISR,I}}^{\mathrm{CM}}$	R_{ISR}	$p_{\mathrm{T\ ISR}}^{\mathrm{CM}}$ [GeV]	$p_{\mathrm{T\ I}}^{\mathrm{CM}}$ [GeV]	$p_{\mathrm{T}}^{\mathrm{CM}}$ [GeV]
CR2ℓ_ISR-VV	$\in (80, 100)$	> 20	> 2.0	$\in (0.0, 0.5)$	> 50	> 50	< 30
CR2ℓ_ISR-Top	$\in (50, 200)$	$\in (50, 200)$	> 2.8	$\in (0.4, 0.75)$	> 180	> 100	< 20
VR2ℓ_ISR-VV	$\in (20, 80)$ or > 100	> 20	> 2.0	$\in (0.0, 1.0)$	> 70	> 70	< 30
VR2ℓ_ISR-Top	$\in (50, 200)$	$\in (50, 200)$	> 2.8	$\in (0.4, 0.75)$	> 180	> 100	> 20
SR2ℓ_ISR	$\in (80, 100)$	$\in (50, 110)$	> 2.8	$\in (0.4, 0.75)$	> 180	> 100	< 20

8.1.2 3ℓ regions

The 3ℓ standard tree regions have a requirement for zero central jets in line with the lone signal region SR3ℓ_Low, and are defined in Tables 8.5 and 8.6. The ISR tree regions are defined in exactly the same fashion as the previous iteration of the analysis (Tables 8.7 and 8.8).

Table 8.5: Preselection criteria for the 3ℓ CR, VR and SR3ℓ_Low with the standard decay tree.

Region	n_{leptons}	n_{jets}	$n_{b\text{-tag}}$	$p_{\text{T}}^{\ell_1}$ [GeV]	$p_{\text{T}}^{\ell_2}$ [GeV]	$p_{\text{T}}^{\ell_3}$ [GeV]
CR3ℓ-VV	$= 3$	0	$= 0$	> 60	> 40	> 30
VR3ℓ-VV	$= 3$	0	$= 0$	> 60	> 40	> 30
SR3ℓ_Low	$= 3$	$= 0$	$= 0$	> 60	> 40	> 30

Table 8.6: Selection criteria for the 3ℓ CR, VR and $SR3\ell$_Low with the standard decay tree.

Region	$m_{\ell\ell}$ [GeV]	m_{T}^{W} [GeV]	$H_{3,1}^{\text{PP}}$ [GeV]	$\frac{p_{\text{T PP}}^{\text{lab}}}{p_{\text{T PP}}^{\text{lab}} + H_{\text{T 3,1}}^{\text{PP}}}$	$\frac{H_{\text{T 3,1}}^{\text{PP}}}{H_{3,1}^{\text{PP}}}$	$\frac{H_{1,1}^{\text{P}_b}}{H_{2,1}^{\text{P}_b}}$
CR3ℓ-VV	$\in (75, 105)$	$\in (0, 70)$	> 250	< 0.2	> 0.75	–
VR3ℓ-VV	$\in (75, 105)$	$\in (70, 100)$	> 250	< 0.2	> 0.75	–
SR3ℓ_Low	$\in (75, 105)$	> 100	> 250	< 0.05	> 0.9	–

Table 8.7: Preselection criteria for the 3ℓ CR, VR and SR3ℓ_ISR with the compressed decay tree.

Region	n_{leptons}	n_{jets}	$n_{b\text{-tag}}$	$p_{\text{T}}^{\ell_1}$ [GeV]	$p_{\text{T}}^{\ell_2}$ [GeV]	$p_{\text{T}}^{\ell_3}$ [GeV]
CR3ℓ_ISR-VV	$= 3$	≥ 1	$= 0$	> 25	> 25	> 20
VR3ℓ_ISR-VV	$= 3$	≥ 1	$= 0$	> 25	> 25	> 20
SR3ℓ_ISR	$= 3$	$\in [1, 3]$	$= 0$	> 25	> 25	> 20

Table 8.8: Selection criteria for the 3ℓ CR, VR and SR3ℓ_ISR with the compressed decay tree.

Region	$m_{\ell\ell}$ [GeV]	m_{T}^{W} [GeV]	$\Delta\phi_{\mathrm{ISR,I}}^{\mathrm{CM}}$	R_{ISR}	$p_{\mathrm{T\,ISR}}^{\mathrm{CM}}$ [GeV]	$p_{\mathrm{T\,I}}^{\mathrm{CM}}$ [GeV]	$p_{\mathrm{T}}^{\mathrm{CM}}$ [GeV]
CR3ℓ_ISR-VV	$\in (75, 105)$	< 100	> 2.0	$\in (0.55, 1.0)$	> 80	> 60	< 25
VR3ℓ_ISR-VV	$\in (75, 105)$	> 60	> 2.0	$\in (0.55, 1.0)$	> 80	> 60	> 25
SR3ℓ_ISR	$\in (75, 105)$	> 100	> 2.0	$\in (0.55, 1.0)$	> 100	> 80	< 25

8.2 Data and Monte Carlo samples

The dataset for this run is the full Run 2 ATLAS recorded data, being 36.2, 43.9 and 59.9 fb^{-1} for the periods 2015-16, 2017, and 2018 respectively. The set of Monte Carlo simulation samples is the same as what is used in the previous iteration of the analysis (Section 7.2), with additional MC statistics for the full Run 2.

8.3 Objects

To stay as faithful as possible to the original analysis the object definitions are kept fixed. Exceptions to this are a result of changes in reconstruction and identification of objects, and in the overlap removal and isolation recommendations. These changes are validated in Section 8.4. Photons are no longer needed for the Z+jets estimate and so are not considered.

8.3.1 Triggers

The events used by the searches described in this analysis are selected using high-purity leptons and jets with a trigger logic that accepts events with either two electrons, two muons or an electron plus a muon. The trigger-level requirements on the p_{T} of the leptons involved in the trigger decision are looser than those applied offline to ensure that trigger efficiencies remain high and are constant in the relevant phase space. As presented in Table 8.9 the lowest unprescaled trigger for all periods are recorded for trigger decisions, with trigger matching being applied in both legs for signal events.

Table 8.9: The list of triggers used in this analysis for the four years of Run 2.

Year	ee trigger	$\mu\mu$ trigger	$e\mu$ trigger
2015	2e12_lhloose_L12EM10VH	2mu10	e17_lhloose_mu14
2016	2e17_lhvloose_nod0	mu22_mu8noL1 || 2mu14	e17_lhloose_nod0_mu14 || e7_lhmedium_nod0_mu24
2017	2e17_lhvloose_nod0 || 2e24_lhvloose_nod0	mu22_mu8noL1 || 2mu14	e17_lhloose_nod0_mu14 || e7_lhmedium_nod0_mu24
2018	2e17_lhvloose_nod0 || 2e24_lhvloose_nod0	e17_lhloose_nod0_mu14 || e7_lhmedium_nod0_mu24	mu22_mu8noL1 || 2mu14

Table 8.10: Summary of the electron selection criteria. The signal selection requirements are applied on top of the baseline selection and after Overlap Removal.

Cut	Value/description
Baseline Electron	
Acceptance	$p_{\mathrm{T}} > 10$ GeV, $\lvert\eta^{\mathrm{clust}}\rvert < 2.47$
PID Quality	`LooseAndBLayerLLH`
Impact parameter	$\lvert z_0 \sin\theta\rvert < 0.5$ mm
Signal Electron	
Acceptance	$p_{\mathrm{T}} > 10$ GeV, $\lvert\eta^{\mathrm{cluster}}\rvert < 2.47$
PID Quality	`LLHMedium`
Isolation	`FixedCutTight`
Impact parameter	$\lvert d_0/\sigma_{d_0}\rvert < 5$

8.3.2 Electrons

This analysis uses baseline electrons of at least 10 GeVwith $|\eta| < 2.47$ and *LooseAndBLayerLLH* identification ($|z0| < 0.5$), and signal electrons with the more stringent *MediumLLH* with an additional $d0/\sigma_{d0} < 5$ criterion on the interaction point. The selection is summarised in Table 8.10.

8.3.3 Muons

Baseline muons have $p_{\mathrm{T}} > 10$ GeV, be within $|\eta| < 2.4$, pass *Medium* ID and be within $z_0 < 0.5mm$. Signal muons have an additional $d0/\sigma_{d0} < 5$ requirement. The selections are summarised in Table 8.11.

Table 8.11: Summary of the muon selection criteria. The signal selection requirements are applied on top of the baseline selection after Overlap Removal.

Cut	Value/description
Baseline Muon	
Acceptance	$p_{\mathrm{T}} > 10$ GeV, $\lvert\eta\rvert < 2.4$
PID Quality	`Medium`
Impact parameter	$\lvert z_0 \sin\theta\rvert < 0.5$ mm
Signal Muon	
Acceptance	$p_{\mathrm{T}} > 10$ GeV, $\lvert\eta\rvert < 2.4$
PIDQuality	`Medium`
Isolation	`FixedCutTight`
Impact parameter	$\lvert d_0/\sigma_{d_0}\rvert < 3$

8.3.4 Jets

This analysis uses *EMTopo* jets reconstructed using the Anti-kt algorithm with distance parameter $R = 0.4$, and minimum p_{T} of 20GeV. Jets are also required to pass a JVT cut (JVT >0.59) if the jet p_{T} is less than 120GeV. This analysis defines central jets as being within $|\eta| < 2.4$, while jets outside this bound up to $|\eta| < 4.5$ can be selected to enter into the MET calculation depending on the METWP selection. This is consistent with the jet treatment in the 2015-16 iteration of the analysis. B-tagged jets are selected using the output of the MV2c10 algorithm with the $FixedCutBEff\_77$ (77%) working point. The jet selections are summarised in Table 8.12.

8.3.5 Overlap removal

The overlap removal is listed below, with the major difference between the 2015-16 and full Run 2 iterations being the change in recommendation to not use b-jet aware overlap removal.

Table 8.12: Summary of the jet and b-jet selection criteria. The signal selection requirements are applied on top of the baseline requirements after Overlap Removal has been performed.

Cut	Value/description
	Baseline jet
Collection	`AntiKt4EMTopo`
Acceptance	$p_{\mathrm{T}} > 20$ GeV , $\lvert\eta\rvert < 4.5$
	Signal jet
JVT	$\lvert\mathrm{JVT}\rvert > 0.59$ for jets with $p_{\mathrm{T}} < 120$ GeV and $\lvert\eta\rvert < 2.4$
Acceptance	$p_{\mathrm{T}} > 20$ GeV , $\lvert\eta\rvert < 2.4$
	Signal b-jet
b-tagger Algorithm	MV2c10
Efficiency	77 %
Acceptance	$p_{\mathrm{T}} > 20$ GeV , $\lvert\eta\rvert < 2.4$

1. Any electron that shares an ID track with a muon is removed.

2. If a jet is within $\Delta R = 0.2$ of an electron, then the electron rejected as originating from a semileptonic b-hadron decay.

3. Electrons within $\Delta R = 0.4$ of other jet candidates are rejected due to their likely origins from semileptonic b- and c-hadron decays.

4. If a jet has fewer than three associated tracks, and has a nearby muon which carries a large fraction of the transverse momentum of the jet, $p_{\mathrm{T}}^{\mu} > 0.7\Sigma p_{\mathrm{T}}^{\text{jet tracks}}$ are discarded if the muon is within $\Delta R = 0.2$ or if the muon is track matched to the jet.

5. Muons within $\Delta R = 0.4$ of any remaining jet candidates are discarded to mitigate muons from semileptonic c- and b-hadron decays.

8.3.6 Isolation working point

The isolation working point for the leptons in the previous iteration of the analysis was GradientLoose, based on recommendations from muon and electron experts. The recommendation was made to move to FixedCutLoose (FCLoose) as it was deemed to be the closest to GradientLoose. However, the performance of FCLoose was not commensurate with the results seen previously, with an increase in fake and non-prompt leptons and poor agreement between data and background predictions in the control regions. However using FixedCutTight (FCTight) leads to fewer fake lepton contributions and better shape agreement in data versus background measurements. FCTight is therefore used in this analysis.

8.3.7 $E_{\mathrm{T}}^{\mathrm{miss}}$ working point

The measurement of the missing transverse momentum vector $\vec{p}_{\mathrm{T}}^{\,\mathrm{miss}}$ (and its magnitude $E_{\mathrm{T}}^{\mathrm{miss}}$) is based on the calibrated transverse momenta of all electron, photon, muon and jet candidates and all tracks originating from the primary vertex and not associated with such objects [48]. The missing transverse momentum is the negative of the vector sum of the object momenta.

In the previous iteration of the analysis the $E_{\mathrm{T}}^{\mathrm{miss}}$ working point was Loose in accordance with the recommendations at the time. With the addition of 2017 and 2018 data with higher pileup and the changes in object reconstruction, Tight $E_{\mathrm{T}}^{\mathrm{miss}}$ is the default. The difference between the working points is in the treatment of the forward jets ($|\eta| > 2.4$), with Loose allowing for jets of 20 GeV transverse momentum and greater within $2.4 < |\eta| < 4.5$ and Tight requiring that those forward jets be at least 30 GeV. The difference in Loose versus Tight $E_{\mathrm{T}}^{\mathrm{miss}}$ is described in Section 8.4.

8.4 Validation of updated object definitions

Since no refinement of the signal regions is possible, the effect of the changes in reconstruction and recommended treatment of objects must be examined to determine

the effect on the analysis. Moving from $E_{\mathrm{T}}^{\mathrm{miss}}$ working point Loose to Tight not only affects the magnitude of $\vec{p}_{\mathrm{T}}^{\,\mathrm{miss}}$, but the direction in ϕ. Since RJR uses both pieces of information as input into the calculation of the boost to the centre-of-mass frame, the subsequent variables are dependent on the $E_{\mathrm{T}}^{\mathrm{miss}}$ treatment. The most sensitive variable in the standard decay tree reconstruction is $p_{\mathrm{T\,PP}}^{\mathrm{lab}}/(p_{\mathrm{T\,PP}}^{\mathrm{lab}} + H_{\mathrm{T\,3,1}}^{\mathrm{PP}})$, testing for unaccounted transverse boost. The x and y boosts and $p_{\mathrm{T\,PP}}^{\mathrm{lab}}/(p_{\mathrm{T\,PP}}^{\mathrm{lab}} + H_{\mathrm{T\,3,1}}^{\mathrm{PP}})$ for diboson MC is shown in Figure 8.1. The ISR tree has a similar variable $p_{\mathrm{T}}^{\mathrm{CM}}$, which is small for well constructed events and grows larger as the reconstructed CM frame has more transverse momentum. The x and y boost and $p_{\mathrm{T}}^{\mathrm{CM}}$ is shown in Figure 8.2. From these basic checks it is clear that there will be more background events entering into the well reconstructed category for some of the variables used.

The next step is to determine whether the two variables are dependent on pile-up, which can be an extra unwanted four-vector entering into an event and altering the reconstruction. To do this for SR3ℓ_Low the total background was evaluated in two regions: the signal region itself, and a region with an inverted $p_{\mathrm{T\,PP}}^{\mathrm{lab}}/(p_{\mathrm{T\,PP}}^{\mathrm{lab}} + H_{\mathrm{T\,3,1}}^{\mathrm{PP}})$. The pile-up distributions of these two regions show no significant shape differences, shown for 2015-16, 2017, and 2018 in Figure 8.3. The procedure is repeated for SR3ℓ_ISR and the variable $p_{\mathrm{T}}^{\mathrm{CM}}$. Again no significant shape differences are seen in Figure 8.4.

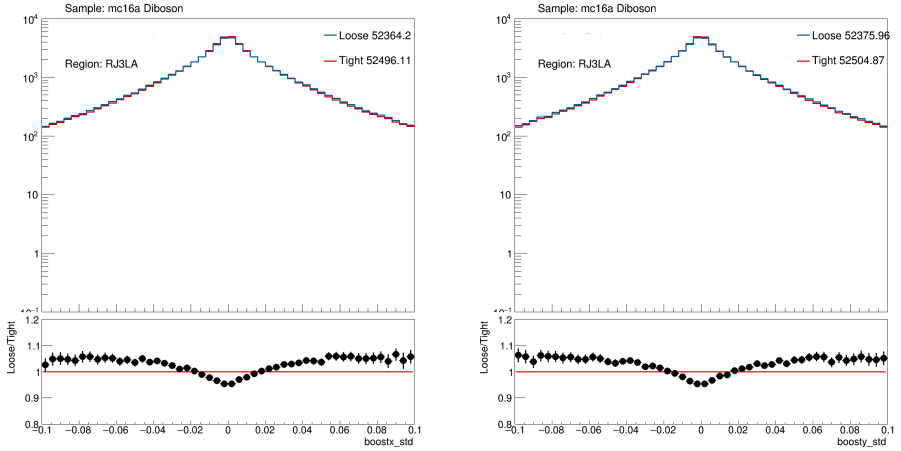

a b

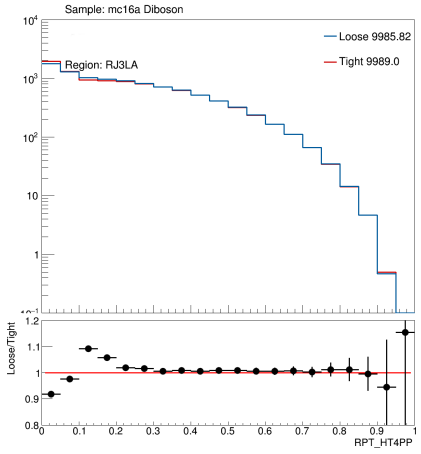

c

Figure 8.1: The x (Figure 8.1a), and y (Figure 8.1b) components of the boost between the lab frame and the PP frame in the 3ℓ standard tree preselection region. This results in more Tight $E_{\mathrm{T}}^{\mathrm{miss}}$ events being defined as well reconstructed in Figure 8.1c.

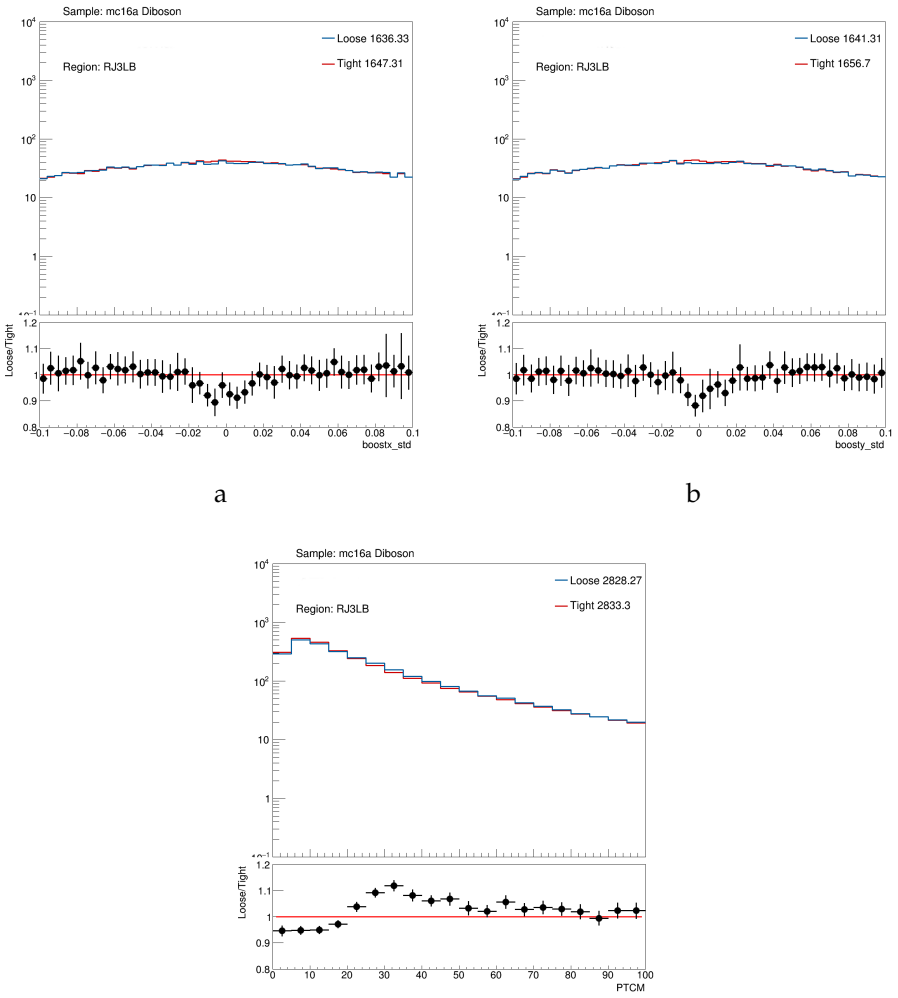

Figure 8.2: The x (Figure 8.2a), and y (Figure 8.2b) components of the boost between the lab frame and the CM frame in the 3ℓ ISR tree preselection region. This results in more Tight $E_{\mathrm{T}}^{\mathrm{miss}}$ events being defined as well reconstructed in Figure 8.2c.

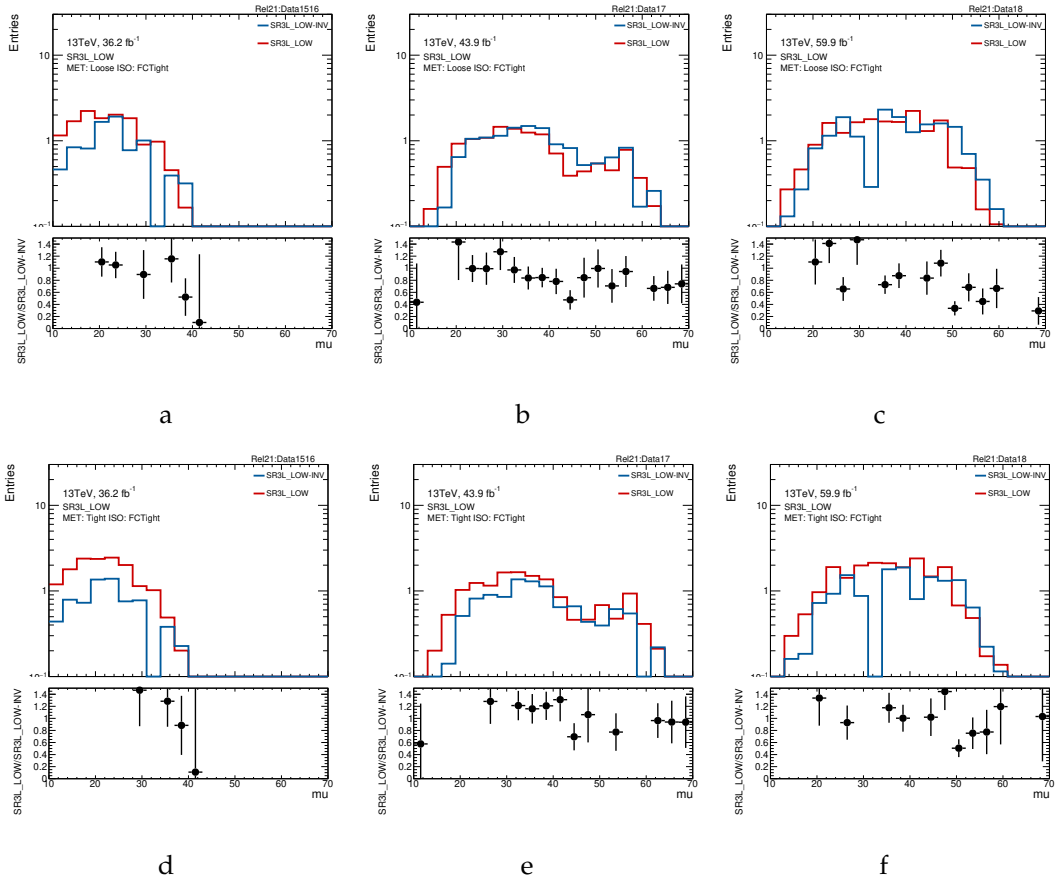

Figure 8.3: The overlaid SR and inverted $\frac{p^{\text{lab}}_{\text{T PP}}}{p^{\text{lab}}_{\text{T PP}}+H^{\text{PP}}_{\text{T 3,1}}}$ selection $< \mu >$ distributions for all backgrounds in SR3ℓ_Low for Loose and Tight $E^{\text{miss}}_{\text{T}}$ in 2015-16 (Figures 8.3a and 8.3d), 2017 (Figures 8.3b and 8.3e), and 2018 (Figures 8.3c and 8.3f).

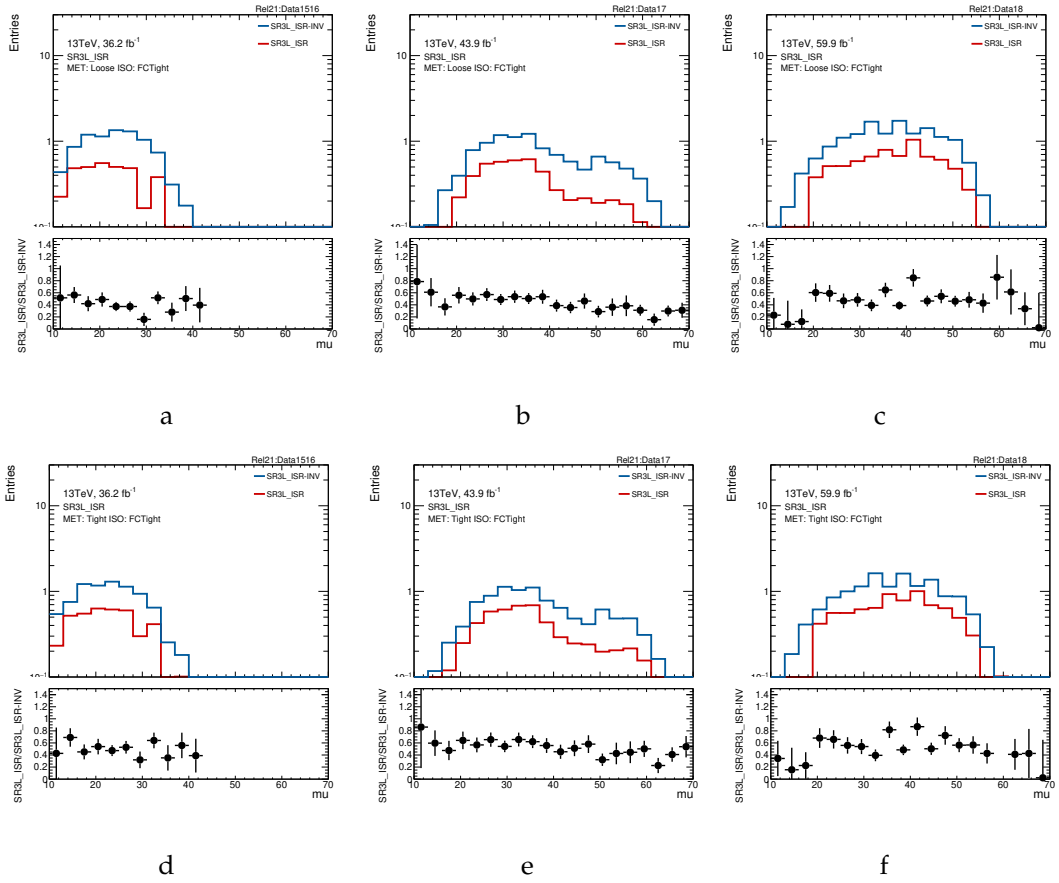

Figure 8.4: The overlaid SR and inverted $p_{\mathrm{T}}^{\mathrm{CM}}$ selection $< \mu >$ distributions for all backgrounds in SR3ℓ_ISR for Loose and Tight $E_{\mathrm{T}}^{\mathrm{miss}}$ in 2015-16 (Figures 8.4a and 8.4d), 2017 (Figures 8.4b and 8.4e), and 2018 (Figures 8.4c and 8.4f).

8.5 Statistical and systematics treatment

Confident in the inputs and methodology of the reconstruction, the statistical treatment and uncertainties can be considered.

The fit procedure for the 2ℓ channel is somewhat more complicated than in the previous iteration due to the ABCD method, which relies on sideband regions in two uncorrelated variables to fit for the Z+jets contributions in the SRs. The VV and $t\bar{t} + tW$ MC normalisation is derived in the control regions and tested in the VRs. The ABCD regions are also floated simultaneously in this fit to allow for the

systematics on the MC backgrounds in those regions to affect the normalisation of the Z+jets signal extracted. The 3ℓ channel is more straightforward with the single normalised background being VV.

There are experimental systematics considered for all background MC samples:

- Muons- Momentum resolution and scale, reconstruction efficiency, identification, isolation efficiency, trigger.
- Electrons- Energy scale, reconstruction efficiency, identification, isolation, trigger.
- Jets- Energy scale and resolution, flavour tagging, Jet Vertex Tagger (JVT).
- MET- Uncertainty from "hard" objects are propagated, in addition the soft term scale and resolution is considered.
- Pileup reweighting- The uncertainties on the scaling are evaluated by adjusting the nominal rescaling.

Some of these require the recalculation of $E_{\mathrm{T}}^{\mathrm{miss}}$, while others are applied as scale factors to the overall weight of the nominal events. In addition there are systematics related to the ABCD region definitions and the data-driven Matrix Method fake lepton estimation. Finally there are theoretical systematics relating to the MC generation of the dominant VV and $t\bar{t}+tW$ backgrounds. The renormalisation and factorisation scales of QCD affect the calculation of matrix elements and are the major uncertainty, especially where extra jet activity is required. Other parameters such as PDF choice and nominal PDF variations are also considered.

8.6 Control and validation regions

8.6.1 2ℓ channel

The 2ℓ control and validation regions for the standard and ISR regions are shown in Tables 8.13 and 8.14, with the VV and $t\bar{t}+tW$ backgrounds shown pre- and post-fit.

Table 8.13: Background fit results for the 2ℓ standard CRs and VRs. The nominal predictions from MC simulation are given for comparison for the $Wt + t\bar{t}$ and VV backgrounds. The "Other" category contains the contributions from Higgs boson processes, $V\gamma$, VVV, $t\bar{t}V$ and non-prompt and non-isolated lepton production. Combined statistical and systematic uncertainties are given. The individual uncertainties can be correlated and do not necessarily add in quadrature to the total systematic uncertainty.

Region	CR2ℓ-VV	CR2ℓ-Top	VR2ℓ-VV	VR2ℓ-Top
Observed events	186	1975	257	418
Total (post-fit) SM events	186 ± 14	1975 ± 44	286 ± 37	435 ± 24
Other	4 ± 4	31 ± 11	4 ± 3	8 ± 5
Fit output, VV	181 ± 14	18 ± 3	166 ± 26	20 ± 3
Fit output, $t\bar{t} + tW$	$0.7^{+1.0}_{-0.7}$	1908 ± 45	52 ± 9	304 ± 23
Z+jets MC	0 ± 0	18 ± 1	64 ± 8	104 ± 6
Fit input, VV	204 ± 2	20 ± 3	187 ± 24	22 ± 3
Fit input, $t\bar{t} + Wt$	$0.72^{1.0}_{-0.7}$	1958 ± 17	53 ± 9	312 ± 22

The normalisation factors for standard (ISR) VV and $t\bar{t} + tW$ are 0.88 (0.80) and 0.97 (0.84) respectively, and show good agreement when applied in the validation regions. Some distributions for the control (Figure 8.5) and validation regions (Figure 8.6) indicate good modelling of background shapes.

8.6.2 3ℓ channel

The control and validation region yields are shown in Table 8.15, with the fitted VV background shown pre- and post-fit. Both the normalisation factors for standard and ISR CRs are 0.92, and when applied to the VRs give good data versus background agreement. Figures 8.7 and 8.8 shows some distributions in the control and validation regions, with the normalisation factors of 0.92 being applied from both of the control regions.

Table 8.14: Background fit results for the 2ℓ ISR CRs and VRs. The nominal predictions from MC simulation are given for comparison for the $Wt + t\bar{t}$ and VV backgrounds. The "Other" category contains the contributions from Higgs boson processes, $V\gamma$, VVV, $t\bar{t}V$ and non-prompt and non-isolated lepton production. Combined statistical and systematic uncertainties are given. The individual uncertainties can be correlated and do not necessarily add in quadrature to the total systematic uncertainty.

Region	CR2L_ISR_VV	CR2L_ISR_TOP	VR2L_ISR_VV	VR2L_ISR_TOP
Observed events	111	376	41	322
Total (post-fit) SM events	111 ± 11	376 ± 19	43 ± 4	329 ± 41
Other	11 ± 6	12 ± 5	17 ± 4	26 ± 9
Fit output, VV	99 ± 11	4.3 ± 0.8	26 ± 3	2.5 ± 0.5
Fit output, $t\bar{t} + tW$	$0.65^{1.49}_{0.65}$	347 ± 20	$0.20^{+0.55}_{-0.20}$	288 ± 47
Z+jets MC	0 ± 0	12.5 ± 0.5	0.09 ± 0.01	20 ± 1
Fit input, VV	124 ± 2	5.4 ± 0.8	31.9 ± 1.4	3.2 ± 0.5
Fit input, $t\bar{t} + tW$	$0.80^{+1.79}_{-0.80}$	415 ± 7	$0.24^{+0.66}_{-0.24}$	334 ± 50

Table 8.15: Expected and observed yields from the background fit for the 3ℓ CRs and VRs. The normalisation factors for VV for the standard and ISR decay trees are different and are extracted from separate fits. The nominal predictions from MC simulation are given for comparison for the VV background. Combined statistical and systematic uncertainties are given. The individual uncertainties can be correlated and do not necessarily add in quadrature to the total systematic uncertainty.

Region	CR3ℓ-VV	VR3ℓ-VV	CR3ℓ_ISR-VV	VR3ℓ_ISR-VV
Observed events	629	331	328	277
Total (post-fit) SM events	629 ± 26	300 ± 22	329 ± 18	293 ± 39
VVV	0.48 ± 0.03	0.24 ± 0.04	0.17 ± 0.07	0.35 ± 0.09
$t\bar{t} + V$, rare top	0.21 ± 0.09	0.10 ± 0.05	2.1 ± 0.9	8 ± 3
Fake and non-prompt	88 ± 21	3.6 ± 1.9	7.1 ± 1.6	11 ± 2
Fit output VV	540 ± 36	296 ± 23	319 ± 18	274 ± 38
Fit input, VV	584 ± 20	324 ± 16	343 ± 78	295 ± 102

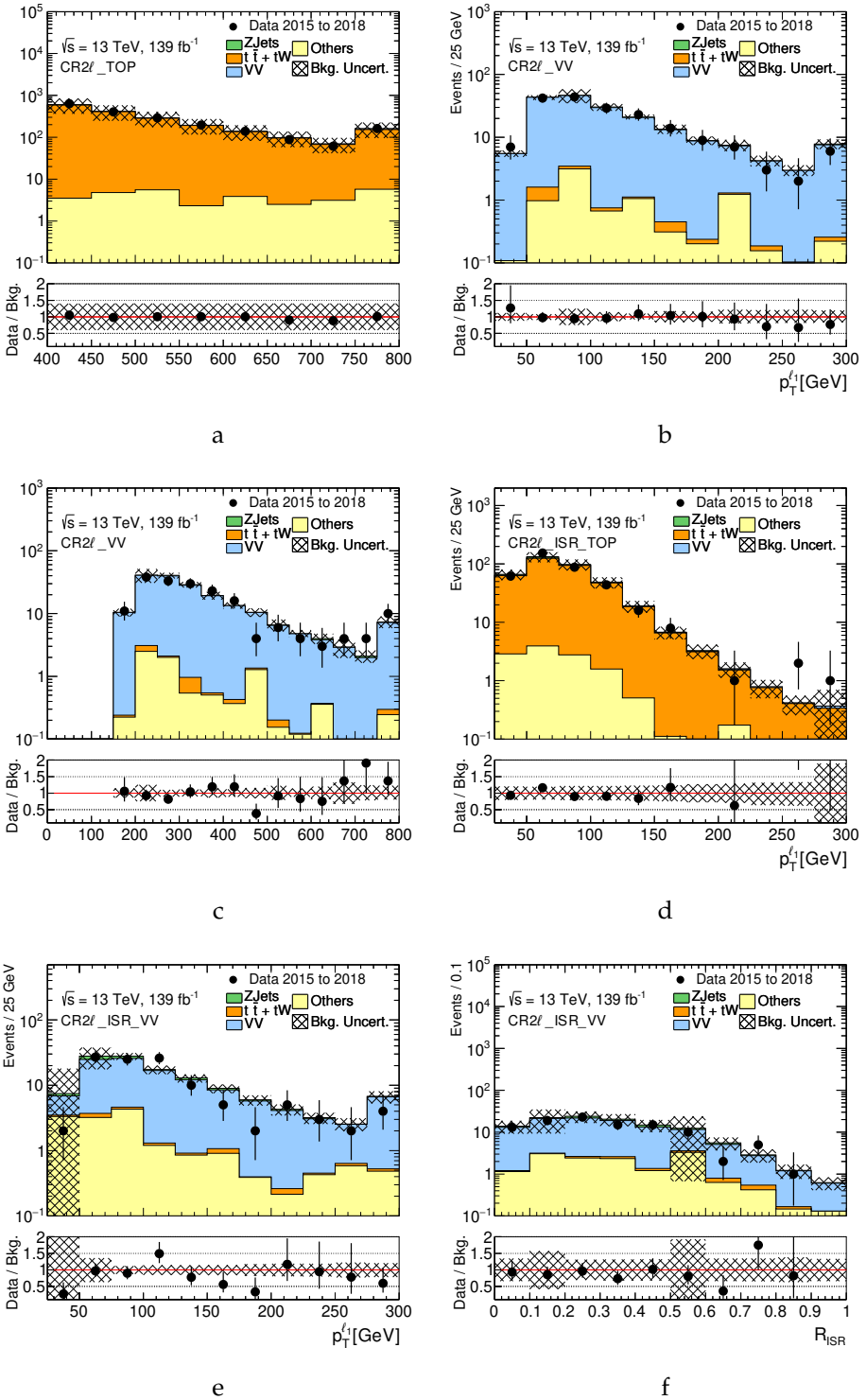

Figure 8.5: Distributions of kinematic variables in the control regions for the 2ℓ channel after applying all selection criteria described in Tables 8.2 or 8.4. (Figure 8.5a) $H_{4,1}^{\mathrm{PP}}$ for the standard top CR, $p_{\mathrm{T}}^{\ell_1}$ (Figure 8.5b) and (Figure 8.5c) $H_{4,1}^{\mathrm{PP}}$ for the standard diboson CR, (Figure 8.5d) $p_{\mathrm{T}}^{\ell_1}$ for the ISR top CR, (Figure 8.5e) $p_{\mathrm{T\,ISR}}^{\mathrm{CM}}$ and (Figure 8.5f) R_{ISR} for the ISR diboson CR.

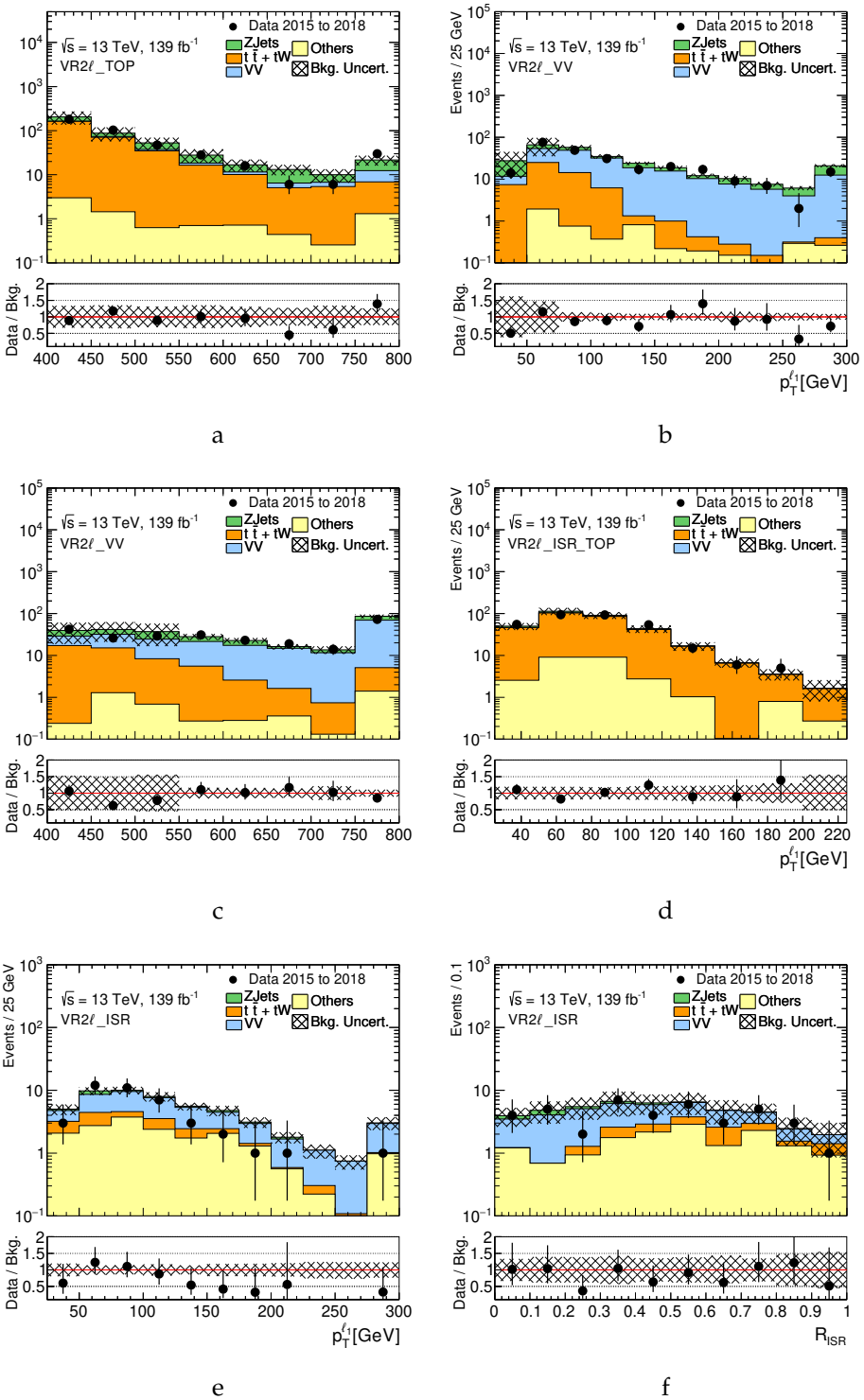

Figure 8.6: Distributions of kinematic variables in the validation regions for the 2ℓ channel after applying all selection criteria described in Tables 8.2 or 8.4. (Figure 8.6a) $H_{4,1}^{\mathrm{PP}}$ for top VR, $p_{\mathrm{T}}^{\ell_1}$ (Figure 8.6b) and (Figure 8.6c) $H_{4,1}^{\mathrm{PP}}$ for the standard diboson VR, (Figure 8.6d) $p_{\mathrm{T}}^{\ell_1}$ for the ISR top VR, (Figure 8.6e) $p_{\mathrm{T\,ISR}}^{\mathrm{CM}}$ and (Figure 8.6f) R_{ISR} for the ISR diboson VR.

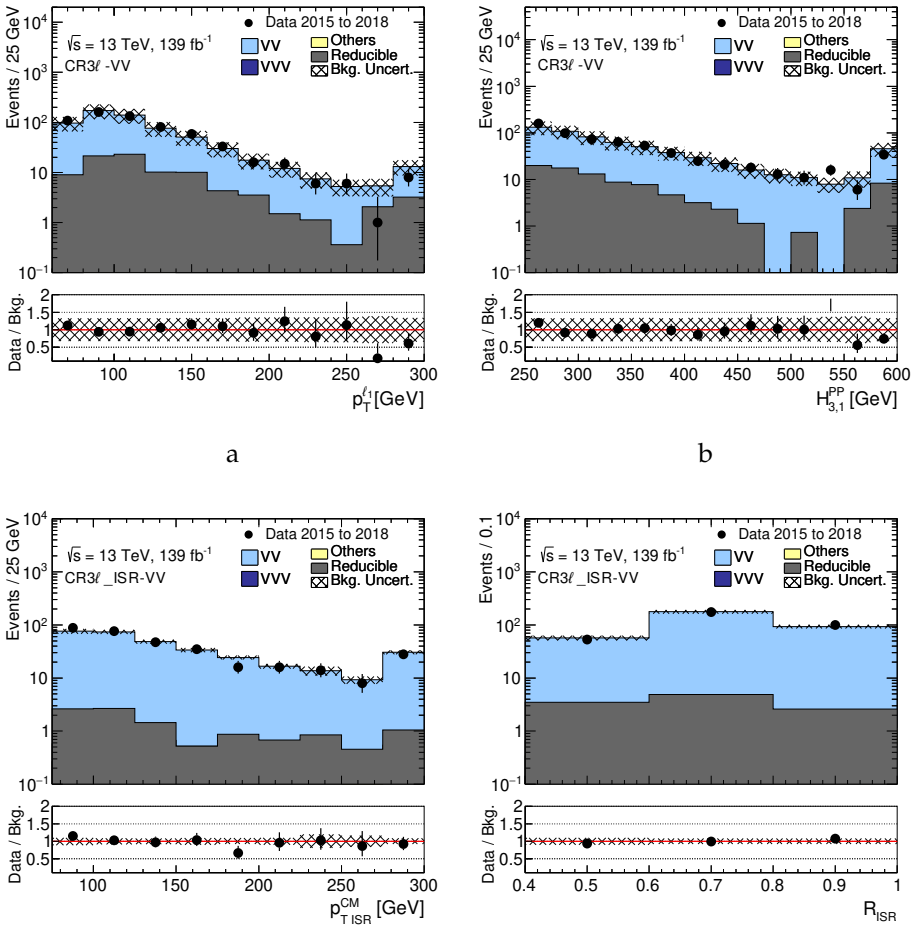

Figure 8.7: Distributions of kinematic variables in the control regions for the 3ℓ channel after applying all selection criteria described in Tables 8.6 or 8.8. The histograms show the post-fit MC background predictions. The last bin includes the overflow. $p_{\mathrm{T}}^{\ell_1}$ (Figure 8.7a) and (Figure 8.7b) $H_{3,1}^{\mathrm{PP}}$ for the diboson CR in the standard decay tree, (Figure 8.7c) $p_{\mathrm{T\,ISR}}^{\mathrm{CM}}$ and (Figure 8.7d) R_{ISR} for the diboson CR in the ISR decay tree. The hatched error bands indicate the combined theoretical, experimental and MC statistical uncertainties.

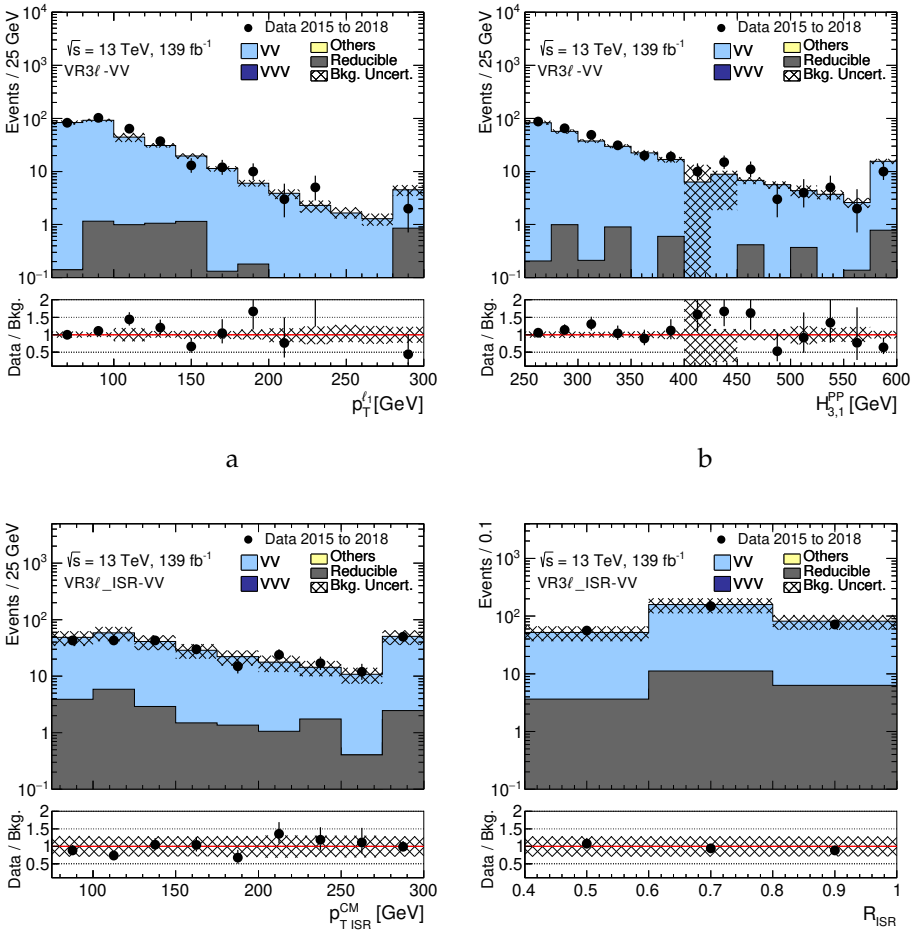

Figure 8.8: Distributions of kinematic variables in the validation regions for the 3ℓ channel after applying all selection criteria described in Tables 8.6 or 8.8. The histograms show the post-fit MC background predictions. The last bin includes the overflow. Plots show () $p_{\mathrm{T}}^{\ell_1}$ and () $H_{3,1}^{\mathrm{PP}}$ for the diboson CR in the standard decay tree, () $p_{\mathrm{T\,ISR}}^{\mathrm{CM}}$ and () R_{ISR} for the diboson CR in the ISR decay tree. The hatched error bands indicate the combined theoretical, experimental and MC statistical uncertainties.

8.7 Signal regions

8.7.1 2ℓ regions

The signal region yields are shown in Table 8.16. Distributions of some discriminating variables are shown in Figure 8.9. The SR plots show Z+jets MC reweighted to match the yield extracted from the ABCD method, so the shape of the distributions will not necessarily match that of the data or other backgrounds due to the large weights in the events. There are also large MC statistical errors due to the large weights.

Table 8.16: Expected and observed yields from the background fit for the 2ℓ SRs. The normalisation factors for VV and $t\bar{t}+Wt$ for the standard and ISR decay trees are different and are extracted from separate fits. The nominal predictions from MC simulation are given for comparison for the VV and $t\bar{t}+tW$ background. Combined statistical and systematic uncertainties are given. The individual uncertainties can be correlated and do not necessarily add in quadrature to the total systematic uncertainty.

Region	SR2ℓ_LOW	SR2ℓ_ISR
Observed events	41	33
Total (post-fit) SM events	45 ± 9	32 ± 9
Other	$0.48^{+0.89}_{-0.48}$	1.2 ± 0.6
Fit output, $t\bar{t}+tW$	4.6 ± 2.6	8.3 ± 3.2
Fit output, VV	11 ± 2	9.0 ± 4.2
Z+jets, data-driven	29 ± 8	13 ± 8
Fit input, $t\bar{t}+tW$	4.7 ± 2.7	10 ± 4
Fit input, VV	12 ± 2	11 ± 5

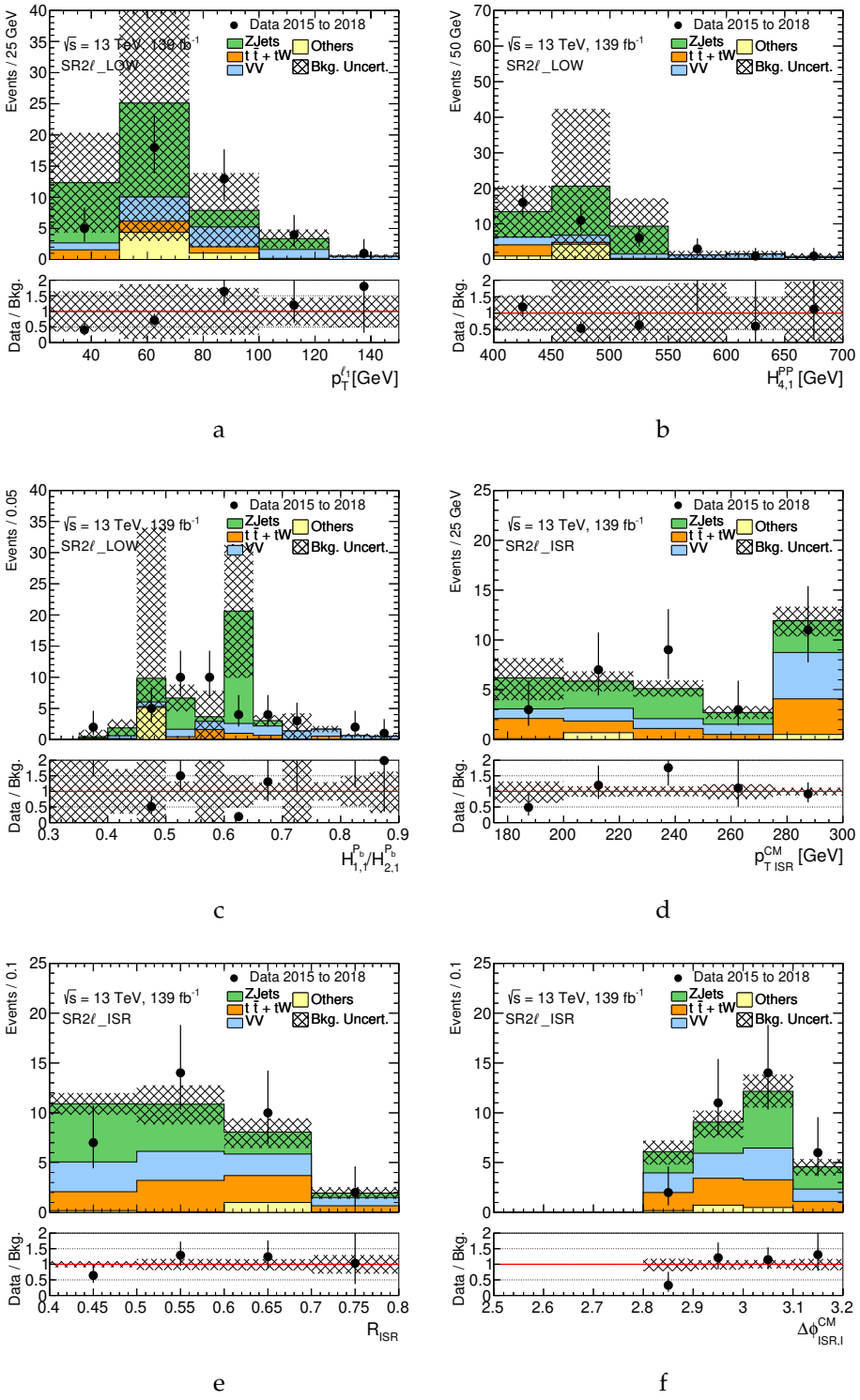

Figure 8.9: Distributions of kinematic variables in the signal regions for the 2ℓ channel after applying all selection criteria described in Tables 8.2 or 8.4. The histograms show the post-fit background predictions. Z+jets is reweighted MC. The last bin includes the overflow. The hatched error bands indicate the combined theoretical, experimental and MC statistical uncertainties.

Table 8.17: Expected and observed yields from the background fit for the 3ℓ SRs. The normalisation factors for VV for the standard and ISR decay trees are different and are extracted from separate fits. The nominal predictions from MC simulation are given for comparison for the VV background. Combined statistical and systematic uncertainties are given. The individual uncertainties can be correlated and do not necessarily add in quadrature to the total systematic uncertainty.

Region	SR3ℓ_LOW	SR3ℓ_ISR
Observed events	53	25
Total (post-fit) SM events	49 ± 5	17 ± 3
VVV	$0.71^{+2.18}_{-0.71}$	$0.33^{+0.79}_{-0.33}$
$t\bar{t} + V$, rare top	0.05 ± 0.03	0.41 ± 0.19
Fakes and non-prompt	1.4 ± 0.4	0.83 ± 0.16
Fit output, VV	47 ± 6	16 ± 3
Fit input, VV	51 ± 5	17 ± 5

8.7.2 3ℓ regions

The two signal region yields are in Table 8.17, with some distributions shown in Figure 8.10.

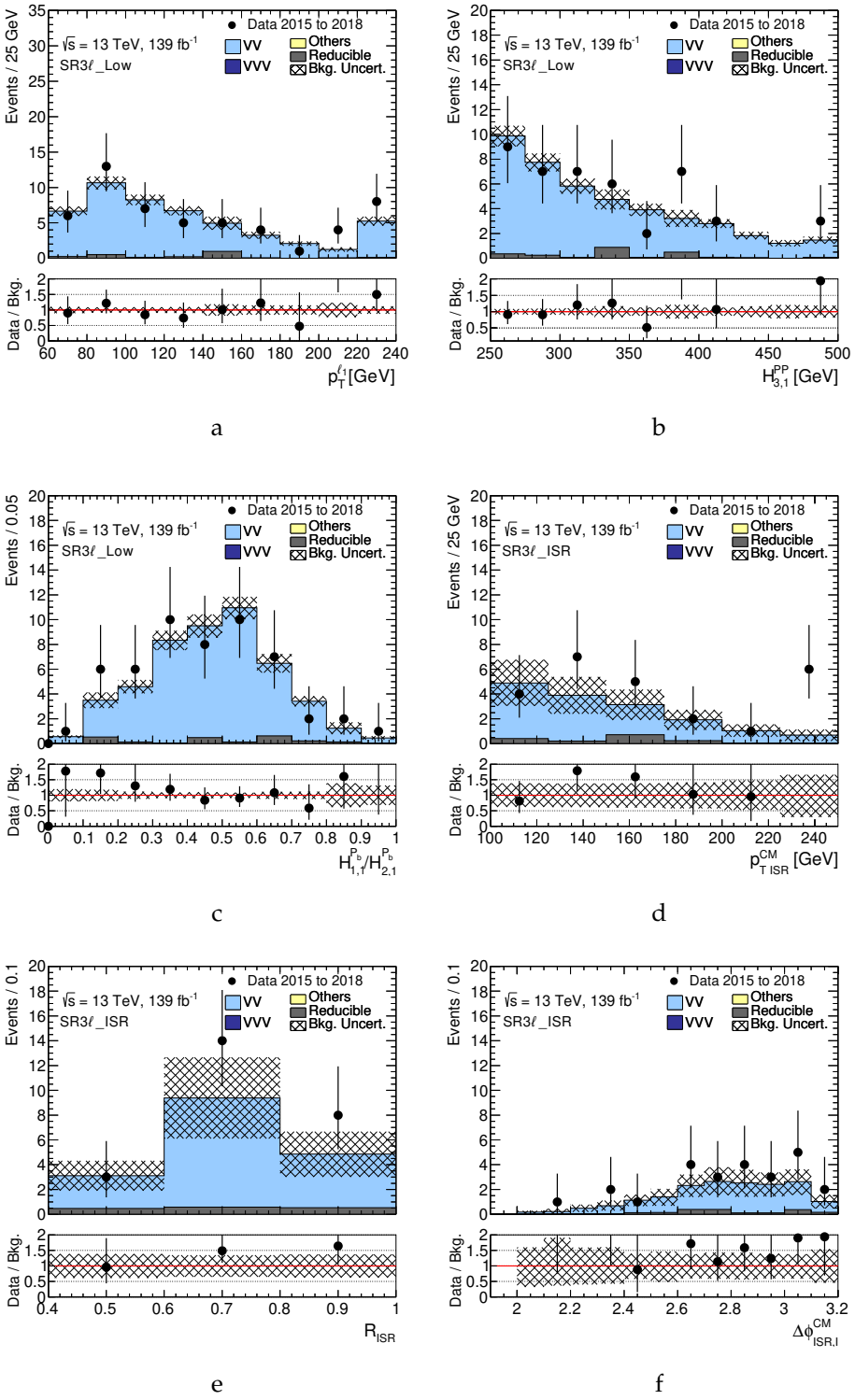

Figure 8.10: Distributions of kinematic variables in the signal regions for the 3ℓ channel after applying all selection criteria described in Tables 8.6 or 8.8. The histograms show the post-fit MC background predictions. The last bin includes the overflow. The hatched error bands indicate the combined theoretical, experimental and MC statistical uncertainties.

8.8 Interpretation

This analysis no longer considers exclusions on the simplified model, with the low mass points being excluded by other analyses. Instead a model-independent limit is derived on the cross section of possible new physics processes on top of the existing standard model contribution in the signal regions. The model independent limits for the regions are listed in Table 8.18, with the significance of the four signal regions SR2ℓ_Low, SR2ℓ_ISR, SR3ℓ_Low, and SR3ℓ_ISR being -0.49, -0.07, 0.41, and 1.42 respectively.

The set of excesses observed in the first $36.2 fb^{-1}$ of LHC Run 2 data do not persist, with less data passing the analysis selections in 2017 and 2018, and background MC contributions increasing in the signal regions. The local significance of all regions is less than two standard deviation from the background predictions. The most discrepant region, SR3ℓ_ISR has some interesting features in $p_{\text{TISR}}^{\text{CM}}$ (Figure 8.10d), n_{jets} and m_{T}^{W} (Figure 8.11), but other variables show good agreement between data and backgrounds.

While the excesses did not persist, the process from initial optimisation with 2015-16 data to end of Run 2 result raised some pertinent points regarding the way BSM searches are conducted and interpreted:

Table 8.18: Left to right: 95% CL upper limits on the visible cross section ($\langle\epsilon\sigma\rangle_{\text{obs}}^{95}$) and on the number of signal events (S_{obs}^{95}). The third column (S_{exp}^{95}) shows the 95% CL upper limit on the number of signal events, given the expected number (and $\pm 1\sigma$ deviations from that expectation) of background events. The last two columns are the confidence level for the background estimate, and the discovery p-value ($p(s=0)$). The 2ℓ limits do not contain VV or $t\bar{t}$ theoretical uncertainties.

Region	$\langle\epsilon\sigma\rangle_{obs}^{95}$[fb]	S_{obs}^{95}	S_{exp}^{95}	CL_B	$p(s=0)$ (Z)
SR2ℓ_Low	0.15	21.4	$21.0^{+5.6}_{-7.7}$	0.31	0.69 (-0.49)
SR2ℓ_ISR	0.17	23.3	$22.5^{+1.6}_{-4.0}$	0.47	0.53 (-0.07)
SR3ℓ_Low	0.22	30.3	$30.3^{+9.4}_{-8.1}$	0.50	0.50 (0.00)
SR3ℓ_ISR	0.10	14.4	$11.7^{+3.5}_{-2.9}$	0.75	0.22 (0.78)

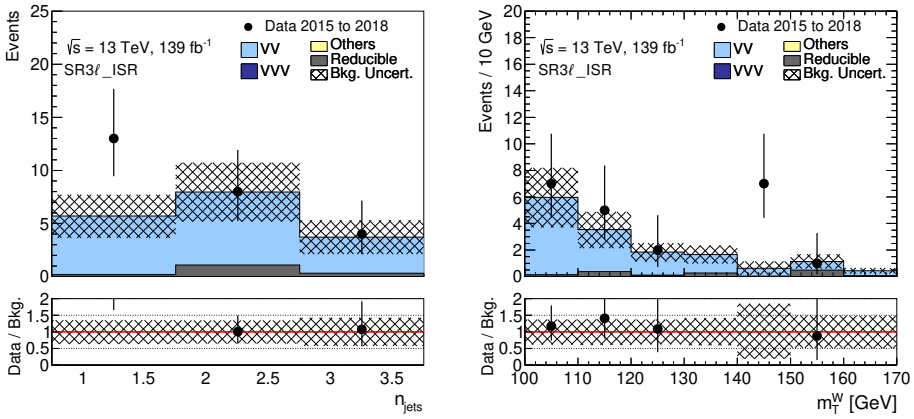

a b

Figure 8.11: Distributions of kinematic variables in SR3ℓ_ISR after applying all selection criteria described in Tables 8.6 or 8.8. The histograms show the post-fit MC background predictions. The last bin includes the overflow. The hatched error bands indicate the combined theoretical, experimental and MC statistical uncertainties.

- The kinematic reach of an analysis cannot be measured just in the parameter space of the models considered.
- Different analysis methodologies focusing on the same parameter space can yield seemingly conflicting, but complimentary results.
- The parameter space of BSM models, here electroweak SUSY, are in general poorly constrained by existing experimental searches.
- A variety of analysis techniques will be required to fully explore the space of new physics.

9 Analysis development and future work

This chapter describes other work undertaken in a more developmental vein, with a view to informing the design of future analyses. Some of the processes considered are unfeasible or very difficult with current techniques and/or integrated data. The focus on electroweak SUSY continues with electroweakino pair decays to four lepton final states. In addition there are explorations of decays with top quark pairs and other objects ($t\bar{t} + X$), where the X can be a Higgs boson, W or Z bosons, or even other top quarks. These are the first steps towards a complete $t\bar{t} + X$ reconstruction framework.

9.1 Electroweak SUSY with four lepton final states

A natural extension of the $\tilde{\chi}_2^0\tilde{\chi}_1^\pm$ decay process is $\tilde{\chi}_3^0\tilde{\chi}_2^0$ where both neutralinos decay via Z bosons to $\tilde{\chi}_1^0$, leading to final states with 2 sets of same-flavour opposite-sign lepton pairs and a combinatoric problem if the lepton flavours are all the same, in addition to the existing need to split the singular $E_{\mathrm{T}}^{\mathrm{miss}}$ into two parts. The Feynman and decay tree diagrams are shown in Figure 9.1. It was decided to assign the leptons based on mass minimisation, finding the configuration of lepton pairs which reduces the overall CM mass in the PP frame. This step is done before any flavour or charge requirements are made on the leptons themselves, providing the opportunity to have useful flavour and charge adjacent regions for data driven background estimates or validation. In addition for lower mass differences between the $\tilde{\chi}_3^0/\tilde{\chi}_2^0$ ISR boosting can be used as in previous analyses. Some distributions with both standard and ISR

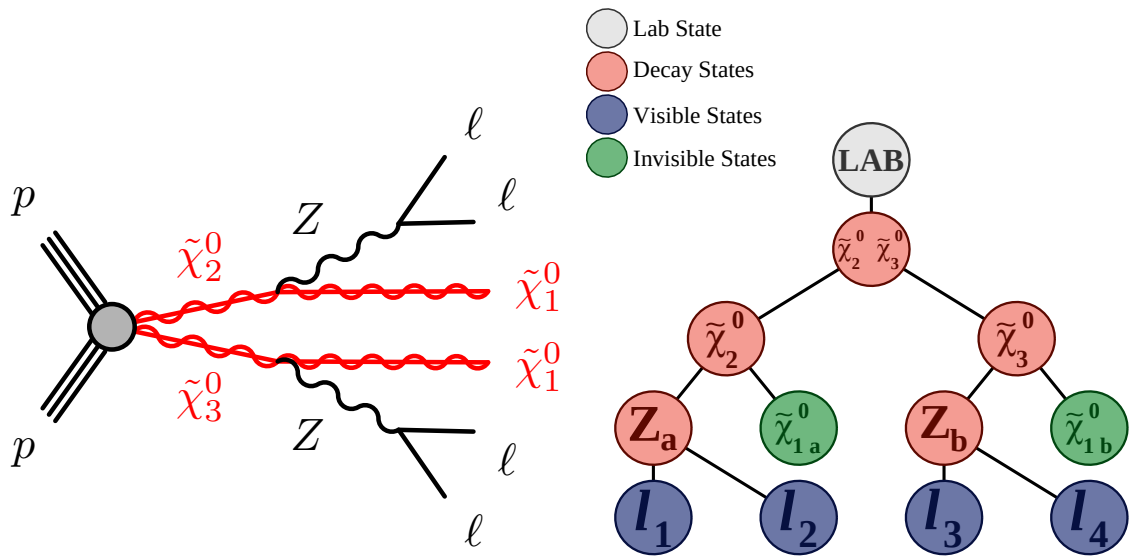

a b

Figure 9.1: Figure 9.1a shows the $\tilde{\chi}_3^0\tilde{\chi}_2^0$ decay process via leptonic Z bosons, Figure 9.1b is the standard RJR decay tree designed for this process.

Table 9.1: Standard and ISR preselection criteria for 4ℓ final states. These are orthogonal in jet multiplicity.

Region	$p_{\mathrm{T}}^{\ell_1}$ [GeV]	$p_{\mathrm{T}}^{\ell_2}$ [GeV]	$p_{\mathrm{T}}^{\ell_3}$ [GeV]	$p_{\mathrm{T}}^{\ell_4}$ [GeV]	n_{jets}	$n_{b-\mathrm{jets}}$	$n_{\mathrm{jets,ISR}}$	$n_{\mathrm{jets,S}}$
Standard preselection (RJ4ℓA)	> 25	> 25	> 10	> 10	0	0	0	0
ISR preselection (RJ4ℓB)	> 25	> 25	> 10	> 10	≥ 1	0	≥ 1	0

treatments are shown in Figure 9.2 and Figure 9.3, with loose preselections on lepton momenta and same-flavour opposite-sign pairs of leptons as defined in Table 9.1 for 36.1 fb^{-1} integrated luminosity.

Even from the preselection level it is clear that the major background process is diboson, with the majority being true $ZZ \to \ell\ell\ell\ell$. In a typical analysis the strategy would be to cut on $E_{\mathrm{T}}^{\mathrm{miss}}$ to remove most of this background but in this case other handles such as $\frac{\min(H_{1,1}^{\mathrm{Pa}}, H_{1,1}^{\mathrm{Pb}})}{\min(H_{2,1}^{\mathrm{Pa}}, H_{2,1}^{\mathrm{Pb}})}$ (Figure 9.2b) could be more useful along with a lower bound on $H_{4,1}^{\mathrm{PP}}$ (Figure 9.2a) as the overall scale variable.

In the ISR boosted case, the simplified tree with the four leptons and $E_{\mathrm{T}}^{\mathrm{miss}}$ recoiling

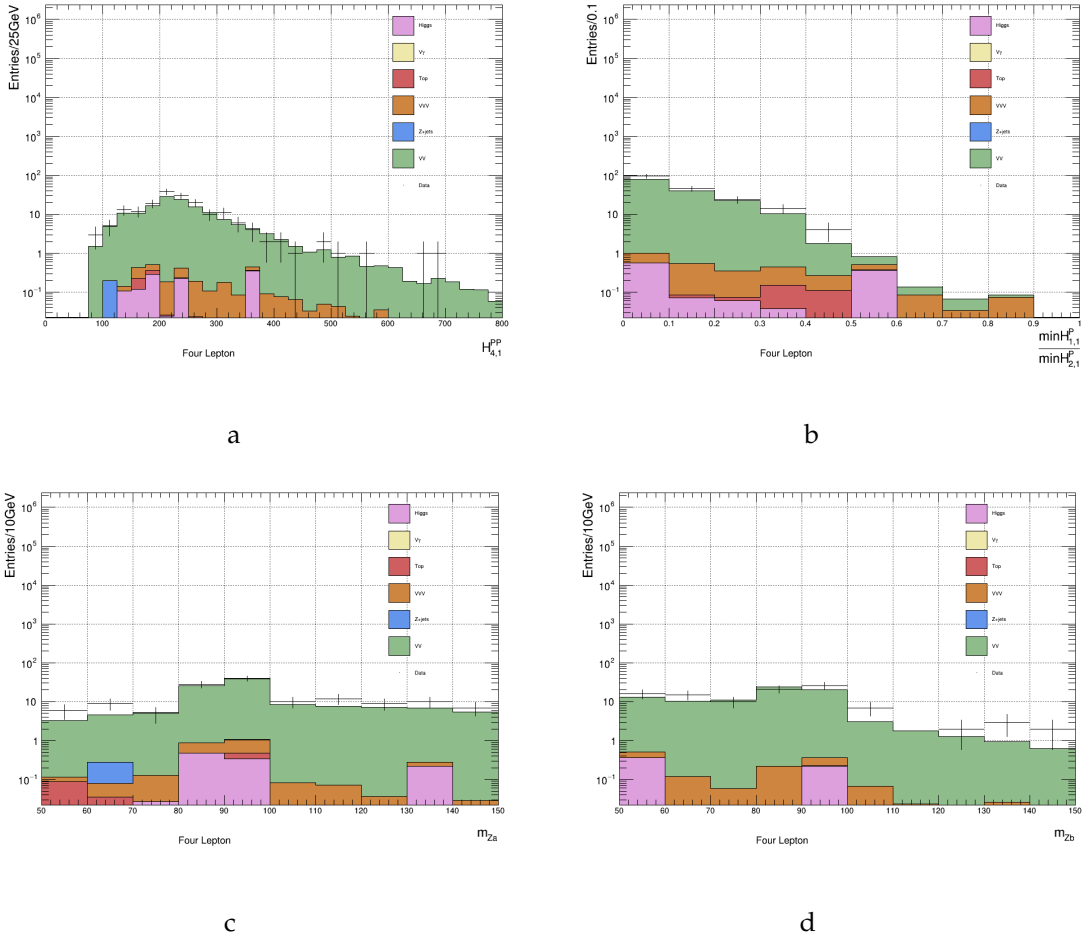

a b

c d

Figure 9.2: Figures 9.2a to 9.2d are some important RJ variables for RJ4ℓA, the standard decay tree implementation preselection region. The data is 36.1 fb^{-1}taken in 2015-16, and the MC is scaled accordingly.

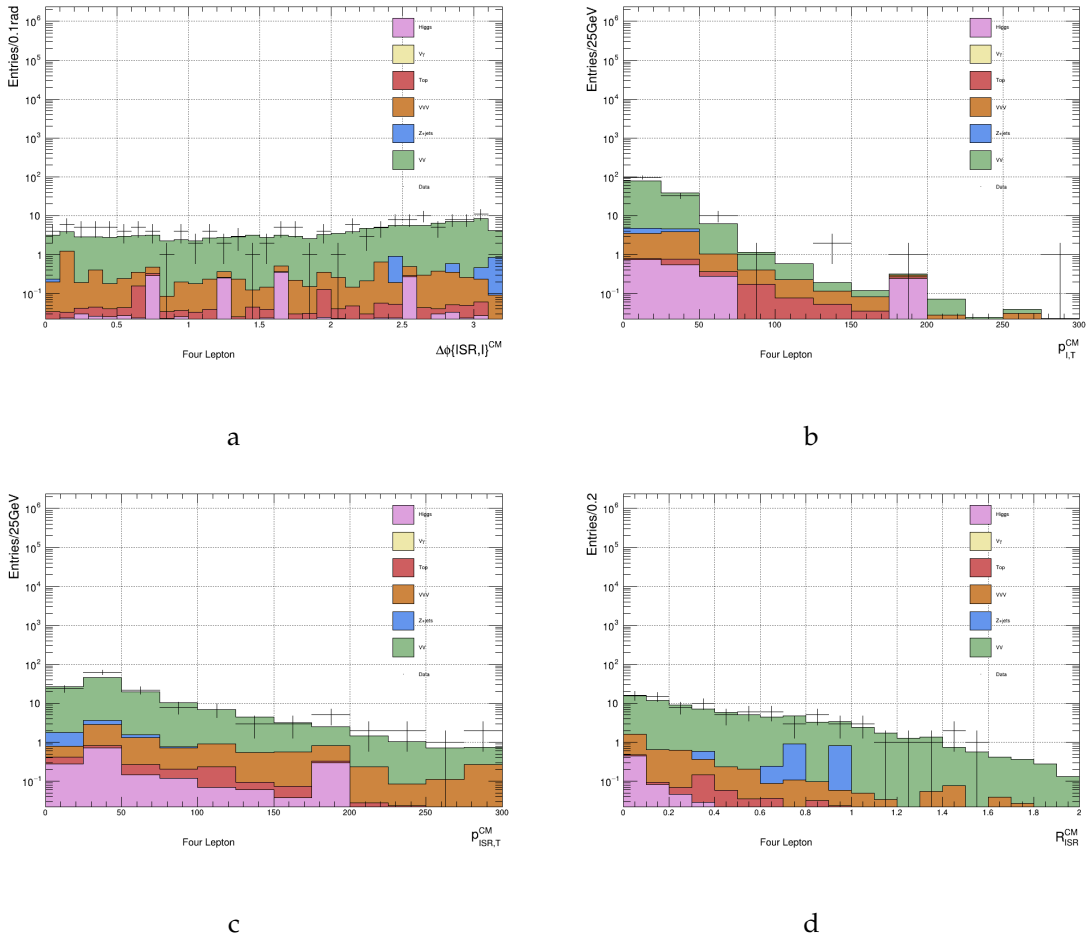

Figure 9.3: Figures 9.3a to 9.3d are general ISR variables for RJ4ℓB. The data is 36.1 fb^{-1}taken in 2015-16, and the MC is scaled accordingly.

against an ISR jet system. The regular suite of ISR variables, $\Delta\phi^{\text{CM}}_{\text{I,ISR}}$ (Figure 9.3a), $p^{\text{CM}}_{\text{I,T}}$ (Figure 9.3b), $p^{\text{CM}}_{\text{ISR,T}}$ (Figure 9.3c), and $R^{\text{CM}}_{\text{ISR}}$ (Figure 9.3c), all display typical behaviour but at lower values of the scale variables compared to the $\tilde{\chi}^0_2/\tilde{\chi}^\pm_1$ decay case.

Another consideration is whether the intermediate Z boson is on-shell or not, which determines the invariant masses for the two pairs of leptons, shown in Figures 9.2c and 9.2d where there is a notable spike in $m_{\ell\ell}$ at the Z mass, but significant background contributions elsewhere. If the Z is more off-shell then the ISR boosting is much more important for achieving the lepton momenta needed for triggering.

9.2 $HH \to WWb\bar{b} \to \ell\nu\ell\nu b\bar{b}$

The non-resonant production of two Higgs bosons is the next step in Higgs sector studies, and though the expected production cross sections are low for SM -di-Higgs processes, they act as a probe of Higgs self coupling and are sensitive to possible BSM influences.

A characteristic final state is where one Higgs boson decays to $b\bar{b}$ and the other to leptonic W pairs. This provides a distinctive signature with a high branching ratio and is an ideal benchmark di-Higgs study. The two main gluon-gluon fusion diagrams are shown in Figures 9.4a and 9.4b. The ATLAS analysis targeting this final state with full LHC Run 2 data uses deep learning with relatively simple kinematic inputs such as object momenta and directional information, along with angles between objects and some scale variables [146]. Imposing an RJR decay tree, such as in Figure 9.4c can be useful to get more handles in reconstructing the two Higgs bosons. This is especially useful for the $H \to WW \to \ell\nu\ell\nu$ component of the decay where there are missing degrees of freedom from the neutrinos. The rules applied are: the rapidity of the neutrinos are the same as the visible leptons, the invariant mass of the two neutrinos is as small as possible (while being Lorentz-invariant), and that the two W bosons are of equal mass. The last assumption is not strictly true for the SM Higgs boson, but provides good enough resolution for the Higgs boson, symmetrising both the W boson masses to be somewhat between the on-shell and the sub-leading boson.

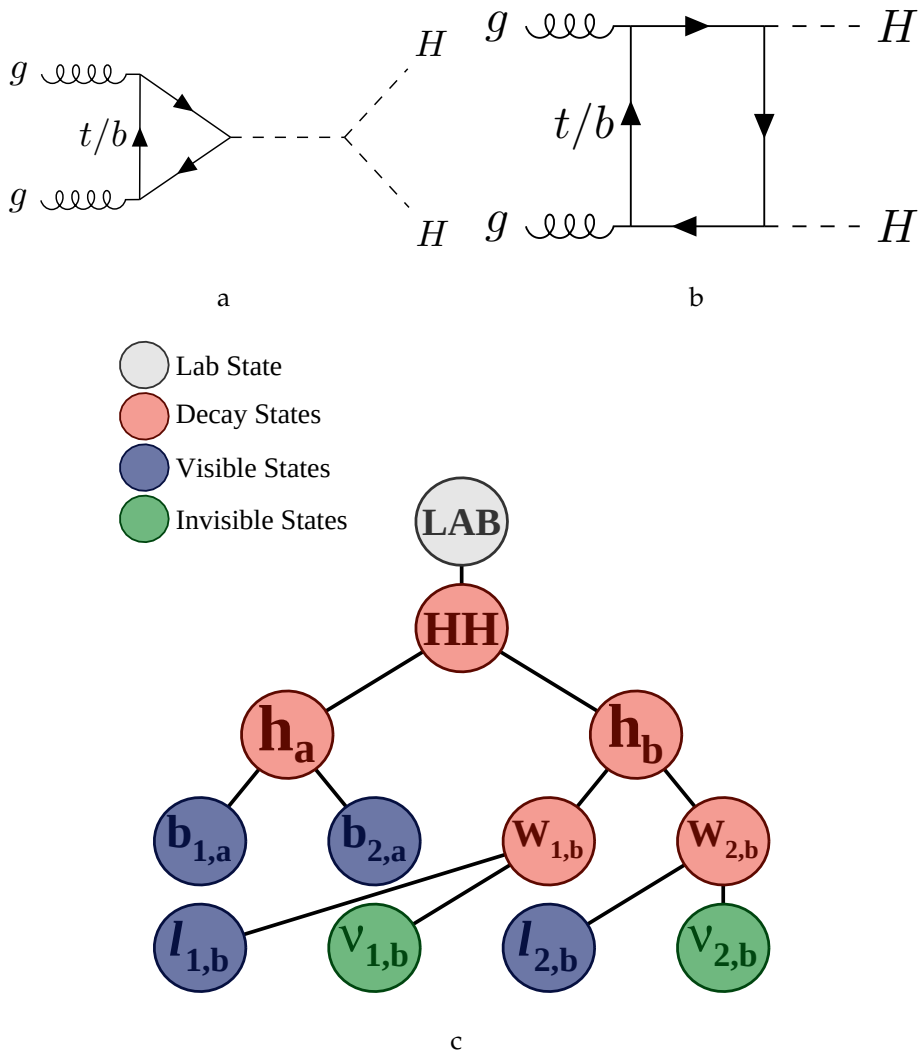

Figure 9.4: The two major ggF Higgs pair production modes (Figures 9.4a and 9.4b), and the RJR decay tree for the process (Figure 9.4c).

Some distributions indicating the how well the centre-of-mass frame is reconstructed (Figure 9.5a), the mass resolution of the W decaying Higgs (Figure 9.5b), the scale variable $H_{1,1}^{\mathrm{HH}}$ (Figure 9.5c), and the azimuthal angle between the two leptons in the CM frame (Figure 9.5d).

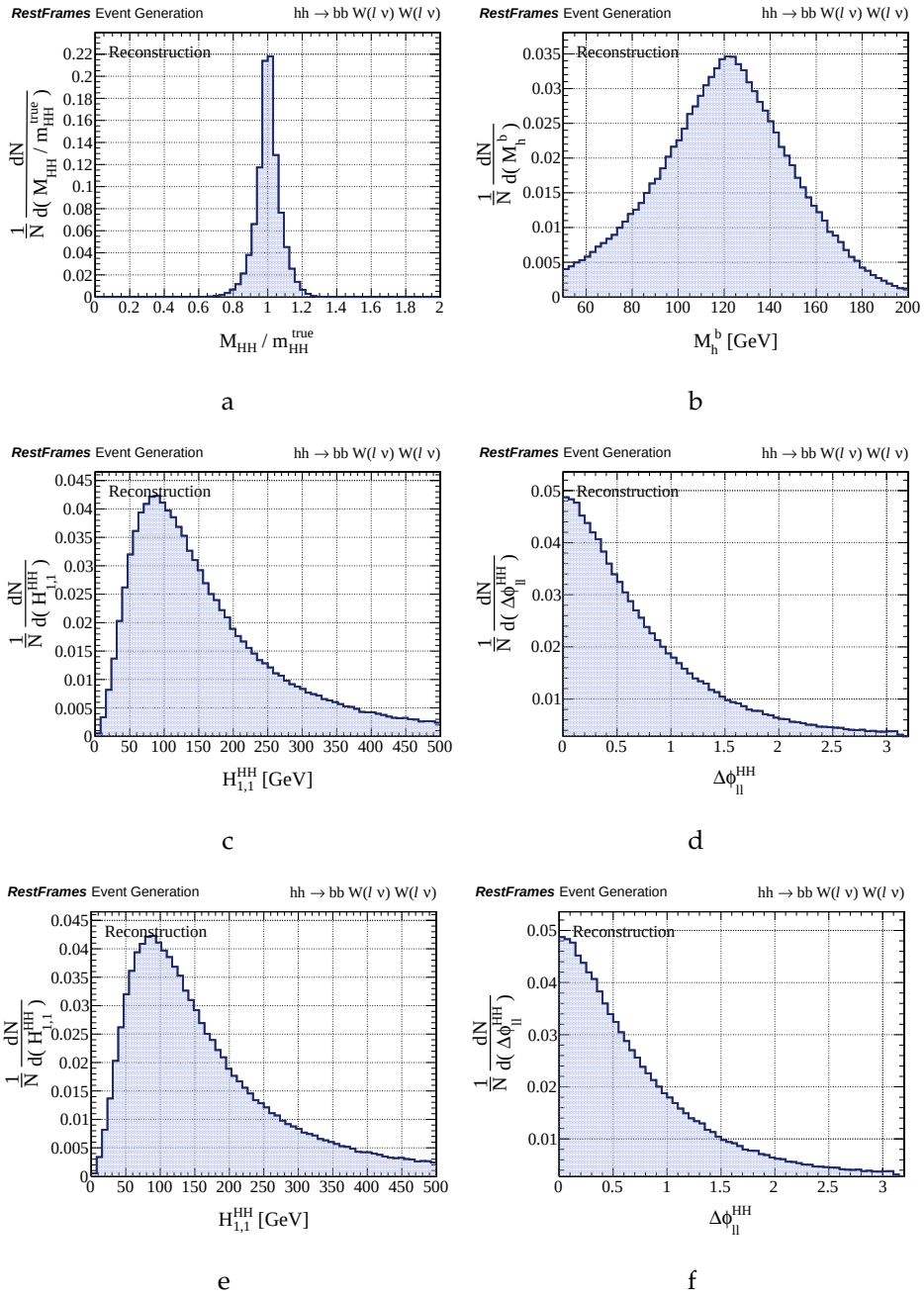

Figure 9.5: (Figure 9.5a) Centre-of-mass mass resolution for the di-Higgs process as a function of the generator mass, (Figure 9.5b) the reconstructed mass of the Higgs decaying to W bosons, (Figure 9.5c) the scale variable $H_{1,1}^{\mathrm{HH}}$ made from the vector sum of visible objects scalar summed with missing energy in the HH frame, (Figure 9.5d) the azimuthal angle between the two leptons in the process evaluated in the HH frame, (Figure 9.5e).

9.3 $t\bar{t}H \to bW^+\bar{b}W^-b\bar{b} \to b\ell\nu\bar{b}\ell\nu b\bar{b}$

The $t\bar{t}H$ production process is experimentally challenging and theoretically important for both top and Higgs physics, being a direct probe of the top quark Yukawa coupling. The final state where the $t\bar{t}$ decays leptonically and the Higgs boson decays to b quarks has been studied by both ATLAS [147] and CMS [148] (Figure 9.6), with signal strengths below what is expected. Improvements in this channel can come from understanding $t\bar{t} + b\bar{b}$ backgrounds, but advancements in analysis technique can also have an effect on sensitivity.

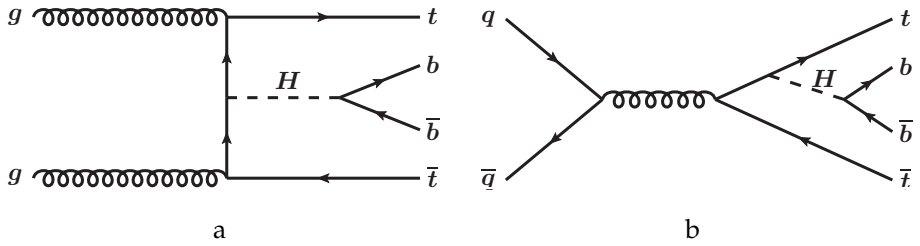

Figure 9.6: Figure 9.6a and Figure 9.6b show the two leading $t\bar{t}H$ production modes.

Figure 9.7a shows the RJR decay tree used to reconstruct the events with the full suite of jigsaw rules linking the various frames. This final state can have up to four b-jets which need to be assigned to either one of the top decays or to the Higgs, done here using mass minimisation jigsaw rules (Figure 9.7b). Importantly, this procedure is independent of the b-tagging score of the jets involved, relying purely on kinematics instead. There is also the matter of resolving the neutrinos associated with the two tops, which is done in this case by associating the rapidity with the two visible leptons and assuming that the W masses are the same (Figure 9.7c). This leads to good centre-of-mass resolution as shown in Figure 9.7d. This procedure leads to decent W mass resolution (Figure 9.7e), with a wider spread in the top mass resolution (Figure 9.7f). Given the good centre-of-mass resolution, using variables derived in that CM frame is a good way to find quantities that cannot be mimicked by processes which do not share the same topology and CM structure. These usually take the form of scale variables (Figure 9.8a), and ratios between those scale variables (Figure 9.8b).

This decay tree is not however specific to the $H \to b\bar{b}$ final state. Any final state where $t\bar{t}$ is recoiling against some jets, regardless of resonance structure, can be targeted by requiring certain numbers of jets into the other frames. For example $t\bar{t}W$, a major background for both $t\bar{t}t\bar{t}$ and $t\bar{t}H$ can also be constructed in this way, along with the alternative two lepton final state as outlined in Section 9.4.

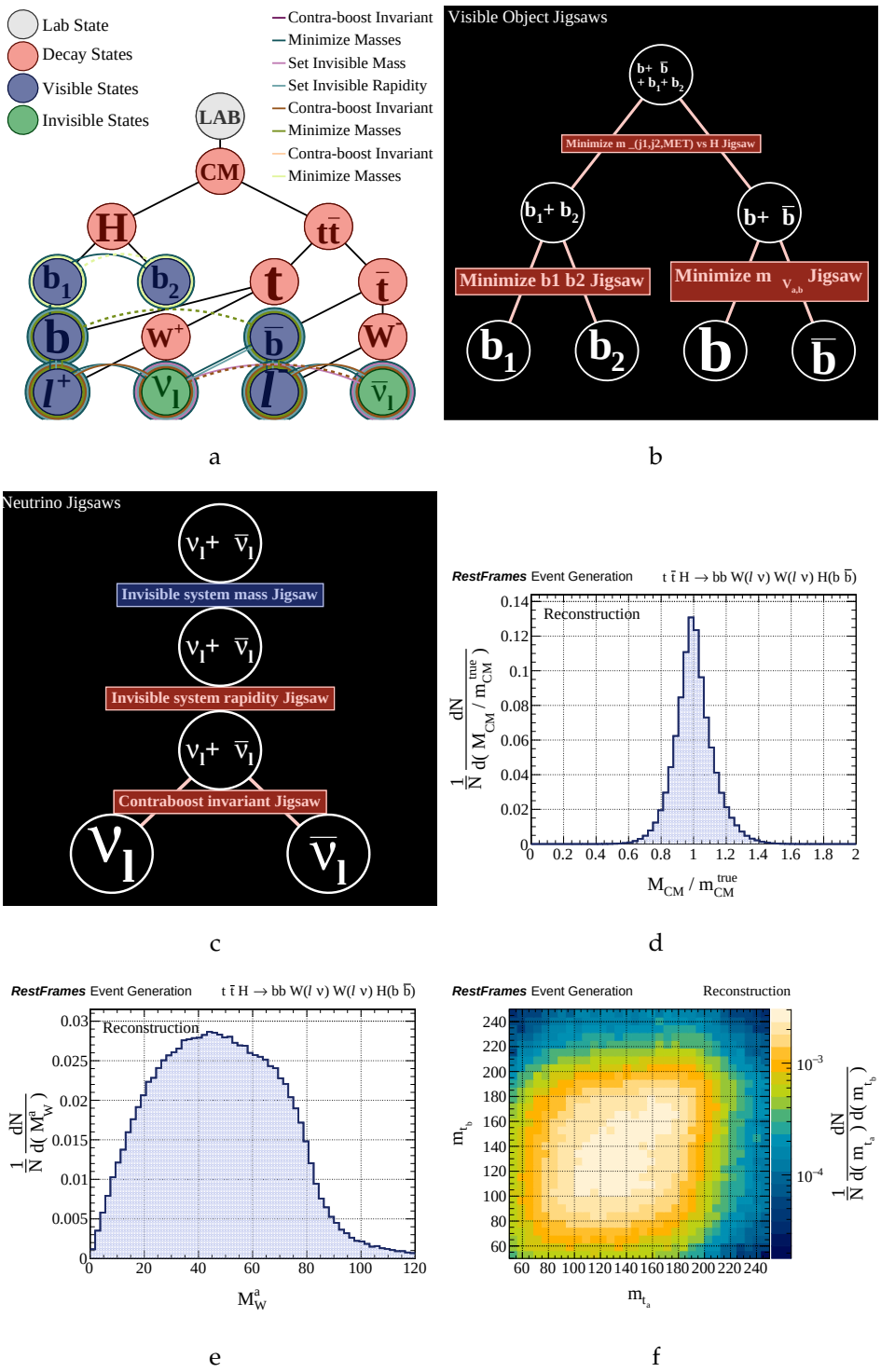

Figure 9.7: (Figure 9.7a) Decay tree structure for $t\bar{t}H$ production with dileptonic $t\bar{t}$ decays, (Figure 9.7b) a schematic representation of the combinatoric rules for assigning jets to the frames, (Figure 9.7c) a schematic of the invisible jigsaw rules for the two neutrinos, (Figure 9.7d) the centre-of-mass resolution for these jigsaw rules, (Figure 9.7e) the W mass resolution, (Figure 9.7f) the mass resolution of the two top quarks.

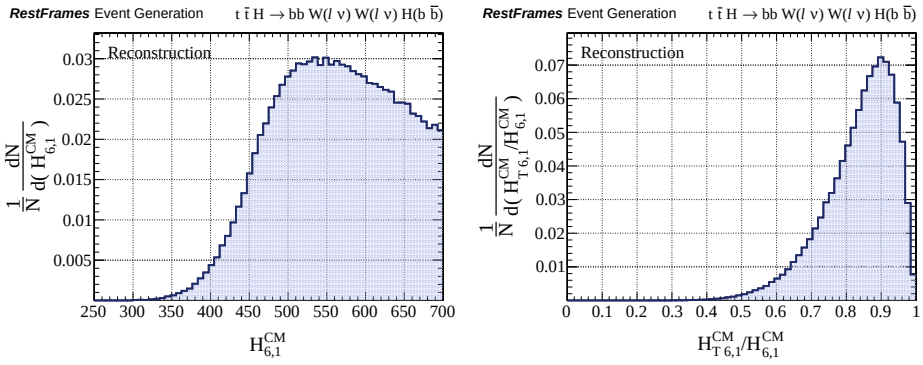

a b

Figure 9.8: (Figure 9.8a) the scale variable $H^{CM}_{6,1}$ made from the scalar sum of all visible objects and the invisible objects, (Figure 9.8b) The ratio of $H^{CM}_{\mathrm{T}6,1}$ and $H^{CM}_{6,1}$ which measures how transverse the event is.

9.4 $t\bar{t}W \rightarrow bjj\bar{b}\ell\nu\ell\nu$

In addition being a background in Higgs and $t\bar{t}t\bar{t}$ searches, the $t\bar{t}W$ process is interesting it its own right. Studies of $t\bar{t}$ polarisation at proton-proton colliders can be done by proxy by measuring the charge asymmetry of $t\bar{t}W$ [149]. Both CMS and ATLAS have made simultaneous measurements of the $t\bar{t}Z$ and $t\bar{t}W$ cross sections using 2015 and 2016 data [150, 151], and the opportunity exists to make use of the full LHC Run 2 dataset to more fully study $t\bar{t}W$.

In a scenario where one top quark decays hadronically, the other leptonically, and the lone W decays leptonically, the charge of the lone W is simple to measure provided the leptons are assigned correctly (Figure 9.9a). Here the additional jets in the hadronically decaying W as well as the combinatoric ambiguity of the lepton assignment between a top and the lone W means two combinatoric rules for assigning the jets and leptons, shown in Figure 9.9b and Figure 9.9d respectively. To assign the jets there are three rules used: one for the W itself, another for the hadronic top, and a third for the hadronic top and the b-jet from the other top. There are also rules relating to the splitting of the $E_{\mathrm{T}}^{\mathrm{miss}}$ into the two neutrinos shown in Figure 9.9c.

To measure charge asymmetry of $t\bar{t}$ at proton-proton colliders, the top and anti-top need to be identified and their pseudorapidities need to be measured. The charge asymmetry is defined by

$$A_c^t = \frac{N\left(\Delta_\eta^t > 0\right) - N\left(\Delta_\eta^t < 0\right)}{N\left(\Delta_\eta^t > 0\right) + N\left(\Delta_\eta^t < 0\right)}, \tag{9.1}$$

with $\Delta_\eta^t = |\eta_t| - |\eta_{\bar{t}}|$. Using the method outlined above the identification of the tops is relatively straightforward since the kinematics dictates the assignment of the leptons and hence the charge of the parent quark. In addition the reconstruction of the top quark rest frames allows for determination of the four vectors of the quarks in any other rest frame, including the lab frame. Figure 9.10a shows the CM frame mass resolution, while Figure 9.10b shows that the mass of the lone W is not as sharply defined as the CM, and Figures 9.10c and 9.10d are the η distributions of the initial top and anti-top quarks.

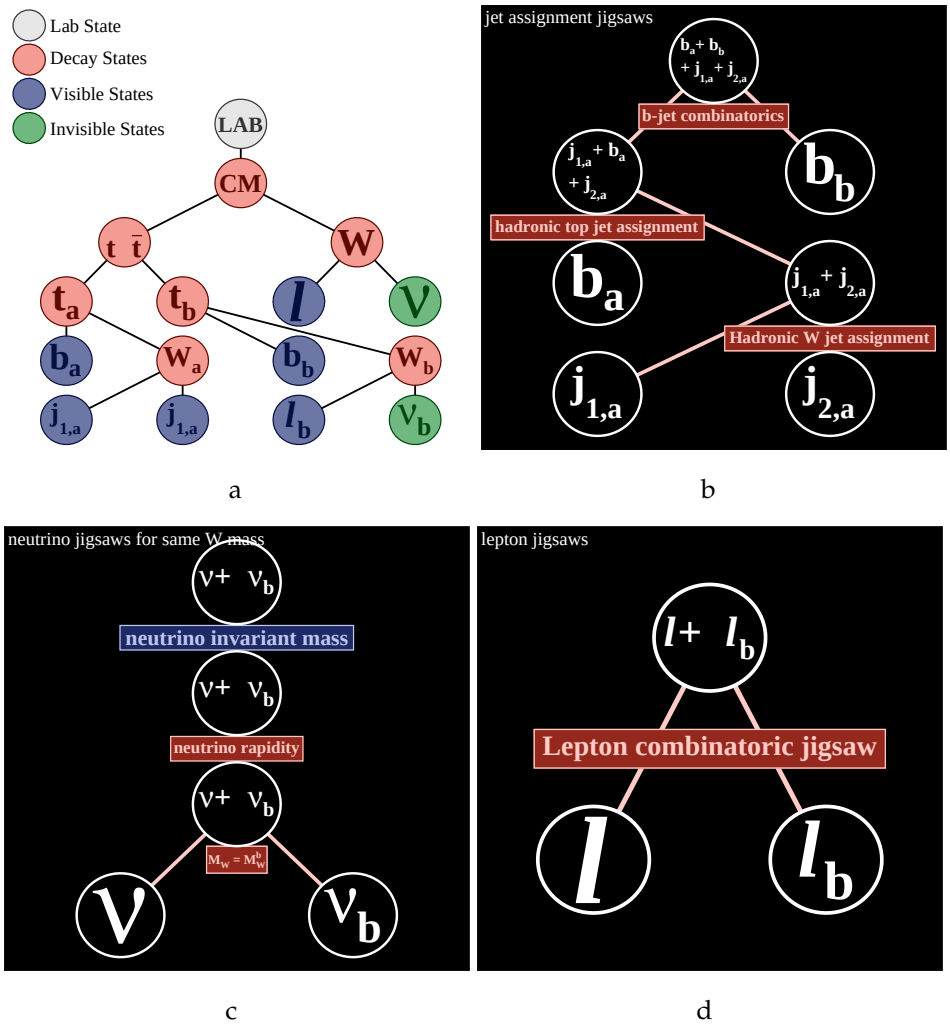

a b c d

Figure 9.9: (Figure 9.9a) Decay tree structure for $t\bar{t}W$ production with 2 lepton final states, (Figure 9.9b) a schematic representation of the combinatoric rules for assigning jets to the frames, (Figure 9.9c) a schematic of the invisible jigsaw rules for the two neutrinos, (Figure 9.9d) a schematic of the combinatoric jigsaw rule for assigning the leptons.

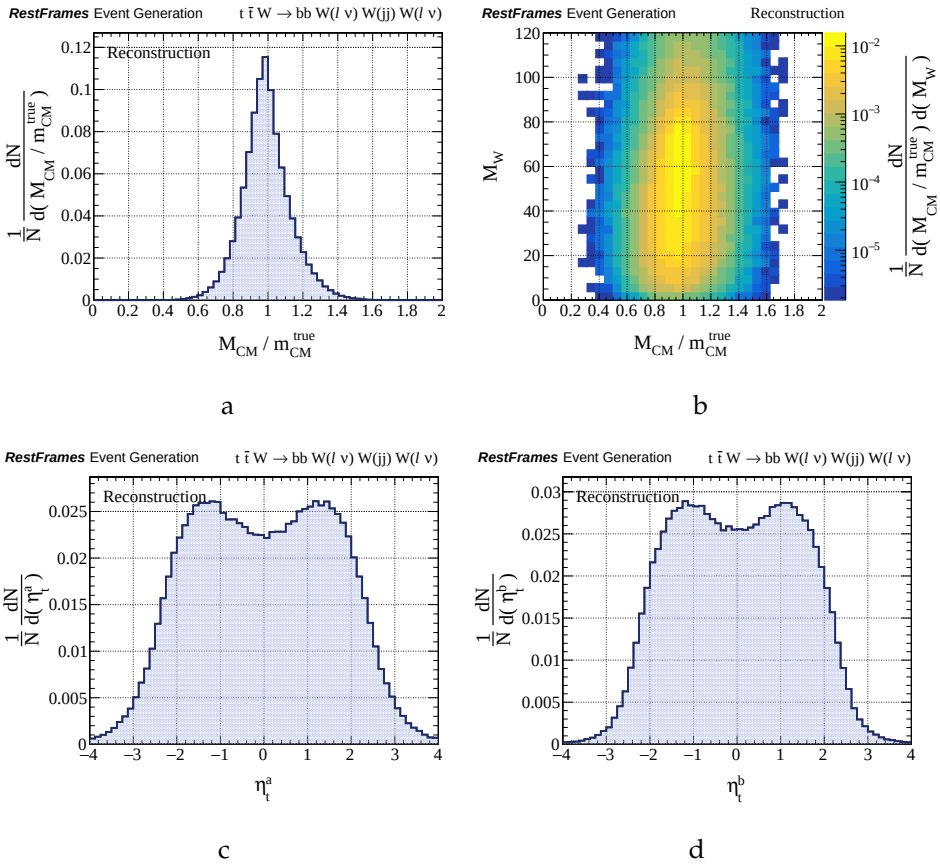

Figure 9.10: (Figure 9.10a) The CM resolution for $t\bar{t}W$ reconstruction, (Figure 9.10b) the relationship between mass of the lone W mass and the CM resolution, (Figures 9.10c and 9.10d) the η of the top and anti-top quark in the lab frame.

9.5 $t\bar{t}t\bar{t}$ decays to 2 and 3 lepton final states

$t\bar{t}t\bar{t}$ is a rare SM process that, aside from being sensitive to many BSM models, is an experimental challenge in its own right. With the top quark decaying nearly universally to $b + W$, the different decay modes of $t\bar{t}t\bar{t}$ are determined by the decays of the four W bosons in the process: from one lepton and many jets, to four leptons and four jets. While the one and two opposite charged lepton channels make up the bulk of the branching ratio, the dominant and difficult to simulate $t\bar{t}$ +jets backgrounds makes them a tough prospect. By asking for two same charge leptons (2ℓSS) or three leptons (3ℓ) the major backgrounds shift to being $t\bar{t} + W$, $t\bar{t} + Z$, and even $t\bar{t} + H$, which are more manageable. Despite the lower branching ratio of these processes there is sufficient sensitivity. Both ATLAS [152] and CMS [153] have recently released results for these final states with LHC Run 2 data, with hadronic τ decays not being considered. While the CMS result is consistent at 2.7 σ with the SM production cross section of around 12 fb, the ATLAS result is at 4.3 σ with a higher cross section of 24 fb, with both results having large uncertainties relating to the difficult to simulate signal and background processes. Both collaborations use BDT classifiers to separate signal from backgrounds, with object momenta and multiplicities as input along with some scale and angular variables relating objects.

Treating this process with RJR involves splitting the two final states into separate decay trees and determining what combinatoric rules are needed to assign objects to various frames. For simplicity the hadronic top decays are treated as single collection of all the relevant jets, while the leptonic top decays are reconstructed in more detail to allow for the calculation of neutrino momenta.

For 2ℓ final states the two leptons are accompanied by at least six jets, which can originate from the W bosons or directly from the top decays. A combinatoric rule that is agnostic to jet flavour is used to assign all jets in the event (with b-tag information) to the frames based on mass minimisation. The missing degrees of freedom for the two neutrinos are calculated in a similar fashion to the other examples. In the 3ℓ channel the situation is similar but with the modification of the invisible jigsaw rule to accommodate the extra neutrino. Both the decay trees with jigsaw rules applied are shown in Figure 9.11.

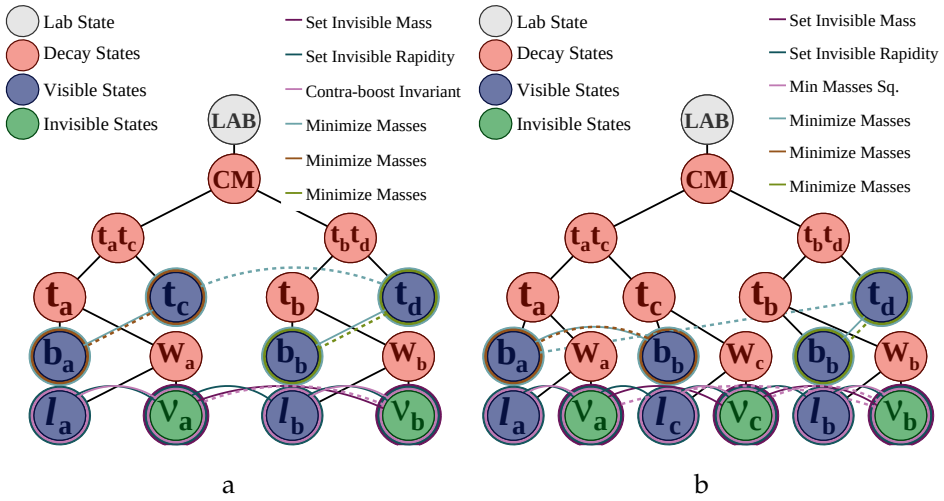

Figure 9.11: Figure 9.11a shows the decay tree for two lepton $t\bar{t}t\bar{t}$ final states, and Figure 9.11b shows the 3 lepton decay tree. The jigsaw rules applied are shown as lines between the frames.

With more granular information regard each of the reconstructed top quarks a number of variables can be derived to separate the $t\bar{t}t\bar{t}$ signal from the $t\bar{t}+W$ and $t\bar{t}+Z$ backgrounds. Distributions of some of the derived variables are shown in Figure 9.12, with signal MC overlaid to highlight shape discrimination, and focusing on those which are common to both types of reconstruction. There is no requirement on the charge of the leptons nor on the jet b-tagging scores in either reconstruction. Figures 9.12a to 9.12c are the scale variables $H_{n,1}^{\mathrm{CM}}$, made of scalar sum of the visible objects and the vector sum of the invisible objects for both final states and their sum: There are clear background peaks separated from the $t\bar{t}t\bar{t}$ signal in the tails. Figures 9.12d to 9.12f shows the b-tagging score (here mv2_c10) for both final states and their sum: the $t\bar{t}t\bar{t}$ peaks at higher b-tag values. The number of jets assigned to each frame can also be counted, such as for the hadronic top frames. The two 2ℓ hadronic tops are shown in Figures 9.12g and 9.12h, and the lone 3ℓ hadronic top is in Figure 9.12i. The jet multiplicity is only really useful in the 2ℓ case where t_c has clear separation between the single jet assigned for most of the backgrounds compared with more jets for the signal. Furthermore, by being more granular in asking for specific multiplicities and flavour content of some frames, the mis-assignment of objects can be mitigated. An example is shown in Figure 9.13, where the b-tagging

score of the reconstructed tops are shown for both 2 and 3ℓ final states.

Other variables to test the $t\bar{t}t\bar{t}$ hypothesis include Tbalance, which measures the momentum taken by $t_a t_c$ against $t_b t_d$ (Figures 9.14a to 9.14c), $\frac{p_{\mathrm{T}}^{\mathrm{lab}}}{p_{\mathrm{T}}^{\mathrm{lab}}+H_{\mathrm{T}n,1}}$ as described in previous chapters (Figures 9.14d to 9.14f), and the ratio of the vector summed $H_{1,1}^{\mathrm{CM}}$ with the previously shown scalar summed $H_{n,1}^{\mathrm{CM}}$ (Figures 9.14g to 9.14i).

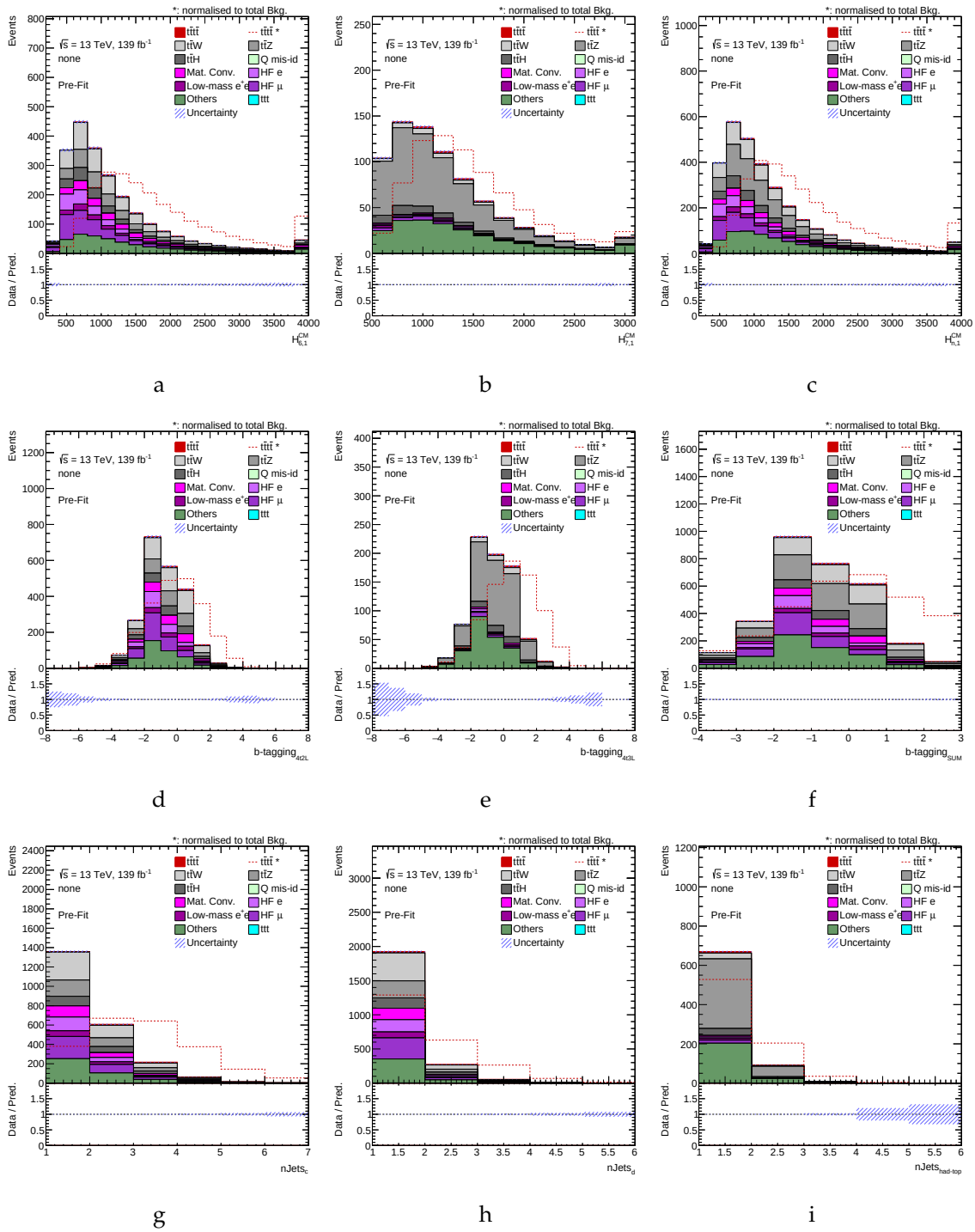

Figure 9.12: 2ℓ and 3ℓ distributions, along with combinations of similar variables. The dashed red line shows the signal MC reweighted to match the total yield of the background, useful for measuring shape differences in the distributions. The description of each variable is given the text.

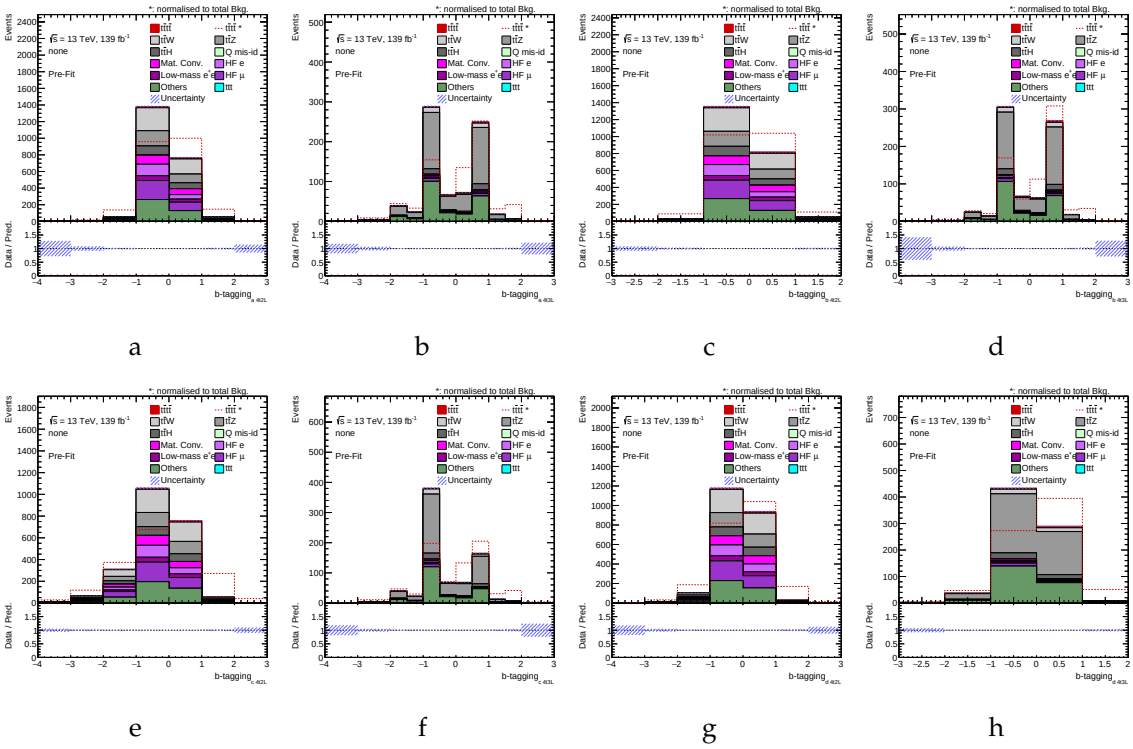

Figure 9.13: 2ℓ (left column) and 3ℓ (right column) b-tagging distributions for the four top frames ($T_a \to J_d$ across rows). The dashed red line shows the signal MC reweighted to match the total yield of the background, useful for measuring shape differences in the distributions.

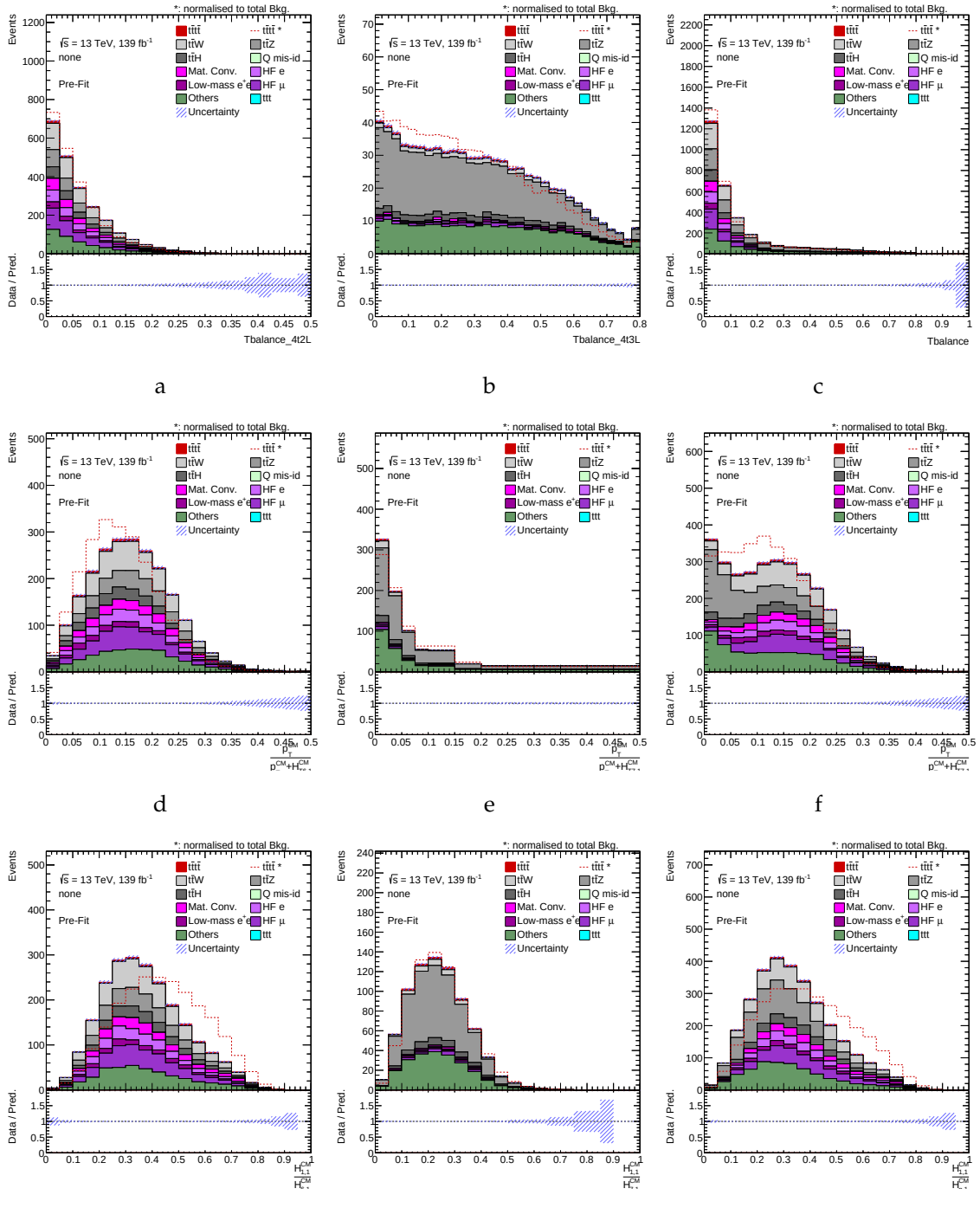

Figure 9.14: 2ℓ and 3ℓ $t\bar{t}t\bar{t}$ distributions, along with combinations of similar variables. The dashed red line shows the signal MC reweighted to match the total yield of the background, useful for measuring shape differences in the distributions. The description of each variable is given the text.

9.6 Orthogonally combining analyses

Very often the same event can be reconstructed under a variety of decay trees. An event with two leptons, four jets, and some $E_{\mathrm{T}}^{\mathrm{miss}}$ can be reconstructed under $t\bar{t}W$, $t\bar{t}H$, or $t\bar{t}Z$ in various combinations of the decay modes for the constituent W, H and Z. The addition of extra jets also brings $t\bar{t}t\bar{t}$ into the mix, and the same logic holds for 3ℓ final states. While in the electroweak SUSY analysis jet multiplicity was used to make different treatments orthogonal, here being inclusive in jets is a desirable feature, especially when extra radiation is commonplace.

Determining whether an event is best described under a certain reconstruction type is important for orthogonally defining analyses. Using boost testing variables as defined in Equations 6.16 and 6.18 can be helpful, with $R_{p_{\mathrm{T}}}$ being a good candidate given the conservation of transverse momentum at hadron colliders:

$$R_{p_{\mathrm{T}}} = \frac{p_{\mathrm{PP,T}}^{\mathrm{lab}}}{\left(p_{\mathrm{PP,T}}^{\mathrm{lab}} + H_{\mathrm{T}\ n,m}^{\mathrm{PP}}\right)}. \tag{9.2}$$

By categorising events based on what reconstruction gives the lowest $R_{p_{\mathrm{T}}}$ value, orthogonal populations of events can be defined. This makes the definition of control and validation regions easier along with extracting signal strengths. There is one caveat: the calculation of $R_{p_{\mathrm{T}}}$ must be robust, and must peak in the same way for the different reconstructions, which is not the case for the two $t\bar{t}t\bar{t}$ final states discussed previously.

10 Conclusion

BSM searches at the LHC have so far not yielded any lasting hints of supersymmetry or other theoretical models. This has encouraged the use of more advanced techniques in event reconstruction and kinematic variable development, allowing for more complete exploration of the space of new physics models. In addition other signatures of new physics with lower production cross sections but cleaner signals are being pursued.

Both advances in detector performance and object reconstruction as well as analysis techniques are required to improve the sensitivity to new physics models. This thesis touched on the first part with improvements in low energy electron identification, and the first electron identification efficiency measurements down to 4.5 GeV at ATLAS. An application to electroweak SUSY searches with very low mass splittings was outlined, with improvements in limits over previous compressed analyses. The next step is Recursive Jigsaw Reconstruction, which has been used in previous SUSY searches at ATLAS. This thesis gave a more analysis design focused description of RJR, with a review of common variables and their usage across a range of kinematic regimes.

This thesis presented a search for electroweakinos of the supersymmetric standard model with two and three lepton final states using Recursive Jigsaw Reconstruction. The use of specific decays trees for fully resolved final states and a generic ISR decay tree allowed for coverage of high, intermediate and Z mass scale splittings in the SUSY models considered. For $m_{\tilde{\chi}_2^0/\tilde{\chi}_1^\pm} - m_{\tilde{\chi}_1^0} \approx 100$ GeV the two types of tree overlapped in efficacy but remained orthogonal by construction. This allowed for probing of a difficult kinematic region without the usual suite of harsh selections on objects. While the high and intermediate mass regions set the strongest limits

on $\tilde{\chi}_2^0/\tilde{\chi}_1^\pm$ production with 2015-16 data, the low and ISR regions showed a set of excesses, with the largest being 3σ from the SM background estimate. This result was at odds with other analyses which had excluded the signal point, but selected a set of events from a largely complementary phase space. This analysis was also implemented into a global fit with GAMBIT, quantifying the relationship of the observed data with possible electroweak SUSY signal models and other analyses.

Given the excesses of the 2015-16 dataset, a follow up analysis concentrating on the four low mass and ISR signal regions was of great importance. The signal regions themselves were frozen, but the full Run 2 dataset required the use of updated object definitions and the data-driven Z+jets estimate was revised to avoid the large uncertainties of the previous analysis. Though the excesses did not persist, the lessons learned in designing BSM analyses away from the usual paradigms are important for future analyses in inconvenient regions of phase space.

Finally this thesis paved the way for some future work with RJR, especially in top physics as part of a combined $t\bar{t} + X$ framework. Various processes from $t\bar{t}H$ to $t\bar{t}t\bar{t}$ can be studied using a set of principles based on resolving the kinematic and combinatoric ambiguities of the event, without needing to know lepton flavour or jet flavour-tagging score.

Bibliography

[1] S. L. Glashow, *Partial-symmetries of weak interactions*, Nuclear Physics **22** (1961) 579, ISSN: 0029-5582, URL: http://www.sciencedirect.com/science/article/pii/0029558261904692.

[2] S. Weinberg, *A Model of Leptons*, Phys. Rev. Lett. **19** (1967) 1264.

[3] A. Salam, *Weak and Electromagnetic Interactions*, Conf. Proc. **C680519** (1968) 367.

[4] ATLAS Collaboration, *Combined search for the Standard Model Higgs boson in pp collisions at $\sqrt{s} = 7$ TeV with the ATLAS detector*, Phys. Rev. D **86** (2012) 032003, arXiv: 1207.0319 [hep-ex].

[5] CMS Collaboration, *Observation of a new boson at a mass of 125 GeV with the CMS experiment at the LHC*, Phys. Lett. B **716** (2012) 30, arXiv: 1207.7235 [hep-ex].

[6] The ATLAS Collaboration, *ATLAS Standard Model*, [Online; accessed 22 September 2019].

[7] E. Noether, *Invariante Variationsprobleme*, ger, Nachrichten von der Gesellschaft der Wissenschaften zu Göttingen, Mathematisch-Physikalische Klasse **1918** (1918) 235, URL: http://eudml.org/doc/59024.

[8] F. Englert and R. Brout, *Broken Symmetry and the Mass of Gauge Vector Mesons*, Phys. Rev. Lett. **13** (9 1964) 321, URL: https://link.aps.org/doi/10.1103/PhysRevLett.13.321.

[9] P. W. Higgs, *Broken Symmetries and the Masses of Gauge Bosons*, Phys. Rev. Lett. **13** (16 1964) 508, URL: https://link.aps.org/doi/10.1103/PhysRevLett.13.508.

[10] G. S. Guralnik, C. R. Hagen and T. W. B. Kibble, *Global Conservation Laws and Massless Particles*, Phys. Rev. Lett. **13** (20 1964) 585, URL: https://link.aps.org/doi/10.1103/PhysRevLett.13.585.

[11] F. Zwicky, *Die Rotverschiebung von extragalaktischen Nebeln*, Helv. Phys. Acta **6** (1933) 110, [Gen. Rel. Grav.41,207(2009)].

[12] A. Bosma, *21-cm line studies of spiral galaxies. II. The distribution and kinematics of neutral hydrogen in spiral galaxies of various morphological types.*, The Astronomical Journal **86** (1981) 1825.

[13] V. C. Rubin, D. Burstein, J. Ford W. K. and N. Thonnard, *Rotation velocities of 16 SA galaxies and a comparison of Sa, SB and SC rotation properties.*, The Astrophysical Journal **289** (1985) 81.

[14] R. Massey, T. Kitching and J. Richard, *The dark matter of gravitational lensing*, Reports on Progress in Physics **73** (2010) 086901, URL: https://doi.org/10.1088%2F0034-4885%2F73%2F8%2F086901.

[15] P. Collaboration et al., *Planck 2018 results. VI. Cosmological parameters*, 2018, arXiv: 1807.06209 [astro-ph.CO].

[16] The ATLAS Collaboration, *ATLAS Dark Matter*, [Online; accessed 23 September 2019].

[17] Tanabashi, M, et. al. (Particle Data Group), *Neutrino Masses, Mixing, and Oscillations*, Phys. Rev, D **98** (2018 and 2019 update) 030001.

[18] Yu. A. Golfand and E. P. Likhtman, *Extension of the Algebra of Poincare Group Generators and Violation of p Invariance*, JETP Lett. **13** (1971) 323, [Pisma Zh. Eksp. Teor. Fiz. **13** (1971) 452].

[19] D. V. Volkov and V. P. Akulov, *Is the Neutrino a Goldstone Particle?*, Phys. Lett. B **46** (1973) 109.

[20] J. Wess and B. Zumino, *Supergauge Transformations in Four-Dimensions*, Nucl. Phys. B **70** (1974) 39.

[21] J. Wess and B. Zumino, *Supergauge Invariant Extension of Quantum Electrodynamics*, Nucl. Phys. B **78** (1974) 1.

[22] S. Ferrara and B. Zumino, *Supergauge Invariant Yang-Mills Theories*, Nucl. Phys. B **79** (1974) 413.

[23] A. Salam and J. A. Strathdee, *Supersymmetry and Nonabelian Gauges*, Phys. Lett. B **51** (1974) 353.

[24] S. P. Martin, *A Supersymmetry primer*, Adv. Ser. Direct. High Energy Phys. **18** (1998) 1, arXiv: hep-ph/9709356.

[25] R. Haag, J. T. Łopuszański and M. Sohnius, *All possible generators of supersymmetries of the S-matrix*, Nuclear Physics B **88** (1975) 257, ISSN: 0550-3213, URL: http://www.sciencedirect.com/science/article/pii/0550321375902795.

[26] S. Coleman and J. Mandula, *All Possible Symmetries of the S Matrix*, Phys. Rev. **159** (5 1967) 1251, URL: https://link.aps.org/doi/10.1103/PhysRev.159.1251.

[27] M. Tanabashi et al., *Review of Particle Physics*, Phys. Rev. D **98** (3 2018) 030001, URL: https://link.aps.org/doi/10.1103/PhysRevD.98.030001.

[28] P. Fayet and J. Iliopoulos, *Spontaneously broken supergauge symmetries and goldstone spinors*, Physics Letters B **51** (1974) 461, ISSN: 0370-2693, URL: http://www.sciencedirect.com/science/article/pii/0370269374903104.

[29] L. O'Raifeartaigh, *Spontaneous Symmetry Breaking for Chiral Scalar Superfields*, Nucl. Phys. **B96** (1975) 331.

[30] L. Evans and P. Bryant, *LHC Machine*, JINST **3** (2008) S08001.

[31] A. Collaboration, *ATLAS detector and physics performance: Technical Design Report, 1*, Technical Design Report ATLAS, CERN, 1999, URL: https://cds.cern.ch/record/391176.

[32] A. Collaboration, *ATLAS detector and physics performance: Technical Design Report, 2*, Technical Design Report ATLAS, CERN, 1999, URL: https://cds.cern.ch/record/391177.

[33] The ATLAS Collaboration, *Computer generated image of the whole ATLAS detector*, [Online; accessed 21 June 2019], 2015.

[34] ATLAS Collaboration, *ATLAS Insertable B-Layer Technical Design Report*, ATLAS-TDR-19, 2010, URL: https://cds.cern.ch/record/1291633, Addendum: ATLAS-TDR-19-ADD-1, 2012, URL: https://cds.cern.ch/record/1451888.

[35] G. Aad et al., *Technical Design Report for the Phase-I Upgrade of the ATLAS TDAQ System*, (2013).

[36] ATLAS Collaboration, *Performance of the ATLAS track reconstruction algorithms in dense environments in LHC Run 2*, Eur. Phys. J. C **77** (2017) 673, arXiv: 1704.07983 [hep-ex].

[37] ATLAS Collaboration, *Muon reconstruction performance of the ATLAS detector in proton–proton collision data at* $\sqrt{s} = 13\,TeV$, Eur. Phys. J. C **76** (2016) 292, arXiv: 1603.05598 [hep-ex].

[38] ATLAS Collaboration, *Electron reconstruction and identification in the ATLAS experiment using the 2015 and 2016 LHC proton–proton collision data at* $\sqrt{s} = 13\,TeV$, Eur. Phys. J. C **79** (2019) 639, arXiv: 1902.04655 [hep-ex].

[39] T. A. Collaboration, *Electron and photon performance measurements with the ATLAS detector using the 2015–2017 LHC proton-proton collision data*, Journal of Instrumentation **14** (2019) P12006, URL: https://doi.org/10.1088%2F1748-0221%2F14%2F12%2Fp12006.

[40] M. Cacciari, G. P. Salam and G. Soyez, *The anti-k_t jet clustering algorithm*, JHEP **04** (2008) 063, arXiv: 0802.1189 [hep-ph].

[41] ATLAS Collaboration, *Jet energy scale measurements and their systematic uncertainties in proton–proton collisions at* $\sqrt{s} = 13\,TeV$ *with the ATLAS detector*, Phys. Rev. D **96** (2017) 072002, arXiv: 1703.09665 [hep-ex].

[42] ATLAS Collaboration, *Constituent-level pile-up mitigation techniques in ATLAS*, ATLAS-CONF-2017-065, 2017, URL: https://cds.cern.ch/record/2281055.

[43] ATLAS Collaboration, *Optimisation and performance studies of the ATLAS b-tagging algorithms for the 2017-18 LHC run*, ATL-PHYS-PUB-2017-013, 2017, URL: https://cds.cern.ch/record/2273281.

[44] ATLAS Collaboration, *ATLAS b-jet identification performance and efficiency measurement with* $t\bar{t}$ *events in* pp *collisions at* $\sqrt{s} = 13\,TeV$, (2019), arXiv: 1907.05120 [hep-ex].

[45] ATLAS Collaboration, *Search for the Decay of the Higgs Boson to Charm Quarks with the ATLAS Experiment*, Phys. Rev. Lett. **120** (2018) 211802, arXiv: 1802.04329 [hep-ex].

[46] ATLAS Collaboration, *Performance and Calibration of the JetFitterCharm Algorithm for c-Jet Identification*, ATL-PHYS-PUB-2015-001, 2015, URL: https://cds.cern.ch/record/1980463.

[47] ATLAS Collaboration, *Measurement of the tau lepton reconstruction and identification performance in the ATLAS experiment using pp collisions at* $\sqrt{s} = 13$ *TeV*, ATLAS-CONF-2017-029, 2017, URL: https://cds.cern.ch/record/2261772.

[48] ATLAS Collaboration, E_T^{miss} *performance in the ATLAS detector using 2015–2016 LHC pp collisions*, ATLAS-CONF-2018-023, 2018, URL: https://cds.cern.ch/record/2625233.

[49] ATLAS Collaboration, *Performance of pile-up mitigation techniques for jets in pp collisions at* $\sqrt{s} = 8$ *TeV using the ATLAS detector*, Eur. Phys. J. C **76** (2016) 581, arXiv: 1510.03823 [hep-ex].

[50] ATLAS Collaboration, *Identification and rejection of pile-up jets at high pseudorapidity with the ATLAS detector*, Eur. Phys. J. C **77** (2017) 580, arXiv: 1705.02211 [hep-ex], Erratum: Eur. Phys. J. C **77** (2017) 712.

[51] V. N. Gribov and L. N. Lipatov, *Deep inelastic e p scattering in perturbation theory*, Sov. J. Nucl. Phys. **15** (1972) 438, [Yad. Fiz.15,781(1972)].

[52] G. Altarelli and G. Parisi, *Asymptotic Freedom in Parton Language*, Nucl. Phys. **B126** (1977) 298.

[53] Y. L. Dokshitzer, *Calculation of the Structure Functions for Deep Inelastic Scattering and e+ e- Annihilation by Perturbation Theory in Quantum Chromodynamics.*, Sov. Phys. JETP **46** (1977) 641, [Zh. Eksp. Teor. Fiz.73,1216(1977)].

[54] B. Andersson, G. Gustafson, G. Ingelman and T. Sjöstrand, *Parton fragmentation and string dynamics*, Physics Reports **97** (1983) 31, ISSN: 0370-1573, URL: http://www.sciencedirect.com/science/article/pii/0370157383900807.

[55] S. Agostinelli et al., *GEANT4: A Simulation toolkit*, Nucl. Instrum. Meth. A **506** (2003) 250.

[56] P. Clark, *The ATLAS Detector Simulation*, Nuclear Physics B - Proceedings Supplements **215** (2011) 85, Proceedings of the 12th Topical Seminar on Innovative Particle and Radiation Detectors (IPRD10), ISSN: 0920-5632, URL: http://www.sciencedirect.com/science/article/pii/S092056321100212X.

[57] W. Lukas, *Fast Simulation for ATLAS: Atlfast-II and ISF*, Journal of Physics: Conference Series **396** (2012) 022031, URL: https://doi.org/10.1088%2F1742-6596%2F396%2F2%2F022031.

[58] ATLAS Collaboration, *Electron efficiency measurements with the ATLAS detector using the 2015 LHC proton–proton collision data*, ATLAS-CONF-2016-024, 2016, URL: https://cds.cern.ch/record/2157687.

[59] ATLAS Collaboration, *Electron reconstruction and identification efficiency measurements in 2016 Data*, tech. rep. EGAM-2017-003, CERN, 2017, URL: https://atlas.web.cern.ch/Atlas/GROUPS/PHYSICS/PLOTS/EGAM-2017-003/index.html.

[60] ATLAS Collaboration, *Search for electroweak production of supersymmetric states in scenarios with compressed mass spectra at* $\sqrt{s} = 13$ *TeV with the ATLAS detector*, Phys. Rev. D **97** (2018) 052010, arXiv: 1712.08119 [hep-ex].

[61] P. Jackson and C. Rogan, *Recursive jigsaw reconstruction: HEP event analysis in the presence of kinematic and combinatoric ambiguities*, Physical Review D **96** (2017), ISSN: 2470-0029, URL: http://dx.doi.org/10.1103/PhysRevD.96.112007.

[62] UA1 Collaboration, *Experimental observation of isolated large transverse energy electrons with associated missing energy at s=540 GeV*, Physics Letters B **122** (1983) 103, ISSN: 0370-2693, URL: http://www.sciencedirect.com/science/article/pii/0370269383911772.

[63] C. Lester and D. Summers, *Measuring masses of semi-invisibly decaying particle pairs produced at hadron colliders*, Physics Letters B **463** (1999) 99, ISSN: 0370-2693, URL: http://www.sciencedirect.com/science/article/pii/S0370269399009454.

[64] C. Rogan, *Kinematical variables towards new dynamics at the LHC*, 2010, arXiv: 1006.2727 [hep-ph].

[65] M. R. Buckley, J. D. Lykken, C. Rogan and M. Spiropulu, *Super-razor and searches for sleptons and charginos at the LHC*, Physical Review D **89** (2014), ISSN: 1550-2368, URL: http://dx.doi.org/10.1103/PhysRevD.89.055020.

[66] C. Rogan, *RestFrames*, URL: restframes.com.

[67] M. Santoni, 'Probing supersymmetry with recursive jigsaw reconstruction', PhD thesis: CoEPP, School of Physical Sciences, University of Adelaide, 2017, URL: http://hdl.handle.net/2440/113432.

[68] *SUSY May 2020 Summary Plot Update*, tech. rep. ATL-PHYS-PUB-2020-013, CERN, 2020, URL: http://cds.cern.ch/record/2718947.

[69] P. Jackson, C. Rogan and M. Santoni, *Sparticles in motion: Analyzing compressed SUSY scenarios with a new method of event reconstruction*, Physical Review D **95** (2017), ISSN: 2470-0029, URL: http://dx.doi.org/10.1103/PhysRevD.95.035031.

[70] M. Santoni, *Probing compressed mass spectra in electroweak supersymmetry with Recursive Jigsaw Reconstruction*, Journal of High Energy Physics **2018** (2018), ISSN: 1029-8479, URL: http://dx.doi.org/10.1007/JHEP05(2018)058.

[71] ATLAS Collaboration, *Search for direct top squark pair production in final states with two leptons in $\sqrt{s} = 13$ TeV pp collisions with the ATLAS detector*, Eur. Phys. J. C **77** (2017) 898, arXiv: 1708.03247 [hep-ex].

[72] G. Aad et al., *Searches for electroweak production of supersymmetric particles with compressed mass spectra in $\sqrt{s} = 13$ TeV pp collisions with the ATLAS detector*, (2019), arXiv: 1911.12606 [hep-ex].

[73] ATLAS Collaboration, *Search for squarks and gluinos in final states with jets and missing transverse momentum using 36 fb^{-1} of $\sqrt{s} = 13$ TeV pp collision data with the ATLAS detector*, Phys. Rev. D **97** (2018) 112001, arXiv: 1712.02332 [hep-ex].

[74] ATLAS Collaboration, *Search for chargino–neutralino production using recursive jigsaw reconstruction in final states with two or three charged leptons in proton–proton collisions at* $\sqrt{s} = 13$ *TeV with the ATLAS detector*, Phys. Rev. D **98** (2018) 092012, arXiv: 1806.02293 [hep-ex].

[75] B. Fuks, M. Klasen, D. R. Lamprea and M. Rothering, *Precision predictions for electroweak superpartner production at hadron colliders with Resummino*, Eur. Phys. J. C **73** (2013) 2480, arXiv: 1304.0790 [hep-ph].

[76] ATLAS Collaboration, *Search for direct production of charginos, neutralinos and sleptons in final states with two leptons and missing transverse momentum in* pp *collisions at* $\sqrt{s} = 8$ *TeV with the ATLAS detector*, JHEP **05** (2014) 071, arXiv: 1403.5294 [hep-ex].

[77] ATLAS Collaboration, *Search for direct production of charginos and neutralinos in events with three leptons and missing transverse momentum in* $\sqrt{s} = 8$ *TeV* pp *collisions with the ATLAS detector*, JHEP **04** (2014) 169, arXiv: 1402.7029 [hep-ex].

[78] ATLAS Collaboration, *Search for the electroweak production of supersymmetric particles in* $\sqrt{s} = 8$ *TeV* pp *collisions with the ATLAS detector*, Phys. Rev. D **93** (2016) 052002, arXiv: 1509.07152 [hep-ex].

[79] ATLAS Collaboration, *Search for electroweak production of supersymmetric particles in final states with two or three leptons at* $\sqrt{s} = 13$ *TeV with the ATLAS detector*, Eur. Phys. J. C **78** (2018) 995, arXiv: 1803.02762 [hep-ex].

[80] CMS Collaboration, *Search for electroweak production of charginos and neutralinos in multilepton final states in proton–proton collisions at* $\sqrt{s} = 13$ *TeV*, JHEP **03** (2018) 166, arXiv: 1709.05406 [hep-ex].

[81] CMS Collaboration, *Combined search for electroweak production of charginos and neutralinos in proton–proton collisions at* $\sqrt{s} = 13$ *TeV*, JHEP **03** (2018) 160, arXiv: 1801.03957 [hep-ex].

[82] CMS Collaboration, *Search for new phenomena in final states with two opposite-charge, same-flavor leptons, jets, and missing transverse momentum in* pp *collisions at* $\sqrt{s} = 13$ *TeV*, JHEP **03** (2018) 076, arXiv: 1709.08908 [hep-ex].

[83] ATLAS Collaboration, *Luminosity determination in pp collisions at $\sqrt{s} = 8$ TeV using the ATLAS detector at the LHC*, Eur. Phys. J. C **76** (2016) 653, arXiv: 1608.03953 [hep-ex].

[84] ATLAS Collaboration, *Monte Carlo Generators for the Production of a W or Z/γ^* Boson in Association with Jets at ATLAS in Run 2*, ATL-PHYS-PUB-2016-003, 2016, URL: https://cds.cern.ch/record/2120133.

[85] T. Gleisberg, S. Höche, F. Krauss, M. Schönherr, S. Schumann et al., *Event generation with SHERPA 1.1*, JHEP **02** (2009) 007, arXiv: 0811.4622 [hep-ph].

[86] R. D. Ball et al., *Parton distributions for the LHC Run II*, JHEP **04** (2015) 040, arXiv: 1410.8849 [hep-ph].

[87] T. Gleisberg and S. Höche, *Comix, a new matrix element generator*, JHEP **12** (2008) 039, arXiv: 0808.3674 [hep-ph].

[88] Cascioli, Fabio and Maierhöfer, Philipp and Pozzorini, Stefano, *Scattering Amplitudes with Open Loops*, Phys. Rev. Lett. **108** (2012) 111601, arXiv: 1111.5206 [hep-ph].

[89] S. Schumann and F. Krauss, *A Parton shower algorithm based on Catani-Seymour dipole factorisation*, JHEP **03** (2008) 038, arXiv: 0709.1027 [hep-ph].

[90] S. Höche, F. Krauss, M. Schönherr and F. Siegert, *QCD matrix elements + parton showers: The NLO case*, JHEP **04** (2013) 027, arXiv: 1207.5030 [hep-ph].

[91] H.-L. Lai et al., *New parton distributions for collider physics*, Phys. Rev. D **82** (2010) 074024, arXiv: 1007.2241 [hep-ph].

[92] ATLAS Collaboration, *Multi-boson simulation for 13 TeV ATLAS analyses*, ATL-PHYS-PUB-2016-002, 2016, URL: https://cds.cern.ch/record/2119986.

[93] J. M. Campbell and R. K. Ellis, *An Update on vector boson pair production at hadron colliders*, Phys. Rev. D **60** (1999) 113006, arXiv: hep-ph/9905386.

[94] J. M. Campbell, R. K. Ellis and C. Williams, *Vector boson pair production at the LHC*, JHEP **07** (2011) 018, arXiv: 1105.0020 [hep-ph].

[95] S. Schumann and F. Krauss, *A Parton shower algorithm based on Catani-Seymour dipole factorisation*, JHEP **03** (2008) 038, arXiv: 0709.1027 [hep-ph].

[96] S. Höche, F. Krauss, S. Schumann and F. Siegert, *QCD matrix elements and truncated showers*, JHEP **05** (2009) 053, arXiv: 0903.1219 [hep-ph].

[97] S. Alioli, P. Nason, C. Oleari and E. Re, *A general framework for implementing NLO calculations in shower Monte Carlo programs: the POWHEG BOX*, JHEP **06** (2010) 043, arXiv: 1002.2581 [hep-ph].

[98] ATLAS Collaboration, *Simulation of top-quark production for the ATLAS experiment at* $\sqrt{s} = 13$ *TeV*, ATL-PHYS-PUB-2016-004, 2016, URL: https://cds.cern.ch/record/2120417.

[99] S. Frixione, P. Nason and C. Oleari, *Matching NLO QCD computations with Parton Shower simulations: the POWHEG method*, JHEP **11** (2007) 070, arXiv: 0709.2092 [hep-ph].

[100] P. Artoisenet, R. Frederix, O. Mattelaer and R. Rietkerk, *Automatic spin-entangled decays of heavy resonances in Monte Carlo simulations*, JHEP **03** (2013) 015, arXiv: 1212.3460 [hep-ph].

[101] T. Sjöstrand, S. Mrenna and P. Skands, *PYTHIA 6.4 Physics and Manual*, JHEP **05** (2006) 026, arXiv: hep-ph/0603175.

[102] J. Pumplin et al., *New generation of parton distributions with uncertainties from global QCD analysis*, JHEP **07** (2002) 012, arXiv: hep-ph/0201195.

[103] P. Z. Skands, *Tuning Monte Carlo Generators: The Perugia Tunes*, Phys. Rev. D **82** (2010) 074018, arXiv: 1005.3457 [hep-ph].

[104] M. Czakon, P. Fiedler and A. Mitov, *Total Top-Quark Pair-Production Cross Section at Hadron Colliders Through* $O(\alpha_S^4)$, Phys. Rev. Lett. **110** (2013) 252004, arXiv: 1303.6254 [hep-ph].

[105] M. Czakon and A. Mitov, *Top++: A Program for the Calculation of the Top-Pair Cross-Section at Hadron Colliders*, Comput. Phys. Commun. **185** (2014) 2930, arXiv: 1112.5675 [hep-ph].

[106] N. Kidonakis, *Two-loop soft anomalous dimensions for single top quark associated production with a* W^- *or* H^-, Phys. Rev. D **82** (2010) 054018, arXiv: 1005.4451 [hep-ph].

[107] N. Kidonakis, *Next-to-next-to-leading-order collinear and soft gluon corrections for t-channel single top quark production*, Phys. Rev. D **83** (2011) 091503, arXiv: 1103.2792 [hep-ph].

[108] M. Aliev et al., *HATHOR: HAdronic Top and Heavy quarks crOss section calculatoR*, Comput. Phys. Commun. **182** (2011) 1034, arXiv: 1007.1327 [hep-ph].

[109] P. Kant et al., *HatHor for single top-quark production: Updated predictions and uncertainty estimates for single top-quark production in hadronic collisions*, Comput. Phys. Commun. **191** (2015) 74, arXiv: 1406.4403 [hep-ph].

[110] J. Alwall, R. Frederix, S. Frixione, V. Hirschi, F. Maltoni et al., *The automated computation of tree-level and next-to-leading order differential cross sections, and their matching to parton shower simulations*, JHEP **07** (2014) 079, arXiv: 1405.0301 [hep-ph].

[111] T. Sjöstrand et al., *An Introduction to PYTHIA 8.2*, Comput. Phys. Commun. **191** (2015) 159, arXiv: 1410.3012 [hep-ph].

[112] ATLAS Collaboration, *Modelling of the $t\bar{t}H$ and $t\bar{t}V(V = W, Z)$ processes for $\sqrt{s} = 13$ TeV ATLAS analyses*, ATL-PHYS-PUB-2016-005, 2016, URL: https://cds.cern.ch/record/2120826.

[113] A. Lazopoulos, T. McElmurry, K. Melnikov and F. Petriello, *Next-to-leading order QCD corrections to $t\bar{t}Z$ production at the LHC*, Phys. Lett. B **666** (2008) 62, arXiv: 0804.2220 [hep-ph].

[114] J. M. Campbell and R. K. Ellis, *$t\bar{t}W^{\pm}$ production and decay at NLO*, JHEP **07** (2012) 052, arXiv: 1204.5678 [hep-ph].

[115] ATLAS Collaboration, *Multi-Boson Simulation for 13 TeV ATLAS Analyses*, ATL-PHYS-PUB-2017-005, 2017, URL: https://cds.cern.ch/record/2261933.

[116] G. Corcella et al., *HERWIG 6: An Event generator for hadron emission reactions with interfering gluons (including supersymmetric processes)*, JHEP **01** (2001) 010, arXiv: hep-ph/0011363.

[117] S. Dittmaier et al., *Handbook of LHC Higgs Cross Sections: 2. Differential Distributions*, CERN-2012-002 (2012), arXiv: 1201.3084 [hep-ph].

[118] J. Alwall, P. Schuster and N. Toro, *Simplified Models for a First Characterization of New Physics at the LHC*, Phys. Rev. D **79** (2009) 075020, arXiv: 0810.3921 [hep-ph].

[119] F. Maltoni and T. Stelzer, *MadEvent: Automatic event generation with MadGraph*, JHEP **02** (2003) 027, arXiv: hep-ph/0208156.

[120] ATLAS Collaboration, *ATLAS Pythia 8 tunes to 7 TeV data*, ATL-PHYS-PUB-2014-021, 2014, URL: https://cds.cern.ch/record/1966419.

[121] L. Lönnblad and S. Prestel, *Matching Tree-Level Matrix Elements with Interleaved Showers*, JHEP **03** (2012) 019, arXiv: 1109.4829 [hep-ph].

[122] W. Beenakker, R. Hopker, M. Spira and P. Zerwas, *Squark and gluino production at hadron colliders*, Nucl. Phys. B **492** (1997) 51, arXiv: hep-ph/9610490.

[123] A. Kulesza and L. Motyka, *Threshold resummation for squark-antisquark and gluino-pair production at the LHC*, Phys. Rev. Lett. **102** (2009) 111802, arXiv: 0807.2405 [hep-ph].

[124] A. Kulesza and L. Motyka, *Soft gluon resummation for the production of gluino-gluino and squark-antisquark pairs at the LHC*, Phys. Rev. D **80** (2009) 095004, arXiv: 0905.4749 [hep-ph].

[125] W. Beenakker et al., *Soft-gluon resummation for squark and gluino hadroproduction*, JHEP **12** (2009) 041, arXiv: 0909.4418 [hep-ph].

[126] W. Beenakker, S. Brensing, M. Kramer, A. Kulesza, E. Laenen et al., *Squark and gluino hadroproduction*, Int. J. Mod. Phys. A **26** (2011) 2637, arXiv: 1105.1110 [hep-ph].

[127] C. Borschensky et al., *Squark and gluino production cross sections in pp collisions at $\sqrt{s}$ = 13, 14, 33 and 100 TeV*, Eur. Phys. J. C **74** (2014) 3174, arXiv: 1407.5066 [hep-ph].

[128] M. Baak et al., *HistFitter software framework for statistical data analysis*, Eur. Phys. J. C **75** (2015) 153, arXiv: 1410.1280 [hep-ex].

[129] A. L. Read, *Presentation of search results: the CL_S technique*, J. Phys. G **28** (2002) 2693.

[130] ATLAS Collaboration, *Measurement of the top quark-pair production cross section with ATLAS in pp collisions at $\sqrt{s} = 7$ TeV*, Eur. Phys. J. C **71** (2011) 1577, arXiv: 1012.1792 [hep-ex].

[131] ATLAS Collaboration, *Search for new phenomena in events containing a same-flavour opposite-sign dilepton pair, jets, and large missing transverse momentum in $\sqrt{s} = 13$ TeV pp collisions with the ATLAS detector*, Eur. Phys. J. C **77** (2017) 144, arXiv: 1611.05791 [hep-ex].

[132] CMS Collaboration, *Search for physics beyond the standard model in events with a Z boson, jets, and missing transverse energy in pp collisions at $\sqrt{s} = 7$ TeV*, Phys. Lett. B **716** (2012) 260, arXiv: 1204.3774 [hep-ex].

[133] CMS Collaboration, *Search for physics beyond the standard model in events with two leptons, jets, and missing transverse momentum in pp collisions at $\sqrt{s} = 8$ TeV*, JHEP **04** (2015) 124, arXiv: 1502.06031 [hep-ex].

[134] ATLAS Collaboration, *Expected performance of missing transverse momentum reconstruction for the ATLAS detector at $\sqrt{s} = 13$ TeV*, ATL-PHYS-PUB-2015-023, 2015, URL: https://cds.cern.ch/record/2037700.

[135] ATLAS Collaboration, *Calibration of b-tagging using dileptonic top pair events in a combinatorial likelihood approach with the ATLAS experiment*, ATLAS-CONF-2014-004, 2014, URL: https://cds.cern.ch/record/1664335.

[136] ATLAS Collaboration, *Calibration of the performance of b-tagging for c and light-flavour jets in the 2012 ATLAS data*, ATLAS-CONF-2014-046, 2014, URL: https://cds.cern.ch/record/1741020.

[137] P. Athron et al., *Combined collider constraints on neutralinos and charginos*, The European Physical Journal C **79** (2019), ISSN: 1434-6052, URL: http://dx.doi.org/10.1140/epjc/s10052-019-6837-x.

[138] P. Athron et al., *GAMBIT: the global and modular beyond-the-standard-model inference tool*, The European Physical Journal C **77** (2017), ISSN: 1434-6052, URL: http://dx.doi.org/10.1140/epjc/s10052-017-5321-8.

[139] C. Balázs et al., *ColliderBit: a GAMBIT module for the calculation of high-energy collider observables and likelihoods*, The European Physical Journal C **77** (2017), ISSN: 1434-6052, URL: http://dx.doi.org/10.1140/epjc/s10052-017-5285-8.

[140] T. Bringmann et al., *DarkBit: a GAMBIT module for computing dark matter observables and likelihoods*, The European Physical Journal C **77** (2017), ISSN: 1434-6052, URL: http://dx.doi.org/10.1140/epjc/s10052-017-5155-4.

[141] F. U. Bernlochner et al., *FlavBit: a GAMBIT module for computing flavour observables and likelihoods*, The European Physical Journal C **77** (2017), ISSN: 1434-6052, URL: http://dx.doi.org/10.1140/epjc/s10052-017-5157-2.

[142] G. D. Martinez et al., *Comparison of statistical sampling methods with ScannerBit, the GAMBIT scanning module*, The European Physical Journal C **77** (2017), ISSN: 1434-6052, URL: http://dx.doi.org/10.1140/epjc/s10052-017-5274-y.

[143] P. Athron et al., *SpecBit, DecayBit and PrecisionBit: GAMBIT modules for computing mass spectra, particle decay rates and precision observables*, The European Physical Journal C **78** (2018), ISSN: 1434-6052, URL: http://dx.doi.org/10.1140/epjc/s10052-017-5390-8.

[144] T. Sjöstrand, S. Mrenna and P. Z. Skands, *PYTHIA 6.4 Physics and Manual*, JHEP **05** (2006) 026, arXiv: hep-ph/0603175.

[145] ATLAS Collaboration, *Search for supersymmetry in events with four or more leptons in $\sqrt{s} = 13$ TeV pp collisions with ATLAS*, Phys. Rev. D **98** (2018) 032009, arXiv: 1804.03602 [hep-ex].

[146] G. Aad et al., *Search for non-resonant Higgs boson pair production in the $b\bar{b}\ell\nu\ell\nu$ final state with the ATLAS detector in pp collisions at $\sqrt{s} = 13$ TeV*, Physics Letters B **801** (2020) 135145, ISSN: 0370-2693, URL: http://dx.doi.org/10.1016/j.physletb.2019.135145.

[147] ATLAS Collaboration, *Search for the standard model Higgs boson produced in association with top quarks and decaying into a $b\bar{b}$ pair in pp collisions at $\sqrt{s} =$ 13 TeV with the ATLAS detector*, Phys. Rev. D **97** (2018) 072016, arXiv: 1712.08895 [hep-ex].

[148] CMS Collaboration, *Search for $t\bar{t}H$ production in the $H \to b\bar{b}$ decay channel with leptonic $t\bar{t}$ decays in proton–proton collisions at $\sqrt{s} = 13$ TeV*, (2018), arXiv: 1804.03682 [hep-ex].

[149] F. Maltoni, M. Mangano, I. Tsinikos and M. Zaro, *Top-quark charge asymmetry and polarization in ttbar$W^{\pm}$ production at the LHC*, Physics Letters B **736** (2014) 252, ISSN: 0370-2693, URL: http://dx.doi.org/10.1016/j.physletb.2014.07.033.

[150] ATLAS Collaboration, *Measurement of the $t\bar{t}Z$ and $t\bar{t}W$ cross sections in proton–proton collisions at $\sqrt{s} = 13$ TeV with the ATLAS detector*, Phys. Rev. D **99** (2019) 072009, arXiv: 1901.03584 [hep-ex].

[151] CMS Collaboration, *Measurement of the cross section for top quark pair production in association with a W or Z boson in proton–proton collisions at $\sqrt{s} = 13$ TeV*, JHEP **08** (2018) 011, arXiv: 1711.02547 [hep-ex].

[152] ATLAS Collaboration, *Evidence for $t\bar{t}$ $t\bar{t}$ production in the multilepton final state in proton-proton collisions at $\sqrt{s} = 13$ TeV with the ATLAS detector*, ATLAS-CONF-2020-013, 2020, URL: https://cdsweb.cern.ch/record/2719519.

[153] A. M. Sirunyan et al., *Search for production of four top quarks in final states with same-sign or multiple leptons in proton–proton collisions at $\sqrt{s} = 13$ TeV*, The European Physical Journal C **80** (2020), ISSN: 1434-6052, URL: http://dx.doi.org/10.1140/epjc/s10052-019-7593-7.

List of Figures

List of Tables